Combined Neutron Imaging and Diffraction: Instrumentation and Experimentation

Thesis

Combined Neutron Imaging and Diffraction: Instrumentation and Experimentation

Thesis submitted to The Open University for the degree of

Doctor of Philosophy

in the Faculty of Mathematics, Computing and Technology (MCT)

By

Genoveva Burca

Materials Engineering Group

The Open University

September 2012

DATE of SUBMISSION: 30 SEPTEMBER 2012

DATE of AWARD: 13 APRIL 2013

ProQuest LLC.
789 East Eisenhower Parkway
P.O. Box 1346
Ann Arbor, MI 48106 – 1346

Abstract

A combined neutron imaging and diffraction facility, IMAT (Imaging and Materials Science & Engineering) is developed at ISIS (Target Station 2).

One subject of this thesis was focused on the design and optimization of the imaging part of IMAT, using the Monte Carlo calculation software package McStas. Hence, the neutron guide dimensions, the effects of the gaps in the neutron guide on imaging detectors, gravitation effects in the neutron guide and also the influence of the pinhole size on the image were studied. All these investigations were made taking into account the most important design criteria: to maximise the neutron flux, to obtain a good energy resolution whilst retaining a large neutron bandwidth and a long flight path and to minimize the artefacts obtained in the neutron radiographies.

After a compromise between imaging, diffraction and engineering requirements had been reached, the results from simulations specific to the current IMAT design were studied: wavelength distribution, beam profiles at different points along the beamline, beam divergence, neutron intensity distribution and flux depending on the pinhole size and the wavelength bands. Moreover, generation of IMAT imaging data with a sample led to full tomographic simulations and modelling wavelength effects.

Another objective of the thesis was to study the complementarity between neutron imaging and neutron diffraction experiments. For this, a new instrument control concept that exploits tomography data to guide diffraction experiments on samples with complex structures and shapes named "tomography driven diffraction" (henceforth, TDD) was developed. The method has been proved to be viable using combinations of individual tomography and diffraction instruments: NEUTRA (PSI) and ENGIN-X (ISIS) for different samples drawn from the engineering and heritage sciences. On IMAT it will be possible to perform tomography, mark the measurement points and proceed to the diffraction measurements as one continuous process.

Declaration

The studies outlined in this thesis were undertaken in the Materials Engineering Group, from The Open University, Milton Keynes, UK and supervised by Dr. Jon James, Prof. Mike Fitzpatrick and Dr. Winfried Kockelmann (ISIS). I declare that all of the work was performed by the author except where otherwise indicated, and this thesis has not been submitted in support of an application for another degree or qualification of this or any other university or other institution of learning.

Publications

Work included in this dissertation has been presented in the following publications and conference proceedings:

Journal papers:

Kockelmann W., Zhang S.Y., Kelleher J.F., Nightingale J.B., Burca G., James J.A. (2012). *IMAT – a new imaging and diffraction instrument at ISIS.* In: Physics Procedia (to appear)

Paradowska A.M., Tremsin A., Kelleher J.F., Zhang S.Y., Paddea S., Burca G., James J.A., Ahmed R., Faisal N.H., Grazzi F., Fest G., Andreani C., Civita F., Bouchard P.J., Kockelmann W., Fitzpatrick M.E. (2012). *Modern and Historical Engineering Components Investigated by Neutron Diffraction on ENGIN-X.* In: Journal of Solid Mechanics and Materials Engineering, vol.6, no.6, p.408-418.

Burca G., James J.A., Kockelmann W., Fitzpatrick M.E., Zhang S.Y., Hovind J., van Langh R. (2011). *A new bridge technique for neutron tomography and diffraction experiments.* In: Nuclear Instruments and Methods in Physics Research Section A. Accelerators, Spectrometers, Detectors and Associated Equipment, vol. 651, issue 1, p.229-235.

Van Langh R., James J.A., Burca G., Kockelmann W., Zhang S.Y., Lehmann E., Estermann M., Pappot A. (2011). *New insights of alloy compositions by studying renaissance bronze statuettes by combined neutron imaging and neutron diffraction techniques.* In: Journal of Analytical Atomic Spectrometry, vol.26, nr.5, p.949-958.

Conference proceedings:

James J.A., Burca G., Kockelmann W. (2009). *Image driven diffraction.* In: Proceedings of the 2nd Workshop on Neutron Wavelength Dependent Imaging, Abingdon, UK.

Zhang S.Y., Kockelmann W., Paradowska A., James J.A., Burca G., Chapon L. (2009). *IMAT: an Imaging and Engineering Facility for ISIS TS-II,* 5th International Conference on Mechanical Stress Evaluation by Neutrons and Synchrotron Radiation, Mito, Japan.

Burca G., James J.A., Fitzpatrick M.E., Kockelmann W., Kelleher J.F., Zhang S.Y., Hovind J., van Langh R. (2010). *Tomography driven diffraction experiments.* In: Proceedings of the 3rd Workshop on Neutron Wavelength Dependent Imaging, Saporo, Japan.

Acknowledgments

I would like to express my gratitude toward my supervisor Dr. Jon James, for his enthusiastic guidance, his effort, diligence and patience during these years materialised in intellectual assistance and support for my professional growth. I am also very grateful to my co-supervisor, Prof. Mike Fitzpatrick for providing me with the financial support which made my attendance to conferences and trainings possible. Both of them deserve my praise for unreservedly believing in me right from the beginning of my PhD studies. I thank my co-supervisor Dr. Winfried Kockelmann for his suggestions, introducing me into the Rietveld analysis world and remembering me to take a break from time to time. Without all your helpful comments and encouragements I would not have been able to complete this thesis!

Thanks are also due to the staff at ENGIN-X instrument, at ISIS, Dr. Anna Paradowska and Dr. Shu-Yan Zhang for their friendship, helpful discussions and support with the diffraction experiments.

I also kindly acknowledge Dr. Eberhard Lehmann and Peter Vontobel for valuable discussions during my imaging experiments at the NEUTRA instrument at the PSI.

I thank all the staff members of Materials Engineering Group (OU) and all my friends: Sue, David, Foroogh, Yuki, Gabriela, Richard. I thank Courtney for his openness, unreserved willing to help and most of all for his encouraging smile.

I would like thank to my wonderful parents, my parents in law, my sister Catalina and her husband for their love and moral support.

There is one person without whom this work would never been started, developed or finalised. This thesis is dedicated to you, my beloved husband, Cyprian!

Contents

List of Figures

List of Tables

1 Introduction

Neutrons form a highly penetrating radiation, passing through matter without damaging or structurally modifying it, a property that makes them the ideal tool for many kinds of complementary material investigations.

Among the experimental techniques which are using neutrons one should enumerate: neutron activation analysis related to the capture of neutrons and applied for isotope and element analysis [1-3], neutron imaging techniques [4] based on the capture and scattering of neutrons which provide information about the inner structure and, indirectly, about the composition of a sample due to the fact that different materials attenuate neutrons to a greater or lesser extent or neutron scattering experiments. Neutron diffraction [5] is one of the scattering methods offering data about a sample on the atomic level, such as the atomic arrangement within the sample or magnetic structure of the material. The combination of neutron imaging and neutron diffraction will enable a more complete characterization of a sample in a combined analysis. The neutron imaging data will help to improve and guide the diffraction measurements. Vice-versa, the diffraction data will give a structural interpretation of the imaging data. Combining imaging and diffraction measurements on one beamline will allow new types of experiments to be carried out, otherwise not possible with any other presently available single instruments (e.g. ENGIN-X at ISIS [6] for diffraction experiments or NEUTRA at PSI [7] for imaging applications).

The IMAT instrument at ISIS [8], which is one of the main subjects of this thesis, will be `the very first thermal and cold pulsed neutron imaging and diffraction facility for materials science, materials processing and engineering studies. IMAT will be the first neutron imaging instrument in the UK and the first facility at a pulsed neutron spallation

source. Others imaging facilities at the spallation sources are in the design process (VENUS at the SNS, Oak Ridge, USA [9] and ERNIS at J-PARC, Japan [10]).

In addition to the conventional neutron radiography, tomography and diffraction applications IMAT will be able to combine these techniques so that, for example, imaging information can be used to steer diffraction measurements. Further, because IMAT is being built at a pulsed source, it will be able to perform energy selective imaging applications, which offer improved contrasts between different materials and in the future, the possibility of tomographic strain measurements. Some pilot studies on the energy-selective imaging at a pulsed source were already been done at the ENGIN-X instrument ([11], [12]).

Combining different analysis techniques on one beamline imposes design constraints on the individual parts of the instrument which have to be solved without compromising the future instrument applications. Imaging applications require a large beam (in order of many cm^2) and highest possible neutron flux. Diffraction applications require a small beam (in order of mm^2) and a good spectral resolution. The choice of a coupled moderator ensures a high thermal and cold neutron flux for imaging and for rapid diffraction analysis. For a good diffraction resolution a long-flight path is required and this could be achieved by using of a neutron guide. Therefore, a supermirror neutron guide is required to combine imaging and diffraction modes at the same sample position. On the other hand, for neutron imaging the neutron beam profile at the sample position has to be homogeneous in space and time and the open beam images should be symmetric and smoothly varying. This requirement is at odds with the use of a neutron guide which causes geometrical artefacts and wavelength-dependent divergences. In order to minimise these effects and to maximize the neutron flux on the sample for imaging and diffraction experiments the neutron guide needs to be optimized.

The instrument optimization and evaluation can be done using Monte Carlo simulations. For this purpose a free simulation package software, McStas [13] was used for

reproducing the realistic neutron scattering instrument by assembling different virtual components into a computer model of the instrument.

To exploit the complementarity between the neutron tomography and neutron diffraction a new method, Tomography Driven Diffraction (TDD) [14], was developed. TDD allows a complete investigation of the object by 2D or 3D imaging where the characteristics of the whole sample are revealed, in the sense of dimensions, shape, internal defects or density and then uses these data to focus the diffraction analysis on particular components of the object for determining compositions, strain and texture.

TDD was demonstrated to be viable using combinations of individual tomography and diffraction instruments such as NEUTRA (PSI) and ENGIN-X (ISIS). Different structurally and complex samples drawn from engineering and heritage sciences were used for the experiments. Because the TDD method is ideally suitable on the coupled imaging-diffraction instruments, one future development is to apply this technique on the IMAT instrument. On such an instrument it will be possible to perform the tomography, mark the measurement points and proceed to the diffraction measurements as one continuous process.

The chapters of this dissertation are organised as follows: Chapter 2 provides an overview of the neutron sources and instrumentations, notions and techniques met in the neutron imaging and diffraction fields. Then, a summary of the instrument design methods and simulation packages used for designing an instrument is presented. Chapter 3 reports investigations into IMAT components, relevant to its performance as an imaging instrument based on the McStas modelling approach. The results were combined with similar investigations into the diffraction case (performed elsewhere and not part of this thesis) leading to the design considerations for the combined imaging and diffraction instrument, IMAT. Based on the preliminary results of Chapter 3 there were investigated in Chapter 4 particular aspects of the neutron beam relevant to future white beam or energy-selective imaging applications and performance of the complete IMAT imaging

instrument. Chapter 5 deals with the TDD method for exploiting the complementarity between the neutron tomography and neutron diffraction and illustrates its application to the samples selected from different fields (engineering and archaeometry). Chapter 6 discusses the final conclusions and points out future research lines.

In addition to the chapters, there are three appendixes containing additional information:

Appendix 1: presents the C++ code for the calculation of the projection of the image onto the moderator, reflection angle and number of neutron reflectivities in the neutron guide

Appendix 2: offers the IMAT imaging instrument model in McStas (the initial stage, used in the simulations from Chapter 3 of the thesis).

Appendix 3: displays the IMAT imaging instrument model in McStas (the last stage, used in the simulations from Chapter 4 of the thesis).

2 Neutron imaging and diffraction – a general overview

Neutron and X-rays are two types of radiation which can be used as complementary, non-destructive probes for material investigations over a wide range of length scales from centimetres to the size of the atoms [15].

2.1 Neutron properties and applications

Neutrons and X-ray photons are quite different in their natures: for example, the neutron has a mass and its energy depends on its velocity. On the other hand, the X-ray photon has no mass but is characterised by its wavelength. In the following sections we will review some aspects concerning the neutrons characteristics and their applications.

2.1.1 Neutron characteristics

The neutron was reported for the first time in 1932 by the English physicist James Chadwick. Only the hydrogen nucleus has no neutron; all other atoms have one or more neutrons in their nuclei. The neutron has no net electric charge; it is a spin $1/2$ particle with a mass (m_n) slightly larger than that of a proton,

$$m_n = 1.675 \times 10^{-27} kg.$$

The magnetic moment of the neutron (μ) is negative

$$\mu = -9.6491 \times 10^{-27} (\mathrm{JT}^{-1})$$

which means that the neutron has a tendency to align antiparallel to a magnetic field rather than parallel to the field. The non-zero magnetic moment of the neutron enables neutrons to be used to explore microscopic magnetic structures [16] and study magnetic fluctuations

[17], and thus the study of magnetic properties of materials using neutrons is significant in the neutron scattering and imaging field.

The concepts of quantum physics tell us that particles have wave-like and particle-like properties via the principle known as *wave-particle duality*. Neutrons are subject to this principle as described by the de Broglie relationship:

$$\frac{h}{\lambda} = mv; \quad E = \frac{h^2}{2m\lambda^2} \tag{2.1.1}$$

where λ is wavelength measured in Angstrom ($1\text{Å} = 10^{-10} m$); E is energy which is measured in Joules (J) or electron volts (eV) where $1eV = 1.602\times10^{-19} J$; m = mass; v = velocity; $h = 6.6261\times10^{-34} Js$ is the Planck constant.

Depending on their kinetic energy neutrons may be classified as follows:

Table 2.1.1: *Classification of neutrons according to their energy*[1]*([18]).*

	Wavelength, λ (Å)	Energy range	Velocity, v (m/s)
Ultra-Cold	≥500	≤300neV	≤8
Cold	26.1-2.6	0.12meV-12meV	152-1515
Thermal	2.6-0.9	12meV-100meV	1515-4374
Epithermal	0.9-0.28	100meV-1eV	4374-13.8×10^3
Intermediate	0.28-0.01	1eV-0.8MeV	13.8×10^3-39.56×10^4
Fast	<0.01	>0.8MeV	>39.56×10^4

While bound neutrons in stable nuclei are stable, free neutrons are unstable and they undergo radioactive beta decay into a proton, an electron and an electron antineutrino [5]. The time taken by neutrons in neutron scattering experiments to travel from source to the detector is considerably less than the time taken for half of the neutrons to decay (i.e.

[1] The classification of the neutrons is arbitrary and can vary in different contexts.

"half-life") of $\tau_{1/2} = \tau \ln 2 = 614\,\text{sec}$ where $\tau = 886 \pm 1\,\text{sec}$ is the "lifetime" of the neutron (i.e. the time after which the number of neutrons is reduced to $1/e$) [19].

Neutron interaction with matter and neutron cross-section

Neutron and X-ray radiations interact differently with materials. While a neutron of a particular wavelength interacts with the nucleus itself, an X-ray photon interacts primarily with the electrons surrounding the atomic nucleus. Due to their properties the neutrons easily pass through atoms, and so they form a highly penetrating radiation, interacting with matter through collisions with atomic nuclei.

The interaction between neutrons and matter is described by a numeric quantity known as the *neutron cross section*, which depends on the material properties and the neutron energy. The unit of the cross section is the barn ($1\text{barn}=10^{-24}\text{cm}^2$) and it has the dimension of the cross-sectional area of a chemical element towards an incoming neutron interacting with the material (i.e., analogous to the target size). For a compound (a material made up of a number of elements) the individual cross sections need to be summed over each element. The measure of the effective interaction area for a neutron with a single nucleus is defined by the *microscopic cross section* (σ). The units of the microscopic cross section are m^2. The *macroscopic cross section* $\Sigma\,(\text{cm}^{-1})$ defines the probability of interaction between a neutron and bulk material and has the formula $\Sigma = N\sigma$, where $N\,(\text{cm}^{-3})$ is the nuclear number density (i.e., the number of nuclei per unit volume) and is defined as $N = \frac{\rho}{A} A_0$ with A the atomic weight, $A_0 = 6.02 \times 10^{23}$ the Avogadro number and ρ the density.

The interaction of neutrons with matter can lead to the one of the following situations: scattering, absorption or transmission (Figure 2.1.1).

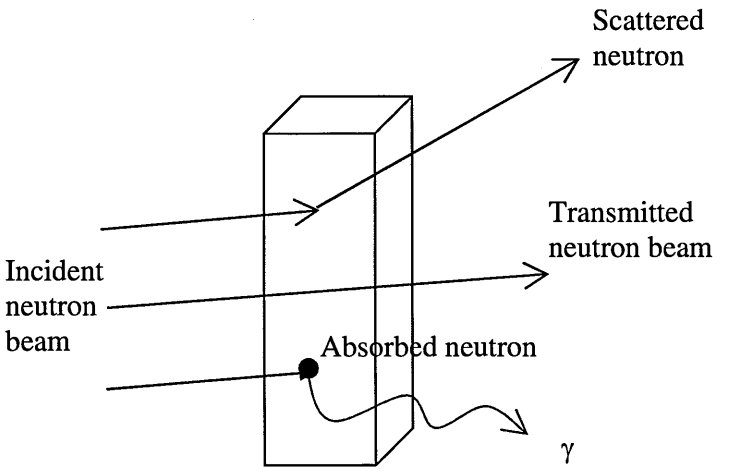

Figure 2.1.1: *The interaction of neutrons with matter.*

When a neutron is scattered by a nucleus, its speed and direction may be changed but the nucleus is left with the same number of protons and neutrons which it had before the interaction. There are two types of scattering events: elastic and inelastic. When the energy of the total system (in our case, the neutron and nucleus it collides with) is conserved, i.e. it is the same before and after the collision there was elastic scattering. Moreover, each type of scattering has a coherent and incoherent part (i.e. elastic coherent scattering, inelastic coherent, elastic incoherent and inelastic incoherent). A coherent event is one where the scattering may be considered as occuring at a number of centres simultaneously (e.g. nuclei in a lattice) such that the scattered waves interfere as described by Bragg's law. The incoherent scattering does not involve inference of neutron waves from different scattering centres, but results from scattering on individual atoms giving information about them.

Instead of being scattered by a nucleus, the neutron may be absorbed or captured. In this case, the nucleus internal structure is rearranged and one or more gamma rays is released (Figure 2.1.1).

Transmitted neutrons pass through the sample, without changing their direction. The overall intensity (relative to the incident neutron beam) is reduced depending on the thickness and density of the material through which the neutron beam is passed.

The total microscopic cross section can be written as $\sigma_t = \sigma_{\text{scattering}} + \sigma_{\text{absorption}}$ and the total macroscopic cross section as $\Sigma = \Sigma_{\text{scattering}} + \Sigma_{\text{absorption}}$. The macroscopic cross section is also known as *the attenuation coefficient* μ.

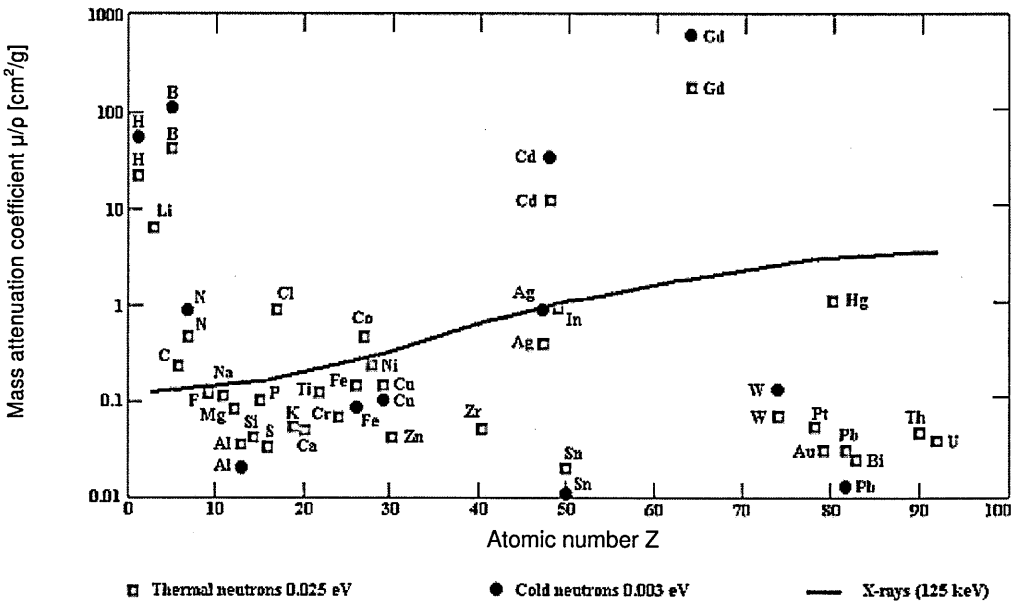

Figure 2.1.2: *The mass attenuation coefficient for neutrons and X-rays is plotted as function of atomic number [20].*

Neutrons and X-rays are considered to be complementary probes. For example if X-rays are less sensitive to light atoms, neutrons are particularly sensitive to hydrogen (the lightest atom). From Figure 2.1.2 we can see that the mass attenuation coefficients (i.e. the attenuation coefficient divided by the density of the target material, which represents a

measure of the probability for a reaction between a neutron, with a specific velocity, and the target material) increases, for X-rays, with atomic number. On the other hand, the neutron attenuation is more selective and depends on the nuclear characteristics as well as the neutron energy.

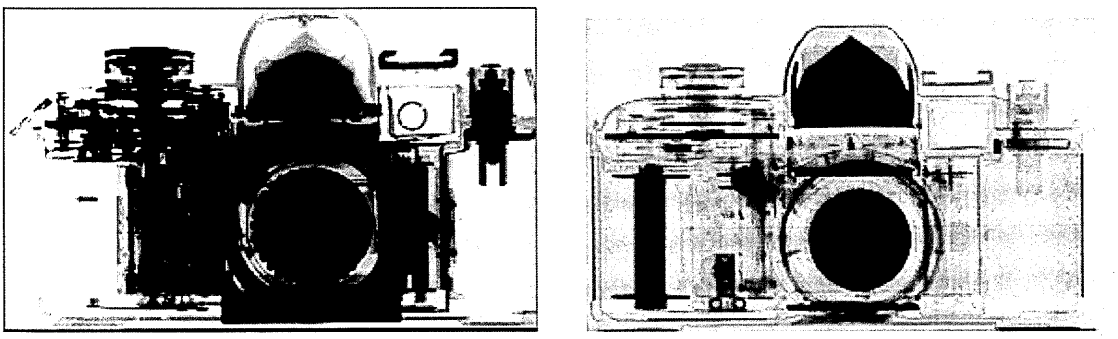

(a) (b)

Figure 2.1.3: *X-ray radiography (a) and neutron radiography (b) of a camera. While the X-rays visualise the metallic parts of the object, the neutrons have a greater penetration depth revealing the inside plastic parts (with a high hydrogen content) of the camera [21].*

For example, neutrons have a lower interaction with metals than do X-rays, leading to a relatively high penetration depth through these materials as shown in Figure 2.1.3.

2.1.2 Neutrons in material sciences

Neutrons are used for investigations in many fields related to industrial, engineering or scientific research as it will be exemplified throughout this thesis.

The complementarity of neutron and X-rays investigations has encouraged the option of making both available within one site, such as the Paul Scherrer Institute in Switzerland [18] (with Swiss Light Source, SLS [22] and Swiss spallation neutron source, SINQ [23]), The Harwell Science and Innovation Campus in Oxfordshire, UK [24] (with synchrotron science facility, Diamond Light Source [25] and neutron pulsed source, ISIS

[26]) and The European Photon & Neutron Science Campus in Grenoble, France [27] (with ESRF (Synchrotron Radiation Facility) [28] and the steady-state neutron source Institute Laue-Langevin [29]).

There are two basic groups of neutron experiments which allow different insights into the structure of materials: neutron imaging and neutron scattering. Whereas neutron imaging provides information about the inner structure and composition of a sample, based on the fact that different materials attenuate neutrons to a greater or lesser extent, the neutron scattering experiments offer data about a sample on the atomic level, such as the atomic motion, arrangement of atoms within the sample or magnetic structure of the material.

Neutron instruments are usually dedicated for a certain scattering or imaging approach, including diffractometers (e.g., ENGIN-X at ISIS [6]) providing structural determinations of the samples by elastic scattering, or spectrometers (e.g., TOSCA at ISIS [30]) giving information about atomic motions by inelastic scattering.

Scattering methods are successfully applied in fields such as engineering (in-depth determination of residual stresses in industrial components) [31], biology (in order to study the structure and dynamics of molecules and membranes), in medicine [32], or in geosciences (for examination of structure and compositions of rocks [33] and fossils [34]). The archaeological domain is another application field for neutrons where they allow non-destructive testing of archaeological artefacts and museum objects [35]. For instance, within the archaeological domain it could be possible to identify phase composition of objects or the crystal structures of the phases. Such data may be used to provide information about important aspects of such objects, including manufacturing methods and authenticity [36].

The disadvantages of using neutrons

Because of the weakly scattering nature of neutrons large samples may be required in order to produce sufficient signal. Also, neutron sources are generally characterized by relatively low fluxes when compared to, for example, synchrotron X-ray sources (radiation obtained by accelerating bunches of electrons at relativistic energies). For this reason they may have limited use in investigations of very rapid time-dependent processes. Among the financial disadvantages we can count the high construction cost of the neutron sources. Moreover, neutron scattering experiments are quite time consuming often taking several days. They are also expensive and take place at large-scale facilities with typical running costs of thousands of pounds per instrument per day.

2.2 Neutron production

The production of neutrons which are suitable for imaging or diffraction experimentation is a complex and expensive procedure. As well as the technical challenge of producing the neutrons there are certain sensitive aspects that need to be thoroughly considered in terms of biological protection and safety measures.

2.2.1 Neutron sources

Two methods are commonly used for generating neutrons for research purposes: 'fission' (in research reactors) or 'spallation' (in accelerator-driven spallation neutron sources). The common goals of neutron sources are to produce the highest possible neutron flux (expressed in number of neutrons/cm^2/second) and neutrons in the suitable energy range for certain applications (see Table 2.1.1).

2.2.1.1 Research (steady state) reactor sources

In reactors, fission takes place when a heavy nucleus such as Uranium-235 (U-235) is hit by a neutron which breaks it into two fission fragments, at the same time discharging two or three fast neutrons (Figure 2.2.1).

This process is illustrated by, for example, the equation [37]:

$$^{235}_{92}U + ^{1}_{0}n \rightarrow ^{236}_{92}U \rightarrow ^{144}_{56}Ba + ^{89}_{36}Kr + 3\,^{1}_{0}n + 177MeV \qquad (2.2.1)$$

where $^{1}_{0}n$ indicates neutrons produced by nuclear fission and 177 MeV is the energy released in this nuclear fission reaction.

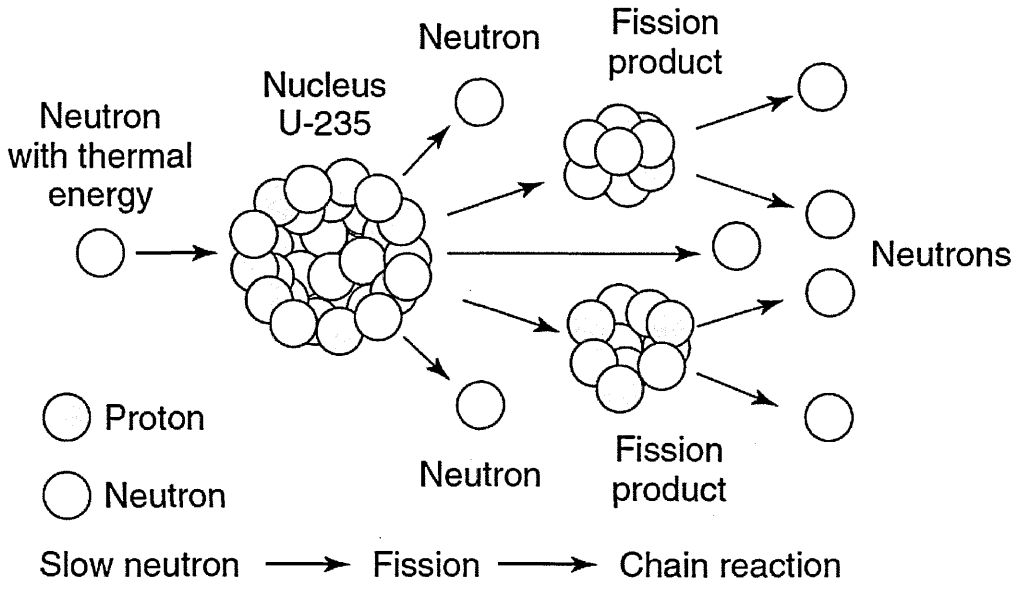

Figure 2.2.1: *Nuclear fission process [37].*

The fission reaction becomes self-sustaining considering the fact that one of the three free neutrons causes further fission in another U-235 generating a chain reaction. The remaining neutrons are either absorbed by materials that do not fission or escape from the system. The escaped neutrons will form the source of slow neutrons (after moderation) used for scattering experiments.

2.2.1.2 Neutron spallation (pulsed) sources

Neutrons can also be produced by the spallation process (Figure 2.2.2) in which high-energy particles (e.g. protons of energies from 100 MeV up to several GeV) collide with a target of dense and high-mass number material such as uranium, tungsten, tantalum or mercury. The spallation reaction is described by the following steps:

1. an internal nucleon cascade within the excited target nucleus;
2. an inter-nuclear cascade when high-energy particles including neutrons are ejected and absorbed by other nuclei;
3. de-excitation of the various target nuclei followed by the evaporation of many lower-energy neutrons and a variety of nucleons, photons and neutrinos;

Again, the escaped neutrons from these processes form the source of neutrons used for scattering and imaging experiments.

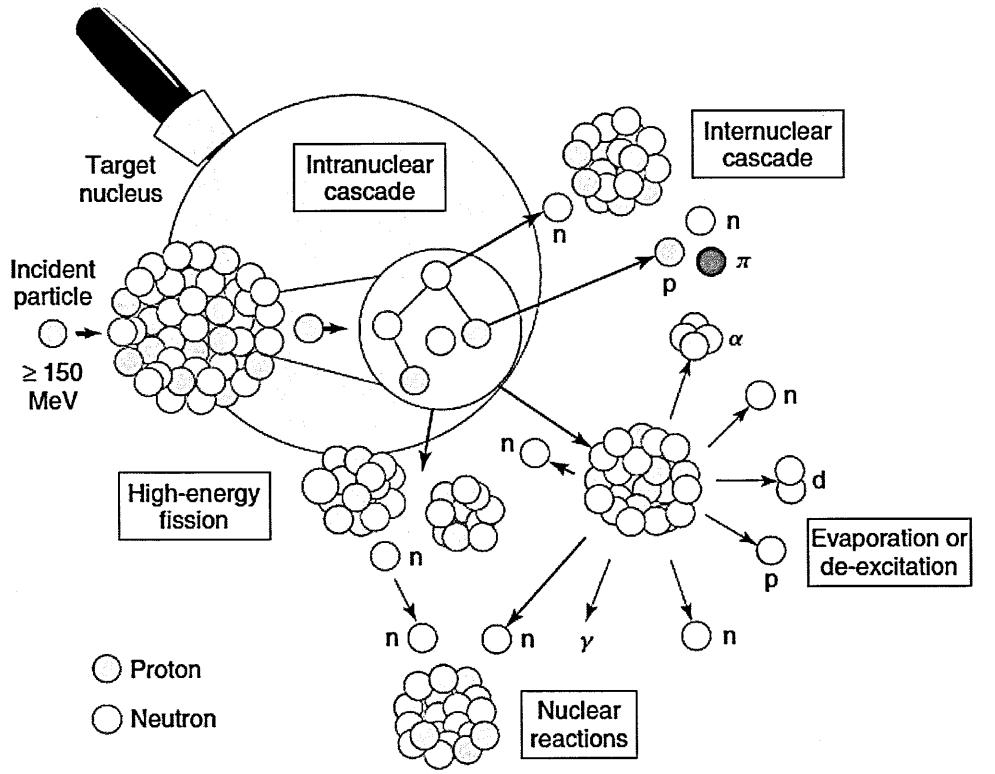

Figure 2.2.2: *Spallation process [37].*

Spallation neutron sources use a high energy proton beam which can be produced in one of following types of accelerator:

- Linear accelerator (linac) – is a high current and a high-repetition rate accelerator which directs the proton beam onto a target where neutrons are produced through spallation reactions.

At the end of the linac is placed a proton storage ring in order to compress the long pulses (1ms) into short pulses (1μs) and to extend the time between pulses necessary for neutron scattering experiments. This kind of linac is used at the SNS at Oak Ridge, USA [38].

Another alternative is to use the long pulse (≈2 ms) from the linac directly on the target, without the presence of a storage ring. The extra neutrons generated in this case can be used by specific instrumentation. The European Spallation Source is an example of the application of this method [37].

- Cyclotrons – these produce a continuous beam of energetic protons (590MeV) and generate a steady current of neutrons via a spallation reaction. The SINQ source at the Paul Scherrer Institute, Switzerland is an example of this approach [39].

- The synchrotron approach has a lower energy linac and a rapid cycling synchrotron. The synchrotron is basically a doughnut shaped vacuum tank with a large radius (e.g. 26m at ISIS) surrounded by a ring of magnets. The H^- ion beam produced in the linac passes through a thin alumina foil; the foil strips two electrons from the ions producing protons. These protons are injected into the synchrotron where they are accelerated to 1GeV or higher and then extracted into a single turn onto the target. The pulse length is about 1μs. This process repeats 10-60 times every second. The ISIS facility is a synchrotron-based spallation source [40].

The main advantage of the synchrotron over the linear accelerator is that the particles are going around many times, getting multiple kicks of energy every time around. From the financial point of view we can assert the building costs for the linear accelerators

are much lower than for the synchrotrons because they do not need magnets to drive particles in the ring [41].

2.2.2 Neutron moderators

Whether we are dealing with the steady-state reactors or spallation sources the "fast" neutrons produced by both of them have high energies of a few MeV. These neutrons must be moderated to obtain neutrons with energy and wavelength useful for scattering experiments.

2.2.2.1 Moderators in research reactors

The moderator is one of the main components of a research reactor. The moderator comprises of a material with a low atomic mass, such as light water, heavy water or graphite which does not absorb neutrons. The fast neutrons collide with the light nuclei from this substance and they are slowed down until they are in thermal equilibrium with the moderator. To control the neutron losses and to keep neutrons inside the reactor to give them a second chance to cause fission, the inner surface of the reactor core is surrounded by an external moderator which serves also as a reflecting material (reflector) with a low absorption of neutrons. In the area where the flux is maximum a beam tube is placed tangential to the reactor core (for minimising the background effects of the high fluxes of gamma rays generated by fission reaction or by decaying fission fragments) which extracts moderated neutrons from the reactor core.

The energy spectrum of the moderated neutrons obtained in a research reactor can be considered similar to the motion of atoms in an ideal gas and it has a statistical Maxwell-Boltzmann distribution determined by the temperature of the moderator:

$$E = \frac{h^2}{2m\lambda^2} = K_B \mathrm{T} \tag{2.2.2}$$

where K_B is Boltzmann's constant, which is in fact a conversion factor between energy and temperature units, and T is the moderator temperature.

In terms of the number of neutrons, the Maxwellian neutron distribution in the thermalized area is given by the relation ([42]):

$$n(E) = \frac{2\pi\sqrt{E}}{(\pi K_B \mathrm{T})^{3/2}} e^{-\frac{E}{K_B \mathrm{T}}} \tag{2.2.3}$$

Based on equation (2.2.3), the wavelength distribution of the thermalized neutron flux [42] can be described as well by the Maxwellian distribution (Figure 2.2.3):

$$\phi_{th} = \frac{E}{(K_B \mathrm{T})^2} e^{-E/K_B \mathrm{T}} \tag{2.2.4}$$

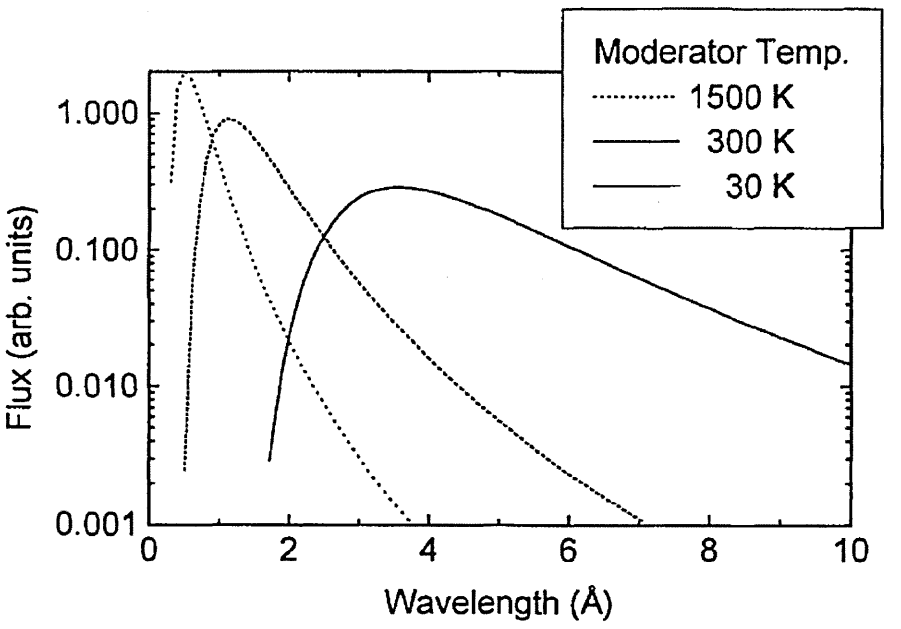

Figure 2.2.3: *Flux distribution corresponding to the operating temperatures of cold, thermal and hot moderators in reactors [43].*

Depending on the moderator temperature we have the following classification of neutrons: cold (moderated at 30 K), thermal (moderated at 300 K) and hot neutrons (moderated at 1500 K) (see also Table 2.1.1). Most research reactors are designed for a

moderator temperature 300-350 K corresponding to the middle curve in Figure 2.2.3. For some neutron experiments, such as small-angle scattering, there are used long-wavelength neutrons obtained from a cold source; these neutrons give a spectrum similar to the one shown in the right hand curve. For a shorter wavelength spectrum (i.e. higher energies) a hot source is employed.

2.2.2.2 Moderators in spallation neutron sources

The moderators on the pulsed sources have the main purpose to slow down the fast neutrons to the useful energies for scattering experiments. The under-moderated (partially moderated) neutrons created by the spallation sources are typically in the *epi-thermal* range. In addition, the moderators produce thermal or cold neutrons dependent on the moderator temperature. To provide a good coupling to the fast neutrons in the target, to maximise the neutron beam intensity and to maintain a narrow pulse, the moderators must be positioned closely to the primary source. Depending on the target size the moderator will have a different size and shape and this has implications on the neutron pulse shape. For pulsed neutron sources, the time spent by the neutrons in the moderator broadens the pulse. To obtain a very narrow pulse it is required to have a thin moderator (to reduce the time spent by the neutrons in the moderator) which yields a decrease in the time-integrated neutron flux and also in the peak intensity.

By controlling the temperature of the moderator, for example filled with liquid hydrogen or liquid methane, it is possible to slow down the fast neutrons to speeds corresponding to the desired wavelength range. The neutrons after moderation have a Maxwellian distribution at low energies and $1/E$ distribution at high energies depending on the temperature of the moderator (Figure 2.2.4).

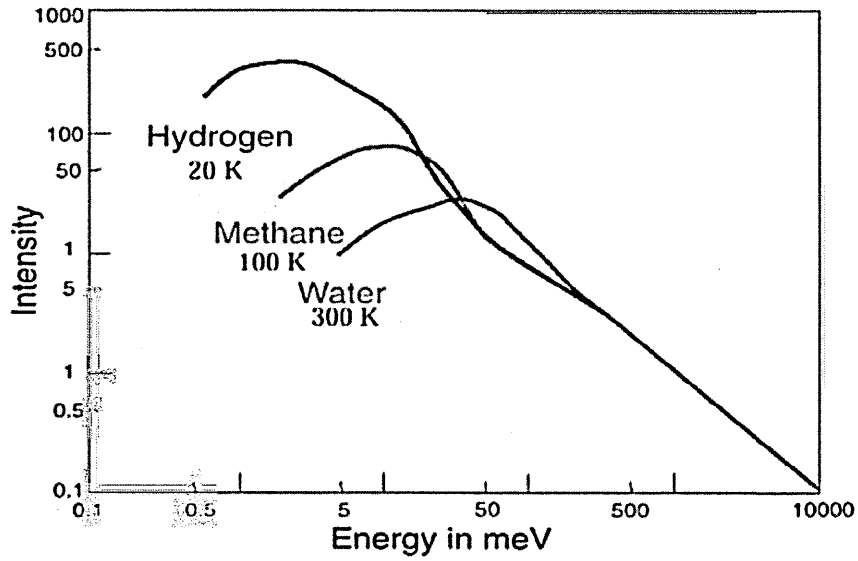

Figure 2.2.4: *Maxwellian neutron thermalization distributions for ISIS moderator temperatures of 20, 100 and 300 K [44]. The colder moderator has a higher neutron flux for a given energy interval ΔE in the area where the spectrum has a maximum.*

The neutrons that missed the moderator can be reflected into the moderator using a reflector that surrounds the target and moderator. Moreover, to the neutrons that were moderated or partially moderated in the moderator and leave the moderation into a direction different from the instrument port give a chance to be reflected back into the moderator and further to be slowed down. These neutrons have then the opportunity to leave the moderator in the direction of the beam port. The reflector materials used, such as Be, D_2O, C or Ni, must have a minimal absorption, a large scattering cross section and low atomic mass. Introducing a reflector causes the pulse to broaden since the neutrons can spend a longer time in the reflector before going to the moderator. In that case, to control the width of the moderated pulse, cut off long tails in the neutron pulses and keeping the high peak intensity a decoupling material (sheets of Gd or Cd), surrounding the whole moderator vessel, separates the moderator from the surroundings (reflector). This is true for slow neutrons because Gd and Cd are transparent for epithermal and fast neutrons. A decoupled moderator can have additionally a poisoning foil inside the moderator container

which has the function of limiting the depth of the moderator viewed by the instrument port. Also, the foil has an additional sharpening effect on the pulse shape.

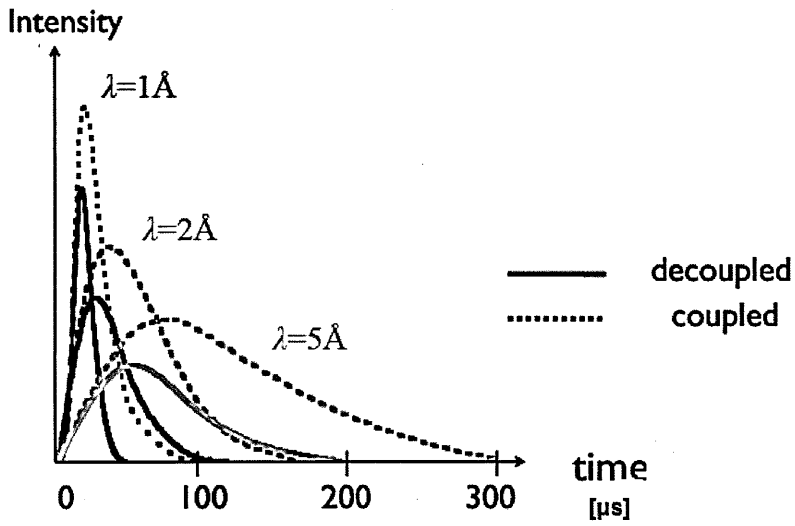

Figure 2.2.5: *The pulse shape diagram after moderation for a spallation pulsed source. The pulse width depends on the moderator type and the energy used. The decoupled moderator produces a more narrow pulse than a coupled moderator at the cost of flux [44].*

If there is no barrier for neutron transport between reflector and moderator, the moderator is considered fully coupled. So, the reflected neutrons can return to the moderator and hence a coupled moderator will generally produce a flux several times that of a decoupled moderator, but at the cost of a broader pulse (Figure 2.2.5), since neutrons can spend longer time in the reflector and the moderator before going out from the moderator.

2.2.3 Examples of neutron sources

Some of the reactor sources optimized for neutron scattering applications are:

Institute Laue-Langevin (ILL - Grenoble, France) built in 1972 ([45], [46]), FRM-II in Munich, Germany [47], BENSC (The Berlin Neutron Scattering Centre) in Germany [48], JRR3 at the Japan Atomic Energy Agency [49], OPAL at the Australian Nuclear Science

and Technology Organisation [50], HANARO at the Korea Atomic Energy Research Institute [51] and CARR at CIAE (China) [52]. All the reactors (except, ILL) are medium-sized research reactor sources (power 10-20 MW).

As already mentioned in the paragraph 2.2.1.2, spallation sources can be continuous or pulsed.

➢ ***Continuous spallation source***

The only continuous spallation source is at the Paul Scherrer Institute, SINQ, Switzerland [23].

➢ ***Pulsed spallation sources***

- *Short-pulse spallation source*

These sources are at ISIS (Oxfordshire, UK) ([53], [26]) , LANSCE (Los Alamos Neutron Science Center, USA) ([54]), SNS (Oak Ridge, Tennessee, USA) ([55]) and J-PARC (Tokaimura, Japan) ([56]).

- *Long-pulse spallation sources*

An example is the ESS (European Spallation Source) ([57]) in Lund, Sweden, a project in development including 17 European Partner Countries. The ESS is scheduled to produce first neutron beams in 2019.

An important difference between long-pulse sources and short-pulse sources comes from the time required to generate the neutron pulse. Hence, if the time required to generate the pulse is significantly shorter than the moderation time of the neutrons, then the source can be classified as a short-pulse source; when this time is comparable or greater than the moderation time the source is a long-pulse source.

The spallation sources and research reactors (steady state sources) are complementary, each of them being optimized for different types of experiment (see section 2.4.1). Whilst, the neutron reactors provide the maximum neutron fluxes that are available at the current stage the spallation sources have not yet attained the neutron flux limit from the research reactors.

Time-of-flight method

Fundamental to the time-of-flight method is the pulsed nature of the beam. Each pulse obtained in the spallation process contains a wide range of wavelengths (energies), and the beam is known as "polychromatic" or "white-beam".

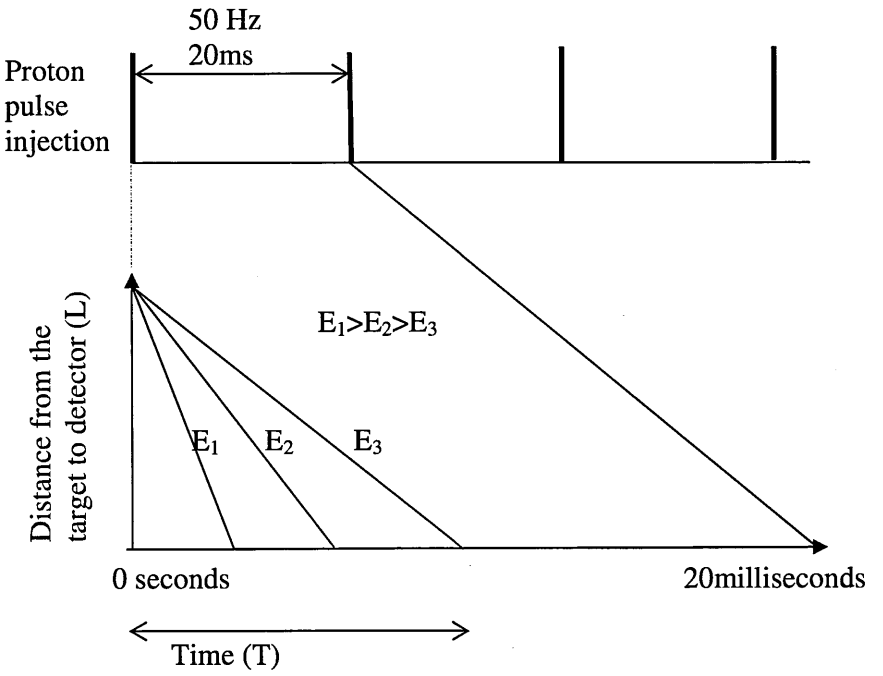

Figure 2.2.6: *Schematic description of Time-of-Flight method adapted from [58].*

The neutron energy (and hence its wavelength) can be determined from the distance it has travelled to the detector position (L) and the travel time (T) taken to do so and is given by equation (2.2.5), as follows:

$$E = \frac{m}{2}\left(\frac{L}{T}\right)^2 ; \ \lambda = \frac{hT}{mL} \tag{2.2.5}$$

For long flight paths it is possible to have frame overlap between one pulse and the next. This problem can be solved by using disc choppers to reduce the range of wavelengths in the neutron pulse (see section 3.5.1).

Because the IMAT instrument is developed at the ISIS neutron pulsed source we will explore below the main characteristics of this source.

The ISIS neutron pulsed source

The ISIS accelerator starts with the ion source creating negatively charged hydrogen ions made up of two electrons and one proton. The ions are accelerated from 35 keV to 665 keV in the first accelerator, called the Radio Frequency Quadrupole (RFQ), which focuses them into the second accelerator, the linac (70 MeV). The ions are then transported into the third accelerator, the synchrotron (800 MeV) (Figure 2.2.7). From the synchrotron two bunches of protons (of 800 MeV) are extracted which are guided by magnets along an evacuated beamline to the target stations. The average beam current is about 200 μA (2.9×10^{13} protons per pulse). Initially (1984) at ISIS one Target Station (TS-1) was built which operates at 50 Hz. This target was made, in the early years, from uranium, but now is made from tantalum coated tungsten. More recently (2003), a second Target Station (TS-2), also using a tantalum coated tungsten target, was built in order to allow new instruments to be added. On TS-1 40 proton pulses per second (thermal power 148 kW) are sent to obtain almost 15-20 neutrons/proton, i.e. 4×10^{14} neutrons/pulse. On target 2 the proton beam is operated with a frequency of 10 Hz, i.e. 10 proton pulses per second (thermal power 36 kW). With this frequency and the moderators used Target 2 is optimized to provide cold neutrons. One pulse from five generated by the synchrotron ISIS is directed to TS-2.

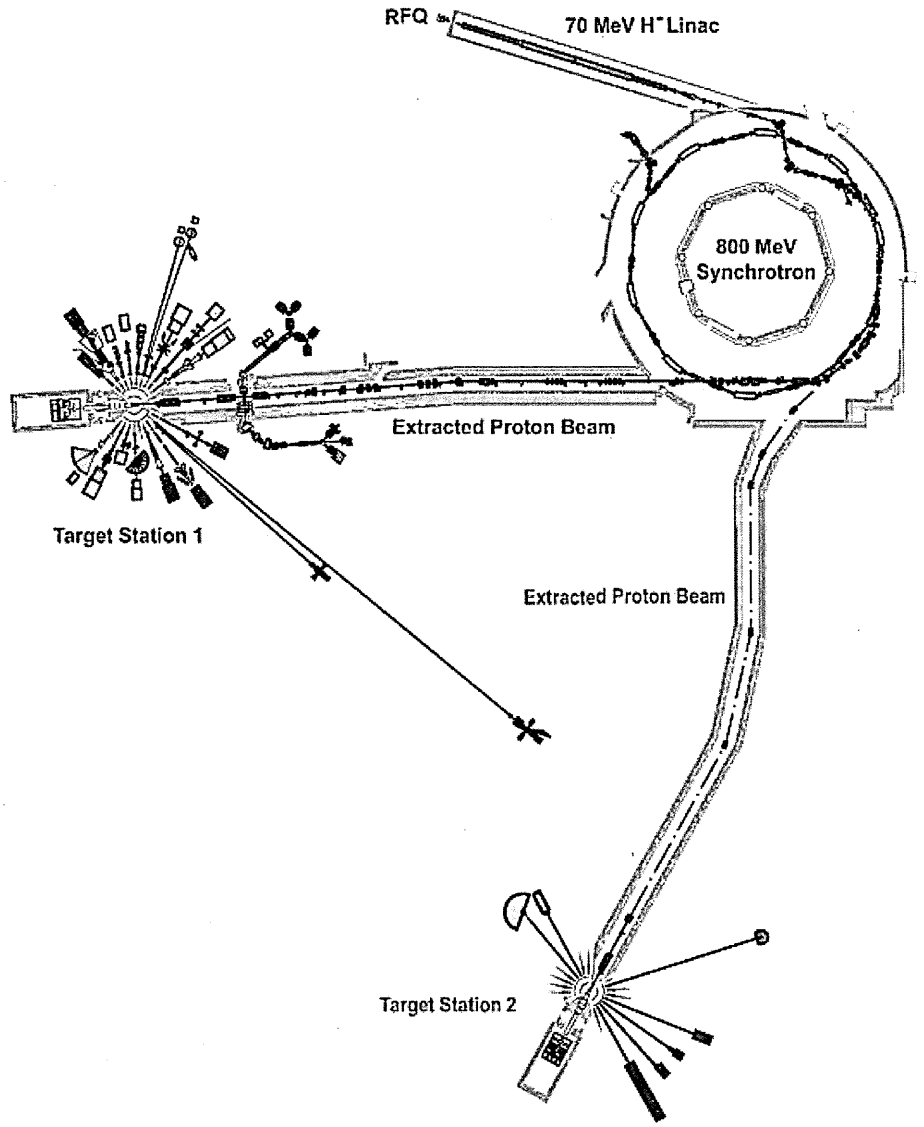

Figure 2.2.7. *Schematic diagram of ISIS accelerators and targets [59].*

TS-1 is surrounded by a beryllium reflector and four moderators are placed close to the target: the first two are water moderators at ambient temperatures, providing thermal neutrons and narrow pulse widths, the third moderator material is liquid methane at 100 K providing cold neutrons and a narrow pulse width, and the last is a liquid hydrogen moderator at 20 K offering cold neutrons with high intensity and wide pulse width.

The design of the 2nd Target Station was optimized for long wavelength neutrons and allows the moderators to be positioned very close to the target, leading to an important gain in moderated neutron flux. In that case, the low power of the proton beam required

appropriate design of target and moderator for the optimization of long neutron wavelength production which should be more efficient than those on TS-1 [60]. TS-2 produces neutrons of two pulse shape categories: one of wide pulse with full width at half-maximum height no larger than about 500 μs generated by a coupled moderator, and the other a pulse shape decoupled moderator at 30-50 μs.

The coupled moderator is a composite liquid hydrogen (L-H_2) 22 K – solid methane (S-CH_4) 26 K moderator without a decoupler or poisoning layer, generating a long-wavelength flux with broad pulse shapes from both faces. The (S-CH_4) 26 K decoupled moderator has two faces with solid-methane, one giving a narrow pulse shape but much cooler neutrons similar to the liquid methane moderator and the other a broader pulse shape (also, much cooler) similar to the hydrogen moderator.

2.3 Neutron imaging

In this thesis we are concerned with both imaging and diffraction based neutron investigations and moreover, with the modelling of the imaging part of the IMAT instrument. Therefore, in the following sections, we briefly review both these techniques. We begin by looking at the fundamentals of neutron imaging.

2.3.1 Fundamentals

Exploiting neutron properties such as deep penetration into a sample, hydrogen detection, and the ability to interact with external magnetic fields via the neutron's magnetic moment, various techniques of neutron imaging have been developed over the last few decades. The term *neutron radiography* was used to describe the direct production of images by transmitting a neutron beam through a sample onto a detector. Later, this method was

extended to *neutron tomography,* where, by rotating the sample in the neutron beam at an angular range from 0° to 180° (or even 360°, depending on the beam divergence and the sample size) and taking neutron radiographies of the sample, a complete three dimensional representation of the object can be reconstructed. From a mathematical point of view, tomography is defined by this reconstruction of a three-dimensional object from its projections.

There are three types of the beam geometries used to obtain sample projections: parallel beam, fan beam and cone beam (Figure 2.3.1).

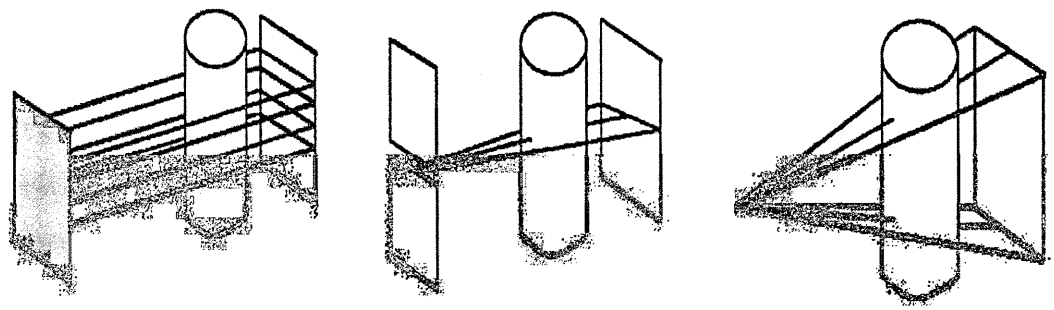

Figure 2.3.1: *Parallel beam, fan beam and cone beam geometry [61].*

Cone beams are produced naturally since the radiation is emanated equally in all directions from a source point. In fan beam geometry the rays at a given projection angle diverge and they have a fan aspect. If we take a small portion of a cone beam far from the source (at large distance) we can approximate that all rays are almost parallel, so we have a parallel beam. For cone and fan beam geometries the images are magnified allowing to identify various features, but with the cost of distortions. Whereas the fan and cone beams require a rotation of the object for measurement of at least $180^\circ + \alpha$ where α is the angle of the fan or the cone, for the parallel beam it is required sample's rotation of 180°, since any projection of the object $P_\theta(t)$ (see section 2.3.3.1) will be an exact mirror image of the projection $P_{\theta+180^\circ}(t)$. Hence, the number of projections necessary for sample

reconstruction in the parallel beam is less in principle, leading to a shorter exposure time. In practice, sample rotations of 360° are often applied to avoid varying blurring conditions for different parts of a sample (see below).

Whilst the fan beam and cone beam geometries are applied at the point sources (X-ray tubes and linear accelerators), the parallel beam (exhaustively presented in [62]) is specific to the synchrotron radiation and neutron beamlines.

2.3.2 Neutron radiography

The basic principle of neutron radiography (NR) is that a neutron beam passing through a sample is attenuated. The detector registers the fraction of the initial beam intensity that remains after it has been transmitted by each point in the object. Neutron radiography is found to be very useful for thick samples with high-density components which can be impenetrable to X-rays.

The relationship between the incident intensity (I_0) and the transmitted intensity (I) of the neutron beam is given by the exponential attenuation law:

$$I = I_0 e^{-\mu t} \tag{2.3.1}$$

where μ is the attenuation coefficient along the path of the neutron through the sample and depends on the selected material and its density (see section 2.1.1) and t is the sample's thickness along this path. The inverse of μ is called the mean free path of the neutrons in the material.

The ratio between the transmitted and incident neutron beam is called *transmission*:

$$Tr = \frac{I}{I_0} = e^{-\mu t} \tag{2.3.2}$$

Hence, depending on the sample thickness the incident intensity is affected by an exponential decrease.

The geometry of neutron radiography

A schematic neutron radiography system involves four main components: neutron source, collimator, object and detector. For neutron radiography purposes the neutrons used are thermal or cold because most materials provide a higher attenuation for low energy neutrons. For this reason, the neutrons generated from a source which are too fast to be helpful for radiographic experiments are thermalized in the moderator. Because the moderator scatters the neutrons in all directions a collimator system ([63], [64]) is required to form the moderated neutrons into a useful neutron beam in order to reduce the propagation direction of the radiation and to obtain a well defined image of the sample. The beam intensity emanated by a neutron source decreases at a specific distance r, inversely proportional to the distance from the source, $\frac{1}{r^2}$, according to the inverse square law. Many of the neutron radiography facilities are using, currently, the pinhole geometry [65] for neutron beam collimation. The pinhole, placed close to the neutron source, is a small aperture with a circular shape (with a diameter D) in order to obtain a symmetric image (see section 3.6).

Image quality from neutron radiography

The quality of a radiographic image collected over a finite measurement time depends on several parameters. The most important are:

- The incident neutron flux $\Phi = \frac{neutrons}{cm^2 \times \sec}$;
- The beam divergence L/D, as expressed by the ratio of the pinhole-sample distance (L) and the pinhole diameter (D).
- Detector characteristics such as resolution.
- The distance of the sample from the detector (l).
- Any motion of the sample during the experiment or other physical issues.

The divergence of the neutron beam at the sample position is defined by the ratio L/D:

$$\tan\alpha = \frac{D}{L} = \frac{1}{L/D} \tag{2.3.3}$$

where α is the divergence angle, L is the distance between pinhole and object and D is the opening (diameter) of the aperture (Figure 2.3.2a).

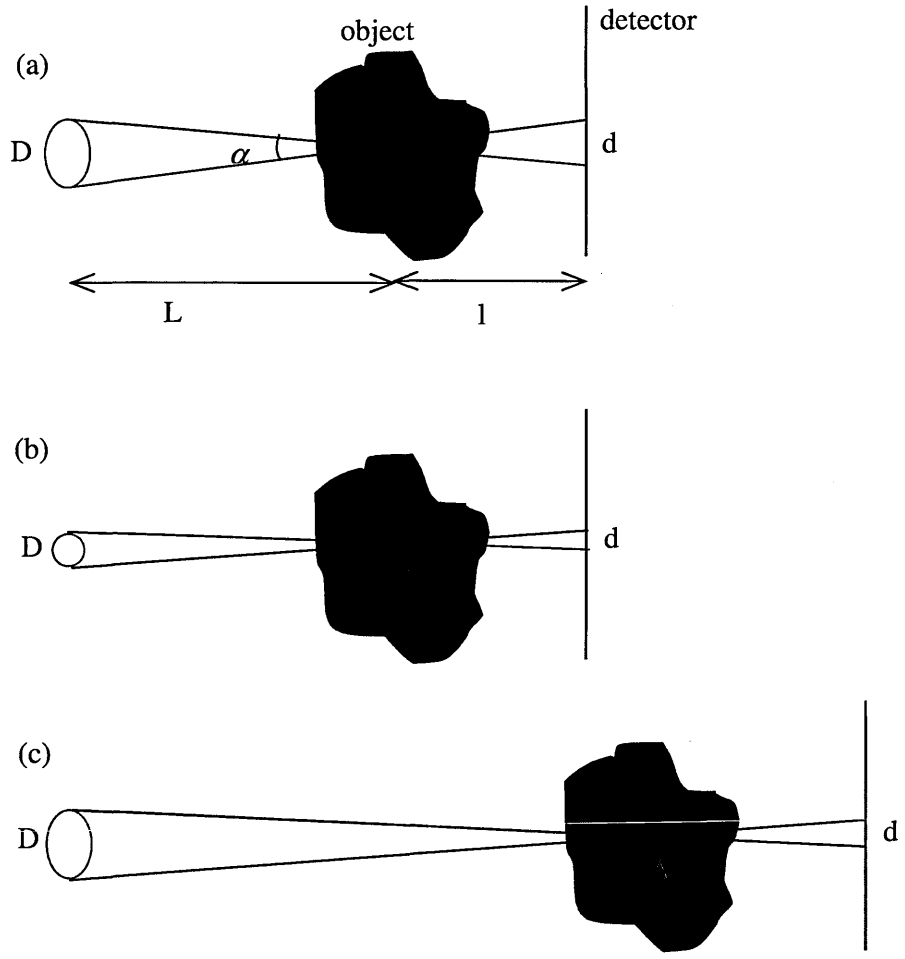

Figure 2.3.2: *The geometry of the system, and thus the quality of the radiography, can be controlled by varying the size of the pinhole (D), changing the distance between sample and pinhole (L) or the distance object-detector (l). The point A selected in the object is enlarged up to an area with the diameter (d) on the detector as* $d = \frac{l}{L/D}$.

For each radiographic set-up, the ratio L/D must be adapted to certain conditions including the neutron flux, spatial resolution of the detector, and size of the sample. If the distance L is constant, a larger collimation ratio L/D will produce a sharper image, but, unfortunately at the cost of a lower neutron flux (Figure 2.3.2b). Inversely, a smaller L/D conducts to a larger beam size (gaining in the neutron flux) and more divergent, producing a "blurred" image (Figure 2.3.2a). The point A (selected arbitrarily from within the sample) is blurred up to geometrical resolution,

$$d = l \cdot \left(\frac{L}{D}\right)^{-1} \tag{2.3.4}$$

In addition to the blurring effect the image size is magnified (enlarged) with the magnification factor $M = \frac{L+l}{L}$. To minimise the magnification effect and to realize a point-to-point image, a longer L distance is required, despite the lower neutron flux (Figure 2.3.2c).

Moreover, the object needs to be placed close to the detector to reduce the sample blur edges to zero. If the object is moved away by the detector, the object is magnified onto the detector, so the blur of the edges will appear.

If on neutron radiography station neutron optical devices such as neutron guides are used to transport the neutrons to the sample they can influence the beam divergence and beam cross section. This issue will be discussed in detail in Chapter 3 and Chapter 4.

To eliminate or minimise the inhomogeneities of the images obtained due to the spatial variations in intensity caused by the beam onto the radiography or due to the noise generated by the camera system one uses the *normalization* procedure. At the same energy range and exposure time, images are taken with and without the sample present in the beam. The image taken with the sample in the beam is then divided by the "open beam image" (without sample), with the result that variations due to beam inhomogeneity are removed.

2.3.3 Neutron tomography

The step from neutron radiography to neutron tomography may seem small but is quite significant. It consists in the creation of three-dimensional sample information from multiple projections from different directions, as produced by rotating the sample in small angular steps through 180° or 360°.

2.3.3.1 Mathematics of neutron tomography

The theory of tomographic reconstruction using parallel beam is detailed in [62]. Here it will be given only a summary.

Tomography is performed in two major steps:

- *data acquisition* (recording of projections)
- *image reconstruction from projections*

A three-dimensional map of the attenuation coefficients of the sample can be reconstructed using a computed tomography method presented in [62] from a set of transmission images of the sample rotated by different angles (Figure 2.3.3).

The volume coordinate system is (x, y, z) defined by the neutron beam in y-direction. The coordinate system (t, s, z) is attached to the sample after its rotation around the z- axis by the angle θ. The object may be considered as divided into thin slices parallel to the (x, y) plane. Each slice is a two-dimensional function $f(x, y)$ which describes the position-dependent attenuation coefficient $\mu(x, y)$. The slices are scanned at the different angles (θ) from 0° to 180°, with equal angle steps and their projections, $P_\theta(t)$, are measured. After a rotation, the equation of the ray line in the s direction is

$$x\cos\theta + y\sin\theta = t \tag{2.3.5}$$

The transmitted intensity of the rays follows the Lambert-Beers attenuation law

$$I_\theta(t) = I_0(t)\, e^{-\int_{path} \mu(x,y)ds} \tag{2.3.6}$$

as generalisation of equation (2.3.1).

The projection $P_\theta(t)$ is defined as

$$P_\theta(t) = \ln\left(\frac{I_0(t)}{I_\theta(t)}\right) = \int_{path} \mu(x,y)ds \tag{2.3.7}$$

Depending on the new reference system, the relation (2.3.7) can be reformulated such that:

$$P_\theta(t) = \int_{-\infty}^{\infty}\int_{-\infty}^{\infty} \mu(x,y)\,\delta(x\cos\theta + y\sin\theta - t)dxdy \tag{2.3.8}$$

where $\delta(x)$ is the Dirac delta function (it selects the path of the line integral) [62]. We replace from this point forward the function $\mu(x,y)$ with the general function $f(x,y)$.

The collection of all projections $P_\theta(t)$ of $f(x,y)$ is called the *Radon transformation* of $f(x,y)$. The acquisition of data from medical imaging involves a similar process of projecting the beam through a sample and the data is described in a similar way to equation (2.3.7) of Radon transformation [66]. The plots of Radon transformations as a function of angles is known as *sinogram* due to its characteristic sinusoid shape (in practice, sinogram is usually a 2D data obtained after stacking together all projections taken for different angles).

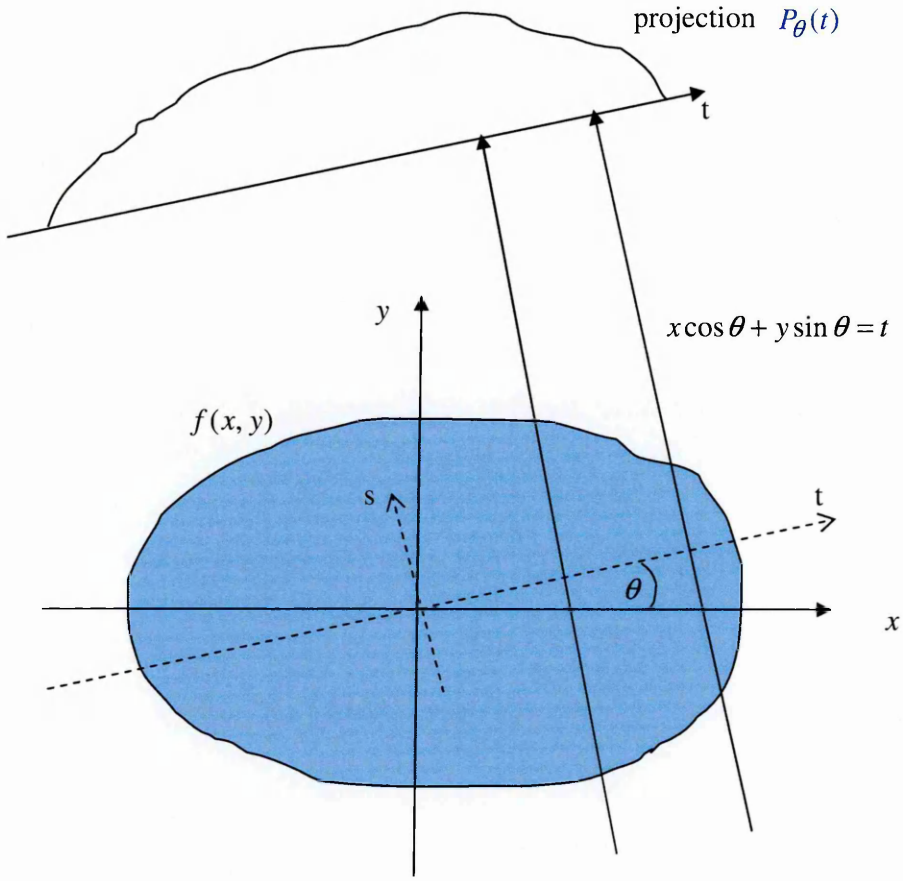

Figure 2.3.3: *The sample* $f(x, y)$ *is rotated and a slice is scanned in the plane* (x, y); *the line integral is measured as its projection* $P_\theta(t)$.

A two-dimensional image is reconstructed from the projections $P_\theta(t)$ using the Fourier Slice Theorem:

> *1D Fourier transform of a projection taken at angle* θ *equals the central radial slice at angle* θ *of the 2D Fourier transform of the original object.*

Schematically, this can be rewritten as:

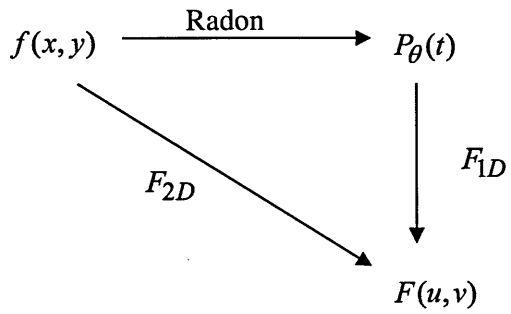

Figure 2.3.4: *The Fourier Slice theorem representation.* $F(u,v)$ *is the 2D Fourier transform of the function* $f(x,y)$ *where* $u = w\cos\theta$ *and* $v = w\sin\theta$.

Giving the projection data $F(u,v)$ and applying the 2D inverse Fourier transform we can estimate the object, i.e. $f(x,y)$ (Figure 2.3.4).

From a mathematical point of view we can summarize the Fourier Slice Theorem as follows:

- We will define first the 2D Fourier transform of the function $f(x,y)$ as:

$$F(u,v) = \int_{-\infty}^{\infty}\int_{-\infty}^{\infty} f(x,y)e^{-2\pi i(ux+vy)}dxdy \tag{2.3.9}$$

where $u = w\cos\theta$ and $v = w\sin\theta$.

- For a specific angle θ the 1D Fourier transform of the projection $P_\theta(t)$ is

$$S_\theta(w) = \int_{-\infty}^{\infty} P_\theta(t)e^{-2\pi iwt}dt \tag{2.3.10}$$

For a particular situation $\theta = 0$ (i.e. $v = 0$) when the coordinate system (x,y) coincides with (u,v), equation (2.3.9) is reformulated such as:

$$F(u,0) = \int_{-\infty}^{\infty}\int_{-\infty}^{\infty} f(x,y)e^{-2\pi iux}dxdy \tag{2.3.11}$$

The integral from relation (2.3.11) can be split into two parts:

$$F(u,0) = \int_{-\infty}^{\infty}\left[\int_{-\infty}^{\infty} f(x,y)dy\right]e^{-2\pi iux}dx \tag{2.3.12}$$

where the term in the square bracket represents the equation of a projection along a line, $P_{\theta=0}(x)$. In that case, equation (2.3.12) becomes:

$$F(u,0) = \int_{-\infty}^{\infty} P_{\theta=0}(x) e^{-2\pi i u x} dx \tag{2.3.13}$$

From (2.3.10) and (2.3.13) we get the relationship between the 1D Fourier transformation of the projection $P_{\theta=0}(x)$ and the 2D Fourier transform of the object:

$$F(u,0) = S_{\theta=0}(u) \tag{2.3.14}$$

Relation (2.3.14) is the simplest form of the Fourier Slice Theorem where the result does not dependent on the orientation between the sample and the coordinate system. For rotation of the coordinate system by an angle θ, Figure 2.3.5 illustrates the link between the Fourier transform of a projection and the Fourier transform of the sample.

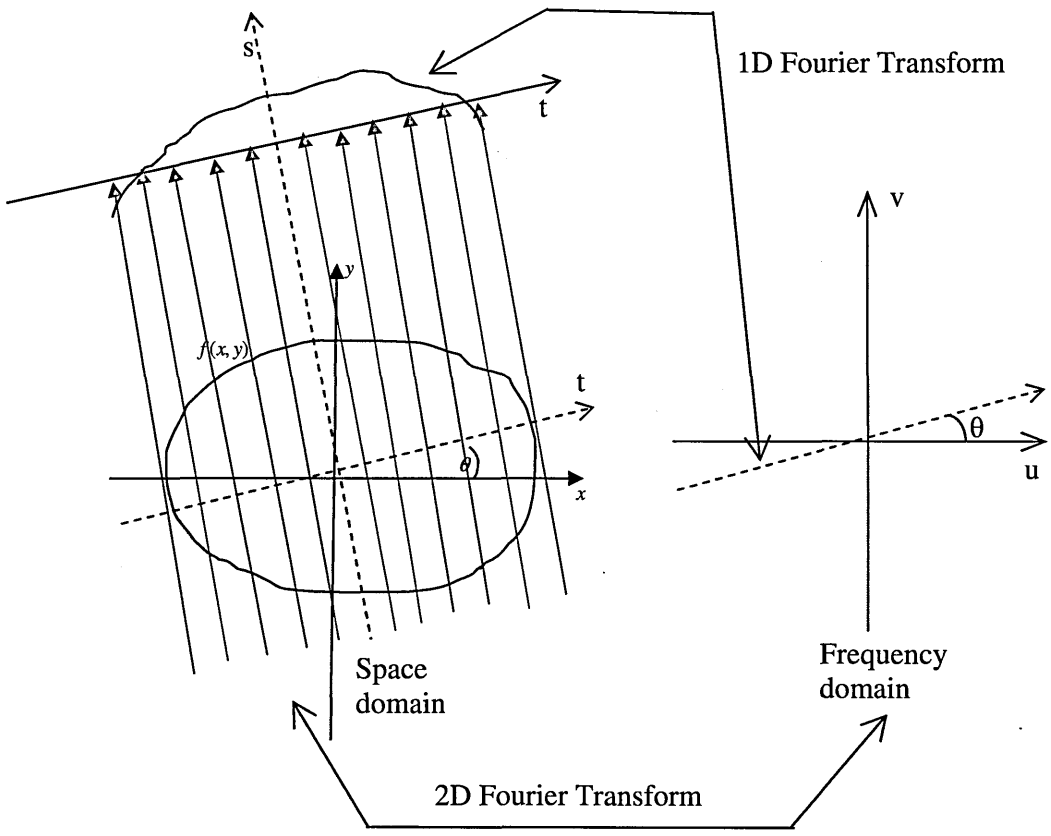

Figure 2.3.5: *The link between the Fourier transform of a projection and Fourier transform of the object [62].*

The 1D Fourier transformation of each $P_\theta(x)$ gives a slice of the 2D Fourier transformation $F(u,v)$ which can be estimated completely if there are sufficient projections obtained for different θ angles. The function $f(x,y)$ is calculated by inversing the 2D Fourier transformation of $F(u,v)$ as follows:

The function $f(x,y)$ is written using the inverse Fourier transformation of $F(u,v)$ in rectangular coordinate as:

$$f(x,y)=\int_{-\infty}^{\infty}\int_{-\infty}^{\infty}F(u,v)e^{2\pi i(ux+vy)}dudv \tag{2.3.15}$$

Due to the numerical reasons, the previous algorithm is implemented by the *filtered back-projection* [62] which is the one employed in this thesis. This is derived from the Fourier Slice Theorem as follows:

Using polar coordinates the relation (2.3.15) is written as:

$$f(x,y)=\int_{0}^{\pi}\int_{-\infty}^{\infty}F(w,\theta)e^{2\pi iwt}|w|dwd\theta \tag{2.3.16}$$

or,

$$f(x,y)=\int_{0}^{\pi}\left[\int_{-\infty}^{\infty}S_\theta(w)e^{2\pi iwt}|w|dw\right]d\theta \tag{2.3.17}$$

according to the relation (2.3.14).

Notating the bracket term with

$$Q_\theta(t)=\int_{-\infty}^{\infty}S_\theta(w)e^{2\pi iwt}|w|dw \tag{2.3.18}$$

(called also "filtered projection") we have:

$$f(x,y)=\int_{0}^{\pi}Q_\theta(t)d\theta \tag{2.3.19}$$

The relation (2.3.19) represents a filtering operation where the *filtering function* or *ramp filter* (or, response function in Fourier space) in the frequency space (u,v) is $|w|$. The reconstruction of the $f(x,y)$ is obtained by summing $Q_\theta(t)$ over all angles θ. The main role of the filter is to suppress or amplify specific frequencies. It was demonstrated [67] that the image obtained using a filter function has a better resolution, a homogeneity density and reproduces a uniform and correct dimension of the sample measured. One of the preferred filters when the image contains a lot of noise is the Shepp-Logan filter to attenuate the high frequency image information.

Another important aspect is described by the number of projections required. If this is too small then we have insufficient data to reconstruct the sample. For determining the number of projections required we know from the Fourier Slice Theorem that the Fourier transform of each projection is a slice of 2D Fourier transform of the object. The sampling points in the frequency domain are equally distanced on radial lines (which represents the projections) with a sampling interval $\Delta\omega_r = \frac{1}{N\mathrm{T}}$, where N is the number of sampling points in the projection (i.e. the number of pixels across the width of the image) and T is the projection sampling interval (i.e. the pixel width).

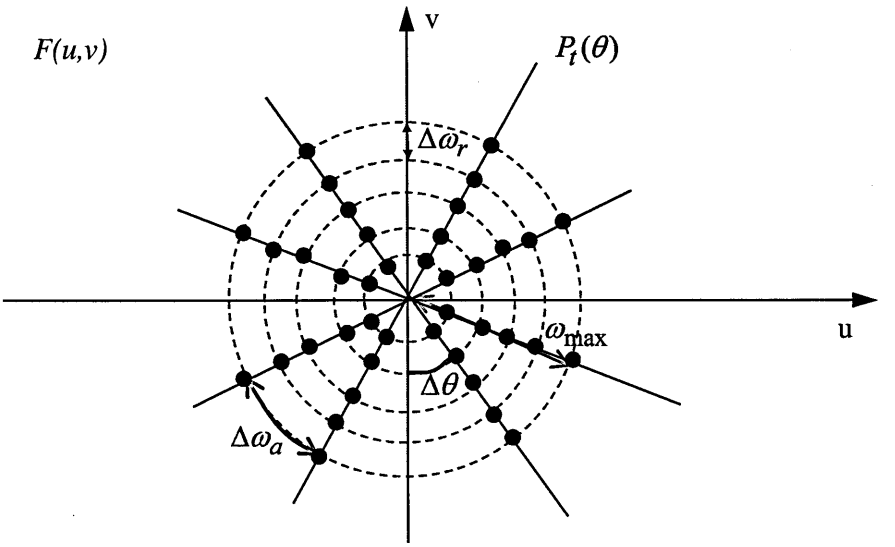

Figure 2.3.6: *The frequency domain with the sampling points equally spaced on radial lines.*

The highest frequency is given through the Nyquist Theorem [62], by the relation $\omega_{\max} = \frac{1}{2T}$, where $\omega_{\max}$ is the radius of the disk (see Figure 2.3.6). The largest interval between two consecutive sampling points will be $\Delta\omega_a = \omega_{\max}\Delta\theta$ where $\Delta\theta$ is the angular spacing between projections. For ensuring sufficient sampling, the angular and radial intervals at all points in the frequency space must be of the same order ($\Delta\omega_a = \Delta\omega_r$). From this equality results the relation between the angular spacing between projections and number of sampling points, $\Delta\theta = \frac{2}{N}$. Finally, we can conclude that for a high quality image the number of projections required over 180° rotation is

$$N_{proj} = \frac{\pi}{\Delta\theta} = \frac{\pi N}{2} \tag{2.3.20}$$

2.3.3.2 Dedicated software for tomographic reconstruction

The reconstruction of the sample projections into a 2D slices of the object can be done using a number of commercial or freeware codes including Octopus software [68], which implements the filtered backprojection algorithm, and is written on the LabView platform [69]. When the reconstruction is finished and slices have been obtained, the volume data can be imported into a 3D volume rendering software such as VgStudio Max 2.1 [70] where the volumetric object is generated by the stack of image slices. VgStudio uses three dimensional arrays of "volumetric pixels", named *voxels* (a volume element representing a value on a regular grid in a three dimensional space). By assigning to each voxel a colour (depending on its grey value) the three-dimensional object is rendered (made visible).

2.3.4 Other neutron imaging techniques

During recent years new techniques have been conceived by taking into account the fact that attenuation coefficients depend on the neutron energy (wavelength), neutron spin and magnetic moment. The following paragraphs will report the essential aspects of these methods.

2.3.4.1 Energy selective neutron imaging

Most neutron imaging facilities still use "white beams" of thermal or cold neutrons with energies extending down to few meV [71]. In the classical neutron transmission technique the attenuation coefficients are integrated over all energies in the neutron spectrum [72]. For this reason, the energy dependent features are mostly lost in the averaged data.

Bragg edges

Neutrons with wavelengths larger than the Bragg cut-off of the polycrystalline material analysed cannot interfere coherently causing the attenuation coefficient to drop significantly since the Bragg equation for a certain set of atomic planes is no longer fulfilled. In a plot of transmitted intensity against wavelength, this behaviour produces a discontinuity known as a *Bragg edge* as shown in Figure 2.3.7.

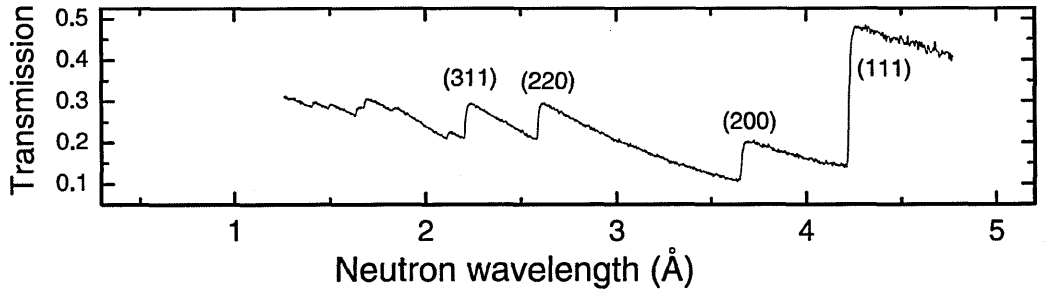

Figure 2.3.7: *The transmission intensity spectrum of an (fcc) iron sample shows Bragg edges at certain neutron wavelengths [11].*

The position of $\lambda = 2d_{\max}$ corresponding to the lattice planes with the largest spacing d_{max} is called the *Bragg cut-off.* For many materials the Bragg cut-off corresponds to thermal or cold neutron wavelengths of about 4 Å (Table 2.3.1).

Table 2.3.1: *The Bragg cut-offs of several engineering materials [73].*

Metal	Al (fcc)	Be (hcp)	Mg (hcp)	Fe (fcc)	Fe (bcc)	Ni (fcc)	Pb (fcc)	Cu (fcc)	Mo (bcc)
λ(Å)	4.67	3.957	5.62	4.169	4.053	4.066	5.72	4.174	4.44

Different crystalline materials show Bragg-edges (characterized by their position, height and slope) in their neutron cross sections. For that reason, Bragg edges will be used to show and point out the spatial variation of the attenuation in a material. This can be done by selecting narrow bands of the neutron energy (one below and one above a Bragg edge).

For each selected energy band a radiography of the sample is taken. Each image is normalized (in same manner as in the white-beam radiography) to remove variations caused by the beam inhomogeneity, revealing the varying contrast between different areas on the sample (Figure 2.3.8).

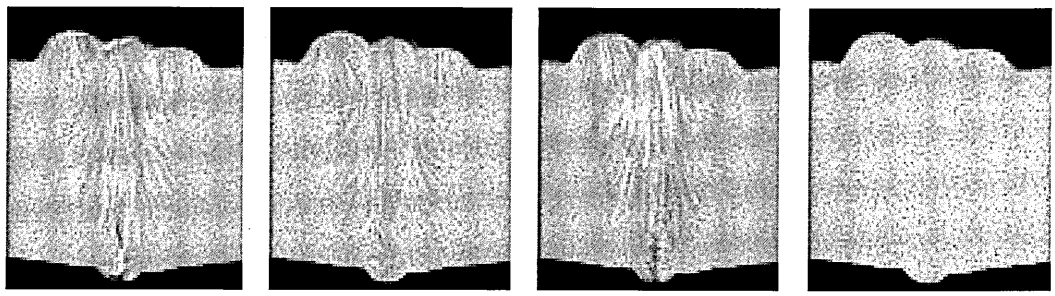

(a) (b) (c) (d)

Figure 2.3.8: *Radiographies taken of a piece of stainless steel weld at three different wavelengths (a) 3.4 Å, (b) 3.6 Å and (c) 4 Å. (d) Represents a white beam image of the sample [74].*

The energy selective radiography technique can be extended to tomography when the reconstructed (horizontal) slices for tomography experiments are performed for a given wavelength or a set of wavelengths. The advantage of the energy-selective tomography is that it gives information about the crystallographic structures and compositions [75]. It should be noted however that energy-selective tomographies require a very high flux to have a sufficient number of neutrons in the wavelength bins.

Three main options for the practical energy selection of neutrons could be considered:

1. At continuous neutron sources (e.g. SINQ facility, PSI) it is realised using a rotating turbine device (i.e., neutron velocity selector) acquiring images at different rotation speeds for obtaining contrast variation [76];

2. At other continuous sources energy selection may be achieved using monochromator crystals [77];

3. At pulsed facilities, the energies are selected via time-of-flight measurements [12].

Whilst the first two methods give a limited energy resolution (from 5% to 15% in $\Delta\lambda / \lambda$) [74] and whilst only one wavelength band can be used at a time, the third possibility from pulsed sources allows the full spectrum to be used in principle, if a suitable detector with a multiple wavelength band selection is available. In this case TOF has the advantage that each pulse contains the full thermalized neutron spectrum, and so a large number of Bragg edges can be observed in a single measurement. The energy resolution for TOF measurements is usually better than 1%.

In addition other phenomenon related to crystallographic structure such as strain and texture can be investigated using Bragg edge features [11].

2.3.4.2 Phase contrast imaging

Whilst the standard neutron imaging techniques are based on the attenuation of the neutron beam, by absorption and scattering, the technique of phase contrast imaging, introduced in 1980 by Baruchel et al. [78], is based on the fact that not only the transmitted beam contributes to the image, but also the refracted beam. Consequently, the sample interferes with the phase of the wave field and induces a phase shift.

When the attenuation is very small, detection of the phase shift can provide a good image contrast. To get the phase contrast using neutrons it is necessary to use a good collimation (with a pinhole with a very small diameter and a large distance between pinhole and object, i.e. high L/D) and increase the distance between the sample and detector as required. If the distance is too short then we will only have absorption contrast. On the other hand the distance should not be too long either, in order to detect the intensity variations along the edges and interfaces of the sample (Figure 2.3.9).

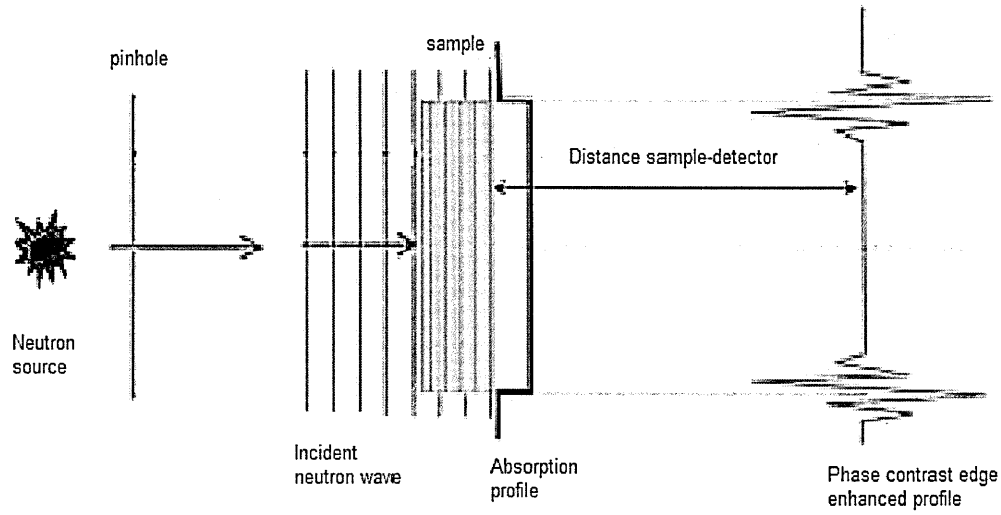

Figure 2.3.9: *Set-up of phase contrast imaging experiment on NEUTRA (PSI) [79]. Due to the different refractive index in the sample and the surrounding medium there is a phase shift between the waves transmitted through the object and surrounding. Phase interference effects at edges of the phase object enhance absorption contrast.*

The comparison of images obtained with a monochromatic beam [80], one using standard neutron radiography and another using the phase contrast imaging method, illustrates the edge-enhancement effect in phase contrast imaging (Figure 2.3.10). The edge-enhancement reveals in detail the sample contours. The phase contrast imaging can be applied in weakly absorbing objects where transmission does not provide sufficient contrast.

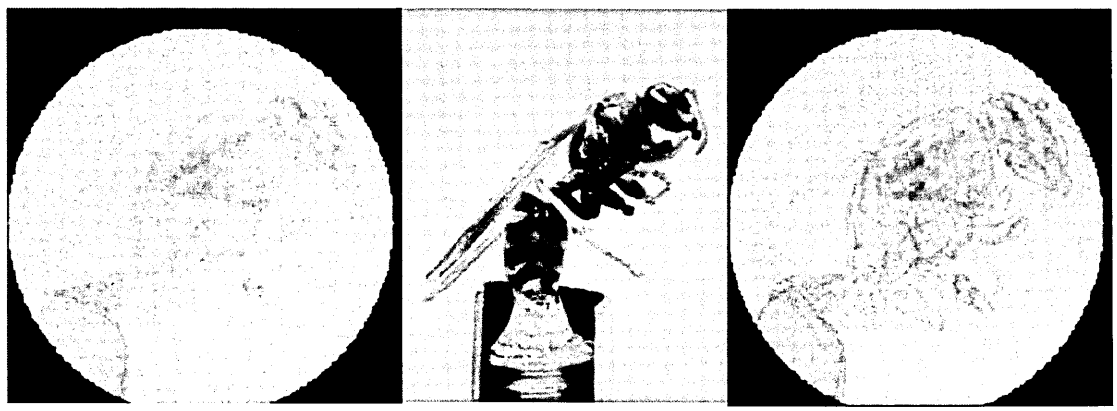

Figure 2.3.10: *Comparison between standard neutron radiography and phase contrast radiography [80] of a yellow jacket wasp. A higher clarity for finest features (e.g. antenna, legs) is revealed through phase contrast imaging.*

Discussions on the optical magnification determined by the pinhole size, the distance between pinhole-sample and sample-detector which improves the spatial resolution in the phase-contrast imaging experiments are well developed in [81].

Phase contrast radiography was initiated in the year 2000 at the National Institute for Standards and Technology (USA) using a pinhole [80, 82], and based on this phase contrast tomography was developed [83], where a series of projection images produced for different phase contrasts are recorded and integrated in the reconstruction computer tomography algorithms. This technique was successfully applied on the NEUTRA instrument at SINQ (PSI) which uses thermal neutrons [84].

2.3.4.3 Real time radiography

Another non-destructive imaging technique is real time radiography (RTR) or time-resolved radiography, based on producing an image electronically and having very short exposure times. The process [85, 86] can be visualized by registering as many images at a sufficiently high frame rate for the sample with 1:1 time scale observation. With the help of positioning equipment, the object can be rotated or tilted so the inspected area can be analysed in a few seconds. This method is viable if we have a good neutron flux and a high contrast medium for the sample. It can be applied to dynamic events or static objects for a rapid examination [4]. Dynamic imaging of a repetitive process (such as in the automotive engineering sector for seeing how the oil flows in the machine) uses a synchronization between the process and detector known as stroboscopic imaging.

2.3.4.4 Neutron resonance transmission imaging

The neutron resonance transmission imaging (NRTI) [87] is a fast, non-destructive technique offering element-sensitive imaging possibility with the help of epithermal neutrons. The bulk technique NRTI was initiated at the neutron time-of-flight facility GELINA (IRMM) [88] and set up on the beamline INES (ISIS, UK) as an imaging technique as a part of the ANCIENT CHARM project [89]. The main component of the set-up is the 2D-neutron position sensitive transmission detector used to obtain a transmission spectrum by a measurement of the flight time of epithermal neutrons passing through a sample. NRTI is based on the fact that in the epithermal and fast energy range the neutron cross sections exhibit sharp dips, so-called *resonances*, which occur at neutron energies specific to each nuclide. The positions and intensities of the selected neutron resonances in the transmission TOF spectra are used to construct images of different elements. One main advantage of this method is the high penetration of the neutrons in the bulk of the sample allowing study of the homogeneity of the object and also identifying elements and their location in the sample.

2.3.4.5 Polarized neutron imaging

The polarized neutron imaging technique is mentioned here for completeness and because it is conceivable that this technique may be applied on IMAT in the future. Polarized neutron imaging [90] is used to explore the macroscopic magnetic phenomena inside solid materials and is, for example, applied at the cold neutron radiography instrument, CONRAD [91] at the Hahn-Meitner Institute, Berlin.

It is known that the neutron has a magnetic moment which is antiparallel to the internal angular momentum of the neutron described by the spin $\overline{S}$ with the quantum

number $s = 1/2$. Due to their spin neutrons are very sensitive to the magnetic fields. Hence, if neutrons are first polarized, after interaction with the magnetic field inside and around a sample the final spin orientation can be analysed with respect to the initial state.

Combining radiography and tomography techniques with magnetic neutron properties has applications in the field of condensed matter, bulk magnetism or electrical current distribution in conductors [92-94] and also in quantification of the trapped magnetic flux in a bulk superconductor [90].

2.3.5 Types of neutron imaging detectors

As neutrons are neutral non-ionizing particles, they cannot be detected, as X-rays are for example, through a direct detection process. They need an indirect detection process which can be capture, fission or collision. Initially, neutron radiography used films for recording images (as in X-rays radiography), but coupled to a highly absorbing conversion material (e.g. Gadolinium, Li-6 etc) because neutrons do not excite directly due to their neutral charge. Even if with this technique a good spatial resolution was obtained, a new detection system was required for improvement other performances such as the time resolution, dynamic range and quantitative information from the images [95]. In the early 90's, the film techniques were replaced by digital detectors (based on a pixel matrix) which are more sensitive enabling short exposure times (order of seconds) and are also more flexible for use in experiments than films.

Main aspects considered the developing specific types of detector are: high spatial and temporal resolution, the energy dependent absorption rate, the image quality (high signal-to-noise ratio) of neutron radiographies, large detector area and high detector efficiency. Other performance parameters are: fast read-out of data, high linearity and wide dynamic range. For a higher spatial resolution it is preferred that the detector should have a

small pixel size and moreover, the neutron image obtained should have many pixels in both directions (horizontal and vertical). The spatial resolution is determined by the detector and is influenced, also by the beam properties (e.g. the L/D ratio). For exploiting a higher temporal resolution and for improvement in the image quality a large number of neutrons is required. Unfortunately, the neutron beam intensity is often the limiting factor to fully exploit small spatial and temporal pixel sizes. The temporal resolution is the exposure time (how fast an image can be produced in the sensitive area after applying neutrons for measurement and converted into the detectable signal) defined by the detector efficiency. Different detection systems are in use at existing neutron imaging beamlines or are under development. There is a particular request for time resolving systems to develop energy selective measurements at higher performance at the pulsed spallation sources. The most important types of neutron detectors [74, 96] used are:

- Photographic film detectors – X-ray film combined with neutron converter foils. The converter, made for example of Gd, converts neutrons to gamma radiation which blackens the film pixel. The detector has the advantage of being a compact detector assembly. Because this system requires a mechanism to open and close the incident beam to define the exposure time, and required replacement of the film and the converter, it is hardly used for radiography experiments nowadays. The detector is not suitable for tomography, and not suitable for TOF measurements.
- Imaging plates – contain gadolinium as neutron absorber to convert neutron to gamma radiation which excites the so-called "storage phosphor" atoms (e.g. Eu doped BaFBr). The neutron exposure can produce a latent image on the image plate which then can be read out by a laser. Image plates are very useful for high resolution neutron radiography (a resolution better than 0.1 mm) and a high dynamic range. Because they need to be manually inserted into a reader or eraser system, tomography measurements cannot be done. Energy selection via the TOF method is not possible.

- Flat panel detectors – indirect conversion detector such as amorphous silicon in which arrays of photodiodes are integrated and coated with a neutron scintillator. The photodiode array converts the light photons into electric charge. This type of detector [97] is suited for neutron imaging of dynamic processes and acquiring neutron tomography images in a very short time. Another indirect detector is the CMOS flat panel made from a crystalline substrate and where each pixel can be addresses individually because each pixel has its own electronic amplifier and digitizer. In principle these detectors are suitable for TOF measurements.
- Track-etch foils – a plastic foil coated with Li-borate that uses charged particle products of neutron capture to record tracks in the plastic foil. It is advantageous to high-resolution radiography, but unsuited for neutron tomography due to the long exposure, development and scanning time. The detector is unsuited for TOF measurements.
- Gas electron multiplication (GEM) [98] are micro-patterned gas detectors, consisting of a thin composite sheet (an insulating polymer foil) coated with metal layers on both sides and etched with a high-density regular matrix of open channels (i.e., holes with micrometers diameters). The gas in the detector may contain a mixture of ^{3}He/CF4 where the helium-3 is used to capture neutrons and convert them into 3H and proton particles which ionise gas atoms. A voltage is applied between the two conducting sides, leading to a high dipole field created in the channels. Each channel acts as an individual counter. By the ionization process, the electrons released on one side of the foil are drifted into the channels and multiplied in an avalanche before emerging on the other side of the foil. The amplified charge could be let drift in the second GEM foil for a further amplification or can be detected on a patterned electrode [99]. The advantage of this detector is the potential large viewable area (almost of 50×50 cm^2) and a high counting rate capability (up to 10^8 n/cm^2/s). It has a moderate spatial resolution of 0.5-1 mm. Based on the previous principle there was developed recently, other neutron imaging detectors such as THGEM

[100] for fan-beam transmission tomography applications. GEM detectors are suited for tomography and TOF measurements.

- Electronic camera (CCD-charged coupled device) – is the most common type of imaging system with applicability in white-beam radiography, neutron tomography and energy-selective imaging [95]. Because the neutrons are not directly detected (as light in the standard camera) it needs to use nuclear reactions for converting the neutrons into charged particles and therefore to produce a measurable quantitative (countable) electrical signal. The most common approach in digital neutron imaging is the conversion of the neutrons into visible light by a converter (for example ZnS/LiF or gadolinium oxide scintillators). This light is then recorded with a CCD camera via a light-optical system consisting of a 45-degree mirror and a lens system. A detailed description of this type of camera will be presented in Section 3.7.1.

- With a MCP (microchannel plate) pixel detector developed by Space Science Department, Berkeley, USA [101] the conversion of neutrons into secondary particles is achieved by doping the first MCP with boron or gadolinium. The secondary particles generate electrons in the walls of the micro-channels. The neutrons are converted into electrons without light generation and subsequently the electrons are multiplied and registered for each individual pixel. The pixel camera it is fully TOF capable and hence can provide full TOF spectra for every pixel. The combination of both spatial and time information obtained from TOF measurements enables energy selective imaging applications. We will reiterate a description of the pixel detector and its applications as related to this thesis in section 3.7.2.

2.3.6 Applications of neutron imaging

Neutron imaging techniques have a wide range of applications covering biology, palaeontology, archaeology, cultural heritage, material science, medicine, engineering (including non-destructive testing of industrial components) and physics. A detailed review of applications of neutron imaging can be found in [4, 102, 103]. For example, the high sensitivity of neutrons to hydrogen and their high penetration into bulk materials allows neutron imaging to measure humidity transport in soil or water transport in plants [104]; or to monitor the water distribution within a working fuel cell non-invasively penetrating the exterior holding plates easily [105, 106]; or to investigate fuel and oil sediments in engine components [107, 108]. Neutron imaging techniques are widely used in cultural heritage science [109-111], an area of application that this thesis will return to.

2.4 Neutron diffraction

Neutron diffraction is an elastic scattering technique providing information about the structural properties of matter on the atomic or lattice level. This approach can be applied to study gases, liquids, solids (crystals) or amorphous materials.

2.4.1 Theory

The Bragg team (father and son) was awarded the Nobel Prize in physics in 1915 for their work in determining crystal structures (starting with NaCl, ZnS and diamond). Although Bragg's law [112] (see equation 2.4.1) was used to explain the interference pattern of X-rays scattered by crystals, diffraction has been further developed to study the structure of

various states of matter with many different beams, including ions, electrons, neutrons, and protons. The requirement for diffraction with these types of radiation is that the wavelength is of the same order of magnitude as the atomic or molecular distances. Bragg's equation states that constructive interference occurs when the path length difference associated with reflections from adjacent crystal planes (Figure 2.4.1) is equal to the wavelength:

$$\lambda = 2d \sin\theta \tag{2.4.1}$$

Knowing the wavelength λ, the angle between the incident and diffracted beam directions 2θ, we can calculate the distances between the planes, d, and determine the dimensions and symmetry of the unit cell. The d-spacing and angles are functions of the lattice plane indices $K = (hkl)$ (see Figure 2.4.1).

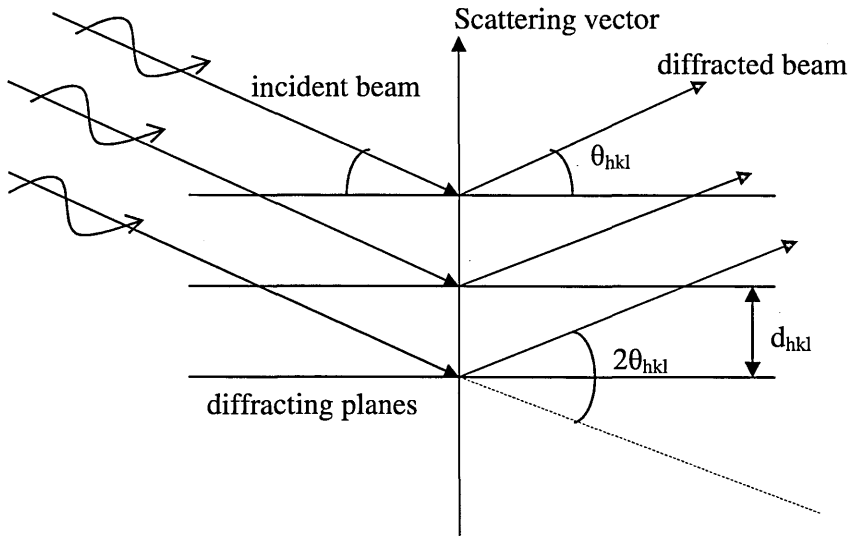

Figure 2.4.1: *Illustration of Bragg diffraction from a set of lattice planes (hkl).*

Neutron diffraction is an elastic scattering method where the scattered neutrons have more or less same energies (or wavelengths) as the incident neutrons. If $\vec{k}_i$ and $\vec{k}_f$ are the initial and final wave vectors (in elastic scattering, $\vec{k}_i = \vec{k}_f$) the scattering vector $\vec{Q}$ ($\vec{Q} = \vec{k}_f - \vec{k}_i$) could be written in scalar mode as $Q = 2k_i \sin\theta = \frac{4\pi \sin\theta}{\lambda}$, where λ is the

wavelength. This relation (equivalent to the Bragg equation 2.4.1, with $Q = \frac{2\pi}{d}$) suggests that there are two different ways to conduct an experiment in the Bragg scattering mode. One mode is known as angle-dispersive, when neutrons of a single, narrow wavelength band (monochromatic) are incident upon the sample and the scattered intensity is measured as function of θ. In the second mode (energy-dispersive) the scattered intensity is measured as a function of wavelength at a fixed θ angle. Both ways will be summarized below.

Neutron diffraction can be applied to study different structural aspects such as: phase and structure [35], texture [113], microstructure and residual stress [114].

For a neutron diffraction measurement one needs a neutron source, a monochromator for wavelength selection, a sample and a detector or a multidetector system (for increasing the rate of collecting data as in modern instruments, e.g. D20 at ILL [115]).

Angle-dispersive diffraction at research reactors

To define the necessary neutron wavelength for diffraction experiments conducted at research reactors, the white neutron beam is monochromated to a chosen wavelength λ by Bragg reflection from a monochromator crystal. After that, the neutrons selected irradiate the sample and they are Bragg scattered in the direction of 2θ angle to the incoming ray (Figure 2.4.2). The diffraction pattern is measured by changing the scattering angle of the detector (2θ).

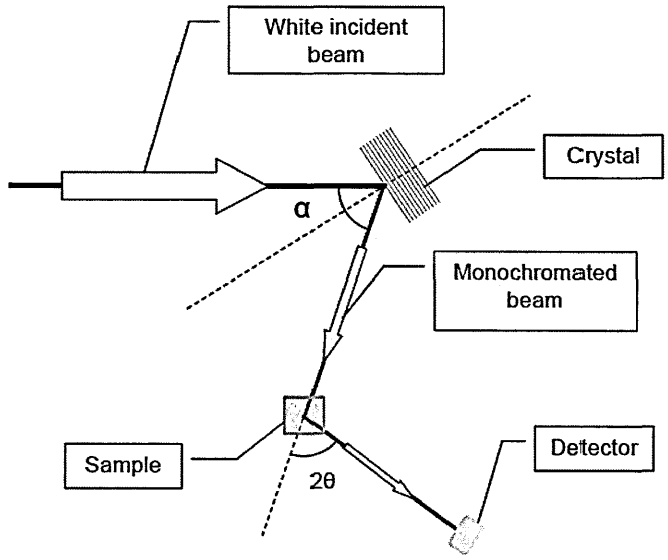

Figure 2.4.2: *Schematic representation of diffraction in angle dispersive mode at the reactor sources [116].*

The intensity of the diffracted beam is plotted (Figure 2.4.3) as a function of the scattering angle and the result shows a series of diffraction peaks whose positions along the θ axis are determined by the Bragg equation (2.4.1). Each Bragg peak represents neutrons that have been scattered from a particular set of planes in the crystalline lattice.

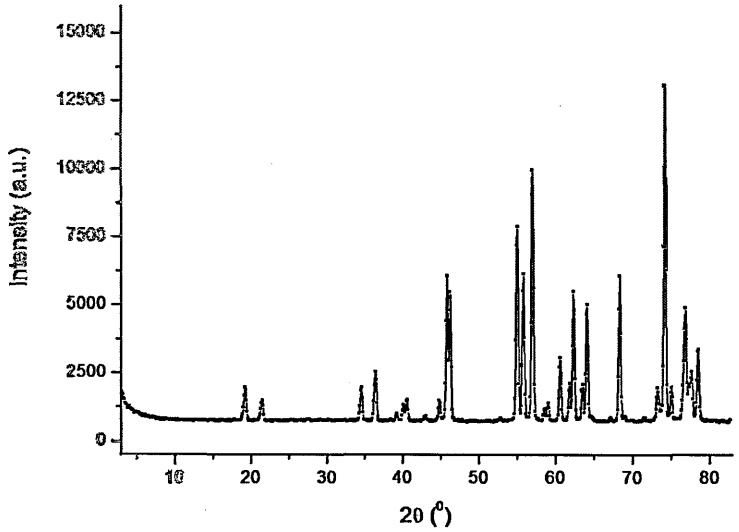

Figure 2.4.3: *A powder diffraction pattern recorded in angle-dispersive mode for* $\lambda = 2.37$Å *at Chalk River Laboratories, Canada for* $Pr_2Ta_2O_7Cl_2$ *sample The plot shows a series of diffraction peaks whose positions along the θ axis are determined by the Bragg equation (2.4.1).*

Diffraction at pulsed sources

In the case of pulsed sources, the neutron beam is polychromatic and the time-of-flight method is applied to select the energies of the incident neutron beam, facilitating the measurement of different d-spacings at a fixed scattering angle 2θ (Figure 2.4.4).

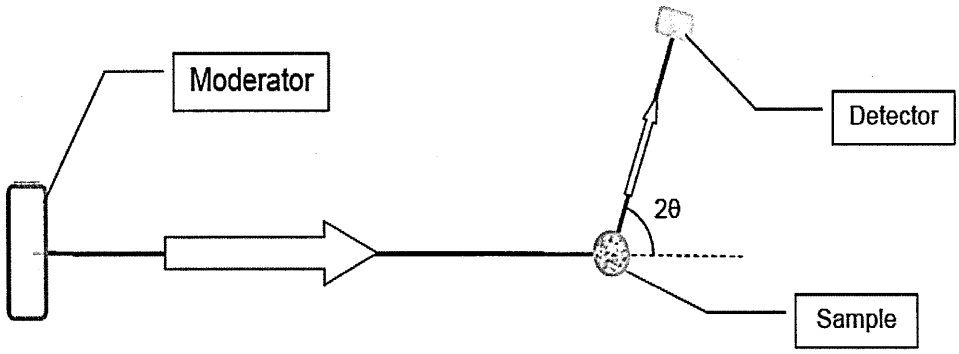

Figure 2.4.4: *Schematic representation of diffraction in energy-dispersive mode at a pulsed source [116].*

As discussed in paragraph 2.2.3, the TOF method is based on the De Broglie relationship which states that the neutron wavelength is inversely proportional to its velocity. So long-wavelength neutrons are slower to arrive at the sample and in consequence at the detector than the faster short-wavelength neutrons. Measuring the time of arrival of a neutron at the detector and knowing its flight path we can calculate its velocity and therefore its wavelength (energy) using the formula:

$$\lambda = \frac{hT}{mL}, \tag{2.4.2}$$

where L is the total neutron's flight path (source-sample distance + sample-detector distance) measured in metres and T is the time-of-flight measured in μs.

Combining the formula (2.4.2) with Bragg's equation we obtain a relationship between T and d-spacing:

$$T = 2daL\sin\theta, \tag{2.4.3}$$

where the constant a is equal to 252.78.

From equation (2.4.3) we can calculate the d-spacing:

$$d = \frac{T}{2aL\sin\theta}. \tag{2.4.4}$$

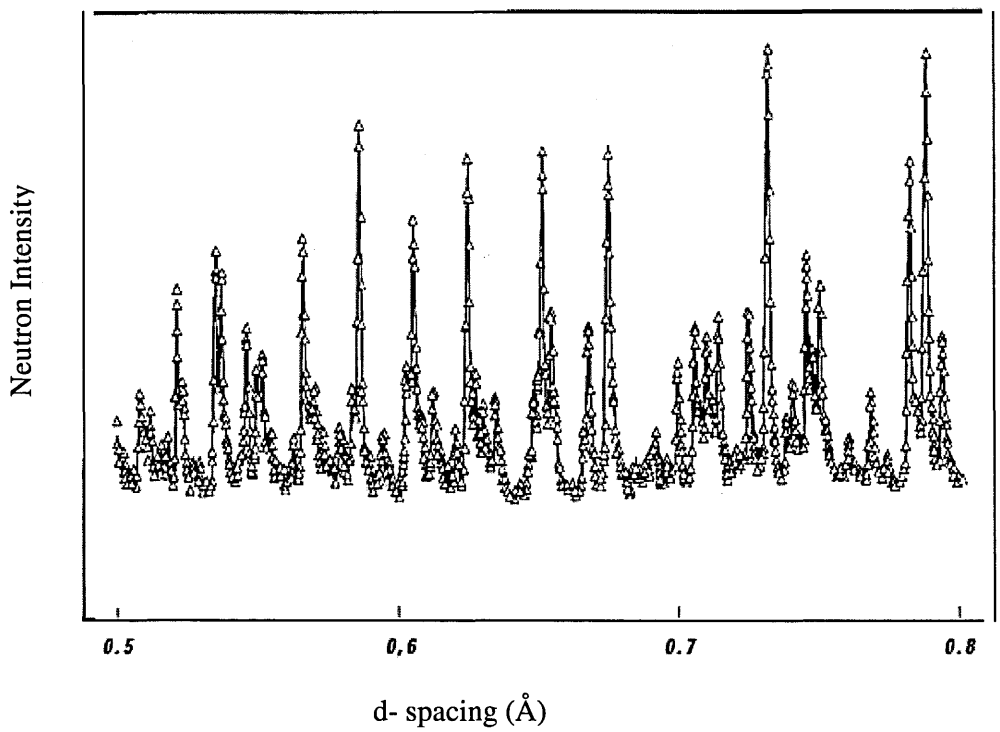

Figure 2.4.5: *A powder diffraction pattern recorded at a spallation source [117] (fat garnet measured at the Neutron Powder Diffractometer at LANSCE). The intensity is plotted as a function of d-spacing between atomic planes. Also, the intensity could be plotted as function of neutron time of flight or the neutron wavelength (cf. equation 2.4.4).*

In TOF experiments, when the neutron beam irradiates a crystalline solid, the detectors are positioned after scattering at a fixed angle 2θ and a diffraction pattern is recorded. The time-of-flight of the neutrons, T, issuing from a single pulse is directly proportional to their wavelength and the diffraction pattern is a plot of the neutron intensity as a function of t or neutron wavelength λ or d-spacing (Figure 2.4.5).

The resolution of a time-of-flight diffractometer

The instrumental resolution of a diffractometer, $\frac{\Delta d}{d}$, is a measure of the spread in the Bragg reflection for a given d-spacing. It is knowledge is very important for establishing the diffractometer quality and for carrying out high-resolution applications such as strain scanning. The sources of this uncertainty include:

- the time flight path uncertainty ΔT;
- the angular uncertainty (of the scattering angle) $(\Delta\theta)$, a consequence of the neutron beam divergence at the detector as the neutrons pass from moderator to the sample and from sample to the detector;
- the flight path uncertainty ΔL (the error in the neutrons flight path) generated by the finite sample size or detector size and the moderator thickness.

Differentiating the relation (2.4.4) ([118]) with respect to each variable L, T and θ we obtain a link between the resolution of a TOF diffractometer and the time uncertainty (ΔT), flight path uncertainty (ΔL) and angular uncertainty $(\Delta\theta)$:

$$\left(\frac{\Delta d}{d}\right)^2 = \left(\frac{\Delta T}{T}\right)^2 + \left(\frac{\Delta L}{L}\right)^2 + \left(\cot\theta\,\Delta\theta\right)^2 \qquad (2.4.5)$$

A highest d-spacing resolution can be achieved minimising the term $\frac{\Delta L}{L}$ (using a long flight path L) and $\frac{\Delta T}{T}$ (maximising time-of-flight values) and by positioning the detector at a high scattering angle (for example, the backscattering case when $2\theta = 180^\circ$) for which $\cot(\theta)$ is zero.

Rietveld refinement

After the diffraction pattern is generated refinement programs are used to fit the neutron data. The Rietveld refinement, a powder diffraction fitting method, was initially invented

for use with constant wavelength neutron beams by Hugo Rietveld [119] and later it was extended to X-ray diffraction and time-of-flight neutron diffraction. The variation of count rates with time-of-flight (or angle) is dependent on a numbers of parameters such as: multiplicity and structure factor, peak shape parameters and lattice parameters. Using these parameters as fitting parameters, the theoretical profile is fitted by least squares minimisation to the entire experimental profile considering all diffraction peaks. Lattice parameters, atom positions and weight fractions can be determined in this way. Another choice of fitting is the Pawley analysis [120] where the calculated intensities of the peaks are not constrained by the theoretical model, but intensities are permitted to be fitted independently with only the peak positions constrained to give the unit cell parameters required for strain measurements.

The steps for calculated diffraction pattern from the Rietveld refinement are:

1. To calculate the intensity at each point in the diffraction pattern based on the formula [121]:

$$Y_{ic} = Y_{ib} + \sum_{k=k_1}^{k_2} G_{ik} I_k, \tag{2.4.6}$$

where Y_{ic} is the total count rate at point i in the diffraction pattern, Y_{ib} is the background count rate at point i, G_{ik} is the value of normalised peak profile function at point i for reflection k, I_k is the Bragg intensity of reflection k and $k = k_1$ to k_2 are the reflections contributing intensity to point i;

2. The Bragg intensity of the reflection K, I_K, is proportional to the square of the structure factor of that reflection [121]:

$$F_{hkl} = \sum_j N_j b_j e^{-W_j} e^{2\pi i(hx_j + ky_j + lz_j)}, \tag{2.4.7}$$

where W_j is the Debye-Waller factor, N_j site occupancy and b_j the scattering length. The Debye-Waller factor, known also as temperature factor, represents the attenuation of

coherent neutron scattering caused by thermal motion of atoms. The site occupancy is a number of atom type j per unit cell. The summation j is over all atoms in the unit cell which are at positions x, y, z.

3. The Rietveld algorithm minimizes the residual function by a least squares algorithm:

$$\sum_i w_i \left| Y_{io} - Y_{ic} \right|^2 \tag{2.4.8}$$

where w_i is the weight assigned to the profile observation at point i and Y_{io} is the observed count rate at the point i.

4. The scale factor S is included to scale the calculated pattern to the observed pattern.

2.4.2 Neutron strain scanning measurements

One important application of the neutron diffraction method, which is particularly relevant to this thesis, is the measurement of the stress in the engineering components.

Neutron diffraction has been already used to address highly complex engineering issues. One relevant application is the non-destructive measurement technique of neutron strain scanning (NSS). Strain measurements were initiated and developed at the Harwell Laboratory, UK in the early 1980s [122] and then at the ILL (France). This method arose from the desire to investigate the residual stresses [123, 124] inside polycrystalline engineering samples. Residual stresses are generated by the misfits (thermal or elastic) between different regions within the sample caused, for example, by welding, turning, grinding or heat treatment operations [125].

The principle of NSS relies on the Bragg equation (2.4.1) that establishes the relationship between the interplanar lattice spacing d in the sampled region. This region nominated as the "gauge volume" is determined by the intersection of the incident and diffracted beams, and its size is defined by optical devices (slits and collimators) (Figure

2.4.6). To be sure that the both orthogonal Q-vectors and strain components are measured the detectors are placed at $2\theta = 90°$. In this case the gauge volume is approximately rectangular. When the slits have same size for height and width, the gauge volume is approximately cuboidal. Because the gauge volume is fixed in space, the strain variation across the sample can be investigated using a translation or rotation table on which the specimen is mounted.

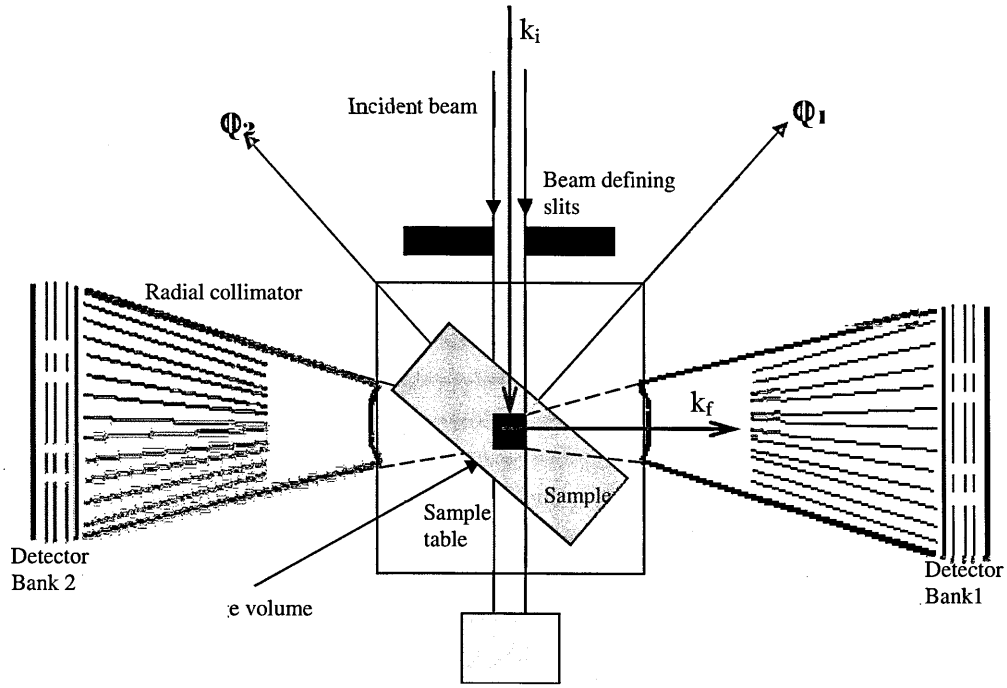

Figure 2.4.6: *Schematics of data collection on the ENGIN-X TOF diffraction instrument [114].*

The strain is calculated from the lattice parameter measured in the direction of the scattering vector perpendicular to the diffracted planes within the gauge volume (Figure 2.4.6) with the magnitude of the wavevector specified by $k = \frac{2\pi}{\lambda}$. For a fixed scattering angle θ the strain is defined as:

$$\varepsilon_{hkl} = \frac{d_{hkl} - d_{0,hkl}}{d_{0,hkl}} = \frac{\Delta d_{hkl}}{d_{0,hkl}} = \frac{\Delta \lambda_{hkl}}{\lambda_{0,hkl}} = \frac{\Delta t_{hkl}}{t_{0,hkl}} \qquad (2.4.9)$$

where $d_{0,hkl}$ is the stress-free lattice spacing for peak hkl, $t_{0,hkl}$ the stress–free time-of-flight and $\lambda_{0,hkl}$ the stress free wavelength.

In its complete notation the strain ε_{ij} can be written as $\varepsilon_{ij} = \begin{pmatrix} \varepsilon_{11} & \varepsilon_{12} & \varepsilon_{13} \\ \varepsilon_{21} & \varepsilon_{22} & \varepsilon_{23} \\ \varepsilon_{31} & \varepsilon_{32} & \varepsilon_{33} \end{pmatrix}$, where the diagonal elements represent normal strains on planes normal to the direction of the chosen axes and the other elements are shear strains between the axes.

In general six measurements are required at each measurement point to fully determine the strain tensor in an isotropic material, however if the principal strain components are identified and measured, the strain tensor reduces to a diagonal matrix and is fully characterised by the three measured strains.

The stress tensor is related to the strain tensor through Hooke's elasticity law:

$$\sigma_{ij} = \frac{E}{1+\nu}[\varepsilon_{ij} + \frac{\nu}{1-2\nu}(\varepsilon_{11} + \varepsilon_{22} + \varepsilon_{33})] \qquad (2.4.10)$$

where E is the elastic constant of the material and ν the Poisson's ratio.

The diffraction pattern contains only the neutrons which are scattered from within the gauge volume. The data extracted can be used for either a single peak fitting or full pattern analysis through the Rietveld method [119].

A dedicated instrument for strain scanning measurements in the engineering field is ENGIN-X at ISIS [6]. The high strain resolution (<50με) and the sampling volumes (1-1000mm^3) which may be measured make ENGIN-X one of the worlds leading strain scanning diffractometers. The ENGIN-X instrument will be used in the neutron diffraction experiments presented in Chapter 5.

2.4.3 Phase and structure analysis

Among the practical applications of the TOF neutron diffraction method (when a full diffraction spectrum is obtained from a single measurement) we can highlight the determination of structural aspects of a material such as phase composition and crystallographic structure. A diffraction measurement provides data about phase and about the structure of this phase. A crystallographic phase is characterized by a crystal structure that is given by the crystal symmetry (space group), unit cell dimensions, and the atom positions in the unit cell. Information about the microstructures and material treatment can be deduced from the shape and intensities of diffraction peaks in the spectra. The phase analysis employs determination of the quantities of different phase components in a mixture of phases. A description of the quantitative phase analysis based on the Rietveld method is developed in [126]. Briefly we can say that the quantitative phase information is obtained assuming that the weight fraction W_p from the $p-$th phase in a mixture is given by the normalized product of the Rietveld scale factor S_p with M_p, V_p and Z_p:

$$W_p = \frac{S_p Z_p M_p V_p}{\sum_i S_i Z_i M_i V_i}, \tag{2.4.11}$$

where M is the mass of a formula unit, Z is the number of formula units per unit cell[2], V the unit cell volume and the summation $\sum_i S_i Z_i M_i V_i$ represents the sum over all phases.

The phase analysis can be applied in geology for study of rock compositions or in cultural heritage science to determine the crystallographic parameters and phase content of a material. An accurate determination of phase compositions and crystal structures of materials requires diffractometers with a good resolution and good flux.

[2] The unit cell is the smallest physical unit of a crystal's structure and by repeating translations-symmetry operations the crystal is generated. The unit cell may contain several units of atoms. The number of formula units per unit cell is the integer number Z.

2.4.4 Software used in neutron diffraction measurements

From TOF neutron diffraction experiments each detector records spectra covering a wide d-range spacing. The spectra intensities are dependent on the wavelength range, flight path, collimation geometry and d-spacings of the Bragg peaks. From each spectrum we can extract information about: lattice parameters (using peak positions); crystal structure; texture or phase composition (from peak intensities); microstructure (from peak shape); or internal stress from the deviations from the ideal (stress-free) peak positions. These calculations are based on a least squares approach, the Rietveld refinement method [119], to refine a theoretical line profile (calculated from a known or assumed crystal structure) until it matches the measured profile.

The General Structure Analysis System (GSAS) is one of the software packages used for diffraction pattern analysis, developed by Larson and Von Dreele [127] and written in Fortran. B.H. Toby [128] elaborated a graphical user interface EXPGUI for GSAS.

Other programs based on Rietveld analysis include Fullprof [16], used for magnetic scattering experiments, and MAUD [129] dedicated to texture analysis studies from diffraction data.

2.5 Instrument design methods

The design of neutron scattering instruments involves a long and expensive process. Various design tools were available first for modelling the performance of synchrotron beamlines and afterwards they were developed for neutron stations. During the last two decades these tools have evolved quickly allowing beamline designers to predict the performance of new beamline concepts.

2.5.1 Monte Carlo method

To produce optimal neutron instrument configurations on the neutron sources simple analytical calculations there were used, initially. More complicated analytical calculations (e.g. acceptance diagrams [130]) and Monte-Carlo modelling were elaborated to maximize the data rate and to improve the data quality.

The Monte Carlo method (known as "random sampling" or "statistical simulation") is a sampling technique employing random numbers and probability statistics and is used for solving complex problems that cannot be modelled by deterministic methods. Monte Carlo simulation packages are not used only for the evaluation of the instrument performance, but also for designing neutron experiments, experimental results analysis, estimation of complex effects like absorption, multiple scattering, geometry, resolution, for comparing virtual experiments with real ones and also for training new users of the neutron scattering instruments.

The Monte-Carlo approach was created by J. von Neumann, N. Metropolis and S.Ulam [131] and it was named after the Monte Carlo Casino (allusion to Ulam's "hobby" of gambling). The method was implemented for the first time in the Manhattan Project to estimate the neutron diffusion in fissionable materials by solving the equations which describe interactions between hundreds of atoms.

General principles

The Monte Carlo simulation method first defines a domain of possible inputs (e.g. an interval$[a,b]$), then randomly generates inputs $(X_1, X_2, ..., X_n)$ from the domain $[a,b]$ according to certain probability distributions. The method then uses the inputs to perform certain computational calculations before collecting the results of the individual computations into the final result.

An example of the Monte Carlo simulation is the calculation of a definite integral ($\int_a^b f(x)dx$) when this cannot be solved analytically. A numerical approach is to evaluate the function $f(x)$ at a uniformly sampled interval $a<x<b$ with n values and summing all these values:

$$\lim_{n\to\infty}\frac{1}{n}\sum_{\substack{i=1\\ a\le x_i\le b}}^{n} f(x_i)=\frac{1}{b-a}\cdot\int_a^b f(x)dx \qquad (2.5.1)$$

An alternative to this method (with intervals) is the estimation of the function at random values and summing up all these values. In this case, the equation (2.5.1) will be the Monte Carlo approximation for the integral.

Monte Carlo simulations of neutron scattering instruments

In the context of instrument design, the purpose of the Monte Carlo simulation is to reproduce a realistic neutron scattering instrument by assembling different virtual components into a computer model of the instrument. Virtual neutrons are then generated and their interaction with the instrument recorded. The neutrons used in such simulations may have a *state* defined by (r, v, s, t, p) where r is the position vector, v is the velocity vector, s the spin vector (considered in the polarization experiments), t is the travel time (important for time-of-flight experiments) and the neutron weight, p (which is either 1, if the neutron is present after it interacts with each component from the virtual instrument or it has been absorbed or scattered, or 0 if the neutron is lost in his travelling process). Actually, the neutrons are simulated in *rays* by which we mean the neutron trajectory (i.e. position r as a function of time t) and p has a typical initial value of thousands or millions neutrons per second when the ray is generated by the source. When the ray reaches the detector (on the final destination) p may be only a fraction of a neutron per

second. Each random state of a neutron is generated according to a probability distribution defined by the type of neutron source. All neutron states are recorded by the detectors and analyzed as in a real experiment. For this reason, Monte Carlo simulation of a neutron scattering instrument can be considered as a *virtual experiment.*

2.5.2 Simulation packages: McStas, VITESS, IDEAS

In recent years the field of neutron ray-tracing simulations for scattering projects has developed significantly. The start was given by the neutron transport code MCNP [132] and for scattering purposes by the NISP package [133]. After 1990, new free Monte Carlo simulation packages including McStas (Monte Carlo Simulation of Triple-Axis Spectrometer) [134], VITESS (Virtual Instrumentation Tool for ESS) [135] or IDEAS (Instrument Design and Experiment Assessment Suite) [136] were elaborated to develop the virtual experiments [13] when the scientists were interested in building or upgrading an instrument. The answer to the question "What is a virtual experiment?" [13] can be summarized in the next steps:

- create a model for a complete instrument including details about the components;
- the description of the instrument should be as close as possible to the real instrument;
- the virtual instrument can be controlled like a real instrument.

While the VITESS package is specially designed for the simulation of future instruments at the European Spallation Source, McStas ([134], [137]) developed by Risø National Laboratory and The Institute Laue Langevin (ILL) is an alternative because it can be applied for all types of neutron scattering instruments and materials and has other features such as: a large component library, multiple output formats, user support and parallel computing. Also, it is freely available [138]. In [139] a comparative study is presented after using various simulation packages including McStas, VITESS and IDEAS on the same instrument (Triple-Axis Spectrometer from the beamline H8 of the High Flux Beam

Reactor at Brookhaven National Laboratory). The results obtained are in good overall agreement.

Throughout this thesis the McStas package was used for the IMAT instrument optimization. McStas is based on a Meta Language and is designed for modelling neutron scattering instruments such as diffractometers, spectrometers, reflectometers or small-angle scattering instruments. In McStas, all instruments or components are written by users and are automatically translated into practical simulation codes in ANSI-C [140]. A complete installation of McStas package requires: a C-compiler (e.g., Dev-CPP sub-package [141]), for graphic output and user interface Perl or Perl-Tk [142] or Matlab [143], Scilab [144], PgPlot [145]. All these can be installed from the source code following the usual procedures. The McStas software package also permits parallel computing, i.e. each simulation can be processed by a different number of CPUs for decreasing the simulation time. GridMP platform provided by ISIS, UK [146] was used frequently for Monte Carlo simulations along this research. The Grid works in two basic modes: parameter scan mode (when a bat file with many small runs is taken and each smaller run is executed on a distributed machine) and one large scan (when one large simulation, e.g. 10^{10} neutrons is broken into smaller chunks and these chunks are executed in parallel over many machines. After that, the results are then merged together and the result is same as in one large simulation, but in far less time).

The current McStas version 1.12c [138] can be run on different operating systems (Windows XP, Vista, Windows7, Linux or Mac OSX). It actually includes a library which contains around 110 components and 70 instruments and can be updated with new modules by the users.

What does an instrument look like in McStas?

An instrument in McStas (written as a text file) is described as a set of components with physical (for example, in the case of the sample component, defining the d-spacing value)

and geometrical properties (e.g. the distance from source to sample etc).

The virtual instrument consists of a source component which generates each neutron (randomly) after which the particle is propagated through the different instrument components (such as guide, pinholes or detectors). These components influence the neutron's characteristics such as: position, velocity, direction, time and where relevant spin. When neutrons encounter an optical component, they may be transmitted, absorbed, scattered or reflected. To monitor and record several parameters of interest, like the wavelength, or the Cartesian components of the wave vector or the energy of the neutrons some virtual monitors and detectors may be placed along the path of neutrons. Beside that, the intensity of the neutron beam and the statistical errors associated with the events and the number of counts can be recorded by monitors, at different positions in the instrument (see Appendix 2). In the current version of McStas software applied during this research, the effect of the gravity was not taken into account by the components used in the modelled instrument; only in Section 3.4.3.5 a study of gravitational effect in the neutron guide is presented.

3 The IMAT instrument (imaging case)

This chapter reports investigations into IMAT components, relevant to its performance as an imaging instrument. Based on the McStas modelling approach different components such as neutron guide and pinhole were investigated. Moreover, effects of the beam on the neutron imaging detectors were evaluated. The results were combined with similar investigations into the diffraction case (performed elsewhere and not part of this thesis) leading to the design considerations for the combined imaging and diffraction instrument, IMAT.

3.1 The ISIS neutron facility

Entering its fourth decade of existence, ISIS, the pulsed spallation neutron and muon source at the Rutherford Appleton Laboratory in Oxfordshire, UK, has made significant contributions to the neutron scattering research in different fields including physics, chemistry, materials sciences, engineering, biology, archaeology and geology.

3.1.1 Overview of existing neutron imaging and diffraction facilities at the ISIS

ISIS is a pulsed neutron facility (see section 2.2.3) which comprises two target stations (Figure 3.1.1): TS-1 operating since 1984 and presently with 24 neutron instruments and TS-2 project built from 2003 with a capacity for 18 instruments, seven of them being already fully operational since 2009. Each one of the instruments is optimised for different types of measurements, providing diverse and complementary information. A suite of diffraction instruments such as GEM, POLARIS, HRPD and ENGIN-X (on TS-1) and

WISH (on TS-2) are designed to provide phase and structure analysis, texture analysis, microstructure analysis and residual stress analysis.

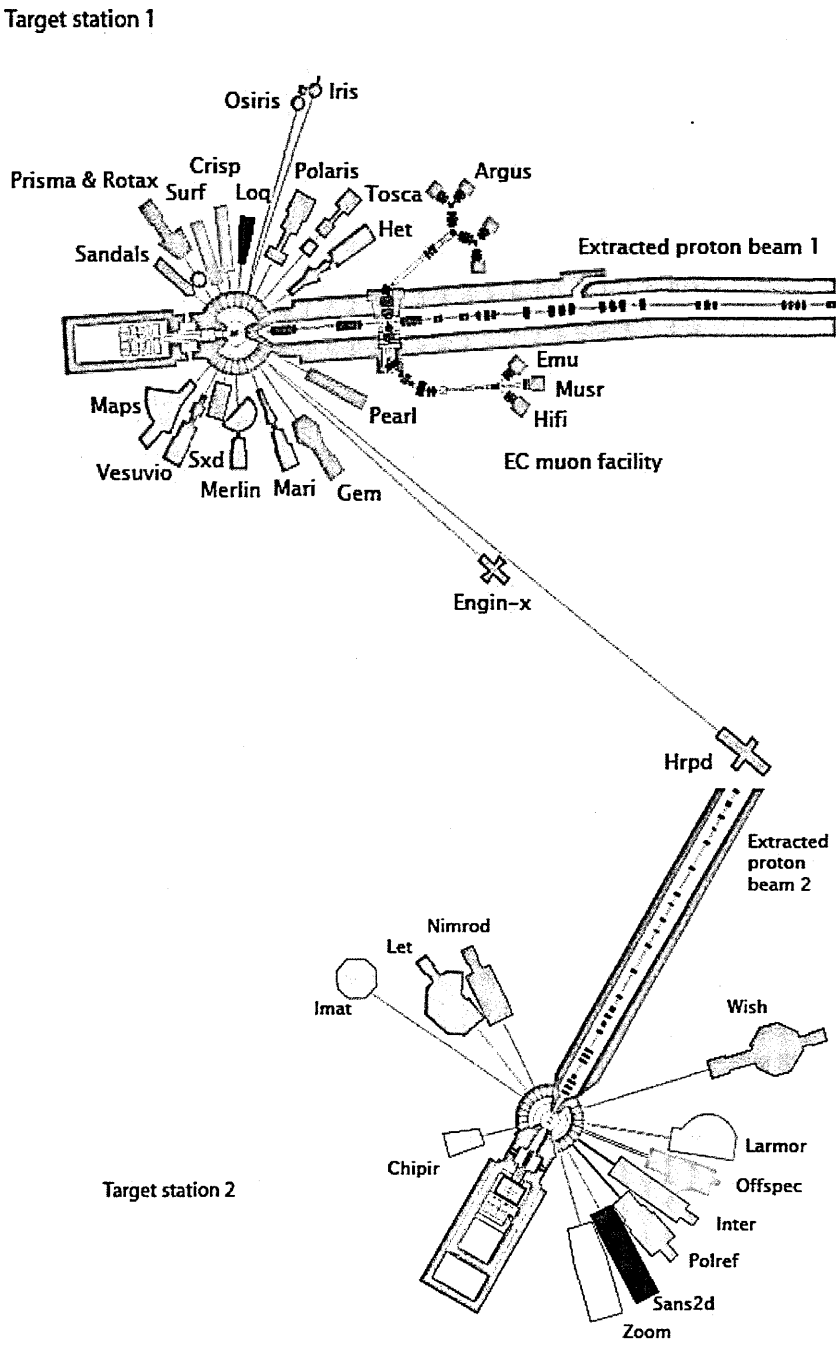

Figure 3.1.1: *The instrument layout of the ISIS neutron spallation source [26].*

The particular project, ENGIN-X [6], which we refer to later in this thesis, is used for strain and stress analysis of engineering components and materials as well as, for example, archaeological objects and geological materials.

Instruments dedicated to imaging experiments are not currently available at ISIS (some pioneering Bragg edges measurements have been performed on ENGIN-X [11]). But a neutron imaging and diffraction instrument IMAT (the investigation of our research) will be built during a second phase of the TS-2 project at the ISIS facility.

3.1.2 The need for IMAT

The neutron imaging facilities have to serve numerous users worldwide whether they are under operation at research reactors or continuous spallation sources. Presently no neutron imaging instrument exists at a pulsed neutron source (which would enable them to take advantage of the timing structure), but few are in the design stage (e.g. IMAT at ISIS, UK [147], VENUS at the SNS, Oak Ridge, USA [9], and ERNIS at J-PARC, Japan [10]). IMAT will be a thermal and cold neutron facility, combining imaging and diffraction applications. It will be built on the ISIS second target station, a low-power pulsed spallation source of approximately 50 kW and operated at 10 Hz. The combination of imaging and diffraction techniques on one beamline will allow new types of experiments to be carried out, otherwise not possible with any other presently available single instruments (e.g. ENGIN-X at ISIS or NEUTRA at PSI). In addition to the standard neutron radiography and neutron tomography, IMAT will also allow for energy selective imaging applications, such as high-resolution Bragg-edge transmission imaging, taking advantage of the TOF method at a pulsed source. A novel neutron counting detector (with high-spatial and high-temporal resolution) based on microchannel plates (MCP) developed by Space Science Department, Berkeley, USA [148] is currently envisaged as IMAT Bragg edge imaging detector.

The combination of both spatial and time information on IMAT enables texture mapping and strain analyses, as well as studies of phase compositions and phase transitions. IMAT will have sufficient orientation coverage for effective texture analysis and the simultaneous analysis (in a short data acquisition time) of internal stress and texture analysis will be a unique and key capability of this beamline. IMAT can be easily switched from imaging to diffraction mode, making it convenient to use the radiographies to guide diffraction measurements (see Chapter 5).

3.2 IMAT overview and the design process

IMAT will be placed on the Second Target Station (TS-2) situated on the west side (W5) of the low power target [60]. One of five proton pulses produced by the ISIS synchrotron is directed into the TS-2 along a new proton beamline. The target and moderators on TS-2 are designed and optimized to obtain long wavelength neutrons. Details about the IMAT moderator are offered in paragraph 3.3.

Initially there were two options for IMAT taken in consideration:

- Two separate beamlines, each one optimised for its particular purpose (imaging and diffraction);
- One beamline which will operates in interchangeable modes, either imaging or diffraction.

Technically, the first option is more convenient to be implemented and it allows optimisation of the two separate applications more easily. The second option of combining imaging and diffraction on one beamline is more challenging; it requires a neutron guide to be used for obtaining a good time resolution for diffraction and energy-selective imaging.

The use of a neutron guide is unusual for an imaging instrument, and thus neutron optics features need to be optimized, in order to maximize the neutron flux on the sample

for imaging and diffraction experiments and to minimise geometrical artefacts in the "open beam" image at the sample position. From the initial performance requirements as given by the science case [147] it was obtained that the incident energy spectrum and timing resolution requirements for both modes are similar, which is an imperative condition for a combined instrument on the same moderator. Another important aspect favourable to the second beamline option is that IMAT can switch from imaging to diffraction (i.e. interchange from a large beam of 200×200 mm^2 for imaging to a minimum beam of 1×1 mm^2 for diffraction) by simply moving the aperture selector to an open position and adjusting the beam jaws to the desired gauge size) without removing the sample. This allows a complete investigation of the sample by 2D or 3D imaging followed by a detailed diffraction map analysis of the interested regions guided by the tomography data.

These advantages led to the decision of constructing the IMAT instrument on a single beamline with imaging and diffraction combined.

3.2.1 The design parameters

While the imaging mode of IMAT will use a wide beam emanating from a pinhole to study extended object in a single data acquisition or in a scanning mode, the diffraction process of IMAT will offer an alternative to the ENGIN-X instrument and it will provide greater solid angle detector coverage to evaluate texture, phase compositions and strain orientation distributions in a shorter data acquisition time.

The IMAT main components are: the moderator, the guide, the choppers, a pinhole selector, slits, jaws, imaging detectors and diffraction detectors. A basic instrument description is represented in Figure 3.2.1 and it is detailed below.

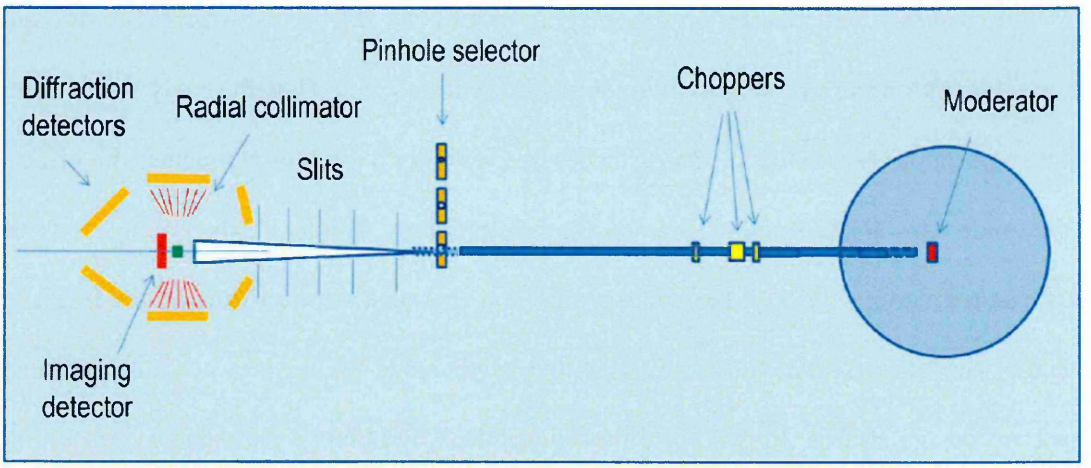

Figure 3.2.1: *A schematic layout of the main IMAT components [147].*

The scientific specifications of the IMAT instrument are in accordance with the performance of the ISIS TS-2 station. In order to maximize the neutron flux on the sample position, IMAT is placed on coupled, L-H2/S-CH4 moderator (see section 3.3). A square, straight supermirror neutron guide (see section 3.4.1) transports the neutrons from the moderator to the pinhole selector (see section 3.6.1) position. The long flight path of 56 m, from the moderator to the sample position, ensures good time-of-flight and energy resolution while preserving a large neutron wavelength bandwidth. Three choppers (see section 3.5.1) will be placed into gaps of the neutron guide: one T0 chopper serving as a fast neutron and gamma radiation filter and two double disk-choppers defining the wavelength band to prevent the frame-overlap of neutrons between successive neutron pulses. With a set of beamline "jaws" (beam delimiters) and one set of slits just in front of the sample, the beam size at the sample position can be adjusted. Two imaging cameras will be available: a gated CCD camera (see section 3.7.1) and a time-of-flight capable high-resolution pixel detector (see section 3.7.2). Two detector banks at 90° have a particular relevance for strain analysis, for simultaneously measuring two orthogonal strain components. Radial collimators will be installed between sample and each detector bank in order to define a diffracting gauge volume for a given beam size.

This thesis was focused on the imaging part of the IMAT instrument. So, through the parameters optimized we can enumerate the neutron guide (length, cross section and wavelength dependent effects), the distances between instrument components, the effects of the guide gaps and the pinhole size on the radiographies. Moreover, the homogeneity of the flux distribution, the average neutron flux and the peak neutron flux on the imaging detector were studied. All these investigations were made taking into account the most important design criteria: to maximise the neutron flux, to obtain a good energy resolution whilst retaining a large neutron bandwidth and a long flight path and on the other hand, to find the optimal beam profile on the sample position.

Initial, given design specifications for the imaging part of the instrument can be summarised as follow:

- the actual wavelength-dependent flux distribution (flux spectrum) on a given moderator;
- moderator face size 11×11 cm^2;
- moderator-guide entrance distance of 1.7 m (the closest possible distance achieved on TS-2);
- an adjustable pinhole aperture with five opening diameters 5, 10, 20, 40 and 80 mm situated at the guide exit;
- a flight path from the pinhole to the sample position of 10 m providing a good collimation ratio (L/D=2000, 1000, 500, 250, 125) and a small vertical and horizontal divergence (up to 0.2°);
- moreover, a maximum field of view of 20×20 cm^2 for radiography and tomography measurements, as well as for many energy-selective applications was another parameter defined.

3.2.2 Modelling approach – choice of McStas

The building and the improvement of a neutron scattering instrument is a comprehensive process. As a result of several European universities and research institutes' collaboration, a neutron scattering ray-tracing simulation tool, McStas (see section 2.5) was developed for both types of sources: continuous or pulsed. McStas has a large library with many components and instruments. The evaluation of the neutron performances of both modes of the IMAT instrument (imaging and diffraction) has been performed based on Monte Carlo calculations using McStas software packages [134]. A complete IMAT instrument was modelled in McStas software calling each main component and translates the instrument metafile into C- code and then compiled into an executable.

In a real neutron instrument detectors and monitors have different roles. While detectors count the neutrons with as high an efficiency as possible, absorbing a part of them in the process, monitors measure the intensity of the incoming beam and they are almost transparent interacting only with 0.1-1% of the neutrons passing through. In McStas simulations every neutron ray is detected without absorbing or disturbing any of its parameters. Because of that both detectors and monitors in McStas function in the same way and they are called altogether "monitors" in the simulations presented below.

A number of 10^{10} neutrons generated in the wavelength range 0.1-10 Å were typically used in the simulations for the IMAT imaging instrument. This number was chosen based on the computing time considerations.

The default McStas coordinate system used in the simulations in this thesis is as follows (Appendix 2):

- z is the direction of neutron propagation. In our case, the IMAT moderator face is positioned at $(x, y, z) = (0, 0, 0)$;
- x is the horizontal direction (left and right);

- y is the vertical direction (up and down);

A number of monitor components are available for use in McStas and in addition to the real detectors measurements (space and time) they are sensitive to any neutron properties such as direction, energy or divergence. We have applied three types of monitors for the IMAT simulations to find out information on, for instance peak intensities and average intensity of the neutron beam, and on the shape of the wavelength distribution or the beam divergence as function of wavelength. All monitors used in modelled IMAT instrument are aligned towards the transmitted beam, one exception being in Section 4.2.3 where the beam divergence on different points on the camera was studied.

- PSD (position sensitive detector): counts where in the detector a neutron is incident, investigates the properties of the neutron beam in terms of divergence and intensity. It is used to display a 2D image of the beam cross section in the (x, y) plane. Each pixel has a colour corresponding to its intensity (blue colour for lower intensity; red colour for higher intensity). The input parameters are the number of pixels per columns `(nx)` and per rows `(ny)` and the boundaries of detector opening `(xmin, xmax, ymin, ymax)` with units in meters. The output from this monitor is reported in the `PSD.dat` file and it shows the total integrated intensity across the surface of the monitor, the error of the integrated intensity and the `x, y` values (with meters as units) of the centre of the beam cross section.

```
COMPONENT PSDdet = PSD_monitor(nx = 100, ny = 100,
filename = "PSD.dat",xmin =-0.1, xmax =0.1,
ymin = -0.1, ymax =0.1)
```

- Lambda monitor (wavelength sensitive monitor): a rectangular monitor in the (x, y) plane and it is sensitive to the incident neutron wavelength. The wavelength histogram is divided in `nchan` (number of channels) bins. The monitor captures the transmitted neutron

intensity inside the wavelength channels. Only the neutrons with the wavelength between l_min and l_max are detected and the monitor's output is a wavelength spectrum.

```
COMPONENT lmon = L_monitor(
nchan = 1000, filename = "lmon.dat", xmin = -.10,
xmax =.10, ymin = -.10, ymax = .10,
Lmin = l_min, Lmax = l_max)
```

- Divergence-lambda monitor (divergence-wavelength sensitive monitor): sensitive to both the horizontal divergence and the wavelength. The input data are the dimension of the monitor (measured in meters), l_min and l_max to define the wavelength window, measured in Å and the filename. The monitor's output is the neutron intensity as a function of the divergence and neutron wavelength. The initial code from McStas for this monitor was modified as discussed in Section 4.2.3.

```
COMPONENT Divlambda = DivLambda_monitor(
filename = "divl", xmin = -0.10, xmax = 0.10,
ymin = -0.10, ymax = 0.10, lambda_0=l_min,
lambda_1=l_max)
```

The other McStas components used in IMAT imaging modelled instrument such as moderator, or neutron guide will be defined later in this chapter. We now present results of modelling studies of IMAT components, commencing with the moderator and moving sequentially along the beamline.

3.3 IMAT moderator

Details about moderators and in particular, the moderator from TS-2, were given in Chapter 2, Section 2.2.3. Here we intend to present more specific aspects of the IMAT moderator, its comparison with the ENGIN-X moderator and the corresponding McStas code used in IMAT imaging modelling.

While ENGIN-X is a dedicated diffraction instrument, IMAT will combine both imaging and diffraction, so it has different expectations in terms of neutron flux and pulse shape. Imaging and in-situ diffraction applications require highest possible primary neutron flux which necessitates the choice of a coupled moderator, at the expense of resolution. This assessment will be demonstrated below by comparing the ENGIN-X decoupled moderator with the IMAT coupled moderator.

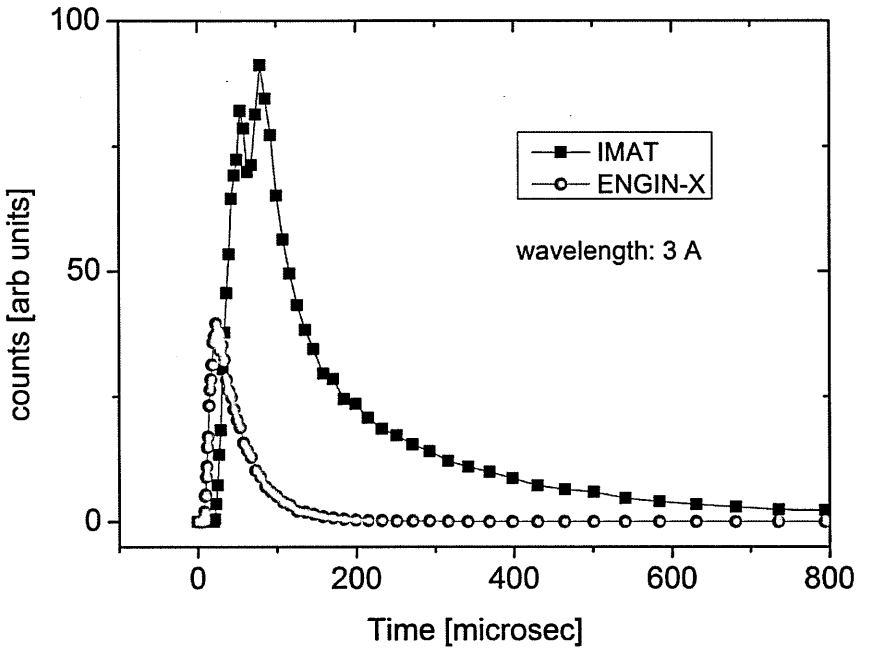

Figure 3.3.1: *The simulated pulse neutron shape for 3Å for different moderators (coupled and decoupled). While the coupled IMAT moderator has a higher intensity than the decoupled ENGIN-X moderator, the "sharp" ENGIN-X moderator pulse allows a better temporal resolution than the coupled moderator.*

ENGIN-X is placed on the port S6 on TS-1 and is using a decoupled, poisoned methane moderator (110 K) combining the narrow pulse width ("sharp" pulse) with relatively high neutron flux over a 1-3 Å wavelength range relevant to most engineering materials. The imaging applications of the IMAT instrument need a higher neutron flux and this can be achieved using a coupled moderator (20 K), though, unfortunately at the expense of energy resolution. Moreover, the quality of energy-selective imaging and the diffraction resolutions depends on the pulse width of the moderator.

Figure 3.3.1 displays two neutron pulse shapes (decoupled moderator used at ENGIN-X from TS-1 and coupled moderator used at IMAT from TS-2) for a fixed wavelength of 3 Å indicating a higher intensity and a broader pulse for the coupled moderator. Whilst the cold, coupled moderator from IMAT is best for high-intensity applications, the ENGIN-X moderator is better for high resolution applications. The pulse shapes in Figure 3.3.1 are extracted from the respective McStas data of the ISIS moderators.

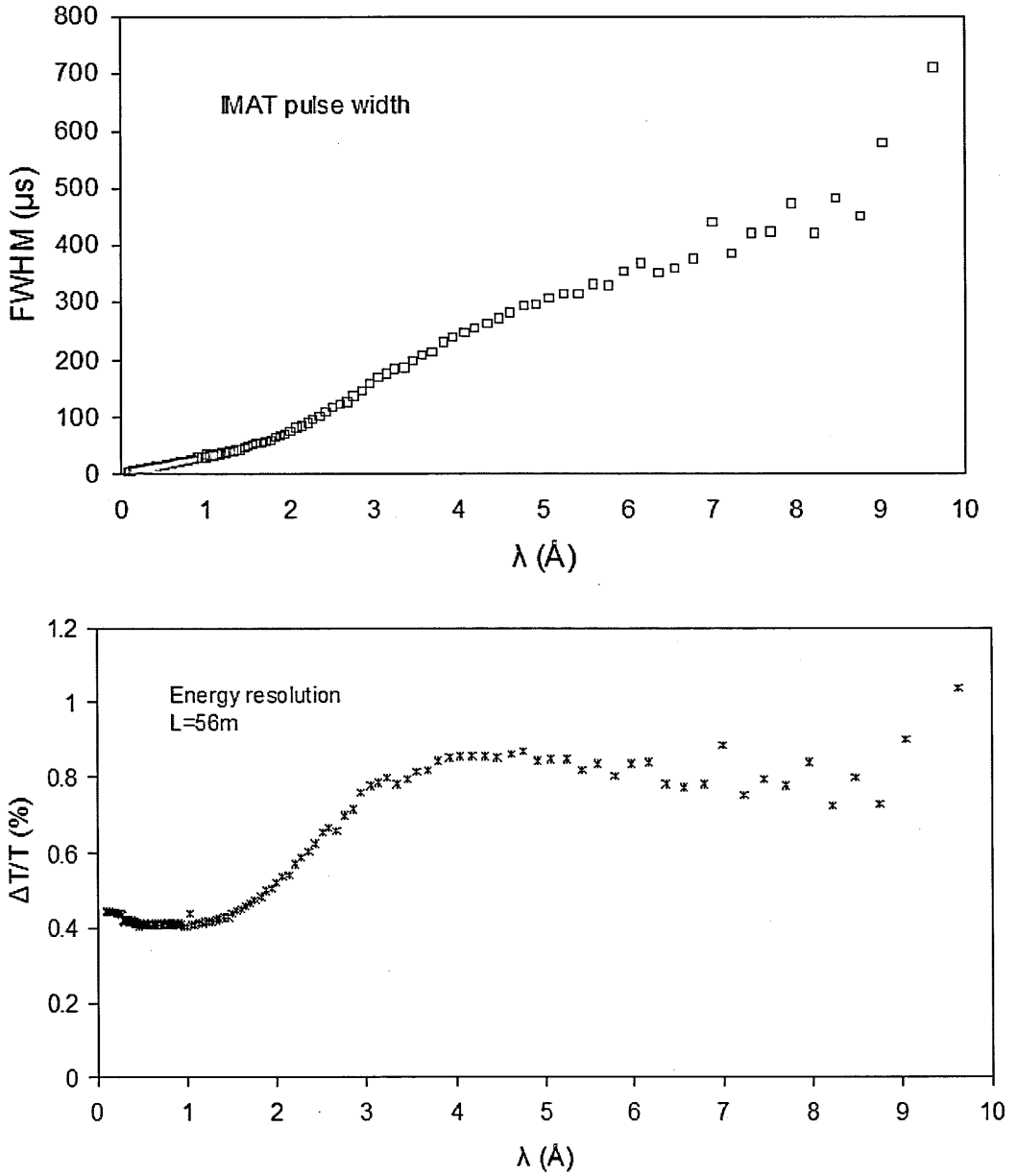

Figure 3.3.2: *Moderator pulse width (FWHM) and resolution (ΔT/T) as function of wavelength.*

The best imaging and diffraction energy resolution are limited by the pulse width of the moderator. Figure 3.3.2 presents the wavelength-pulse width (FWHM), as well as the energy resolution ($\Delta T / T$) at 56 m, i.e. at the position of the imaging detector. The long-wavelength FWHM is 700 μsec which yields a resolution of $\Delta T / T < 1\%$ for all wavelengths, and < 0.8 % for wavelength up to 9 Å, which is considered adequate for proposed scientific applications.

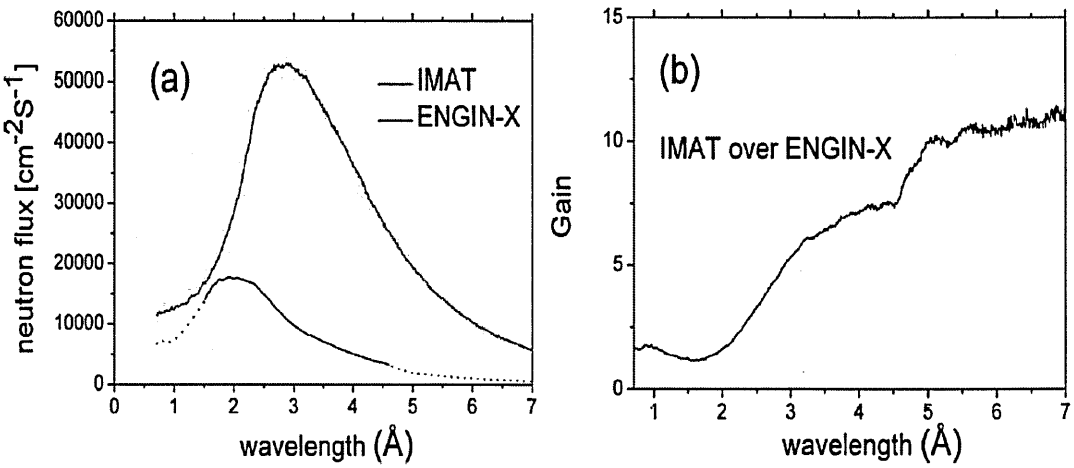

Figure 3.3.3: *IMAT spectrum at sample position (56 m). (a) flux compared to ENGIN-X; (b) gain over ENGIN-X. The full line for ENGIN-X on the left image indicates the wavelength band for 25Hz running.*

Figure 3.3.3 (a) shows the IMAT spectrum at the sample position compared to the ENGIN-X spectrum for 10 Hz and 25 Hz running, respectively. Figure 3.3.3 (b) displays the intensity gain of IMAT compared to ENGIN-X as function of wavelength which shows that there is a clear gain for IMAT of about 5 times in the medium wavelength range 3-5 Å and of 10 times at longer wavelengths above 5 Å. The thermalised IMAT flux has a peak at around $\lambda_{peak}=3$ Å; the maximum single-frame wavelength value is about 6.7 Å, just above twice the value of λ_{peak}, which makes the IMAT wavelength band convenient for efficient collection, i.e. peak wavelengths are not heavily over-counted and long wavelengths are not under-counted. The IMAT disk choppers will limit the wavelength band to 0.7-6.7 Å thus preventing the frame overlap of successive ISIS neutron pulse at the detector position. By operating the choppers at 5 Hz instead the standard 10 Hz the wavelength range can be extended up to 14 Å. The selection of wavelength-bands will be explored in Chapter 4.

On ISIS TS-2 five beamlines W5-W9 separated by an angle of 13° (Figure 3.3.4) look at the same moderator filled with liquid hydrogen on one side and solid methane at the back of the hydrogen container.

Both parts of the moderator (liquid hydrogen and solid methane) are important to produce the characteristic beam flux of IMAT. The hydrogen moderator will determine the high-energy part of the spectrum, while the methane will determine the long-wavelength part of the IMAT spectrum. The pre-moderator [149] (met in the coupled moderator it is one layer which surrounds the moderator core to ensure thermalizing high energy neutrons which enters from reflector eliminating most of the heat load before the neutrons enter in the moderator) will be ambient water, not viewed by the IMAT instrument. The beryllium reflector will surround the target and the moderator and will scatter neutrons back into moderator.

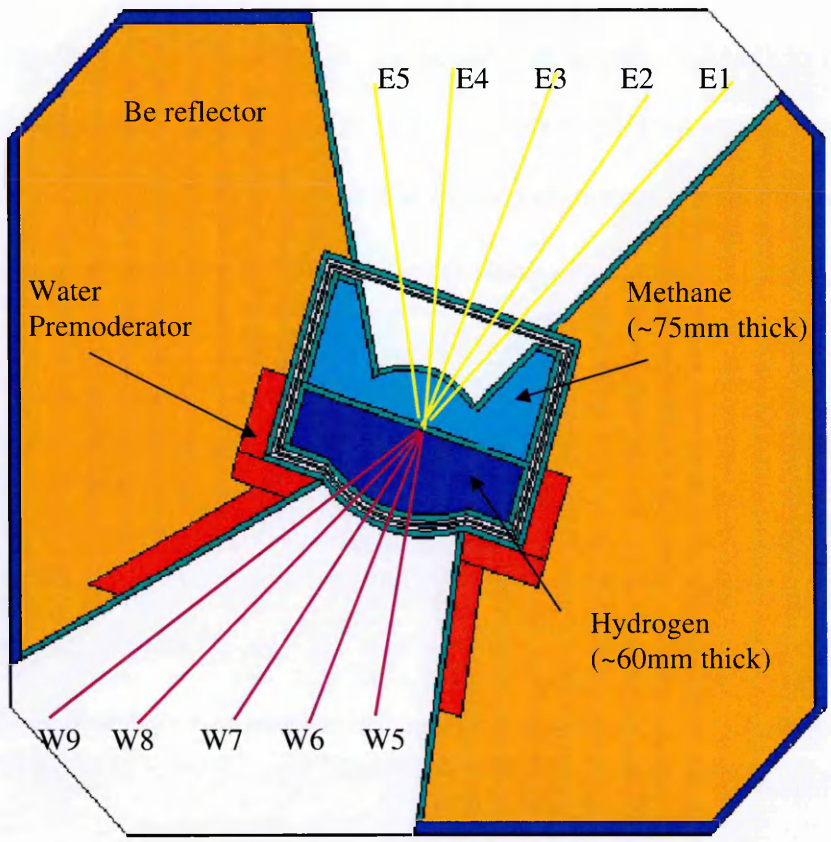

Figure 3.3.4: *Different positions of the coupled moderator on the west side of TS-2.*

For the IMAT instrument there were available beam two ports W5 and W8 which satisfied the requirements for maximum integrated flux and for a broad neutron wavelength range with some restrictions on the flight paths however.

The performance of an imaging instrument for three instrument positions W5/L37, W5/L56 and W8/L40 on the coupled moderator on TS-2 was evaluated (see section 3.4.3.1). The decision on the instrument position and length, and the choice of port for IMAT, was made based on arguments such as the instrument resolution, as well as more practical considerations of costs or the space available for the instrument.

McStas modelling of the TS-2 moderator

The ISIS moderator module employed in the Monte Carlo simulations was elaborated and provided by the ISIS TS-2 Target Development Team.

In the McStas IMAT instrument model we employed the ISIS moderator component as follows:

```
COMPONENT moderator = ISIS_moderator(
Face = "w5", E0 = e_min, E1 = e_max, dist = 1.7,
xw = 0.11, yh = 0.11, modXsize = 0.11, modYsize = 0.11,
CAngle = 0, SAC=1) AT (0, 0, 0) ABSOLUTE
```

Where the neutrons are generated having a range of energies from *E0* to *E1* and pass through the moderator *Face* defined by the moderator size *modXsize* and *modYsize* (meters) and a focusing window (rectangle) with the dimensions *xw, yh* (meters), generally the same as the width and height of the next beam component. In reality, the focusing window of a moderator does not exist and it is used only to improve the efficiency of the simulations. The distance of the focusing window from the moderator face, *dist,* is a given parameter with a value of 1.7 m and represents the distance to the guide entrance. The *CAngle* variable, the angle from the centre line, is used to rotate the viewed direction of the

moderator and reduces the effective solid angle of the moderator face; in this case is it 0 radians. The solid angle correction (SAC) is 1. In all IMAT simulations the moderator was taken as a reference point for the positions of the other instrument components.

3.4 Optimising the neutron guide

One important component used to supply neutrons from the source to different instruments is the neutron guide. The theoretical development of neutron guides was initiated by Maier-Leibnitz and Springer [150] and guides were installed for the first time in 1971 at the ILL. A neutron guide is described by its geometry and its coating. Details about the neutron guide and results corresponding to the IMAT imaging instrument are presented in the following sections.

3.4.1 Characteristics of a neutron guide

Without a neutron guide one could not run experiments at long distances from the neutron source due to the neutron flux loss. Hence, the neutron guide is used to transport neutrons from the moderator to the sample thereby achieving higher neutron flux at the experiment site.

Guides are also used to improve the temporal resolution of pulsed source neutron instruments determined by the relative time uncertainty $\frac{\Delta t}{t}$, where Δt, for a given wavelength, is given by the width of a pulse as shown in Figure 3.3.1 and t is the time-of-flight of neutrons travelling from the source to the detector. Another purpose of the guides is to split neutron beams in order to feed several instruments. An important role of the neutron guide is also to reduce the background radiation constituted from gamma rays and fast neutrons. For that reason, the neutron guides are often curved eliminating the direct

view of the moderator (Figure 3.4.1). The gamma radiation travels in straight lines and goes through the walls of the guides into the shielding around the guide. In reality, a curved guide has the radius of curvature of several kilometres making the curvature to be imperceptible and so, the arc of the curve could be approximated with straight sections.

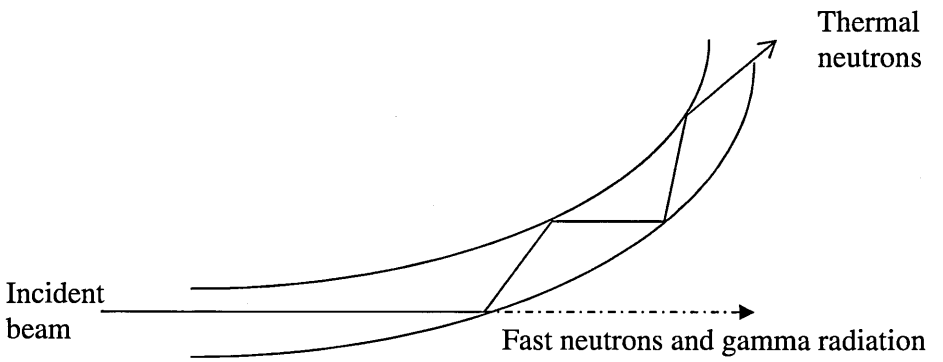

Figure 3.4.1: *Schematic representation of a curved neutron guide. Fast neutrons and gamma rays pass straight through the walls of the guide into the shielding.*

The geometry of the neutron guide and the guide coating determine how many neutrons enter in the guide, how many of them are transmitted through the guide, and how many exit the guide and reach the sample. To avoid the escape of the non-reflected neutrons and gamma radiation and to keep the radiation levels in the experimental areas to a minimum, the guide system is shielded by neutron absorbing material (e.g. concrete, steel, borated wax).

Guide geometry types

Among the neutron guide geometries there are: straight, curved, rectangular, ballistic (when the guide cross section varies along its length to minimise transport losses within the guide), parabolic or elliptical (where the moderator is considered in the first focal point and the sample in the other focal point). The ballistic guide system comprises a linearly expanding section, followed by a straight guide who ends with a focussing "nose" which is

a linearly tapering section that narrows the beam onto the sample and has the advantages of the increasing number neutrons onto the sample and the decreasing divergence of the transmitted beam in the expanding section. At the nose part, the neutron intensity also decreases while divergence increases following Liouville's theorem [151]. The parabolic guide system is, in fact, an improvement of the ballistic guide system where the expanding section and focussing "nose" are both parabolic and ideally makes the beam parallel. Later, in this section it will be explained via Monte Carlo calculations, why a straight rectangular guide is used on the IMAT instrument, instead of a curved guide as in the ENGIN-X case.

Guide coatings

The development of neutron guide coating is based on the fact that the refractive index (n) for neutrons is less than one for most materials and that the total internal reflection can arise at the interface between the vacuum and the material guide (refraction angle is zero, Figure 3.4.2). We know that the refractive index is defined by the relation:

$$n = \frac{\cos\theta_0}{\cos\theta_2}, \tag{3.4.1}$$

where θ_0 is the incidence angle and θ_2 is the refraction angle (Figure 3.4.2).

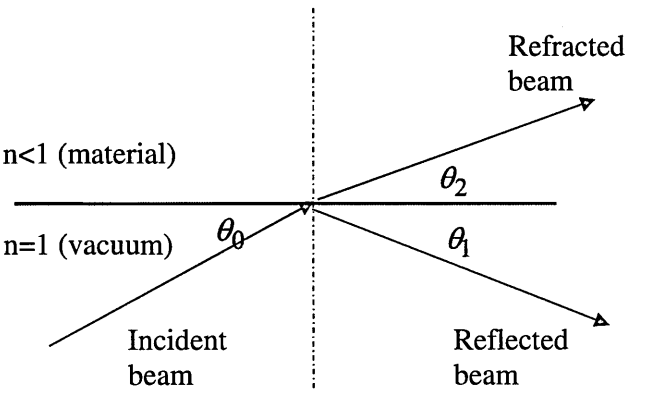

Figure 3.4.2: *The neutron beam path from vacuum to medium (total reflection for* $\theta_0 < \theta_c$).

Knowing that the neutron refractive index is given by [5]:

$$n^2 = 1 - \lambda^2 \cdot \frac{N \cdot b}{\pi}, \tag{3.4.2}$$

where N is the number of atoms per cm^3 and b is the coherent scattering amplitude of the bound atom we obtain:

$$\theta_c = \lambda_c \cdot \sqrt{\frac{N \cdot b}{\pi}}, \tag{3.4.3}$$

where λ_c is the critical wavelength for total reflection θ_c.

Since natural nickel (Ni) is not very expensive and it has a large scattering length density $(N \cdot b)$ and hence a large critical angle θ_c, it is often used as a coating material. Other coating material applied could be iron. Beryllium gives even a larger critical angle than Ni, but because it is toxic it is not recommended to be utilised.

Neutron guides are produced by companies such as SwissNeutronics [152] from Switzerland or Mirrotron Ltd [153] from Hungary and they are made of nickel-coated or supermirror-coated glass assembled as a rectangular cross-section as shown in Figure 3.4.3.

Figure 3.4.3: *Straight rectangular neutron guide section coated with supermirrors (m=3) for J-Parc fabricated by SwissNeutronics [152].*

Sections of guides are butt jointed inside a vacuum vessel to produce the guide. The practical performance of a neutron guide depends on the reflectivity of the surface. The reflectivity could be affected if there are surface undulations or porosity as this can increase the number of non-reflected neutrons. A polishing procedure can optimise the flatness of the surfaces.

In the literature, a guide coated with pure Ni is defined as an "m=1" mirror. For improving the efficiency of surface coatings (i.e. increasing the critical angle and hence the neutron flux and wavelength bandwidth) of neutron guides a supermirror technology [154-156] is applied consisting of an artificial multilayer made of thin layers of alternating materials of different thicknesses (such as ^{58}Ni which has a scattering length 20% higher than natural Ni and titanium (Ti)), with a large contrast in scattering-length density. It was observed that Ni and Ti layers tend to interdiffuse and the interfaces can become rough and so for reducing these effects, C was added to Ni improving the neutron reflectivity characteristics of Ni-Ti supermirror depositions.

The combination of two adjacent layers in the reflection of neutrons can be explained using Bragg's reflection from the lattice planes:

$$\sin\theta = \frac{\lambda}{2d}, \tag{3.4.4}$$

where λ is the neutron wavelength and d the distance between layers (Figure 3.4.4).

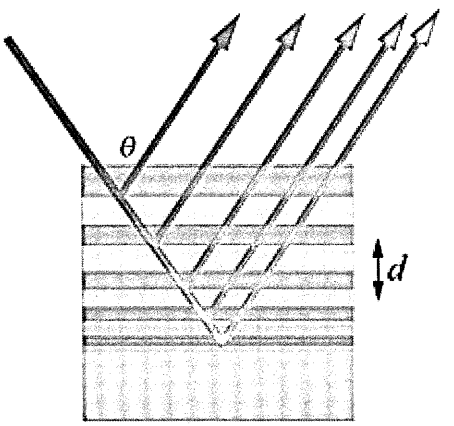

Figure 3.4.4: *Bragg reflections from a supermirror coating [152].*

In the case of a supermirror coating of a straight neutron guide the critical angle depends on the coating and neutron's wavelength and is related to the equation:

$$\theta_c = \frac{0.1^{\circ}}{\text{Å}} \times m \times \lambda, \tag{3.4.5}$$

where m defines the quality of the specific guide coating (m=2 is a supermirror with double the critical angle of Ni etc). Typical multilayer can have m=2, 3 or 4 and most recently, even m=7 can be obtained.

3.4.2 The neutron guide on the IMAT instrument

The installation of neutron guide on accelerator sources requires more attention regarding its alignment and positioning. Because the moderators of spallation sources are relatively small the entrance of the neutron guide must be more carefully aligned and as close to the moderator as possible to ensure maximum illumination. In case of IMAT the guide starts as close as possible to the moderator in the shutter section and ends just upstream from the pinhole selector. The distance guide-exit to pinhole depends on the specific designs of guide, pinhole selector as well as the space reserved for filters and diffusers. The neutron guide should be evacuated to avoid intensity loss due to air scattering.

Since the IMAT instrument combines both imaging and diffraction measurements the design of the neutron guide is challenging especially in the context of the imaging function as we will see in this chapter.

Starting from the idea that the ENGIN-X instrument at ISIS is dedicated to diffraction measurements and uses a curved guide one should ask if it is possible or desirable to use this type of guide for IMAT.

To see the effect of a curved guide on the imaging functionality we tested the virtual IMAT imaging instrument using a curved guide with constant rectangular cross section, and variable radius of curvature. The other possibility considered was a simple

straight and square guide. Both neutron guides had same length (42.8 m), the same cross sections (the same as the moderator, i.e. 0.11×0.11 m^2). The curved guide was given by the slight curvature of 5720 m radius calculated according to equation:

$$R = \frac{L^2}{2 \cdot \Delta x} \text{ ([157])} \tag{3.4.6}$$

where L is the guide length and Δx the guide deflection[3].

For studying the neutron intensity distribution generated by the neutron guide a PSD monitor (with 20×20 cm^2) was placed on the sample position. Simulations were performed using 10^{10} neutrons and the results are shown in Figure 3.4.5 below. The performance in terms of image homogeneity of the imaging instrument with a straight guide is evidently better than the instrument with a curved guide as illustrated in Figure 3.4.5. While the open beam profile at the sample position using a straight rectangular guide is symmetric, the open beam radiography using the curved guide is asymmetric due to the effects of garland reflections [158]. The artefacts from the 2D image will be discussed later in this chapter.

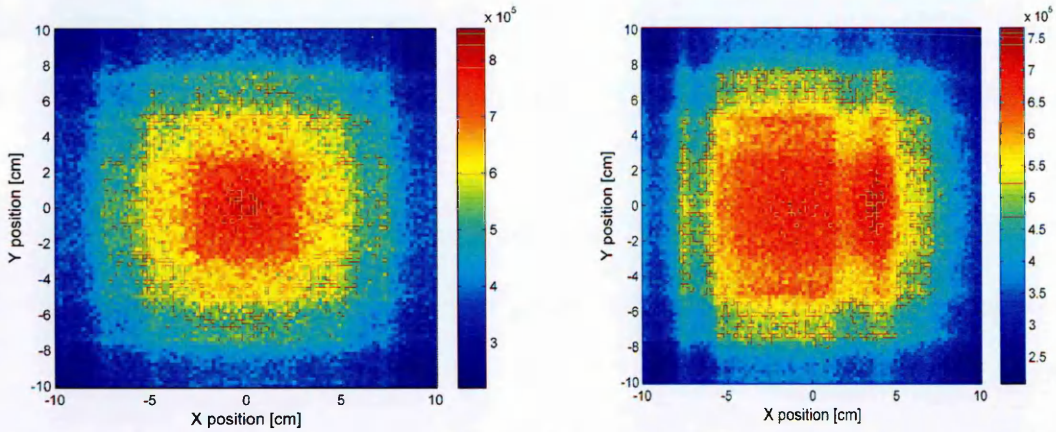

Figure 3.4.5: *Distribution of the neutron intensity on the PSD monitor placed on the sample position (left: straight guide, right: curved guide).*

[3] The radius of curvature was introduced in such way to avoid direct line of sight between moderator and the end of the guide. For this, we choose Δx greater than the moderator cross section 11×11 cm^2. It was considered Δx of almost 16 cm in agreement with the reference 147. Kockelmann, W., Oliver, E.C., Radaelli, P.G., *IMAT- An imaging and materials science & engineering facility for TS-II.* 2007, ISIS Second Target Station Project.

It is beyond the scope of this paragraph to describe all aspects of the decision taken for IMAT neutron guide which included technical details provided by the engineers or diffraction issues. However, the above demonstration was one of the arguments in favour of using a straight rectangular (square) neutron guide instead of a curved guide.

3.4.3 McStas modelling of the straight IMAT neutron guide

The neutron guide for the IMAT instrument consists of several sections with gaps between them for choppers or other components. In the preliminary Monte Carlo simulations these sections were neglected and the guide was considered straight, with a squared cross section, with no gaps. Due to engineering constraints the closest position to the moderator where the guide can start is 1.7 m. The guide is described in McStas by the following component:

```
COMPONENT myguide = Guide
w1 = 0.11, h1 = 0.11, w2 = 0.11, h2 = 0.11, l = 42.8, m = 3)
AT (0, 0, 1.7) RELATIVE moderator
```

The guide component (Figure 3.4.6) runs parallel to the z axis and has a rectangular entrance with dimensions $w1$ (width), $h1$ (height) and exit with $w2$ (width), $h2$ (height). The parameter l represents the length of guide and m defines the m-value of guide material.

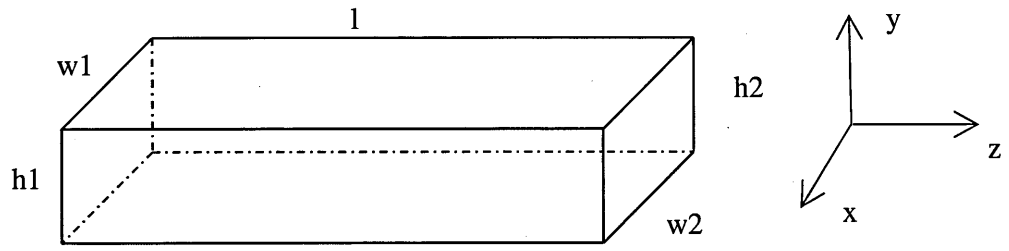

Figure 3.4.6: *The geometry of straight neutron guide.*

The modelled IMAT imaging instrument in McStas is illustrated schematically by moderator-guide-pinhole-monitors configuration as shown in Figure 3.4.7 and based on the parameters offered in Section 3.2.1.

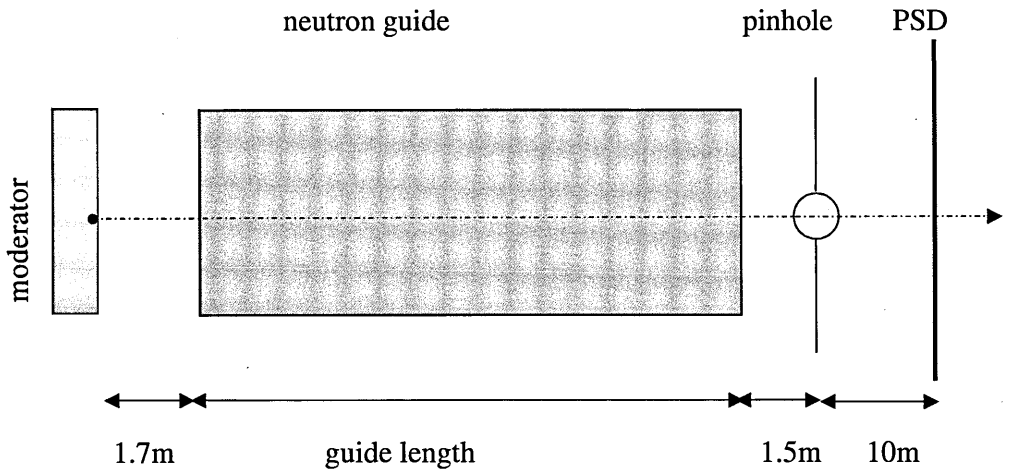

Figure 3.4.7: *The IMAT imaging instrument components in McStas.*

In the upcoming sections we present the results for investigations into the guide cross section, length of guide and optimum m value for the IMAT imaging instrument. It should be noted that the intensity values presented below were obtained by integrating over the wavelength range from 0.1 to 10 Å and using 10^{10} neutrons.

3.4.3.1 Flux comparison for port W5 and W8

Two beam ports on the hydrogen-methane moderator were considered for IMAT: W5 and W8 (see Figure 3.3.4). The difference between W5 and W8 is due to the different view the guide would have on each of these. While W8 has an angle of +26° on the moderator face, W5 has an angle of -13° onto the moderator face (see Figure 3.3.4). The dimensions of the moderator faces (vertical and horizontal), 0.11×0.11 m^2, were established by the ISIS TS-2 Target Development Team.

For analysing the neutron flux at the sample position using Monte Carlo simulations, two PSD monitors with dimensions 20×20 cm^2 were placed along the IMAT imaging instrument: first (PSD1) after moderator at the distance of 0.0001 m and the second (PSD2) at the sample position, 10 m away from pinhole.

Three available positions for IMAT were considered in this preliminary stage:

- W5/L37: guide length 23.8 m; moderator - sample distance: 37 m
- W5/L56: guide length 42.8 m; moderator - sample distance: 56 m
- W8/L40: guide length 26.8 m; moderator - sample distance: 40 m

Other input parameters for the calculations were:

- Wavelength band: 0.1-10 Å;
- Guide coating m=3;
- 10^{10} neutrons;
- Gravity neglected in the instrument and in the guide.

For the calculations below, the gap between guide exit and pinhole was set to a value of 1.5 m, calculated assuming that neutrons reflected in the guide section from *guide length*+1.5 cannot reach the pinhole and thus filling up the end of the guide and pinhole with a neutron guide should be ineffective. Also, this gap needs to allow for sufficient space for the pinhole selector, as well as shielding around the selector. In the

final stage of the IMAT design process this gap was set to 0.3 m (see section 4.1.3), leaving sufficient space for filters between guide-exit and pinhole, and to slightly increase the neutron flux for the diffraction applications.

Table 3.4.1: *The evaluation of the neutron flux for different instrument positions and different guide lengths for a pinhole radius of 0.01m and a wavelength range from 0.1 to 10 Å.*

Moderator/Flight path	Flux on PSD1 (neutrons/cm^2/sec)	Flux on PSD2 (neutrons/cm^2/sec)
W5/L37	0.813E+10	1.312E+07
W5/L56	0.813E+10	1.211E+07
W8/L40	0.914E+10	1.428E+07

The results displayed in Table 3.4.1 indicate that the neutron flux measured on the PSD1 using W8 is almost 10% higher than the flux obtained using W5 due to the larger amount of moderator volume viewed by the instrument. In addition, we can observe that when using same port (in our case, W5) the guide's length has a direct impact on the neutron flux value obtained on the sample position insofar as increasing the length of the neutron guide reduces the neutron flux.

In reality, factors relating to both imaging and diffraction modes needed to be considered and four rankings were considered [159] for the decision on the moderator choice and guide length: (i) imaging case, (ii) macrostrain analysis performance, (iii) access of user operation, and (iv) texture analysis. The average ratings from all four ranking criteria indicated that the best performance was obtained for W5/L56 which has the longest flight path, with an instrument position outside the experimental hall. The second-best performance was obtained for W8/L40 offering the highest neutron flux while W5/L37 obtained the worst ratings, due to the shorter flight path, limited available detector space, and due to constrained access to the instrument.

The evaluation of the IMAT instrument positions identifies W5/L56 as the best option on TS-2 which combines the necessary analysis modes and which is complementary to ENGIN-X.

3.4.3.2 Removing artefacts – guide cross section

The simulated data show artefacts (vertical and horizontal lines or stripes) in the neutron intensity distributions on the PSD monitor at the sample position (see Figure 3.4.5 for straight guide). Initially not much was known about the origin of these stripes. It was noticed that they were increasing in number and width depending on the neutron guide length and width. In order to investigate the origin of the artefacts and how they can be eliminated a simple optical model as shown in Figure 3.4.8 was chosen. From a selected point (B) on the detector the path of a neutron can be traced back to a point F on the moderator.

Based on a programming code written in C++ the number of neutron reflections in the guide was calculated and the coordinates of the point of origin (F) were determined (see Appendix 1) considering an infinitesimal pinhole and two-dimensional imaging instrument (Figure 3.4.8).

In parallel with the calculations using the C++ code we simulated in McStas the IMAT instrument with four guide lengths: 2.8 m, 23.8 m, 26.8 m and 42.8 m. The guide lengths 23.8 m, 26.8m and 42.8 m were taken from the Section 3.4.3.1 where different positions of the IMAT instrument were investigated. The guide length 2.8 m was selected arbitrarily to extend our investigation, not only for longer guides but also for shorter guide sections. 10^{10} neutrons were generated in the wavelength range 0.1-10 Å and a small pinhole (radius 0.005 m) was considered.

For the Monte Carlo simulations and C++ code the positions and distances between components were used as given in Figure 3.4.7.

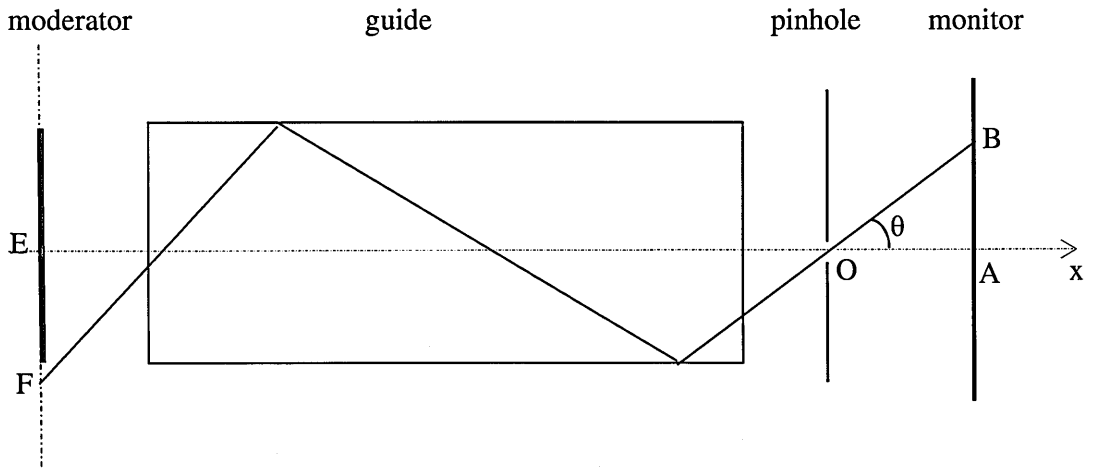

Figure 3.4.8: *Geometrical design of the basic instrument model used in the C++ code. The blue line represents the neutron path traced backwards from the point B on the monitor to the point F on the moderator. The red line is the moderator size (0.11×0.11 m^2). The neutron exits from the guide with the reflection angle θ.*

In the McStas modelled instrument the PSD monitor was placed at 10 m after the pinhole and its dimensions were of 20×20 cm^2 with 100×100 pixels. On the other hand, in the C++ code the half of the monitor size is determined by AB (considering the horizontal symmetry for this 2D instrument model). The position of B (length of AB) was varied from 0 to 10 cm with a step of 0.001 m. For each value of AB the distance EF was calculated. Also, the reflection angle of the neutron originating from point F was determined.

In the following Figure 3.4.9 to Figure 3.4.12 the 2D neutron intensity distribution on the PSD monitor from McStas (left) and the calculated EF values and reflection angles depending on the guide length (right) from C++ code are plotted. Comparisons between the both plots are detailed as follows.

For the shorter guide (2.8 m) the intensity distribution on the PSD monitor does not exhibit artefacts. The neutron intensity drops off at the monitor edges (see left image in

Figure 3.4.9). No stripes are on the PSD monitor. On the right plot in Figure 3.4.9 the neutron guide is indicated by two parallel green lines (one for 0.055 m and the other for -0.055 m). The calculated exit angle θ, of the neutron from the guide, ranges from 0° (for neutrons emanated from the moderator centre and going along the straight line) to almost 0.6° (for neutrons which are arriving on the monitor edge). The pink line (Figure 3.4.9 right) represents the plot of the calculated θ values as function of the (AB) distance on the monitor. The guide is too short for neutrons arriving at the PSD to have been reflected in it.

The area where the neutron intensity is higher (red area on the PSD monitor) corresponds to the calculated EF as function of AB distance, from 0 to 0.055 m (the blue oblique line on the right plot) of Figure 3.4.9.

Figure 3.4.9: *Evaluation of artefacts for the neutron guide length 2.8m.*

Neutron intensity distribution on the PSD monitor for guide length 2.8m	Neutron reflection angle and image originated on the moderator (EF) as function of the distance (AB) on the monitor.
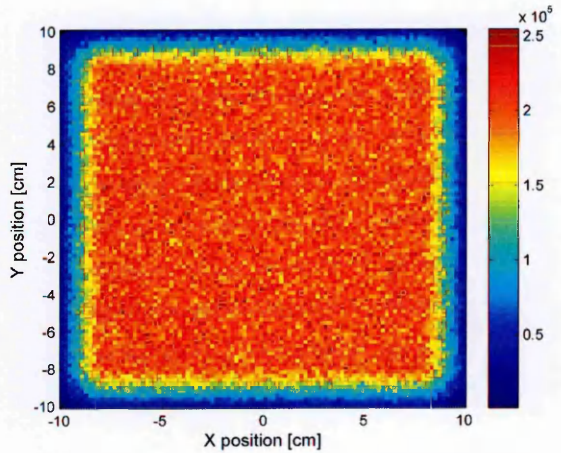	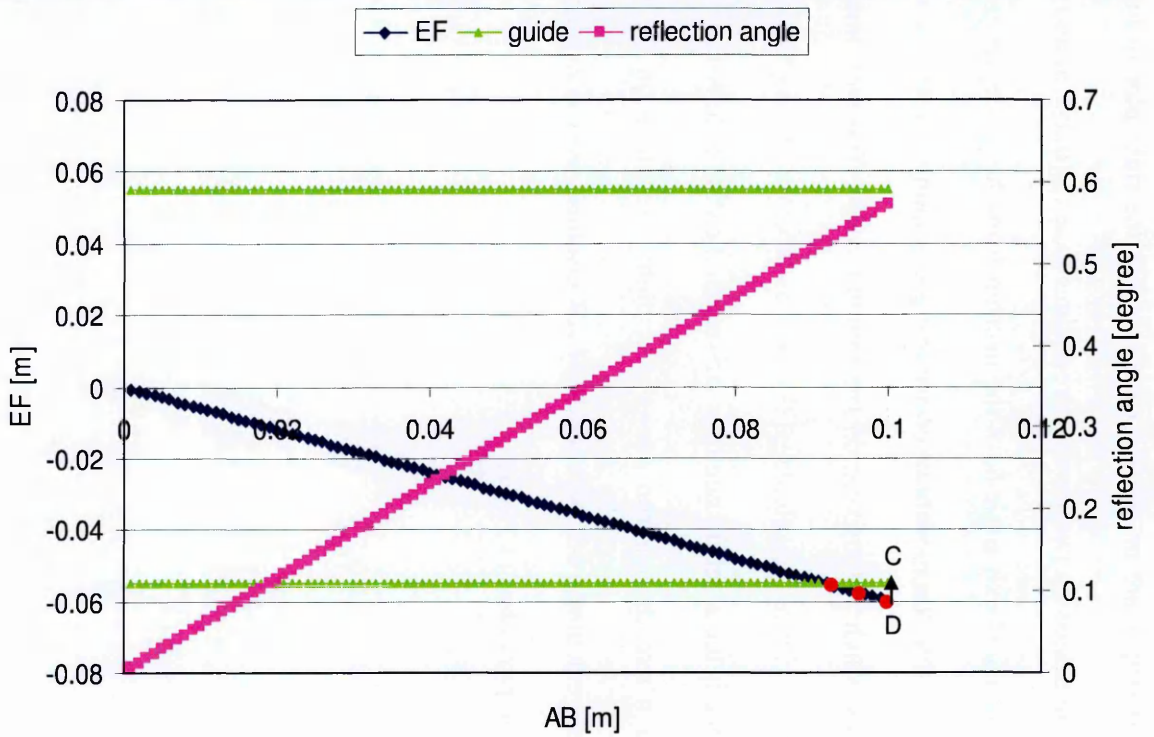

The calculated EF intersects the guide and a small area (the small blue line with red dots in Figure 3.4.9 right) is larger than the moderator cross section, i.e. neutrons arriving at this part of the PSD would have originated from outside of the moderator. The width of the blue area (where the neutron intensity is lower) on the PSD is equal to the distance CD on the C++ plot, almost 0.7 cm. The moderator and guide cross section are the same size (11×11 cm^2) and therefore it was concluded that these shadow lines are caused by the regions outside of the moderator while, for this simulation the red area is the higher intensity region due to neutrons passing straight without being reflected.

The problem became more interesting for longer guides. Repeating the same steps from above (in the simulations and the C++ code) but changing the neutron guide's length, we got results presented in Figure 3.4.10, Figure 3.4.11 and Figure 3.4.12. The maximum reflection angle, almost 0.6°, is the same for all cases.

In the case of the 23.8 m guide some horizontal and vertical shadow blue lines (or stripes) are visible on the upper part of the PSD monitor (Figure 3.4.10 left). The stripes divide the PSD monitor distribution into 5 zones. Due to the symmetry of the image only the horizontal stripes are investigated. From C++ code calculations we determine the number of reflections in the neutron guide. Hence, the centre red area on the PSD monitor corresponds to the neutrons passing straight through without reflection; the upper red area (between line 1 and line 2) corresponds to the neutrons with one reflection and the last area (blue area between line 2 and the monitor edge) to the neutrons which have two reflections.

At the intersection between EF zigzag blue line and the guide two small triangles outside of the guide area are observed(Figure 3.4.10 right). These triangles are equivalent with the stripes on the PSD monitor and they are caused by the regions outside of the moderator. The distance from the peak1 to the guide line -0.055 cm (Figure 3.4.10 right) is equal with the width of the first stripe (line1) on the PSD monitor (Figure 3.4.10 left), i.e. 0.1 cm. The second stripe (line2) has the width same with the distance from the peak2 to the guide line 0.055 cm, i.e. 1.05cm.

Figure 3.4.10: *Evaluation of artefacts for the neutron guide length 23.8m.*

Neutron intensity distribution on the PSD monitor for guide length 23.8m	The plots for neutron reflection angle and image originated on the moderator (EF) as function of the monitor size (AB)

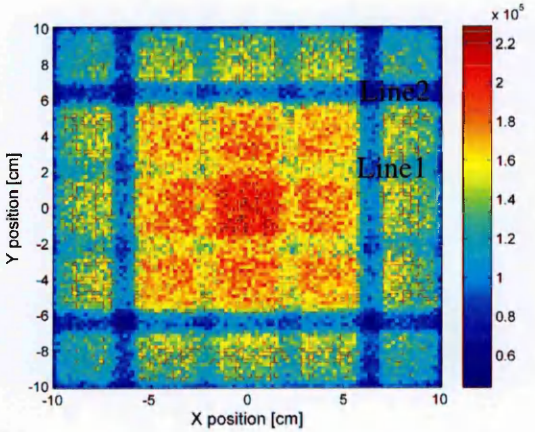

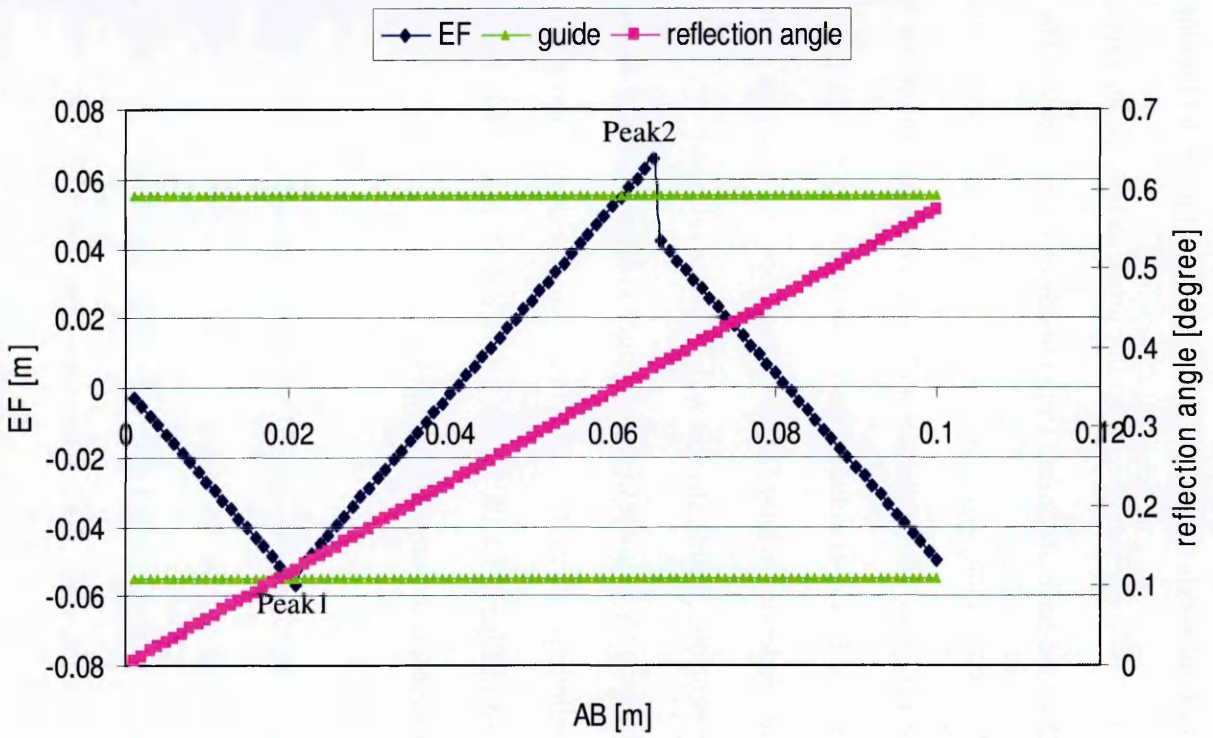

For the guide length of 26.8 m the number of reflections is increasing to three proportionally to the number of artefacts (or stripes) on the PSD monitor (Figure 3.4.11). Repeating the above described procedure, the width of the stripes can be approximated to 0.2 cm, 0.9 cm and 1.6 cm corresponding to the peak1, peak2 and peak 3 from Figure 3.4.11 right.

The final case is the most important one, because the guide length 42.8 m was decided to be used for the IMAT instrument (see section 3.4.3.1). The horizontal shadow lines on the PSD monitor divide the monitor in 9 regions, but due to the image symmetry only the half upper part of the monitor will be considered (Figure 3.4.12 left). The stripes are named line1, line2, line3 and line4. Each of the regions defined by the lines has a correspondence in the neutron reflections: first region (with the highest intensity) has no reflection and it is correlated with the neutrons which are passing straight through the guide without reflections; the second region corresponds to the neutrons with one reflection in the guide etc. The maximum number of reflections is four. In the Figure 3.4.12 right each distance from the peaks to the guide line represents the widths of the artefacts from the PSD monitor. Hence, line1 has the width of about 0.02 cm, line2 has a width of 0.52 cm, stripe3 has the width of 1.02 cm and last stripe has the width of 1.06 cm. As in the above cases, the stripes are determined by the PSD "seeing" regions outside of the moderator (see small triangles defined by the EF zigzag line and guide with peaks 1, 2, 3 and 4 in Figure 3.4.12 right).

Figure 3.4.11: *Evaluation of artefacts for the neutron guide length 26.8m.*

Neutron intensity distribution on the PSD monitor for guide length 26.8m	The plots for neutron reflection angle and image originated on the moderator (EF) as function of the monitor size (AB)

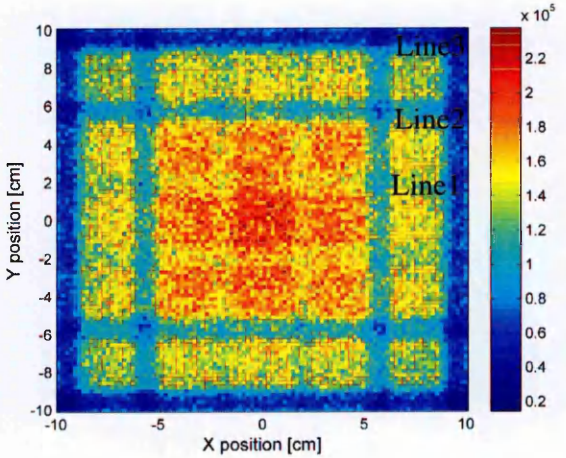

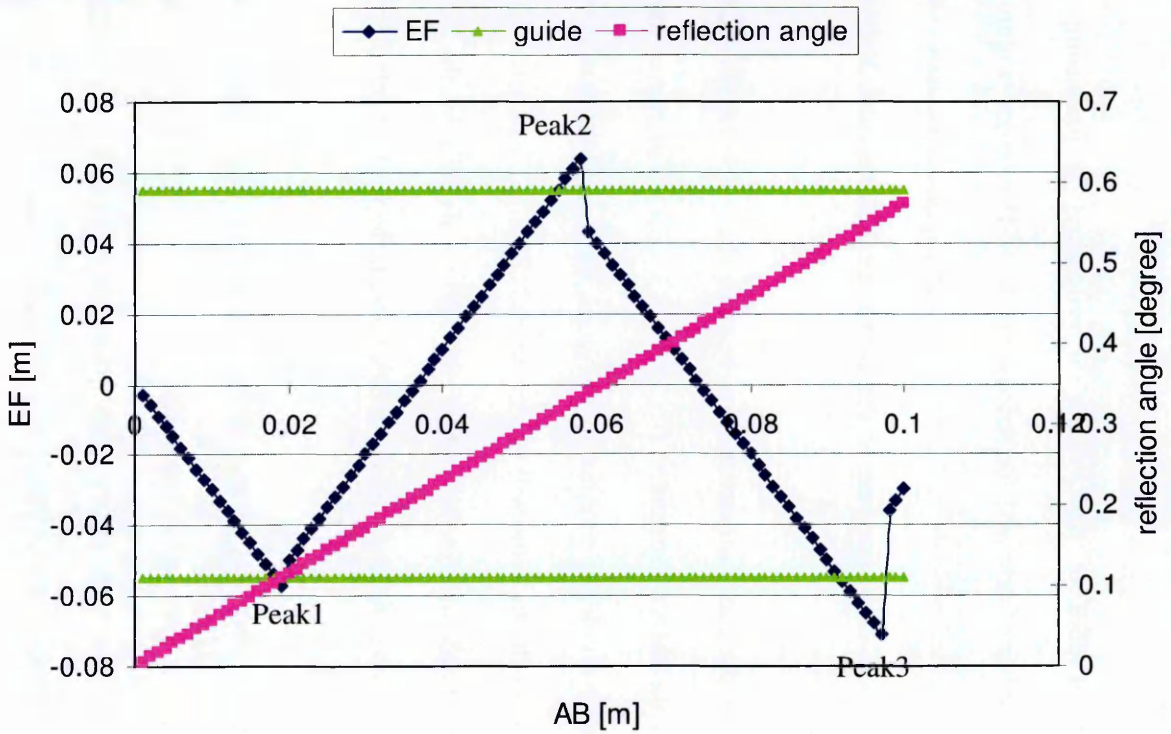

Figure 3.4.12: *Evaluation of artefacts for the neutron guide length 42.8m.*

Neutron intensity distribution on the PSD monitor for guide length 42.8m	The plots for neutron reflection angle and image originated on the moderator (EF) as function of the monitor size (AB)

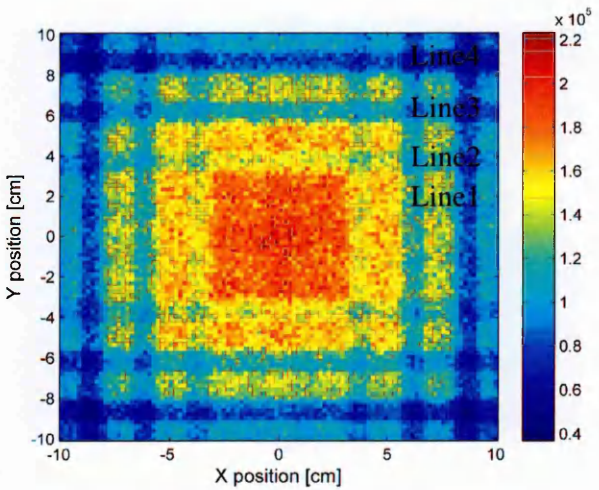

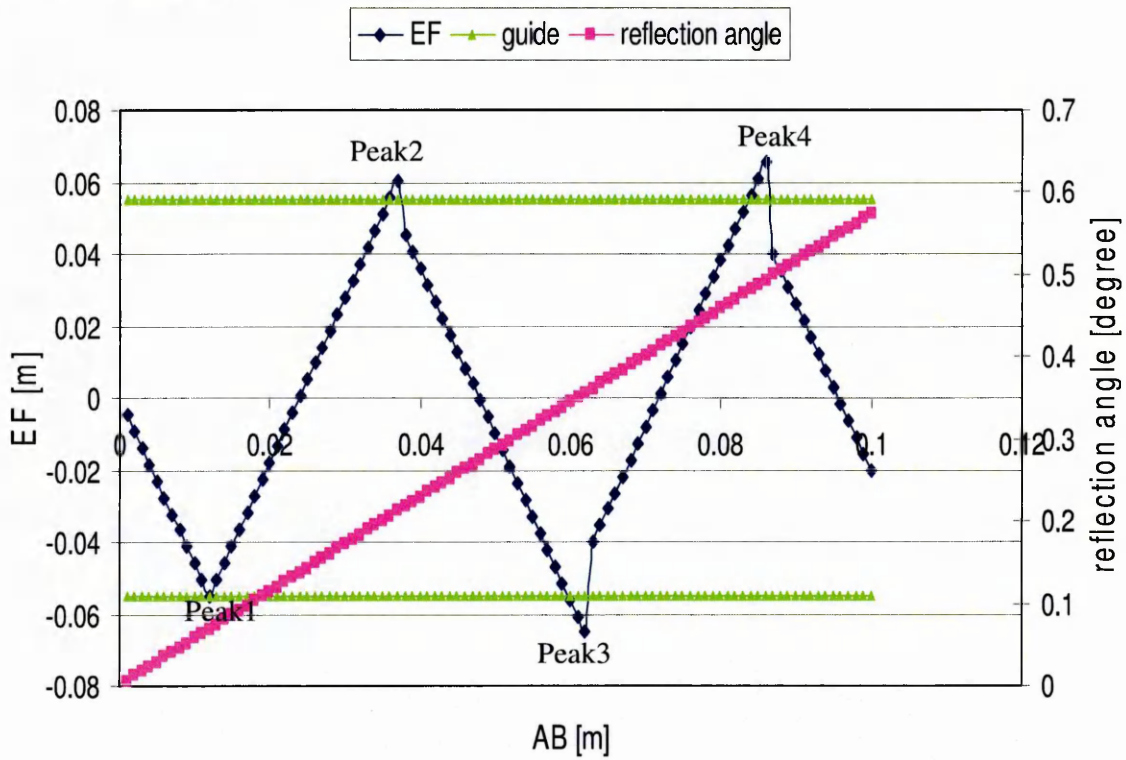

Identifying the cause of the artefacts provided the possibility of removing them. The following actions were taken into consideration:

- to make moderator larger;
- maybe to reduce the distance between moderator and the guide entrance;
- to reduce the guide cross section compared to the moderator size;

While the first two suggestions are precluded due to technical and engineering constraints the last suggestion is more promising, especially as it was demonstrated that the reduction of the guide cross section enables a higher neutron flux (see section 3.4.3.3, imaging case).

3.4.3.3 Compromise with diffraction requirements

Since IMAT is an instrument dedicated both to imaging and diffraction experiments the optimization of guide dimensions depends on the diffraction case also. For a guide length of 42.8 m, in the imaging situation, the neutron flux decreases simultaneously with the increasing of guide cross section (Figure 3.4.13). Plotting the neutron flux for the diffraction mode [160] (and same guide length as in the imaging case, 42.8 m) we can see that the curve is ascending with increasing guide cross section. For a guide cross section of 10×10 cm^2, the imaging flux and diffraction flux drop 5% from their respective maximum values.

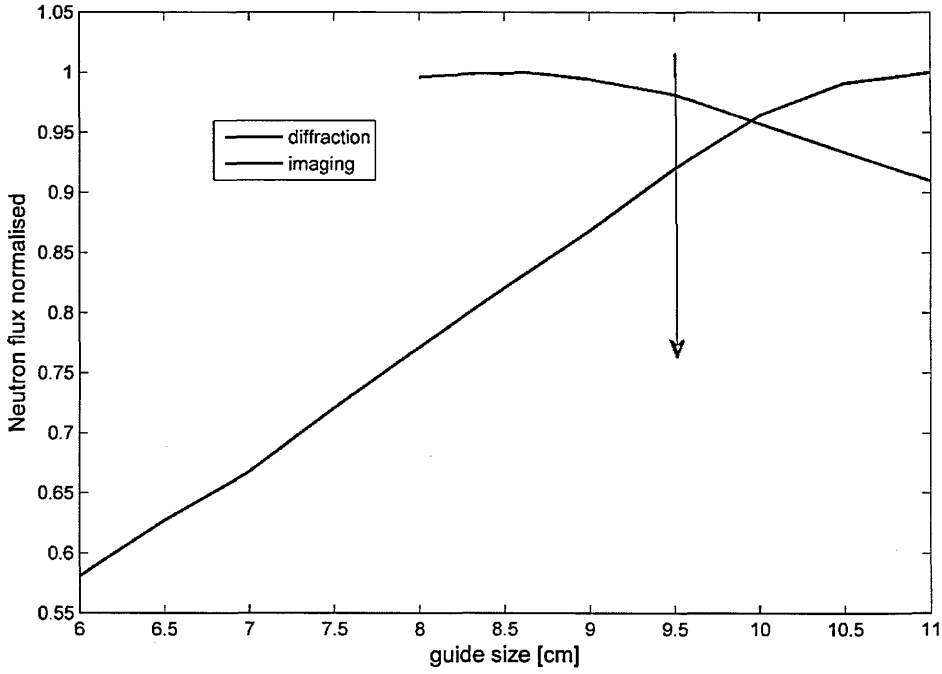

Figure 3.4.13: *Neutron flux normalised as a function of the guide size cross-section for imaging and diffraction.*

We have seen from the previous paragraph that if we increase the guide cross section up to the moderator height (11×11 cm^2) the artefacts appear on the PSD. Also, there is an engineering fact we should mention here: for the W5 port a neutron guide cross section of more than 9.5×9.5 cm^2 cannot be fitted into the available beam tube in the TS-2 target shielding. For 9.5×9.5 cm^2 guide cross section, artefacts are not observed (for larger pinholes the artefacts are washed out due to the poorer resolution) for the standard "working" pinhole (R=0.01 m) so therefore we can choose 9.5×9.5 cm^2 as the best value for neutron guide cross-section of IMAT instrument. Under these circumstances, imaging loses 2% and diffraction loses 8% of the best possible neutron flux for the respective mode. From this point forward this value for guide cross-section will be applied in all our simulations.

3.4.3.4 Study of neutron flux for different guide *m*-values

One parameter which affects the critical angle and the neutron flux is the guide *m*-value. Basically, the neutron supermirror is characterized by its reflectivity via the m-value as described in Section 3.4.1. The guide performance was investigated for different *m*-values: 1, 2, 3 and 4. A lambda monitor of size 20×20 cm^2 was placed at 10m after pinhole to measure the neutron flux and the neutron intensity distribution as a function of wavelength. The simulations parameters remain unchanged and are same with the ones from the previous paragraphs. A pinhole with radius 0.01 m was selected.

As expected, the neutron flux on the sample position increases across the entire wavelength band used with increasing m-values. Compared to the standard Ni-coating (m=1) the most significant improvement is observed for m=2. The gain is due to the fact that, for a given reflection angle, a supermirror guide transports neutrons with shorter wavelengths than a conventional Ni mirror (m=1). The neutron flux increases by 71% from m=1 to m=2 and by approximately 8% from m=2 to m=3 (Figure 3.4.14). For supermirrors with m=3 a large critical angle is obtained and also one achieves a good neutron flux useful for imaging experiments. m=4 gives the highest neutron flux with 1.3% more than for m=3, but financially speaking, m=4 is considerably more expensive than m=3 for a relatively small gain.

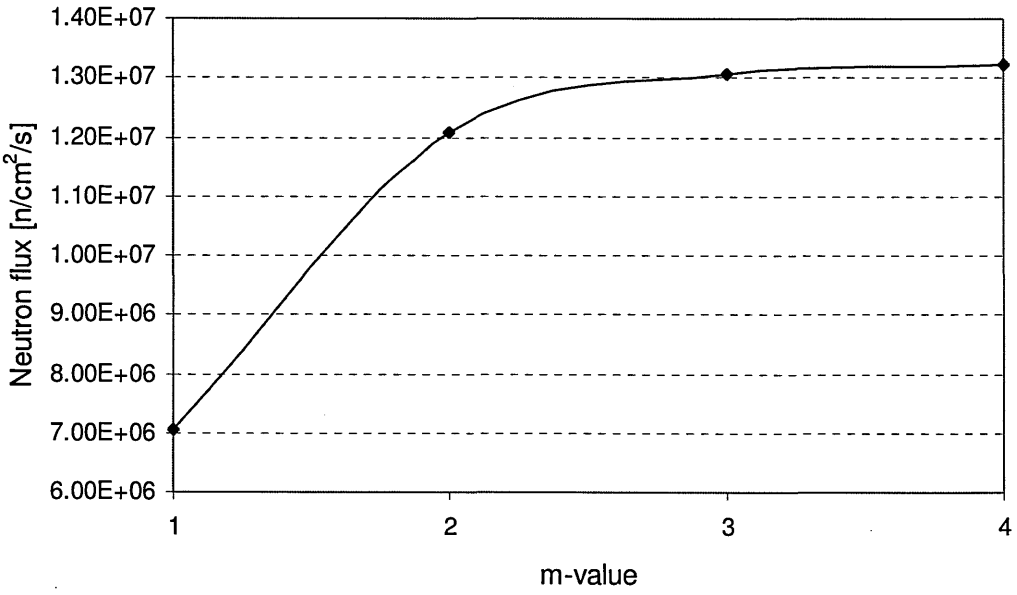

Figure 3.4.14: *The variation of the neutron flux measured at the sample position for different guide m-value.*

Higher m-values improve the performance of the supermirror guide, but only for shorter wavelengths below 3 Å as shown in Figure 3.4.15.

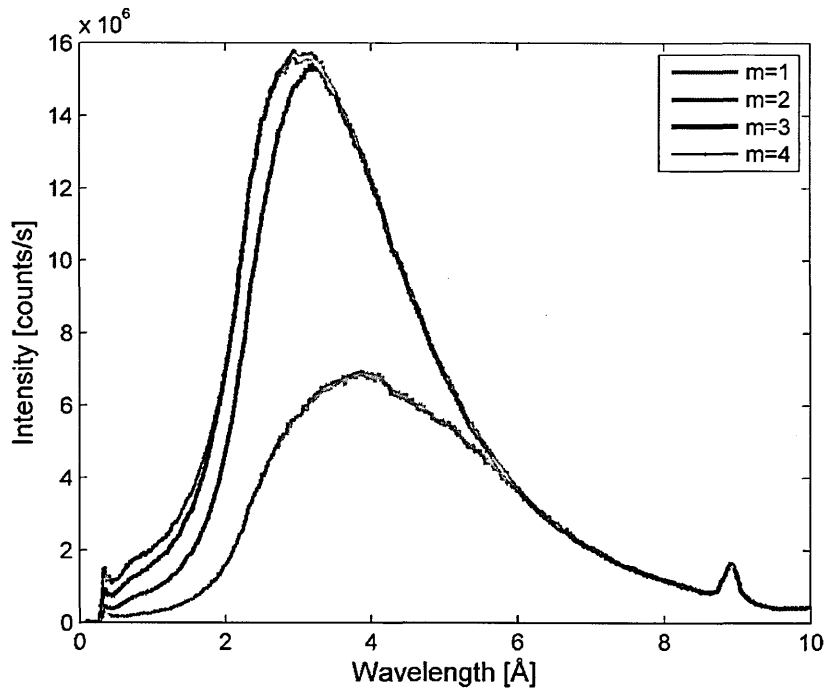

Figure 3.4.15: *Neutron intensity as function of wavelength on the sample position for different m-values.*

For example, at 1 Å the guide with m=3 gives with 84% more intensity than the guide with m=2. (This wavelength range near 1 Å is particularly important for diffraction experiments.) For wavelength above 3 Å neutrons are propagated without additional losses for all guide supermirrors guides and very little can be gained by using advanced coatings (e.g. m=4) in this wavelength band (our case, 3-10 Å). In conclusion, it was decided to use a supermirror guide with m=3 due to its performance and less expensive costs.

3.4.3.5 Study of gravitational effects

The previous studies were made using a straight guide with the gravity parameter neglected. Here we would like to investigate if the gravity effect on the neutrons travelling through the instrument can be ignored. For this reason we compared two situations using the Guide_gravity component of McStas (version 1.12) which models a straight rectangular guide with gravitation handling. Firstly, a straight square guide with gravity turned off ($g = 0\ \mathrm{m/s^2}$) was considered. After that, a straight square guide with gravitation norm switched on ($g = -9.81\ \mathrm{m/s^2}$). It is known that the gravitation coefficient is a constant value ($g = -9.81\ \mathrm{m/s^2}$), but we performed simulations with an "exaggerated" and "impossible" gravitation coefficient ($g = -50\ \mathrm{m/s^2}$).

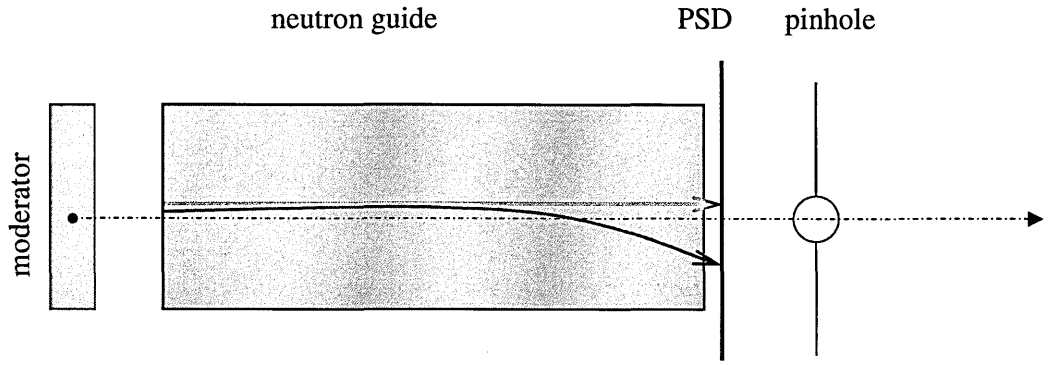

Figure 3.4.16: *Modelled instrument for investigating the guide gravitational effect. Two neutron rays are drawn: (red) for neutron ray passing straight through without supporting gravitation effect and (green) parabolic neutron ray affected by gravity.*

The positions and sizes of instrument components are defined as given in Figure 3.4.7 for the neutron guide of 42.8 m in length and *m*-value 3, with the exception of the position of the PSD monitor. For studying the gravitation effect on the neutron intensity distribution (Figure 3.4.16) and the neutron flux value, with non-zero gravity, the PSD was placed immediately after the guide exit (at a distance of 0.001 m from the exit).

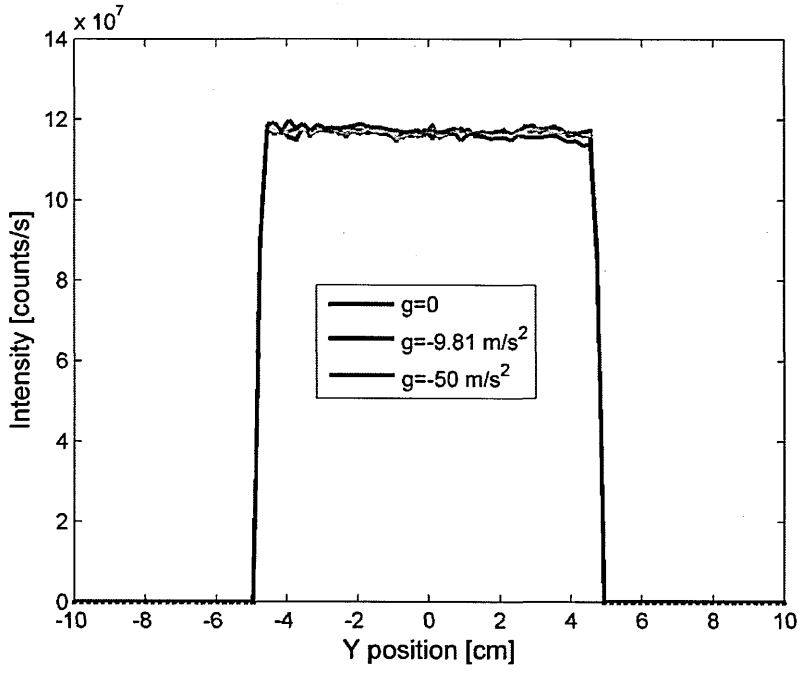

Figure 3.4.17: *Profile plot of the intensity distribution on the 20×20 cm^2 PSD monitor. One vertical row in the middle of the detector was selected and plotted against the position on the monitor.*

It is observed that differences in the intensity profiles on the PSD monitor at the guide exit are negligible (Figure 3.4.17).

While for non-gravity and gravity the neutron flux is almost the same, a very slight difference of the neutron flux is noticed for "non-usual" gravitation factor (Table 3.4.2):

Table 3.4.2: *Variation of the neutron flux depending on the gravity in the neutron guide.*

Neutron flux for g=0 (n/cm^2/sec)	Neutron flux for g=-9.81 m/s^2 (n/cm^2/sec)	Neutron flux for g=-50 m/s^2 (n/cm^2/sec)
0.65937×10^9	0.659368×10^9	0.65915×10^9

For reasons of completeness the effect of gravity on neutron trajectories is added here. For different wavelengths (from 0.1 Å to 10 Å) neutrons were supposed to be generated by an infinitely small pinhole. After that the neutrons travel up to the sample position considering them under the influence of the gravitation effect.

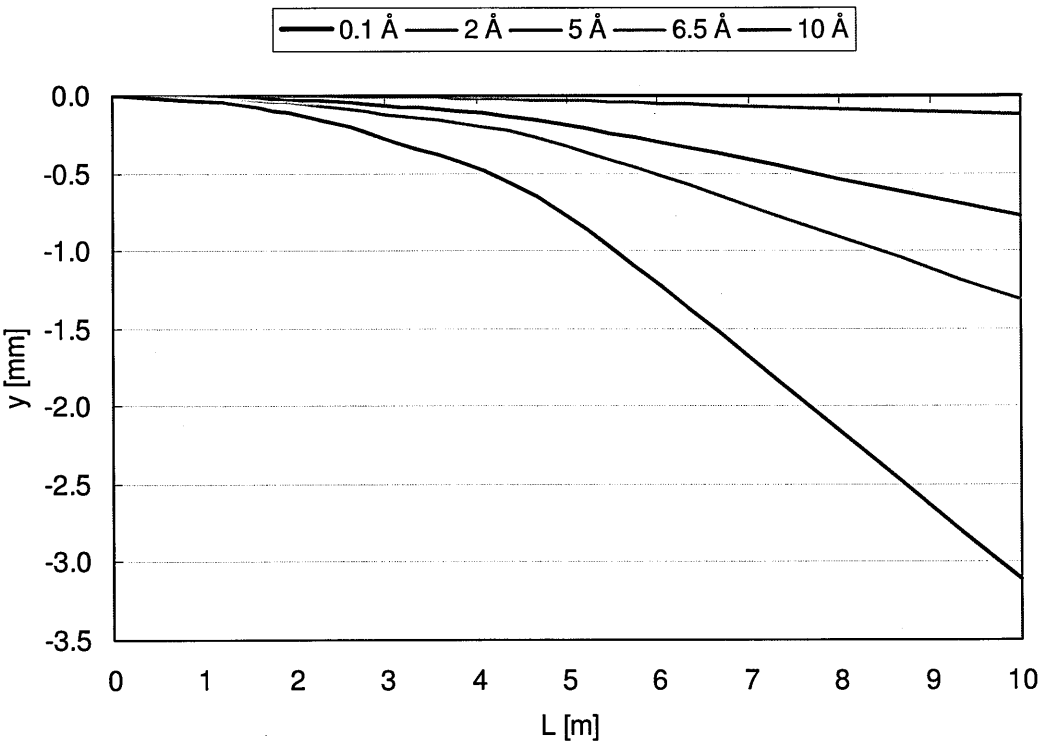

Figure 3.4.18: *The dropping distance (x) of the neutrons under the influence of gravity for different wavelengths and function of flight path (L) from the pinhole to the monitor.*

Taking into account the neutron mass, the neutron's wavelength, Planck's constant, flight path distance and gravitation constant, the dropping distance of the neutrons affected by the gravity follows the formula:

$$y = \frac{g}{2}\left(\frac{Lm\lambda}{h}\right)^2 \tag{3.4.7}$$

Figure 3.4.18 illustrated the formula (3.4.7). The dropping distance of the shorter wavelengths neutrons at the 10 m is less affected by gravity because of their higher speed. For example, for 2 Å the height difference is about 0.12 mm for 10 m flight path. For longer wavelength, e.g. 10 Å there can be a height difference of almost 3 mm for 10 m flight path.

Throughout this thesis the gravity effect in the instrument will be neglected, but from neutron radiography point of view it will be interesting in the future to study the effect of the gravity on the image blurring. Here it will not be presented a detailed investigation, only a preliminary study, as this issue will be a future work for IMAT instrument.

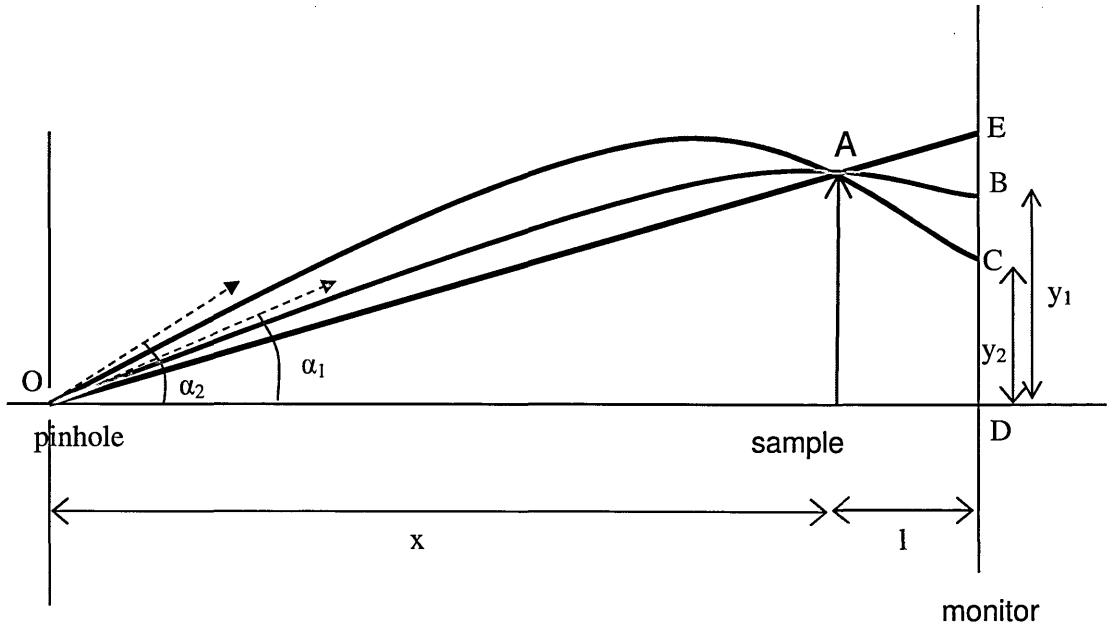

Figure 3.4.19: *Gravitational effect on the image blurring due to the different neutron trajectories followed by higher and lower energy neutrons. The pinhole is considered infinitely small (notated with O).*

In Figure 3.4.19 three neutrons fligh path are represented: one neutron (black line) following a gravity free-path, one high energy neutron (red curve) and one low energy neutron (blue curve). In this instance we consider the effect in relation to a thin sample, so we are able to talk about neutrons passing through a point within the sample, rather than having a trajectory as neutrons would have through thicker sample. Neutrons trajectories passing through point A are arriving on the PSD monitor positions (E, B and C respectively). The result of these different trajectories passing through the same point is that the point A is blurred by amount $BC = y_1 - y_2$ in the vertical direction. The distance between the sample and the PSD monitor is an essential criteria for minimising the blurring effect caused by the gravity, i.e. the closer the sample is to the monitor, the less chance the neutron trajectories will have to diverge and the smaller will be the blurring.

Mathematical analysis

Under gravity, and ignoring air resistance, particles follow parabolic trajectories:

$$\begin{cases} y = v_0 t \sin\alpha + \dfrac{gt^2}{2} \\ x = v_0 t \cos\alpha \end{cases} \tag{3.4.8}$$

where, v_0 is the initial velocity of the particle, t is the motion time of the particle, g the Earth's gravitation acceleration and α the projection angle (Figure 3.4.19).

Based on equations (3.4.8) we determined the distance BC as follows:

1. Firstly, knowing the distance x (from the pinhole to the sample position), the position of point A (in the sample), $A(x, p)$, where the both neutrons (which are under the gravity effect) with different wavelengths met and the velocities corresponding to each neutron based on the De-Broglie relation (2.1.1), i.e. $v_{01} = \dfrac{h}{m\lambda_1}$ and $v_{02} = \dfrac{h}{m\lambda_2}$, there are calculated the projections angles of the both neutrons using the derived formula:

$$\tan\alpha_1 = \frac{\sqrt{v_{01}^4 - g^2x^2 + 2g\,pv_{01}^2} - v_{01}^2}{gx} \tag{3.4.9}$$

2. Using the projection angles determined above, equations (3.4.8) and knowing the distance from the pinhole to the monitor (i.e., $L = x + l$) there are calculated the positions on the PSD monitor of both neutrons $BD = y_1$ and $CD = y_2$:

$$\begin{aligned} y_1 &= L\tan\alpha_1 + \frac{gL^2}{2v_{01}^2\cos^2\alpha_1} \\ y_2 &= L\tan\alpha_2 + \frac{gL^2}{2v_{02}^2\cos^2\alpha_2} \end{aligned} \tag{3.4.10}$$

Here, we do not intend to present more results (as this issue will be more developed in our future work) but one result where the blurring is more evident between one higher energy neutron, 3 Å and one low energy neutron, 10 Å, will be given. For this it was supposed the distance between the sample and PSD monitor of l=0.25 m, the pinhole-sample distance x=10 m and the point A(10 m,0.02 m) in the sample. Following the equations (3.4.9) and (3.4.10) presented above we obtain that the long wavelength neutron (10 Å) is projected with the angle $\alpha_2 = 0.132^\circ$ and the distance on the monitor is $CD = y_2 = 20.42$ mm. The short wavelength neutron (3 Å) is projected with the angle $\alpha_1 = 0.116^\circ$ and the distance on the monitor is $BD = y_1 = 20.493$ mm. Therefore, the point A in the sample is blurred on the monitor by the value of 0.072 mm.

3.4.3.6 Neutron guide in the shutter

The first section of the neutron guide of IMAT is in the shutter. The shutter is made of cast iron with a rectangular hole in the middle for the neutrons. The shutter closes off the neutron beam or lets the beam to pass through down to the beamline. The open/close positions are controlled by the electrical limit switches. In the open position the hole from

the shutter aligns with the neutron beam flight path. Because of its weight the positioning of the shutter is not very accurate and the alignment accuracy is in the order of one millimetre. From the neutron imaging point of view the interest here was to compare the neutron intensity and the effect on the radiographies of the guide size in the shutter section, whether or not the guide in the shutter section was to be made bigger than the main guide such that in case of an offset of the shutter the neutron beam entering into the main guide section is not blocked. Three situations were considered: i) the shutter guide is larger than the rest of the guide, i.e. 11×11 cm^2 for the shutter and 9.5×9.5 cm^2 for the main guide; ii) the shutter guide size is 10×10 cm^2 with the main guide size 9.5×9.5 cm^2; iii) the shutter and guide have same dimensions, 9.5×9.5 cm^2. In the modelled instrument the shutter is perfectly aligned to the neutron beam; misalignment is not considered here. The pinhole radius used was 0.005 m. The neutron flight path from the moderator to the sample position was 56 m as in the previous sections, but the guide was divided into two parts with one small gap between these parts: one section (shutter section) with 2 m length and the other with almost 40.8 m length.

Two PSD monitors of sizes 20×20 cm^2 and 100×100 pixels were placed on the instrument: one just after shutter at 0.001 m and the other on the sample position at 10 m after the pinhole.

The integrated neutron intensity calculated on the PSD monitor placed on the sample position is 1.22e+09 [n/sec] for the guide in the shutter having the same cross section as the main guide cross section (9.5×9.5 cm^2). Increasing the guide size in the shutter section to 10×10 cm^2 results in a drop of intensity by a noticeable 2.7% compared to the 9.5×9.5 cm^2 shutter guide cross section having a value of 1.19e+09 [n/sec].

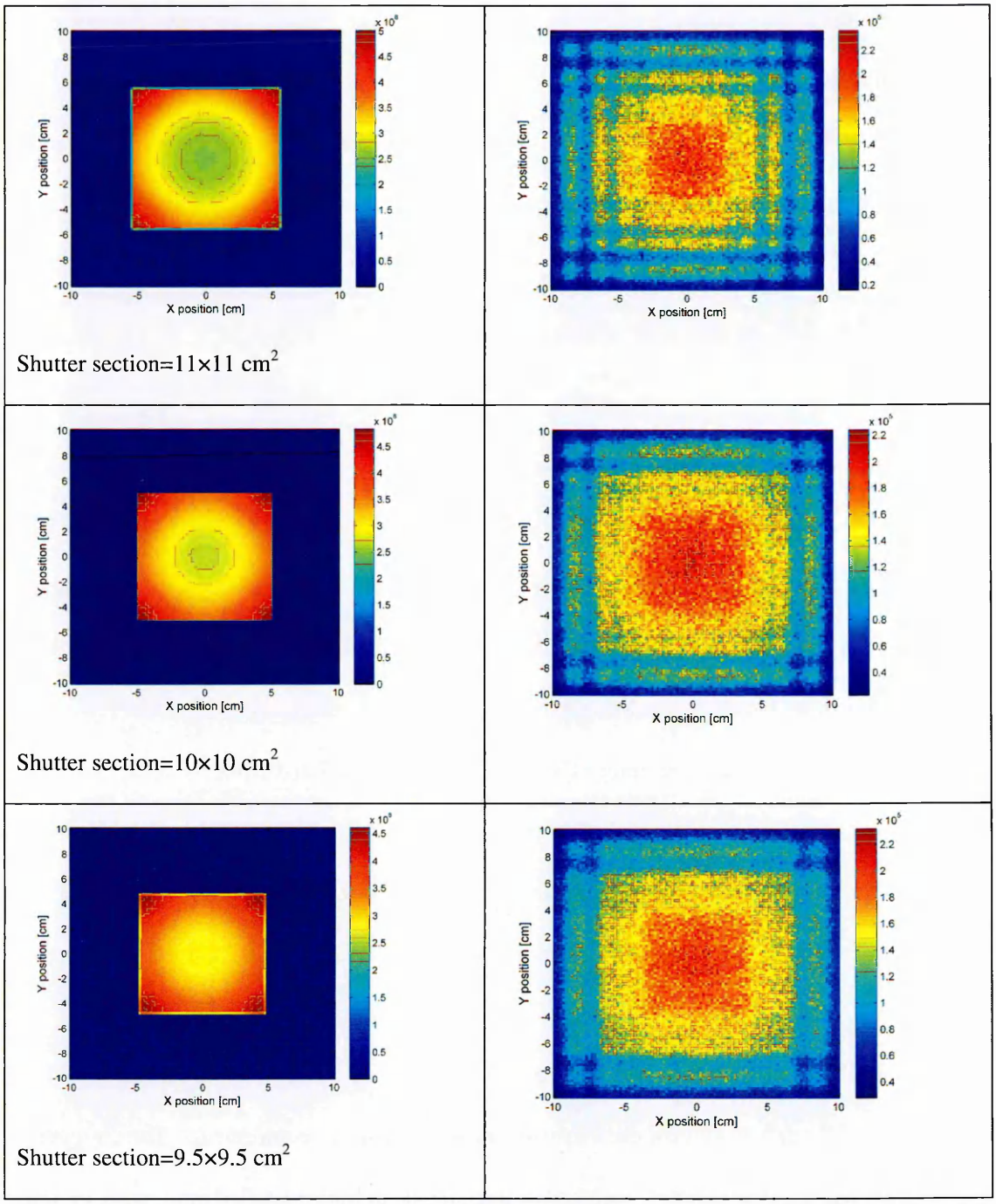

Figure 3.4.20: *Neutron intensity distribution on the PSD monitor placed 0.001 m after the shutter (left column). The red square in the middle represents the shutter projection with source illumination in the middle. Neutron intensity distribution on the PSD monitor placed at 10 m after pinhole (right column).*

Regarding the performance of the instrument for imaging, making the shutter the same size or bigger as the main guide does not have a significant effect on the structure of the stripes in the open beam images. The neutron intensity distributions on the PSD monitors placed on the sample position are presented in Figure 3.4.20.

Although the intensity drop is measureable through simulations it was not considered sufficiently significant to guide the decision in the favour of one or another model of IMAT design. The final decision on the guide size in the shutter (10×10 cm^2) was taken by the engineers, considering the costs and accuracies of the shutter installation.

3.5 Bandwidth selection with choppers

Once the neutrons are generated a single energy or an energy range has to be selected for a specific experiment. While the research reactors produce a continuous spectrum of neutron energies and the selection of a particular energy is made with the help of mechanical choppers or a rotating crystal monochromator, at the pulsed sources the selection of a specific neutron wavelength is achieved by time-of-flight methods. Because IMAT will be running at a pulsed source, the neutron's energy will be calculated from its velocity using the TOF method. The purpose of the choppers on IMAT will be to eliminate the gamma and high-energy neutron background radiation (similar effect as with curved guide) or to prevent the overlap of slow neutrons of a previous pulse with the faster ones of the next pulse.

These kind of high speed rotating equipments are designed, developed and built by ISIS for over 20 years to suit for each instrument and scientific requirements. The choppers will be located at well-defined positions along the beamline, installed into gaps of the neutron guide. The choppers will be synchronized with the pulses of neutrons from the target. The purpose of our work is not to develop technical details on the choppers, but to investigate the effects of the gaps created in the guide for choppers onto the radiographies. However, the following section a brief introduction of how disk choppers work.

3.5.1 Descriptions of neutron choppers

In the Section 2.2.3, a discussion on the time-of-flight method was provided. Frame overlap issue occurs for a sequence of pulses when fast neutrons from a later pulse catch up with slow neutrons from an earlier pulse. The problem can be eliminated by adding disk-choppers to the instrument and so, defining a shorter wavelength band for the measurements. By running the disk choppers at a lower frequency than the pulsed-source frequency, disk choppers can also be used to reject neutron pulses and define a wider time frame, thus using a wider wavelength band (at the expense of intensity). The necessary condition to be respected for avoiding the overlap issue is $\Delta t = t_2 - t_1 \leq t$ where t_2 and t_1 is the maximum and respectively, minimum neutrons time-of-flight from the source to the detector for the slowest and fastest neutrons selected by the choppers and t is the period of the pulsed source, defining a "frame". When there is no chopper in the system neutrons from two different pulses can interfere, but when the chopper system is on it cuts off the slow neutrons from the pulse and prevents them to arrive them in the next pulse. It should be noted that one chopper only is sufficient to separate neutrons from adjacent pulses. In order to avoid higher order frame overlap (e.g. neutrons from pulse-1 leaking into frame-3) more than one disk chopper is required.

IMAT requires two types of choppers: a T0–chopper to reduce the fast neutron and gamma background and two double-disc choppers (DD1 and DD2) to prevent frame overlap between successive pulses (Figure 3.5.1). These choppers will be located in the gaps in the neutron supermirror guide. The total gap size in the neutron guide needs to be strictly minimized (see section 3.5.2). Moreover, the neutron beam should not be interrupted by windows when entering or exiting the choppers sections in order to avoid the Bragg edges in the radiography data from the window material. For this reason, the

choppers need to run in vacuum so that neutrons can travel unimpeded through the chopper system.

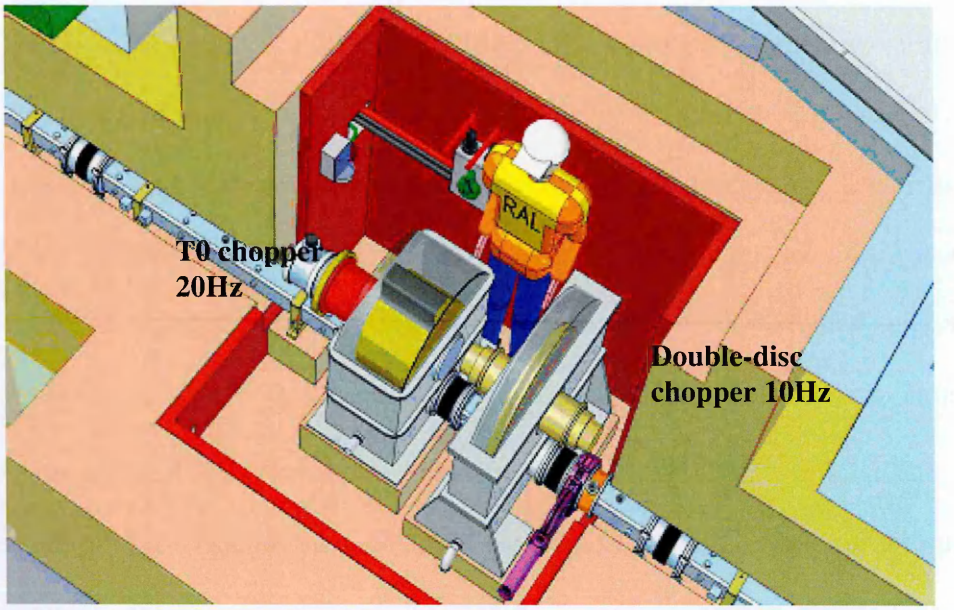

Figure 3.5.1: *Proposed chopper design for IMAT; the beam is coming from the right passing first through a disc chopper (DD1) and then through the T0 chopper.*

A double disc choppers (Figure 3.5.2) has two counter-rotating disks, which in comparison to a single-disk chopper has shorter opening and closing times beneficial to make best use of the neutrons at the short- and long-wavelength edge of the wavelength band.

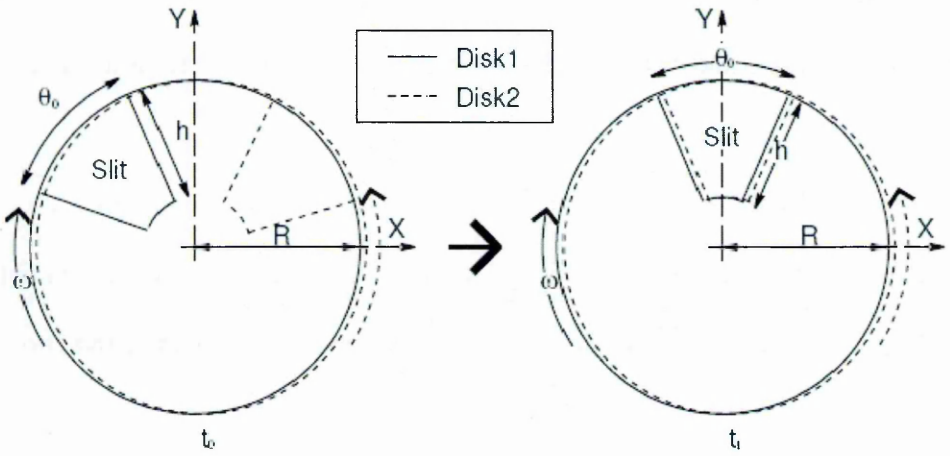

Figure 3.5.2: *Schematics of counter-rotating double disc choppers.*

The choppers will be at about 12 m and 20 m from the moderator to limit the wavelength band to 0.7-6.7 Å (single frame mode) and thus preventing the frame overlap of successive ISIS neutron pulses at the detector position. By operating the choppers at 5 Hz instead (than the standard 10 Hz) the wavelength range can be extended to 14 Å at the costs of about a factor 2 of a lower neutron flux.

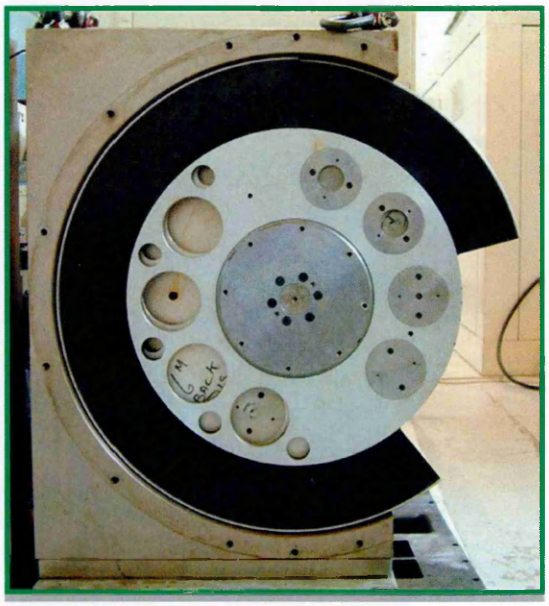

Figure 3.5.3: *ISIS neutron beam disk chopper. The gap in the (black) B4C ring is there to let neutrons pass through.*

The disk choppers will have a thickness of 4 mm Al and 10 mm thick absorbing B_4C material. The radius of the disk choppers will be 325 mm measured from the disc-centre to the beam-centre.

The IMAT T0 chopper is synchronised with the neutron source in such a way that at the time when the neutrons are generated in the target a block of inconnel (Ni rich alloy) with 300 mm thickness blocks the beam path for fast neutrons and gamma radiation.

3.5.2 Effects of chopper gaps on the open beam images

Here we present the results from the simulations run to study the effects of the gap size on the radiography. How much of a gap for the choppers can we afford from the neutron intensity and image homogeneity point of view? Are the images affected by any additional artefacts?

Initially one gap was considered in the guide (at 17 m from the moderator) which splits the guide in two straight guides (Figure 3.5.4). The first guide has a length 15.3 m and the second has a length of $L-(15.3\,m+gap\ size)$ where L is the total length of the guide considered, 42.8 m, with the gap size varying from 0 m to 1 m. Both guide sections have the same square cross section 9.5×9.5 cm^2 with $m=3$.

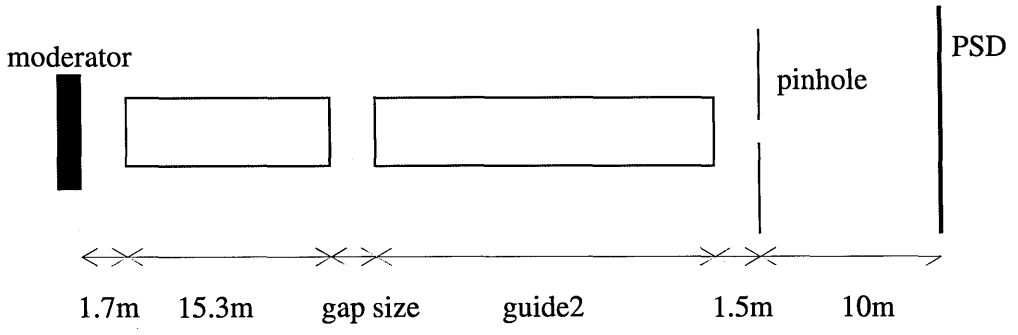

Figure 3.5.4: *Schematic diagram of neutron guide with one gap. The size of the PSD is 20×20 cm^2.*

The wavelength band was 0.1-10 Å. The calculations were performed for two pinhole sizes: 5 mm and 20 mm for the smallest and typical aperture sizes envisaged for IMAT, respectively.

Table 3.5.1: *Average neutron intensity at the sample position for different gap sizes for pinhole diameters 5 mm and 20 mm.*

Gap (m)	Guide1 (m)	Guide2 (m)	Intensity on the PSD monitor for pinhole diameter 0.005m (neutrons/sec)	Intensity on the PSD monitor for pinhole diameter 0.02m (neutrons/sec)
0 (no gap)	42.8m		3.25e+08	5.23e+09
0.2	15.3m	27.3m	3.19e+08	5.13e+09
0.4	15.3m	27.1m	3.12e+08	5.03e+09
0.6	15.3m	26.9m	3.06e+08	4.92e+09
0.8	15.3m	26.7m	2.99e+08	4.82e+09
1	15.3m	26.5m	2.94e+08	4.71e+09

Table 3.5.1 shows that the intensity decreases as the gap size increases for both pinhole sizes. The corresponding intensity loss at the sample position with respect to the gapless model is illustrated in Figure 3.5.5.

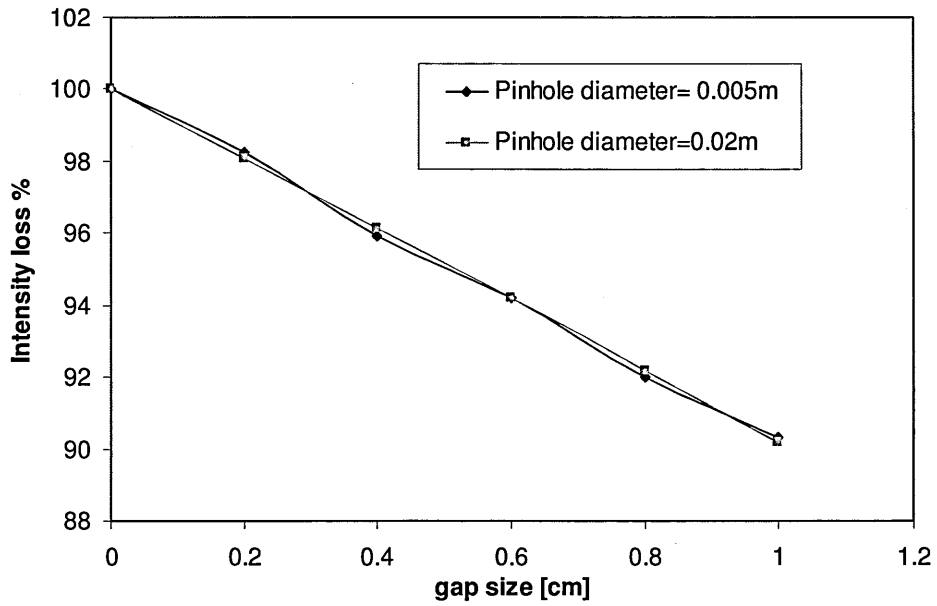

Figure 3.5.5: *The intensity percentage loss for different gaps and two different pinholes.*

The intensity loss is approximately 1% for every 10 cm of a gap size. The intensity distribution on the PSD monitor (Figure 3.5.6, Figure 3.5.7) for different guide gaps shows artefacts (or stripes). These are much more visible for the smaller pinhole (5 mm diameter). Moreover, increasing the gap size leads to an increase in the widths and depths of the artefacts. Fine-line and weak artefacts are visible even when the guide does not have any gap and the pinhole is very small.

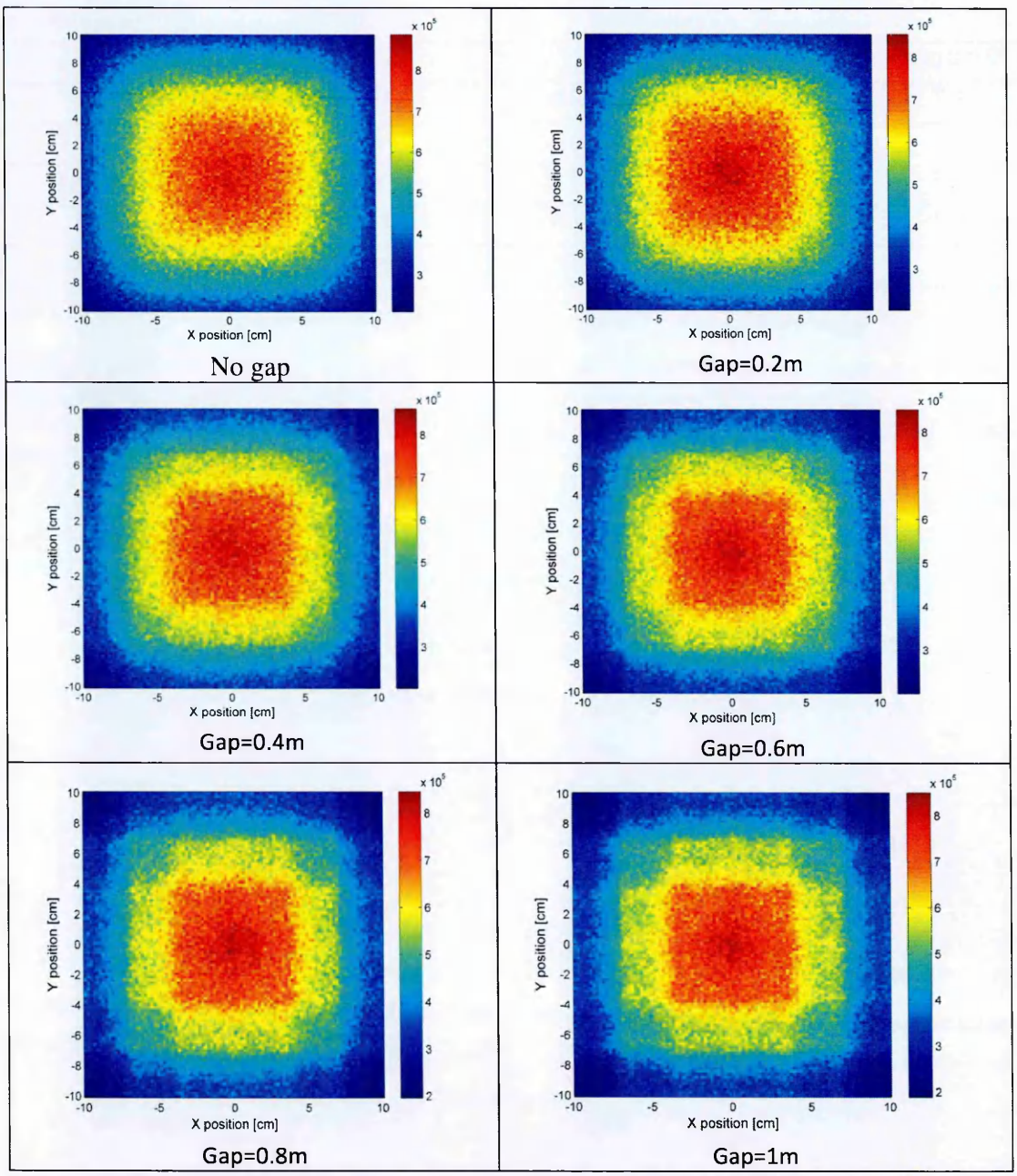

Figure 3.5.6: *Intensity distribution on the sample position for pinhole diameter 20mm.*

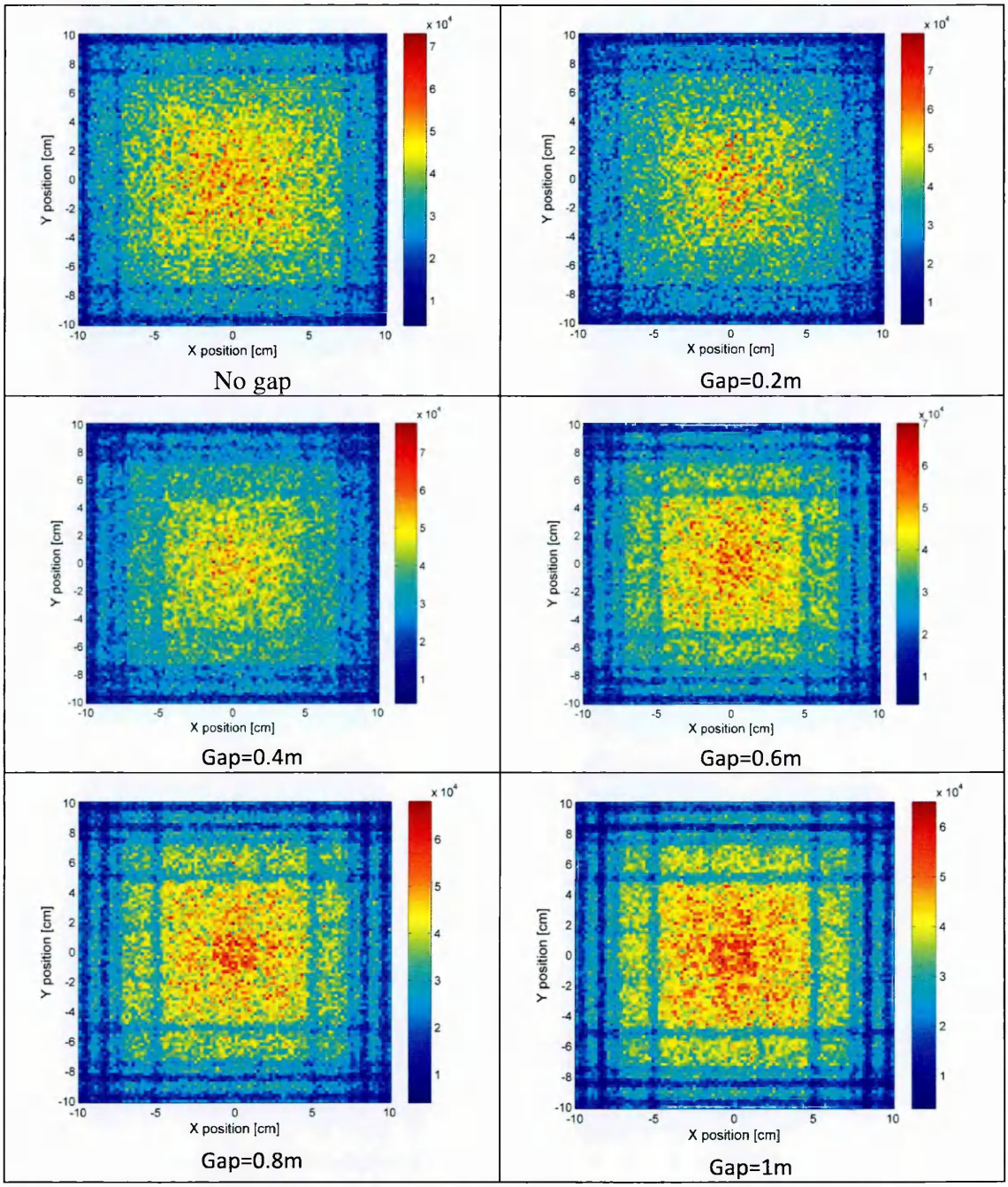

Figure 3.5.7: *Intensity distribution on the sample position for pinhole diameter 5mm.*

The simulations show that geometric artefacts (stripe patterns) clearly appear for gaps bigger than 0.2 m for minimum aperture size of 5mm and are not very pronounced for typical pinhole size of 20 mm if the total gap in the guide is less than 0.5 m. The intensity loss for such a gap is about 5%. IMAT will, in fact, have several gaps for the three choppers, for valves that are inserted to separate the guide vacuum into several sections,

and for three beam monitors for beam diagnosis. The positions and sizes of the main gaps are as follows: gap of 10 cm at 11.8 m from the moderator centre for a gate valve, gap of 5 cm at 12.2 m from the moderator for the first double-disc chopper, gap of 35 cm at 12.75 m from the moderator for the T0 chopper, and gap of 5 cm at 20.4 m for the second double-disk chopper. The total gap size is therefore about 55 cm. A more detailed description of IMAT choppers will be provided in Chapter 4.

3.6 Pinhole collimation performance

The variable spatial resolution necessary for the radiography/tomography mode is obtained with a collimation system, called the pinhole selector, consisting of a set of apertures.

3.6.1 Pinhole description

The IMAT imaging mode will use a wide beam emanating from a pinhole to study extended objects in a single acquisition, if the sample is smaller than the neutron camera area, or in a scanning mode, if the sample is bigger than the camera area. The pinhole neutron experiment is similar to the "classical" optical camera experiment in which the light passes through a pinhole creating an inverted image of the source [65]. It is not our intention to give too many technical design details on the pinhole selector system. We only would like to mention that for IMAT the pinhole will be machined into a 10 mm thick neutron-absorbing material sintered boron carbide which will have a layer of LiF polymer material on the incoming beam side. The latter material has the advantage of not producing gamma radiation on neutron capture. In the Monte Carlo simulations, the pinhole is considered perfectly circular (for achieving a symmetric and homogeneous image), totally absorbing and with no thickness. As mentioned in Section 2.3.2, the divergence

(parallelism) of the neutron beam can be controlled by the L/D ratio, where L is the distance from pinhole to camera position and D is the aperture diameter. In turn, this L/D determines the achievable spatial resolution of the neutron image. Increasing of the aperture's diameter D (i.e. low L/D) leads to gain of neutron flux while reducing the spatial resolution of the image.

In the preliminary IMAT design stage, an aperture selector was positioned at 1.5 m from the end of the neutron guide. At a distance of L=10 m from the detector screen was placed (Figure 3.6.1).

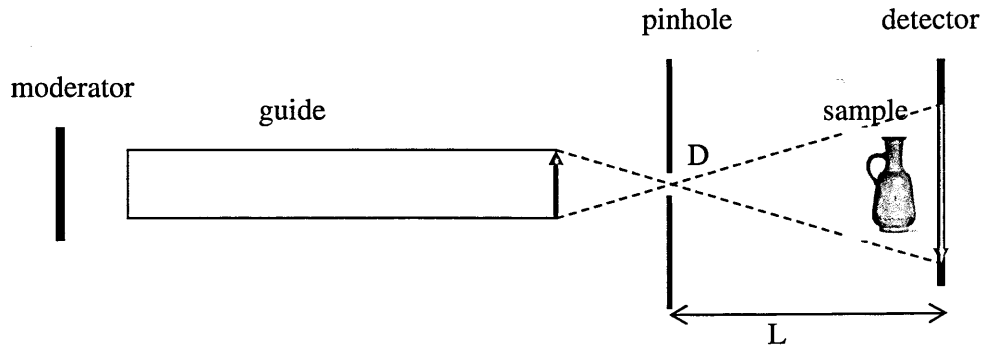

Figure 3.6.1: *The schematic design of the IMAT imaging mode using the pinhole selector. After the neutrons have exited the guide they pass through the circular pinhole of diameter D, are attenuated by the sample and then captured by the detector.*

The remote-controlled pinhole selector on IMAT instrument will offer a choice of five apertures (diameter of 5, 10, 20, 40, 80 mm) for defining different L/D ratios. Moreover, the pinhole selector will have one position with a large enough opening so that the 95×95 mm^2 neutron beam passes through unobstructed for the diffraction mode.

In the following results from the McStas investigations of the pinhole performance are presented, for different pinhole sizes, variations of the neutron flux for different distances between pinhole and detector, and for the influence of the pinhole thickness on the neutron flux.

3.6.2 Imaging performance for different pinholes size

Figure 3.6.2 shows the virtual instrument set-up in McStas using a moderator-guide-pinhole-PSD combination.

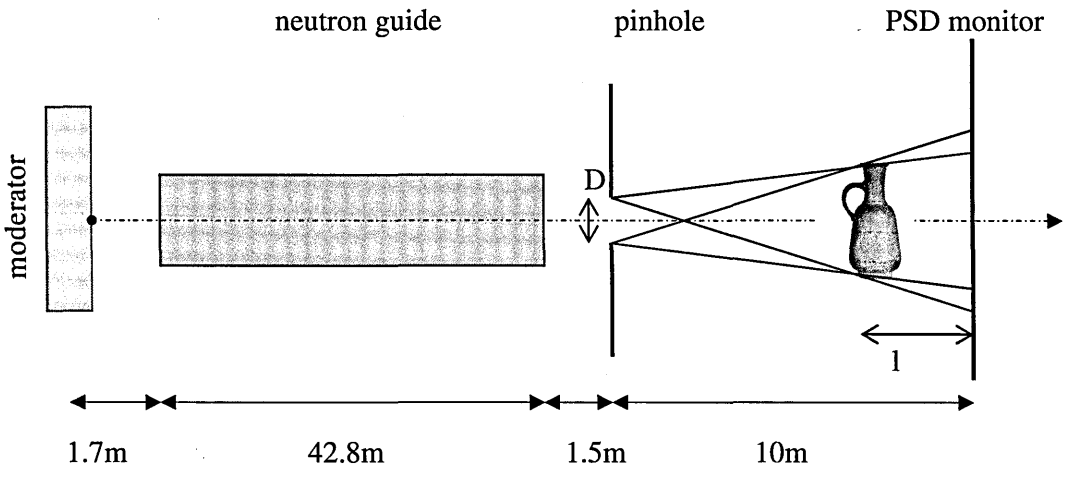

Figure 3.6.2: *Imaging set-up with the geometric blur illustration.*

The PSD monitor with dimension 20×20 cm^2 and 100×100 pixels was placed on the sample position at L=10 m distance from the pinhole. The image resolution or geometric blur relation $d = l/(L/D)$ is depending on L/D ratio and the distance between sample and scintillator screen l, settled in such manner as the sample will have sufficient space for rotation for tomography measurements (see section 2.3.3). A typical value for the distance between sample and monitor is about 10 cm.

Table 3.6.1: *Neutron flux on the PSD monitor depending on pinhole size, integrated for a wavelength range from 0.1 to 10 Å. The spatial resolution is given for a sample-PSD distance of 10 cm.*

Pinhole diameter (mm)	L/D	Image resolution (mm)	Max neutron flux on the PSD monitor ($n/cm^2/sec$)	Total neutron flux on the PSD monitor ($n/cm^2/sec$)
5	2000	0.05	1.86e+06	0.81e+06
10	1000	0.1	5.75e+06	0.33e+07
20	500	0.2	2.12e+07	1.31e+07
40	250	0.4	8.32e+07	0.52e+08
80	125	0.8	3.00e+08	1.94e+08

From the output data (for a defined L/D ratio) of the PSD monitor we can extract the integrated neutron intensity and calculate the total neutron flux (by dividing the total neutron intensity by the detector's area of 400 cm^2) corresponding to an average neutron flux on the PSD. Moreover the maximum neutron flux is evaluated by dividing the maximum neutron intensity to the pixel size (0.04 cm^2). (Table 3.6.1)

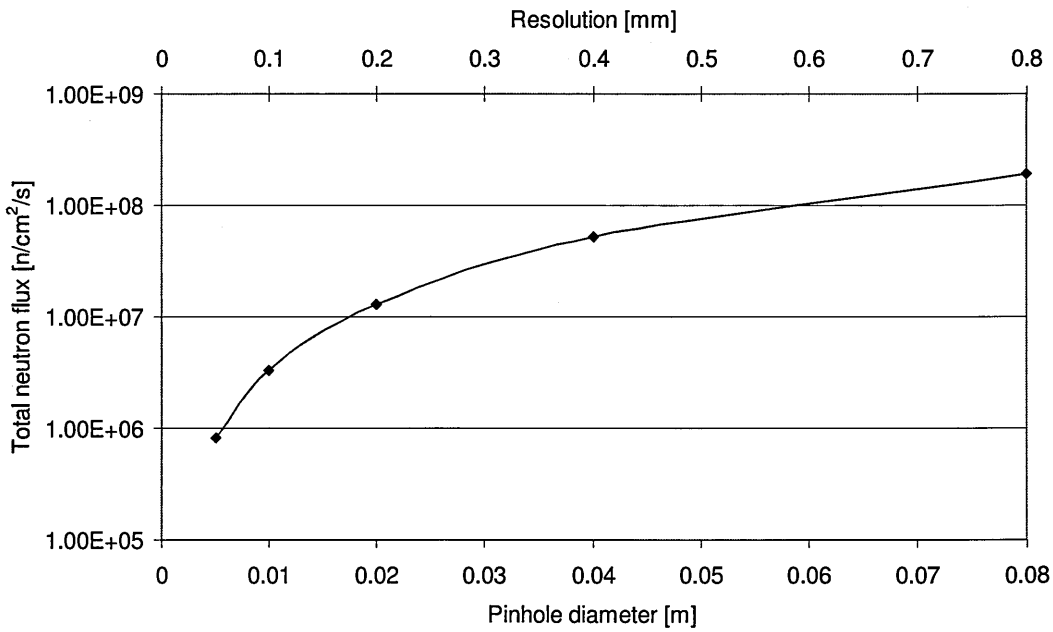

Figure 3.6.3: *Neutron flux integrated over the entire monitor as function of pinhole diameter and resolution. Note the log scale.*

Increasing the pinhole size (decreasing L/D) we gain a higher neutron flux and also the image blurring increases due to the increase of the beam divergence. A small pinhole considerably reduces the neutron flux (Figure 3.6.3). In section 4.2.4 this kind of investigation (pinhole size vs. neutron flux) will be developed for the both wavelength bands used by IMAT instrument (single-frame mode 0.7-7Å and double-frame mode 2-14Å).

The 2D distributions and 1D profiles of the neutron intensity on the PSD monitor (Figure 3.6.4) for smaller pinholes are inhomogeneous indicating geometric stripe patterns. The square profile is determined by the image of the object, in our case the guide exit, which is produced with a "camera obscure" geometry (i.e. the smaller the pinhole, the better the image). As we saw above the primary cause of the geometric artefacts is that there are regions of the detector which look at points on the guide – moderator system from which no neutrons emanate such as regions outside of the moderator and gaps in the neutron guide.

For a larger pinhole (diameter of 80 mm) the beam profile on the PSD monitor is different, i.e. more round due to the blurring effect which distorts the image of the object and the artefacts still exist but they are washed out. The beam profiles measured in both vertical and horizontal directions as a function of pinhole size show the symmetry of the intensity distribution and the positions of the peaks and depths of the artefacts across the PSD monitor.

L/D=2000

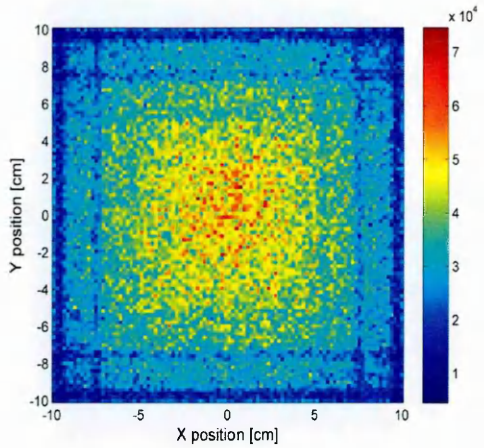

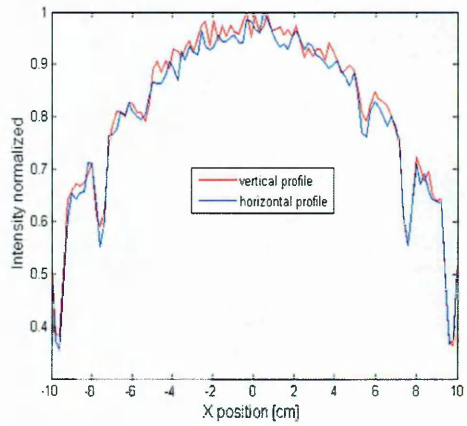

L/D=1000

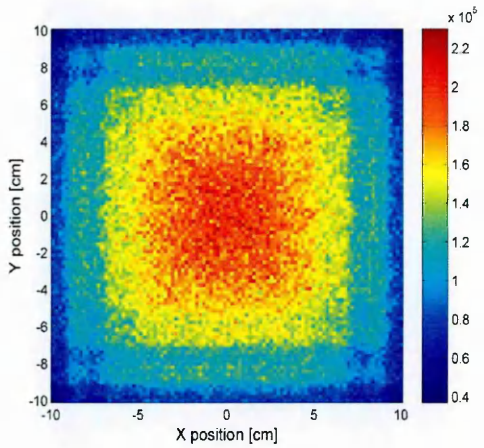

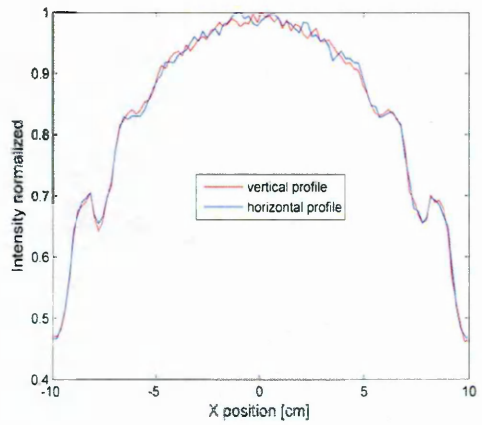

L/D=500

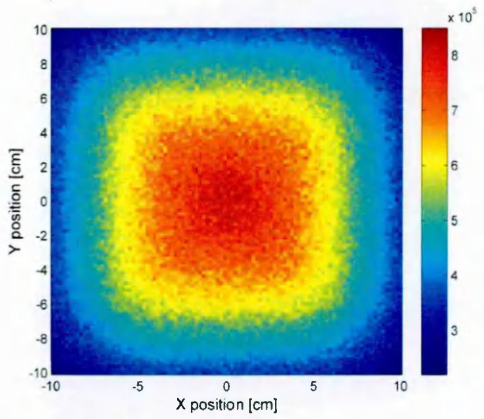

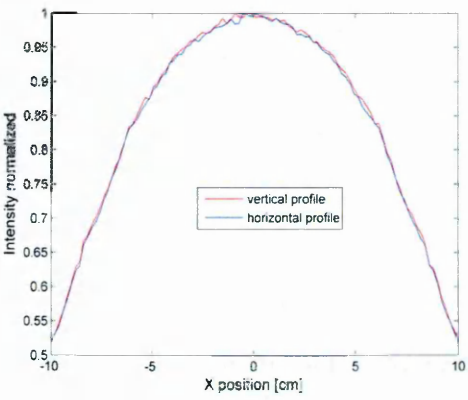

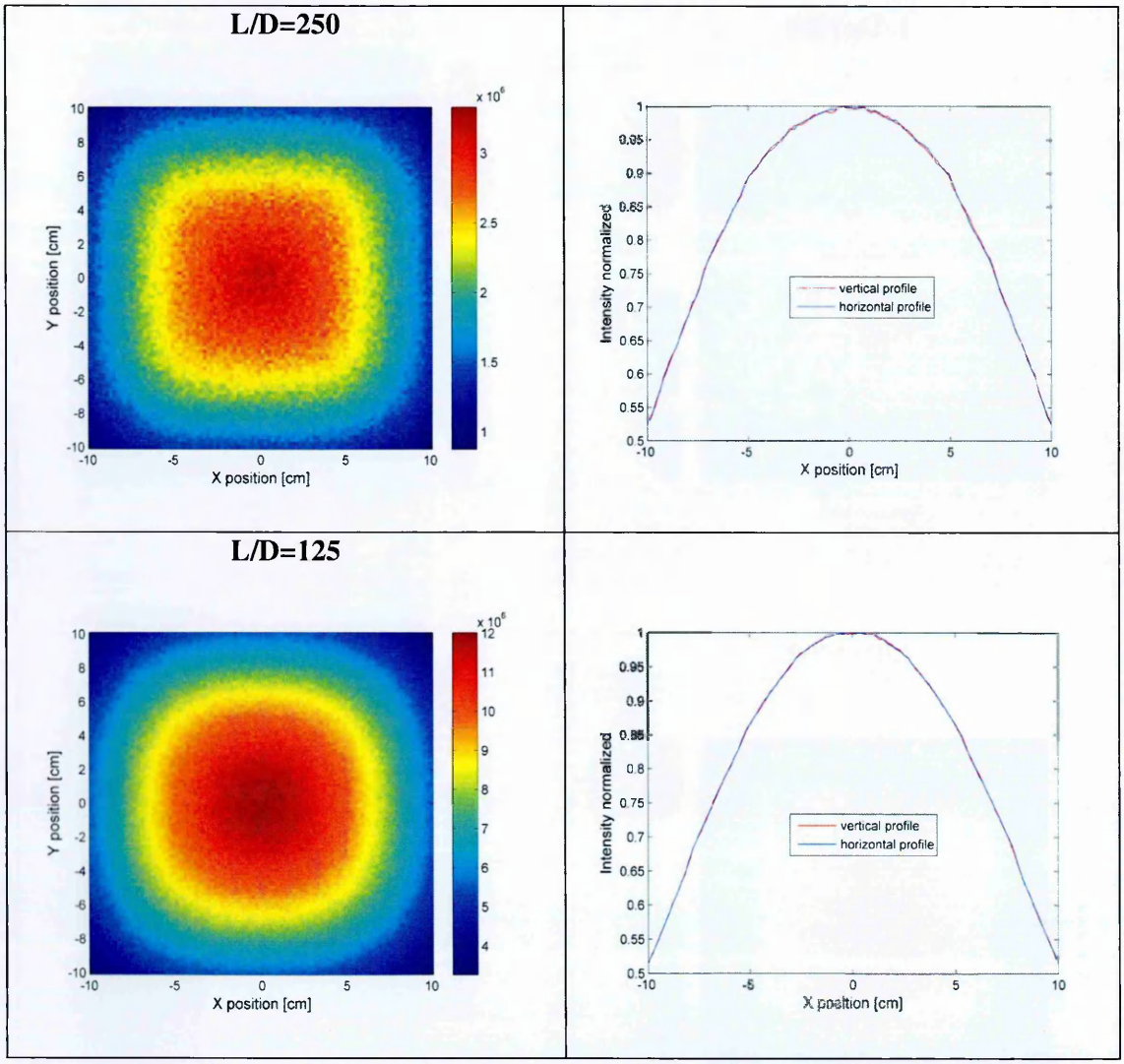

Figure 3.6.4: *Neutron intensity distribution for PSD monitor for different pinholes (left) and horizontal and vertical neutron beam profile (right).*

The image artefacts can be corrected by pixel-by-pixel normalisation. It is expected that routine experiments on IMAT instrument will mostly use L/D ratio of 250 or 500.

3.6.3 The influence of the pinhole thickness on the neutron flux

For the above mentioned Monte Carlo simulations a pinhole with thickness 0 mm was used. In reality, the pinhole has a thickness and could be straight or tapered. We extended our research on the circular pinhole investigating the influence of the pinhole thickness on the intensity distribution on the PSD monitor (Figure 3.6.5).

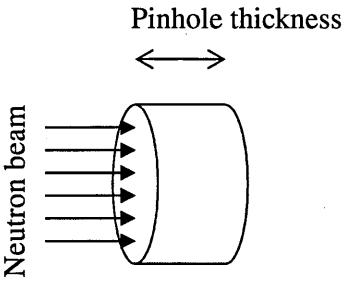

Figure 3.6.5: *Pinhole sketch.*

Two pinhole radii 1 cm and 0.5 cm with thicknesses 0.1 cm, 1 cm and 4 cm were simulated. In McStas two parallel circular pinholes (with same size) made from an absorbing material (i.e. totally black for neutrons) and separated by a distance were used. Otherwise, the imaging set-up in McStas was same as in the previous paragraphs with distance pinhole-PSD monitor selected at 10 m.

Table 3.6.2: *The neutron flux calculated on PSD monitor (20×20 cm^2) depending on pinhole thickness.*

Pinhole thickness (cm)	Neutron flux on PSD (neutrons/sec/cm^2)	
	R=0.005m	R=0.01m
0	0.3258e+07	1.3074e+07
0.1	0.3253e+07	1.307e+07
1	0.3226e+07	1.3008e+07
4	0.31357e+07	1.28057e+07

It is evident that the pinhole thickness does not have an important influence on the neutron flux value; however, a thin pinhole gives a slightly higher flux (see Table 3.6.2).

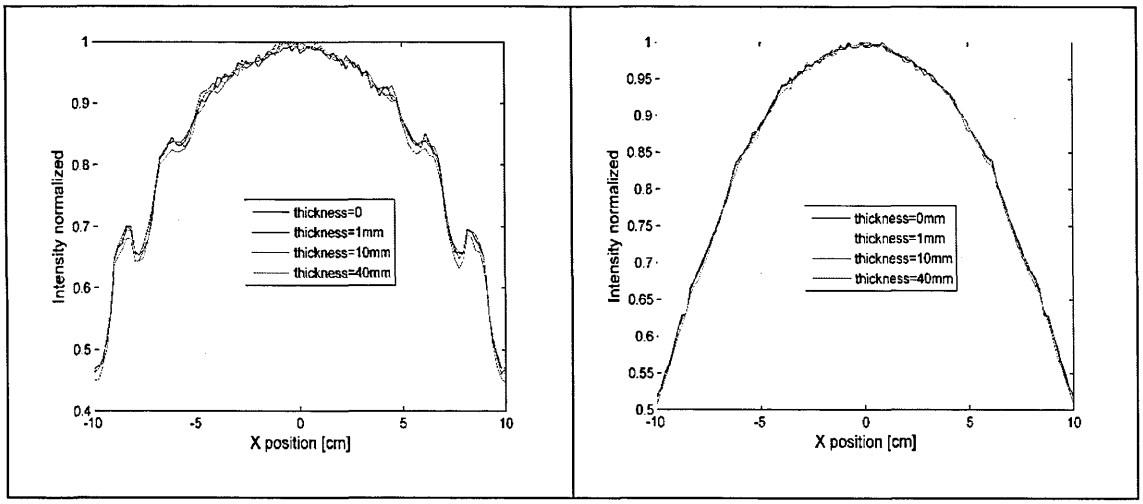

Figure 3.6.6: *Horizontal beam profile on the PSD monitor (left: R=0.005m; right: R=0.01m)*

The neutron intensity distribution profiles (Figure 3.6.6) are almost same for all pinholes thicknesses. This confirms the previous statement that the pinhole thickness (up to 4 cm) does not influence significantly the radiography. In other words, a collimating effect for pinhole thicknesses up to 4 cm can be neglected.

3.7 Effects on neutron detectors

A neutron radiography/tomography experiment requires the placement of the object in the path of the neutron beam and the measurement of the "shadow" image of the sample as projection on a neutron detector.

For IMAT two detector systems are proposed offering a good spatial resolution and high detection efficiency as well as capabilities for energy-selective measurements: a charge-coupled device (CCD) [161] and the pixel camera [162]. In the next paragraphs we will offer a short overview of both systems.

3.7.1 CCD camera

For the standard white-beam radiography/tomography as well as for energy-selective applications a charged-coupled device, CCD camera, is required. The basic principle of the CCD could be described as follows: the neutrons are converted into visible light by a converter called "scintillator" and then this light obtained is recorded with the camera or another optical device via a light-optical system. This camera system for the IMAT instrument is designed by ISIS in collaboration with CNR Messina, Italy [161]. The choice of the CCD camera has been made based on its obvious advantages. One is that the cooled CCD camera has a low intrinsic background (darkfields counts) and another convenience (very important for IMAT) is that the CCD camera can be "gated", i.e. camera can be switched on and off using an external trigger signal. For IMAT, built on a pulsed neutron source, the proton pulse signal at the neutron generation (T0 signal) is used as trigger signal. The camera has a light intensifier which can be switched on/off. The gating allows to switch the light intensifier on after a given time after T0 (time-offset) and leave it active for a given time (time-window). In this way, a wavelength band is selected, and therefore energy selection is achieved.

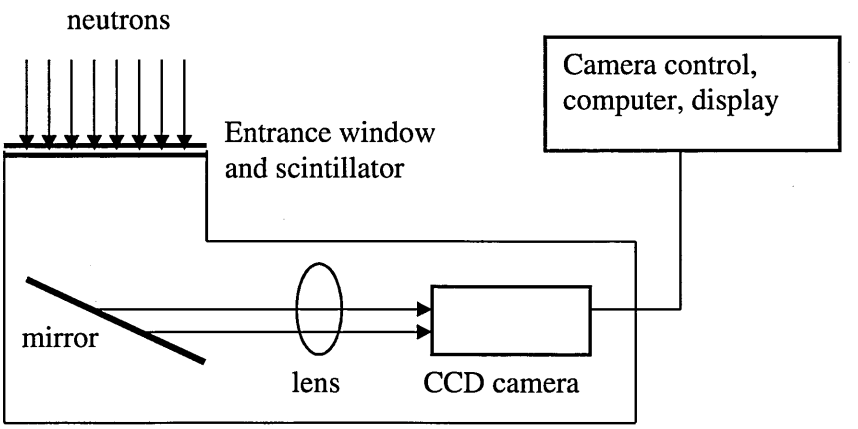

Figure 3.7.1: *Schematic view of CCD camera system.*

The maximum field-of-view for imaging is determined and limited by:

a) The operational space available at the sample position for sample movements and the other hardware such as the diffraction detectors installation;

b) The requirement to build a compact, transportable camera box;

c) The size of the useable portion of the beam at the sample position defined by pinhole and pinhole-camera distance.

For the distance of 10 m between pinhole and camera a reasonable field-of-view (FOV) calculated is 20×20 cm^2. Moreover, the IMAT CCD camera will have at least 1000×1000 pixels per matrix, providing the highest spatial resolution of 0.05 mm for a field of view of 5×5 cm^2 and >0.2 mm for the maximum FOV, 20×20 cm^2. Another feature is that the camera box needs to be light-tight in order to prevent light entering the box and disturbing the collection of light from the scintillator.

Figure 3.7.1 presents a sketch of the CCD camera system. The entrance window is at the front of the camera box. The scintillator screen (e.g. ZnS/LiF) is screwed or glued onto the window (a similar system is used on NEUTRA). A thinner scintillator is preferred because it limits the spread of light in the scintillator and thus a blurring of the signal by the neutron scintillator is reduced. The mirror is mounted at 45 degrees to ensure that all optical paths from the scintillator to the CCD chip are the same. The CCD camera needs to be sufficiently far from the neutron beam to prevent a potential radiation damage of the CCD chip. In addition, the chip must be shielded against the scattered neutrons. The outer dimensions of the CCD camera system are 440×500×1400 mm^3.

As an equivalent component to the CCD camera McStas uses the PSD monitor. It is assumed that the PSD monitor is a "perfect" detector, i.e. all neutrons impinging on the PSD are detected. Furthermore, the PSD monitor in McStas does not have any thickness and is defined as a square with dimensions selected by the users. In the modelling investigations we are interested only in the neutron flux values and not in the detector

resolution. For this reason the PSD monitor employed in the simulations have 100×100 pixels distributed along 20×20 cm^2.

3.7.2 Pixel camera

An interesting feature of the TOF neutron transmission radiography is its capability to produce radiographic images for every energy in a broad neutron energy range, thus taking the advantage of using the full beam spectrum. This is in contrast to white beam radiography which averages over the energy range. IMAT will have a pixel camera (pixel array) that is "TOF capable" and hence can provide TOF transmission spectra for every pixel. The combination of both spatial and time information obtained from TOF spectra enables various studies including Bragg edge transmission imaging, texture mapping and mapping through measuring the spatially resolved parameters of Bragg edges: their heights, widths and positions. The IMAT pixel camera (also called, TOF pixellated Bragg edge detector) is based on microchannel plates (MCP) developed by Space Science Department, Berkeley, USA [101]. The MCP outer dimension is approximately 200×200×100 mm^3.

The MCP system converts neutrons into electrons without light generation and subsequently the electrons are multiplied and registered for each individual pixel. The pixel camera has already been successfully tested at ISIS on ENGIN-X [162]. A spatial resolution of 55 μm is obtained for maximum FOV of about 30×30 mm^2 and its timing resolution is better than 1 μs.

From a McStas modelling point of view, MCP pixel camera can be represented by the PSD monitor, just like the CCD camera. Moreover, the lambda monitor emulated the TOF capability of the MCP pixel camera if we assume that we only have one pixel or we assume that we sum up all pixels of the MCP to obtain a neutron intensity spectrum as

function of wavelength. In Section 4.3.3 the lambda monitor will be used in the modelling of energy-selective experiments as the real pixel camera does in one pixel.

3.7.3 The neutron intensity variations outside the detector area

The maximum camera area or maximum field of view (FOV) was specified as 20×20 cm^2 by the designers. Here we look at the drop of intensity outside the camera area in order to aid the design of the camera entrance window and position of components inside the camera box. It is desired to make the entrance window slightly bigger for minimizing unwanted neutron scattering on the camera materials. For investigating how large the entrance window should be and at what position from the centre the intensity drops off to 10% or 1% we used McStas simulations incorporating a PSD monitor with a large size 70×70 cm^2 placed at the sample position, i.e. 10 m distance from the pinhole. In the schematic Figure 3.7.2 the entrance window for neutrons (yellow) corresponds to the bigger PSD monitor (70×70 cm^2) in our simulations.

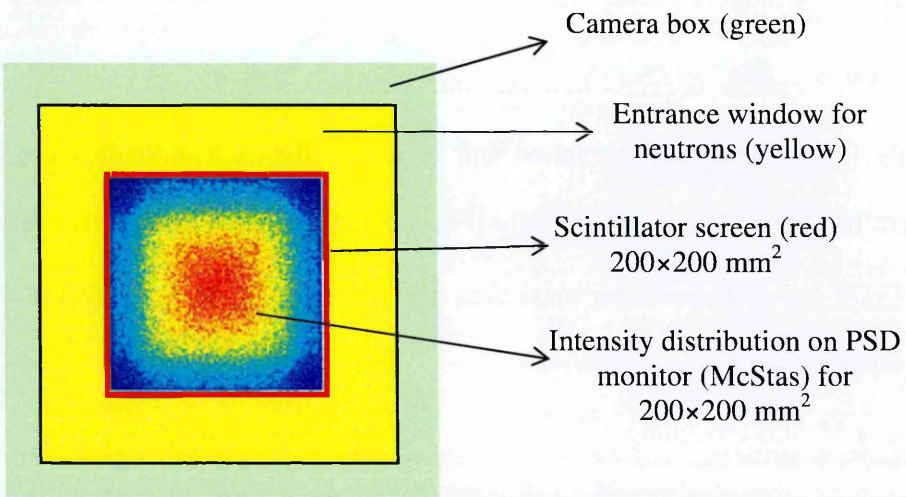

Figure 3.7.2: *Schematic front view of camera box.*

The instrument settings will be same as used in the previously sections. 10^{10} neutrons were generated in the wavelength band 0.1-10 Å for different pinholes diameter (0.01 m, 0.02 m and 0.04 m). We selected one horizontal row in the middle of the PSD and plotting the normalised neutron intensity versus position on the monitor, as displayed in Figure 3.7.3.

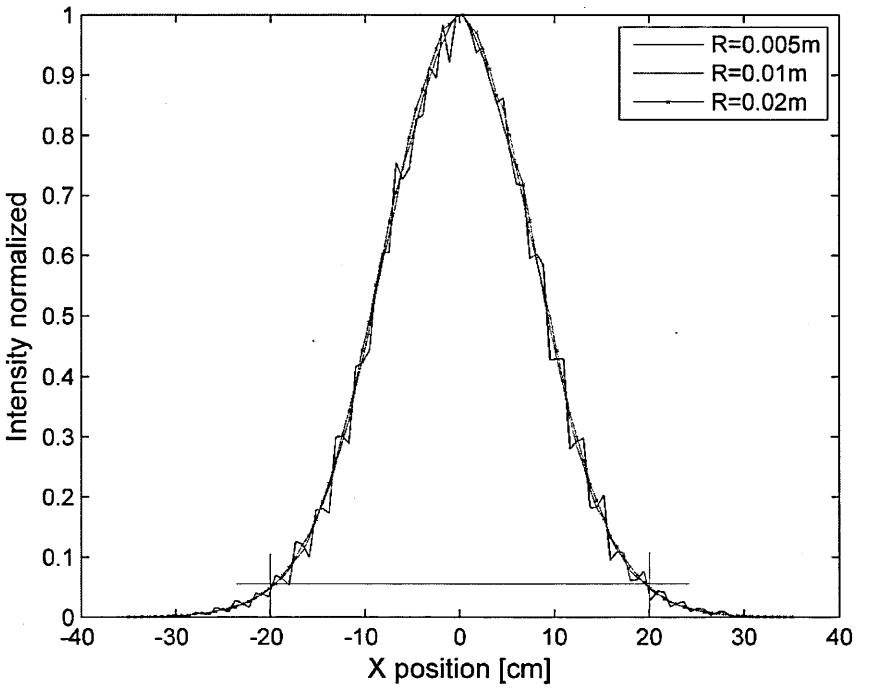

Figure 3.7.3: *The horizontal profile plot of the PSD monitor for different pinholes sizes. The red lines mark out where the intensity drops for -20, +20 cm.*

As shown in Figure 3.6.4 for a PSD monitor with size 20×20 cm^2, the beam profile shape on the bigger PSD is similar for all pinholes sizes (exception being the artefacts which are more visible for the smaller pinholes). Moreover, the drop of intensity at the edges of the monitor is almost independent of the pinhole size. With respect to the centre of the PSD the intensity drops to about 50% for -9,+9 cm, 42% for -10,+10 cm, 10%, for -18,+18 cm, 5% for -20,+20 cm monitor size and almost 2.5% for -25,+25 cm distances. From these results it is concluded that the beam intensity outside the scintillator screen is too high and needs to be reduced in order to avoid unwanted scattering of neutrons on camera box materials. This leads to the investigation of the effect of the beam jaws on the beam profile.

3.7.4 Investigations the effects of jaws for the building of camera box

For imaging and diffraction beam defining beamline "jaws" (beam delimiters) will be used in order to set variable beam diameters/sizes, to control the divergence of the beam or to restrict the size of the beam for imaging to illuminate only part of a sample or the scintillation area of the camera.

Beamline jaws are made of a neutron absorbing material, for example boron carbide, B4C in resin. In theory two pairs of delimiters would suffice to collimate a beam. However, the edges of the jaws will mostly absorb neutrons but they will also partially scatter or transmit neutrons. The idea is to catch these scattered neutrons as effective as possible. Therefore five pairs of jaws are planed for IMAT, one pair serving for horizontal and vertical collimation at a given distance from the pinhole.

To investigate how effective the size of the beam can be limited to the camera area size 20×20 cm^2 we set-up a model in McStas with five pairs of jaws (Figure 3.7.4).

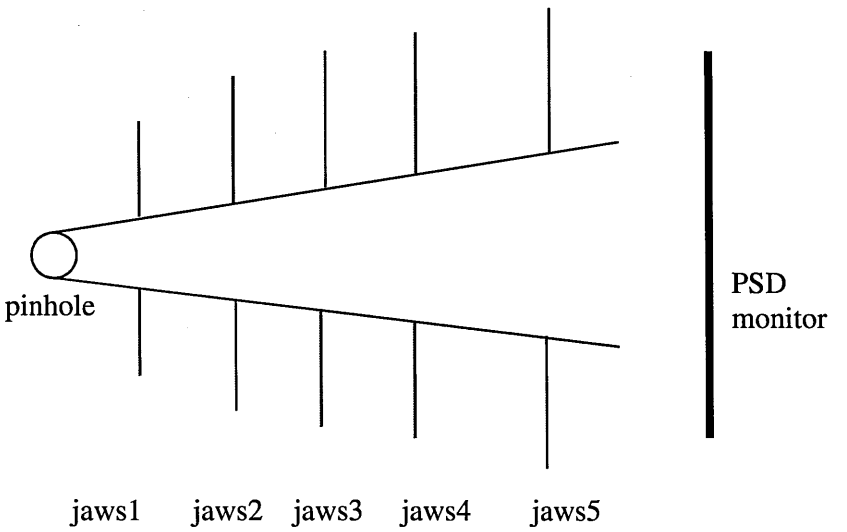

Figure 3.7.4: *System of jaws for IMAT imaging instrument.*

For this investigation two pinhole sizes were considered: fully open beam (pinhole radius is 0.05 m) when the instrument is prepared for diffraction experiments and the "standard" imaging pinhole with radius 0.01 m. For the two pinhole sizes and for the jaws positions suggested by the designers, the half openings of the rectangular jaws were calculated (Table 3.7.1).

The jaws were placed between pinhole and PSD monitor as follows:

1set of jaws positioned at 2 m after the pinhole

2^{nd} set of jaws: 3 m after the pinhole

3^{rd} set of jaws: 4 m after the pinhole

4^{th} set of jaws: 5 m after the pinhole

5^{th} set of jaws: 6 m from the pinhole.

The PSD monitor, as in the previous simulations, was positioned at 10 m after the pinhole.

Table 3.7.1: *Aperture of jaws for R=0.05m and R=0.01m.*

Jaws aperture	Fully open beam (R=0.05m)	Circular beam (R=0.01m)
Jaws-1	0.06	0.028
Jaws-2	0.065	0.037
Jaws-3	0.07	0.046
Jaws-4	0.075	0.055
Jaws-5	0.08	0.064

Four Monte Carlo simulations have been performed using the instrument configuration as used in the previous sections. For two of the four simulations the five sets of jaws were added with dimensions given in Table 3.7.1. The PSD monitor with a large field of view 70×70 cm^2 and 100×100 pixels matrix was used in order to catch up all neutrons arriving at the sample position and with the purpose of observing the entire profile of the neutron beam, within and outside the scintillator area.

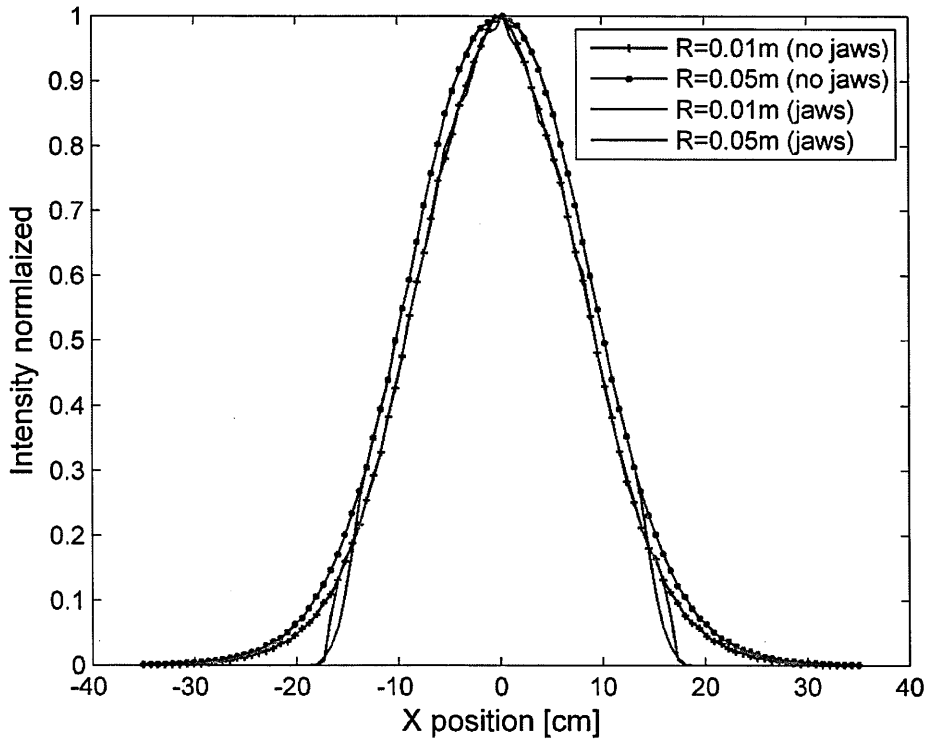

Figure 3.7.5: *Intensity profiles on the PSD monitor derived from the horizontal line selected in the middle of the monitor.*

The simulations with the jaws (Figure 3.7.5) show that we can use the jaws to effectively cut off the tails of the intensity profile. Cutting off the tails is very important as the intensity in the tails is still very high (could be in the range of 10^6 n/cm2/s, as much as on ENGIN-X instrument). The two curves for the model without jaws, and the two curves for the model with jaws are quite similar but not the same. To study the effectiveness of the jaws for limiting the neutron beam some analysis results are reported below:

With respect to the centre of the PSD monitor, the intensity drops to about 50% for -9.5, +9.5 cm, 10% for -16,+16 cm, 5%, for -17,+17 cm monitor size and almost 1% for -17.2,+17.2 cm distances for pinhole radius 0.01 m. For fully open beam the intensity drops to about 50% for -10.5, +10.5 cm, 10% for -15.2,+15.2 cm, 5%, for -16,+16 cm monitor size and almost 1% for -17.2,+17.2 cm distances.

It is concluded that the jaws can be used to effectively adjust the beam profile to the 20×20 cm^2 field-of-view as required.

3.8 Summary

On IMAT instrument the neutron beam will be transported from the moderator to the pinhole selector by a square, straight supermirror guide providing a long flight path to achieve a good time-of-flight and energy resolution. The large cross section of the neutron guide, 9.5×9.5 cm^2, and m=3 provides a sufficient flux at higher energies at reasonable costs and also a symmetric open beam field for neutron imaging. A broad-pulse coupled moderator (filled with liquid hydrogen on one side and solid methane on the other side) with a large viewable area 11×11 cm^2 ensures a high thermal and cold neutron flux for imaging and diffraction analysis. A decision on the guide cross section size was taken after an extensive study of the performance parameters of the imaging beamline and after making compromises with diffraction requirements.

The neutron guide design includes gaps for choppers and other instrument components. The effects of these gaps on the radiographies and neutron flux distribution at the sample position were evaluated. Hence, geometric artefacts (stripe patterns) clearly appear for gaps bigger than 0.2 m for minimum aperture size of 5 mm and bigger than 0.5 m for the standard aperture size of 20 mm. Also, the gaps reduce the neutron flux with almost 1% for every 10 cm gap. The requirement is that the gap sizes for components in the neutron guide need to be strictly minimized, which means for example that the chopper blades need to be as thin as possible.

Depending on the requirements of particular imaging experiments (for example do they require high neutron flux or high spatial resolution) the L/D ratio can be varied via different pinhole sizes, for a fixed distance L between pinhole and imaging detector. Increasing the pinhole size (so, decreasing L/D) the neutron flux is increased, but also the blurring due to the larger beam divergence.

It was not the purpose of this thesis to present technical or engineering details of the instrument components, but our results helped the engineers and designers to take some decisions on certain specifications for components. For example, to minimize unwanted neutron scattering by the CCD camera material beam profile calculations at the entrance window were determined.

4 Generation of simulated IMAT imaging data

Based on the preliminary investigations of the IMAT imaging instrument presented in Chapter 3, particular aspects of the neutron beam relevant to future white beam or energy-selective imaging applications and performance of the complete instrument are investigated here.

4.1 Overview of the IMAT design

Firstly, in this section a summary of the current (at time of writing [8]) IMAT instrument design is presented. In the second part an overview of the staged development of the IMAT (staged due to funding and time constraints) is given, followed by a description of the IMAT imaging instrument as modelled in McStas.

4.1.1 Summary of the present IMAT design

The IMAT instrument will be built on a 56 m flight path (from the moderator to the sample position) being optimized for high neutron flux for imaging and in-situ diffraction studies.

IMAT will be placed on port W5 on ISIS TS-2, which operates at 10 Hz. IMAT will view the broad pulse coupled moderator, composite liquid hydrogen (L-H_2) – solid methane (S-CH_4), at an angle of 1° (horizontal) from the nominal W5 axis. This moderator was chosen to ensure a high thermal and cold neutron flux for imaging and for rapid diffraction analysis. The tilted view of the moderator is required to avoid physical obstructions external to the target station.

A straight, square supermirror guide will start as close as possible to the moderator centre at 1.7 m and will transport the neutrons to the pinhole selector position, thereby

providing a long flight path to achieve the time resolution required for energy selective imaging and diffraction experiments. The total length of the neutron guide is about 44 m, with a cross section of the guide of 100×100 mm^2 in the 2 m shutter section and a cross section of 95×95 mm^2 for the main guide.

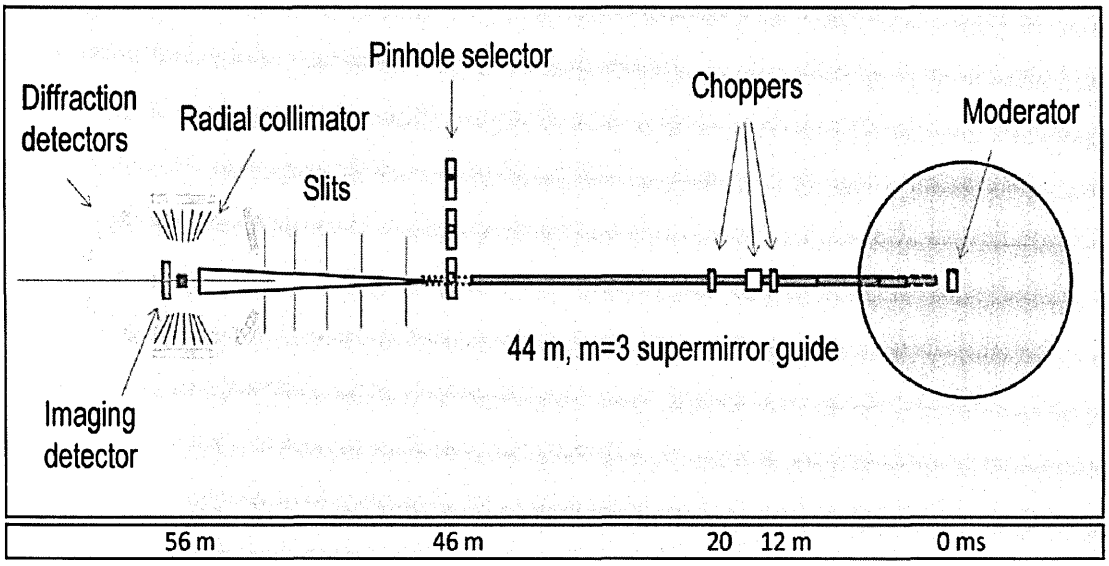

Figure 4.1.1: *IMAT instrument schematic. The neutron beam is transported to the first sample position at 56 m.*

From the pinhole selector the beam is guided in evacuated tubes up to the sample area. There will be two sample positions available. The main sample position is planned for a flight path of 56 m from the moderator centre (i.e. 10 m after pinhole) providing a large area for the installation of imaging cameras in transmission and of diffraction detectors (Figure 4.1.1). The neutron beam size at this sample position (56 m) will vary from 20×20 cm^2 for imaging to a minimum of 1×1 mm^2 for diffraction applications. The second sample position 51 m from the moderator centre (not shown in Figure 4.1.1) (available at a later stage of the instrument development) will enable imaging experiments with higher intensity.

The neutron guide will have gaps for different instrument hardware components such as vacuum gate valves, choppers, neutron monitors etc, which, following the

conclusions from Section 3.5.2, will be minimised due to their effects on the neutron radiographies. The most important such gaps are as follows: gate valve gap (0.1 m) at 11.8 m from moderator centre; first double-disk chopper gap (0.05 m) situated at 12.2 m (see section 3.5.1); a chopper used for filtering fast neutrons and gamma rays, T0 chopper, (see section 3.5.1) will be located in the further gap (0.35 m) at 12.75 m followed by a gap for the second double-disk chopper (0.05 m) at 20.4 m. The pair of double-disk choppers are used to prevent frame overlap and operate in two modes:

(1) a standard single-frame operation when the double-disk choppers will run with the source frequency of 10 Hz and the T0 chopper will run at 20 Hz;

(2) a double-frame mode with a bandwidth of 12 Å when the double-disk chopper will run at 5 Hz and the T0 chopper will run at 10 Hz. For a square neutron beam of 95 mm side length, a standard double-disk radius of 325 mm and for 10 Hz running, the opening time is 2.7 ms. The double frame mode will be available via PC remote control.

The frequency of the source, chopper frequencies, positions and opening angles provide information on the wavelength band: the single frame operation gives a band of 0.7-7 Å and the double-frame mode gives a band of about 2-14 Å. These calculations indicate the wavelengths of neutrons passing through the chopper system (see blue lines in Figure 4.1.2) [163]. They also indicate if neutrons leak through the chopper system. Following these calculations an additional absorbing blade, a so-called tail-cutter, will be added to the T0 chopper in order to prevent frame overlap (see section 2.2.3).

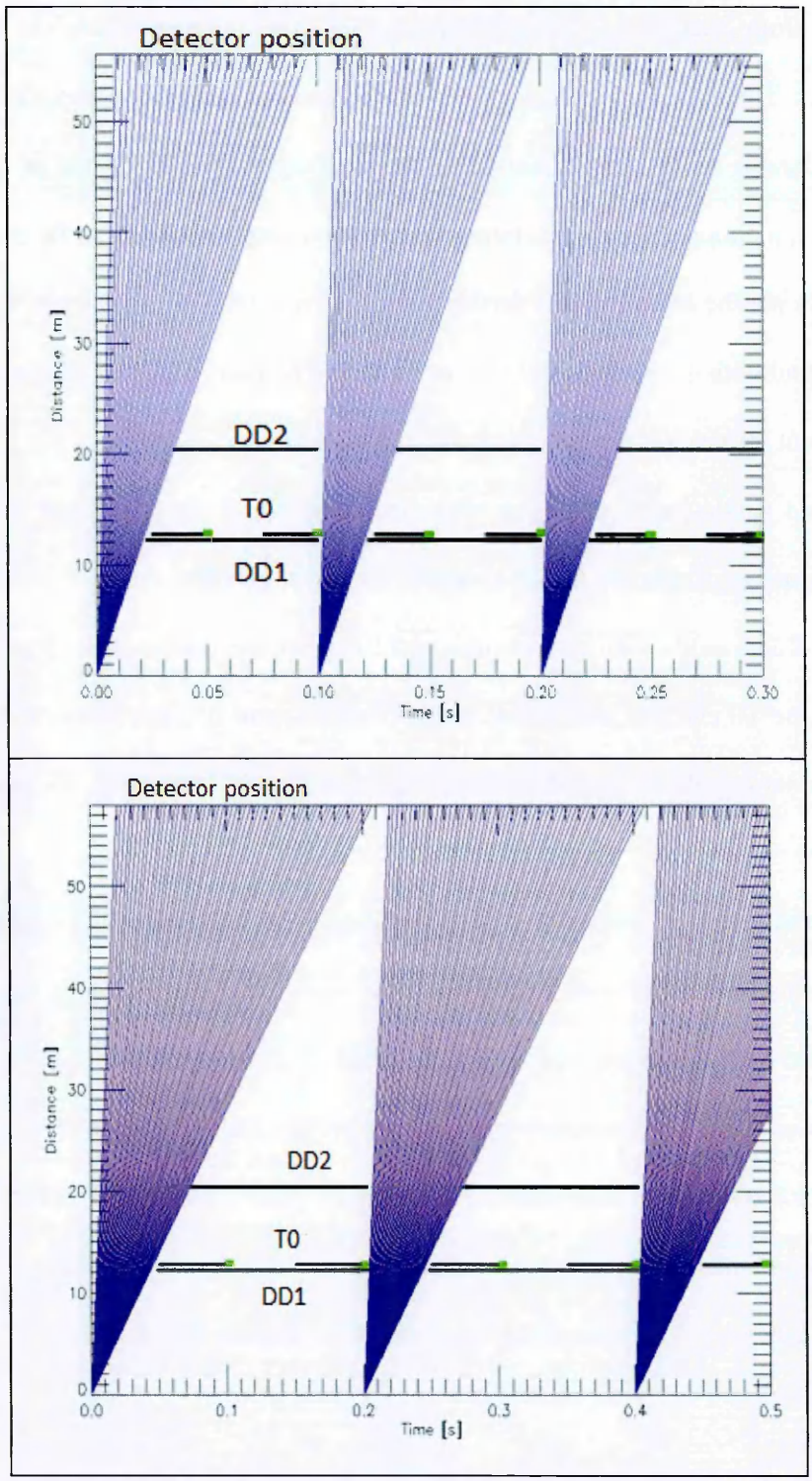

Figure 4.1.2: *Distance-Time diagram for standard chopper settings for the flight path of 56m; (a) bandwidth 6 Å: DD1, DD2 at 10Hz, T0 at 20Hz; (b) bandwidth 12 Å: DD1, DD2 at 5Hz, T0 at 10Hz; The black horizontal bars indicate the time periods of DD1, DD2, and tail cutter blades. The green bars indicate the position of the T0 chopper blade.*

The remote-controlled pinhole selector will offer a choice of five apertures (D=0.08 m, 0.04 m, 0.02 m, 0.01 m and 0.005 m) defining different L/D ratios (125, 250, 500, 1000 and 2000) where L=10 m is the distance from pinhole selector to the imaging camera and D is the pinhole diameter. The pinhole selector will have also a large open position allowing the beam to pass through for diffraction experiments. With a set of beamline jaws (see section 3.7.4) and one set of slits placed just in front of the sample the beam size at the sample position can be adjusted from 200×200 mm^2 for imaging to a minim of 1×1 mm^2 for diffraction applications. The switching from imaging to diffraction experiments will be made by modifying the pinhole size to the open beam position and adjusting the jaws to the desired gauge volume size. Table 4.1.1 summarizes the IMAT beamline parameters and expected performance parameters. Some of the performance parameters presented in Table 4.1.1 are the result of calculations that are described later in this chapter.

Table 4.1.1: *Main IMAT instrument components and the expected performance parameters [8].*

General:	Moderator	L-H2 / S-CH4 (W5 port on TS-2)
	Repetition rate	5, 10 Hz
	Neutron guide	m=3, straight, square 100×100 mm^2 in 2 m long shutter section 95×95 mm^2 for ~42 m guide
	Choppers	T0 (20 Hz), 2 double-disk choppers (10 Hz)
	Single frame bandwidth	0.68 - 6.8 Å
	Double frame bandwidth	2- 14 Å
	Flight path to sample	56 m
Imaging:	L: Distance pinhole – sample D: Aperture diameter	10 m 5, 10, 20, 40, 80 mm
	L/D	2000, 1000, 500, 250, 125
	Best spatial resolution	50 µm
	Max Field of View	200×200 mm^2
	Detector types	Gated CCD camera Max. Field of View: 200×200 mm^2

		High-resolution (TOF) pixel detector Max. Field of View: 30 × 30 mm^2
Diffraction	Secondary flight path	2.0 m (at 2theta=90 degree)
	Detector type	Wavelength-shifting fibre coded ZnS/LiF scintillation detectors at 2theta=20, 45, 90, 125, 155 degrees
	Detector coverage	4 steradian (1 sr at 90 degrees)
	Minimum gauge volume	1×1×1 mm^3

Two imaging cameras will be available: a gated CCD camera (see section 3.7.1) with a maximum field-of-view of 20×20 cm^2 and a TOF capable high-resolution pixel detector (see section 3.7.2) with a field of view of 30×30 mm^2. The two cameras are not used at the same time but can be used in turn. In addition, five highly pixellated diffraction detector arrays at different 2θ scattering angles with a total solid angle coverage of 4sr will be installed for diffraction experiments. Two detector banks at 90 degrees have a particular relevance for strain analysis, allowing simultaneously measurement of two orthogonal strain components. Radial collimators will be installed between sample and each detector bank in order to define a diffraction (gauge) volume for a given beam size. Every collimator unit can be removed or exchanged for a different one; collimators with varying gauge sizes are being designed to provide ample space for samples and diffraction scans. For example, the available space between the collimator faces for a 2 mm gauge will be about 1 m.

4.1.2 The staged development of IMAT instrument

IMAT will be installed in two stages. Figure 4.1.3 shows the initial IMAT experimental area. The blockhouse will be inside the IMAT extension building. A user and computer

cabin ("pod") (not shown in Figure 4.1.3) will be situated on a balcony above the pinhole selector.

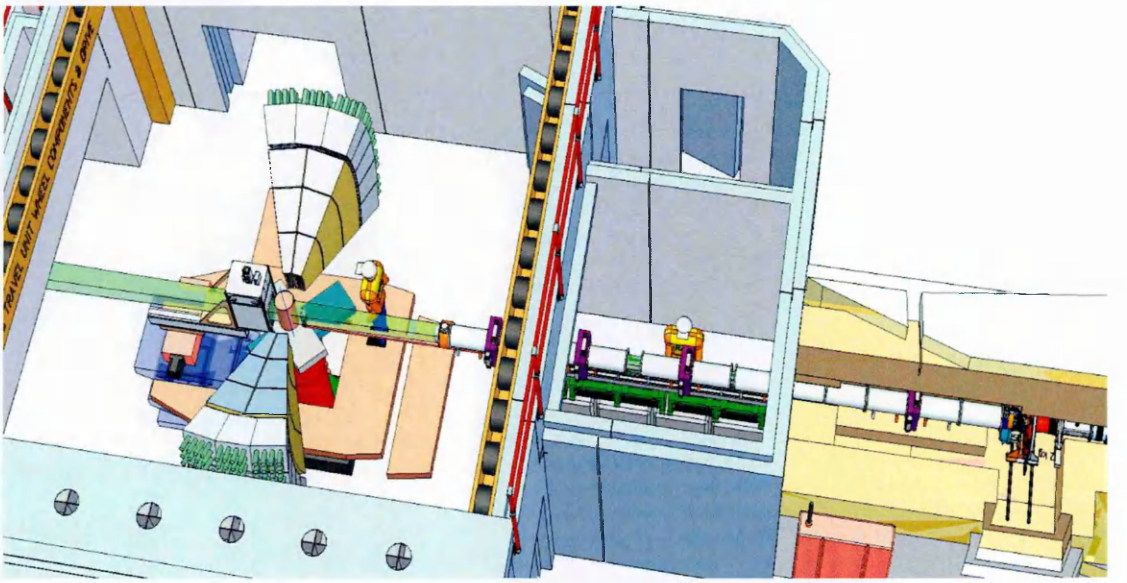

Figure 4.1.3: *Artist's impression of the IMAT Day-1 blockhouse. The IMAT instrument will include: imaging cameras (CCD camera and Bragg edge detector), sample positioning system, and diffraction detectors with collimators at 90 degrees. Note: radial collimators in front of the 90 degree diffraction detectors are not in scale [8].*

The IMAT instrument in the first stage will comprise the following components and features:

- Beam monitors for diagnostics and normalization;
- Pinhole selector for five apertures: range of L/D values from 125 to 2000; IMAT will be working mostly with L/D of 250 or 500.
- Fast experimental shutter for minimizing neutron exposure of samples when no data are collected;
- Adjustable jaws and slit system to vary the size of the incoming neutron beam;
- Heavy duty sample positioning system (SPS) (maximum: 1.5 t), including a tomography rotation stage (maximum: 50 Kg);
- Two imaging cameras and diffraction detectors with specifications as presented in the below table (Table 4.1.2). The CCD system is required for "standard" white-beam

radiography and tomography experiments as well as for many energy-selective applications.

Table 4.1.2: *The detectors for the stage 1 of the IMAT instrument.*

Imaging:	Gated CCD camera:	
	Max Field of View (FOV) Best spatial resolution FOV: 200×200 mm^2 FOV: 100×100 mm^2 FOV: 80×80 mm^2 FOV: 50×50 mm^2 Timing resolution Camera box (retractable)	200×200 mm^2 200 µm +above 100 µm 80 µm 50 µm 100 µs 400×500×1300 mm^3
	TOF pixellated Bragg edge detector (based on A. Tremsin – MCP detector specification)	
	Max Field of View (FOV) Best spatial resolution Timing resolution Camera box (retractable)	30×30 mm^2 55 µm <1 µs 300×300×200 mm^3
	Estimated counting times: White-beam radiography: 1-60 s λ-dependent radiography (CCD): 1-10 min per λ-slice Full TOF spectrum MCP: 10 min-2 hours White-beam tomography: 2-6 hours	
Diffraction:	Two diffraction detector arrays at 90 degrees	
	Area coverage Pixel size d-spacing	1sr (4 m^2) 4×100 mm^2 0.5-4.8 Å (for standard single-frame bandwidth)
	Radial collimator sets (for the two 90 degrees banks)	
	Gauge volumes	1, 2, 5 mm^3

The combination of both spatial and time information enables texture mapping and strain analyses, as well as studies of phase compositions and phase transitions. It should be emphasised that the three IMAT detector systems (two imaging cameras and diffraction detectors) will normally not be operated simultaneously since the corresponding modes need different beam sizes and sample orientations. The blockhouse design will need to take into account the different operational modes of the instrument allowing:

- Switching-over between imaging to diffraction modes;
- Supporting of and reproducible positioning of imaging cameras; retraction and storage of imaging cameras during diffraction experiments;
- Crane access through an opening roof, for changing samples, sample environment and collimators;
- Positioning of samples of up to 1.5 t;
- Sample preparation and off-line testing area outside blockhouse.

For samples larger than the maximum field-of-view, full radiographies and tomographies can be collected in scanning mode and the data obtained merged, post-experiment, to obtain the full sample tomography.

In the Stage 2, further detectors at forward and backscattering angles will be installed, bringing the detector coverage to a total of 4 steradian (Figure 4.1.4). This will enable in-situ texture studies in combination with phase, structure, texture, strain and imaging analyses. The additional detectors will significantly extend the d-spacing range to 0.35-20 Å. Also, the extra angular coverage will permit in-situ texture analyses during tensile testing and/or temperature treatment for a single sample orientation.

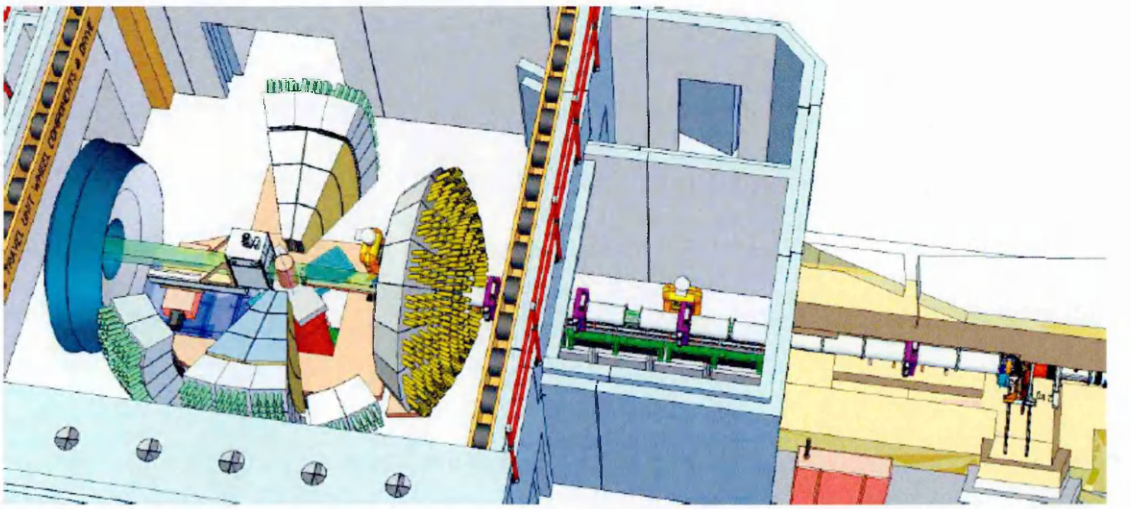

Figure 4.1.4: *Artist's impression of the IMAT Stage-2 blockhouse. Diffraction detectors at forward and backscattering angles will be added [8].*

The instrument in the 2nd stage comprises as extras to the Day-1 set-up:

- Four diffraction banks at off 90 degree positions;
- High pixellation within a bank, with a pixel angular range of about 5 degree;
- Radial collimators for diffraction gauge volumes of 5 and 10 mm in front of detectors;
- Additional radial collimators for the 90 degree banks (e.g. 4 mm and 10 mm).

Future upgrade options

There are a number of possible upgrade options which could extend the capabilities and performance of the instrument. The IMAT instrument design has inbuilt flexibility for further future upgrades at a later stage; the blockhouse design provides ample space for operations and installations. The beam tubes and beam jaws between pinhole and sample are of modular design and can be easily removed or re-positioned. That is to say, the current engineering design does not preclude the future upgrade options:

- Filters: optional filters or diffusers could be inserted between end of guide and pinhole selector;
- Extended detector coverage: some of the detector banks could be extended to increase out-of-plane coverage;
- Second imaging position: adding an imaging camera at 5 m from the pinhole will be relatively straightforward. The intensity increased is about fourfold, at the expense of FOV which would be about 10×10 cm^2. Such a station would increase the flexibility for imaging studies considerably, by trading field of view, resolution and intensity between the two sample positions;
- X-ray tube: if required a tube could be installed at the 5 m position, for complementary X-ray imaging;

- Improved imaging resolution: the pinhole selector will be designed with a flexible cartridge system, i.e. pinhole sizes and materials can be changed at a later stage. The instrument will be sufficiently flexible to upgrade it with state-of-the art imaging cameras.
- Improved diffraction resolution: radial collimator modules for smaller gauge volumes can be added later if required and if flux levels allow this;
- Polariser for magnetic imaging: A polarizer could be installed upstream of the backscattering bank. The instrument setup and the achievable wavelength resolution do not exclude magnetic imaging applications at low magnetic fields.

4.1.3 Modelled IMAT imaging instrument in McStas

Based on the previous descriptions, IMAT was modelled in McStas (see Appendix 3) through the following components: moderator-guide-pinhole-jaws and monitors: position-sensitive-detector and lambda monitor (Figure 4.1.5). Specifically:

1. ISIS_moderator component: cross-section 110×110 mm^2;

2. Rectangular guide:shutter section position 1.7 m, 2 m in length and cross section of 100×100 mm^2;

3. Rectangular neutron guide: 42 m length with cross section 95×95 mm^2 sectioned by the gaps to give section lengths of: 8.05 m, 0.275 m, 0.5 m, 7.3 m and 25.275 m.

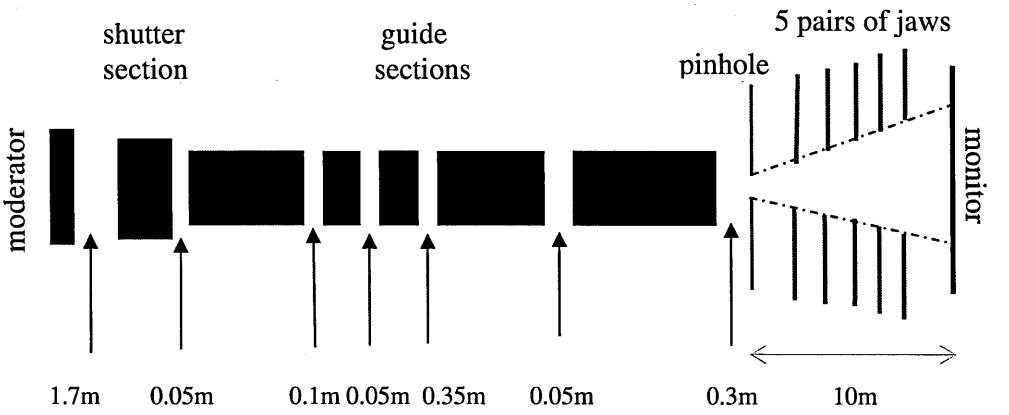

Figure 4.1.5: *Schematic outline of the IMAT imaging instrument modelled in McStas. Note: the rectangular black block represents the moderator and the rectangular blue blocks are the sections of the neutron guide.*

4. Pinhole: At 0.3 m after the guide exit the aperture selector with the circular pinhole is placed.

5. Jaws: The beam collimated by the pinhole is delimited by the five pairs of jaws (see section 3.7.4): first pair at 1.5 m after pinhole, second pair at 3 m, third pair at 4.5 m, the forth pair at 6 m and the last pair at 7 m. The opening size of each jaw was calculated given its position on the beamline and the pinhole diameter

6. Sample: The sample position was considered at 10 m after the pinhole. In Section 4.3 there will be performed two sets of simulations: the one using the standard McStas polycrystalline sample (i.e. the vanadium sample component from McStas), which does not model wavelength dependent attenuation, and another set looking at wavelength dependent attenuation effects where it was used a polycrystalline specimen (i.e. iron bcc powder) described in McStas by the BraggEdge powder component.

The McStas IMAT model detailed above neglects some features and components of the real instrument as they were considered unimportant to the modelling process. These include: air in torpedo, aluminium windows, potential misalignment of the guide sections, 0.03 m circular gaps in top section of the neutron guide for monitors, 0.01 m gap for two additional electronic gate valves, and filters in front of the aperture selector.

The following sections present the results of simulations designed to explore the performance of IMAT as represented by this model.

4.2 Performance simulations of the present IMAT design

4.2.1 Wavelength distribution of the neutron flux

The wavelength spectrum dependency effects introduced by the instrument components such as neutron source, neutron guide, gaps or pinhole are particularly important for energy selective imaging. We had interests to investigate different aspects of the wavelength spectrum as it changes from the exit of the moderator through the instrument up to the sample position. Therefore lambda monitors of the same sizes (20×20 cm^2) were placed at different positions in the McStas IMAT instrument (Figure 4.2.1): first monitor (lmon1) after moderator at 1.699 m, the others in the neutron guide gaps at: 3.749 m (lmon2), 11.899 m (lmon3), 12.224 m (lmon4), 13.074 m (lmon5), 20.424 m (lmon6); one at the guide exit, before the pinhole (lmon7) at 45.701 m and the last (lmon8) on the sample position at 56 m.

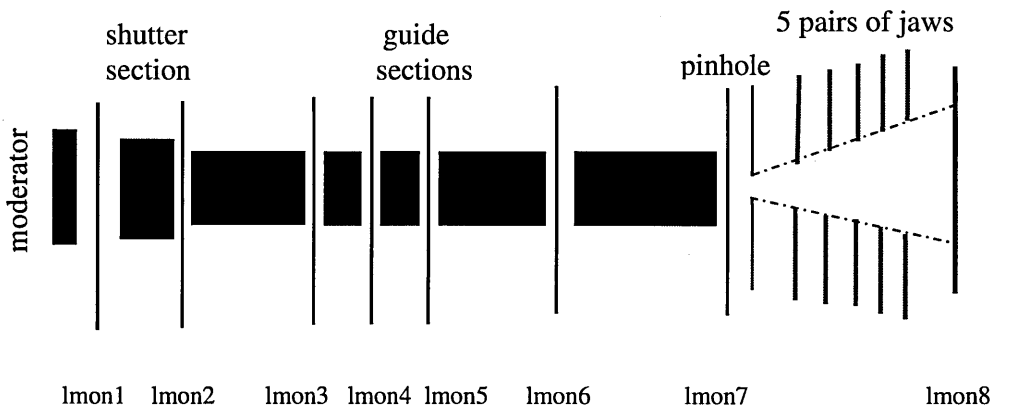

Figure 4.2.1: *The IMAT diagram with lambda monitor positions along the instrument.*

10^{10} neutrons were generated in the standard operational mode 0.7-7 Å (later, in the double-frame mode 2-14 Å) which were then collimated by a pinhole with a diameter of 40 mm. The IMAT set-up in McStas was same with the one defined in Section 4.1.3.

(a)

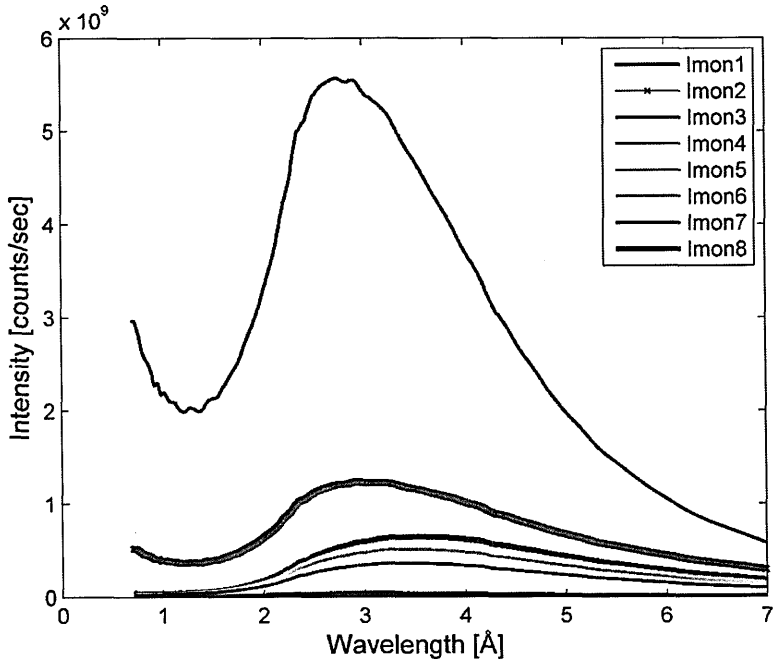

(b)

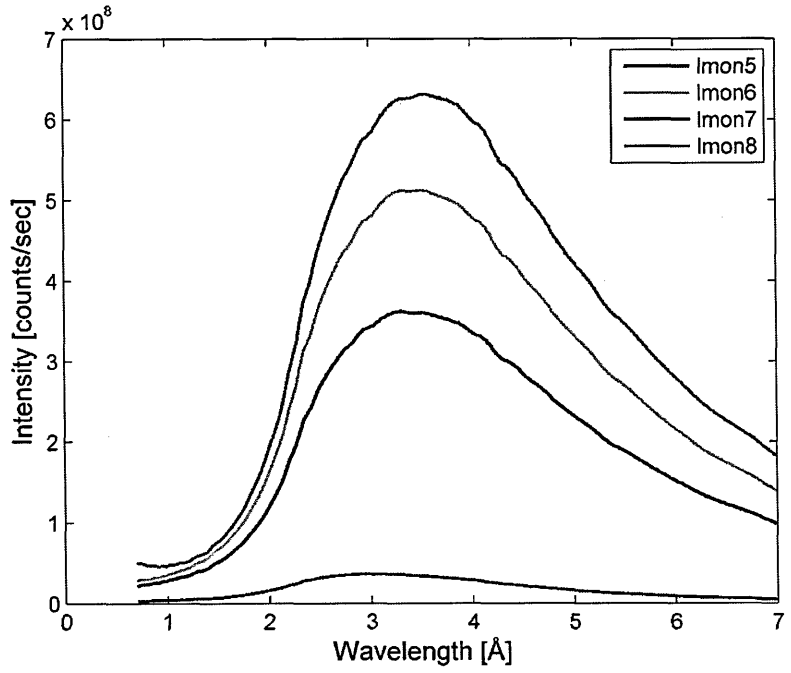

Figure 4.2.2: *The wavelength spectra along the beamline from the moderator to the sample position for the single-frame bandwidth 0.7-7 Å (a) and from the lambda monitor 5 to the lambda monitor 8 (on the sample position) (b).*

(a)

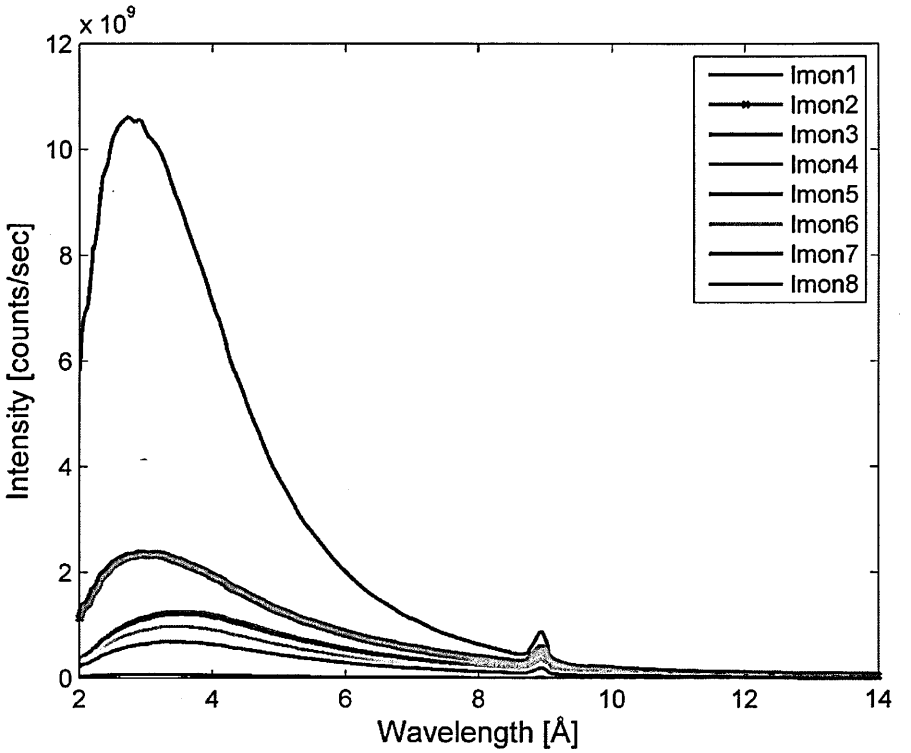

(b)

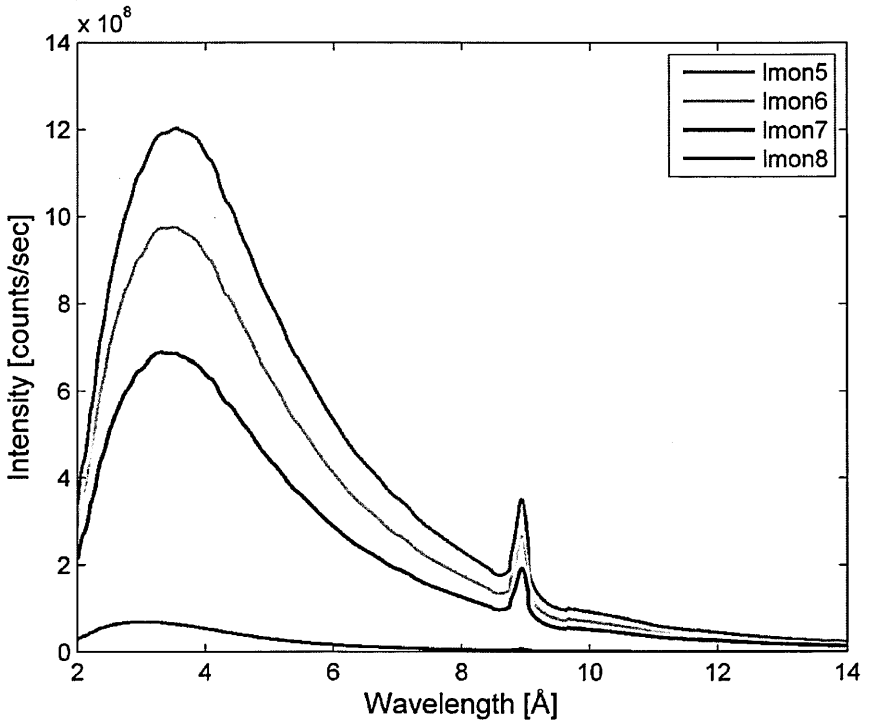

Figure 4.2.3: *The wavelength spectra along the beamline from the moderator to the sample position for the single-frame bandwidth 2-14 Å (a) and from the monitor 5 to the monitor 8 (on the sample position) (b).*

Figure 4.2.2 and Figure 4.2.3 show the distribution of the neutron intensity as a function of wavelength for the different positions along the instrument. (*Note*: Because the low visibility of the plots on Figure 4.2.2 a and Figure 4.2.3 a, two figures zooming into the monitors 5 to 8, i.e. Figure 4.2.2 b and Figure 4.2.3 b, were added). The maximum intensity of lmon1 (placed in the gap between moderator and shutter section) drops by almost 78% on the lmon2 placed after the shutter section (Figure 4.2.1). With almost the same percentage the total neutron intensity (i.e. summed over the entire PSD) drops between lmon1 and lmon2. At the moderator exit we have a mixture of shorter and longer wavelength neutrons, but in the neutron guide only the neutrons with wavelengths in the range $0 \leq \lambda \leq \lambda_{crit}$ (where λ_{crit} represents the wavelength dependant the critical angle) are travelling up to the lmon7 position. We can note that as the neutrons travel through the guide, some of them are reflected, (a part of which are transmitted through the guide walls and absorbed in the shielding) but that others proceed straight ahead passing through the guide, from moderator to guide exit, without being reflected. Increasing the flight path, the maximum neutron intensity (respectively, total neutron intensity) obviously decreases as explained above. Table 4.2.1 lists the maximum and total intensity for the different monitor positions.

Table 4.2.1: *Maximum neutron intensity and total neutron intensity on λ-monitors placed along the beamline as described in Figure 4.2.1.*

Monitor	Maximum neutron intensity (n/s)	Total neutron intensity (n/s)
Lmon1	5.57×10^{9}	2.82×10^{12}
Lmon2	1.24×10^{9}	7.15×10^{11}
Lmon3	6.59×10^{8}	3.72×10^{11}
Lmon4	6.44×10^{8}	3.62×10^{11}
Lmon5	6.32×10^{8}	3.54×10^{11}
Lmon6	5.13×10^{8}	2.84×10^{11}
Lmon7	3.62×10^{8}	2.01×10^{11}
Lmon8	3.66×10^{7}	1.77×10^{10}

A further neutron intensity drop occurs after the pinhole. The maximum neutron intensity (respectively, total neutron intensity) decreases by almost 90% compared to the intensity at the guide exit, because only a small percentage of the neutrons pass through the pinhole and there is a drop of intensity due to the 10 m flight path. In the real instrument that has a pinhole with a finite thickness further neutrons would be absorbed or reflected inside the walls of the pinhole and therefore be removed from the beam.

Based on the previous explanations, a higher proportion of longer wavelength neutrons arrive at the guide exit leading to a shift of the neutron intensity peak from 2.8 Å (after moderator) to 3.4 Å (at guide exit) (Figure 4.2.4). After passing through the pinhole we have a higher proportion of shorter wavelength neutrons and in consequence, the neutron intensity peak is moves someway back to 3 Å.

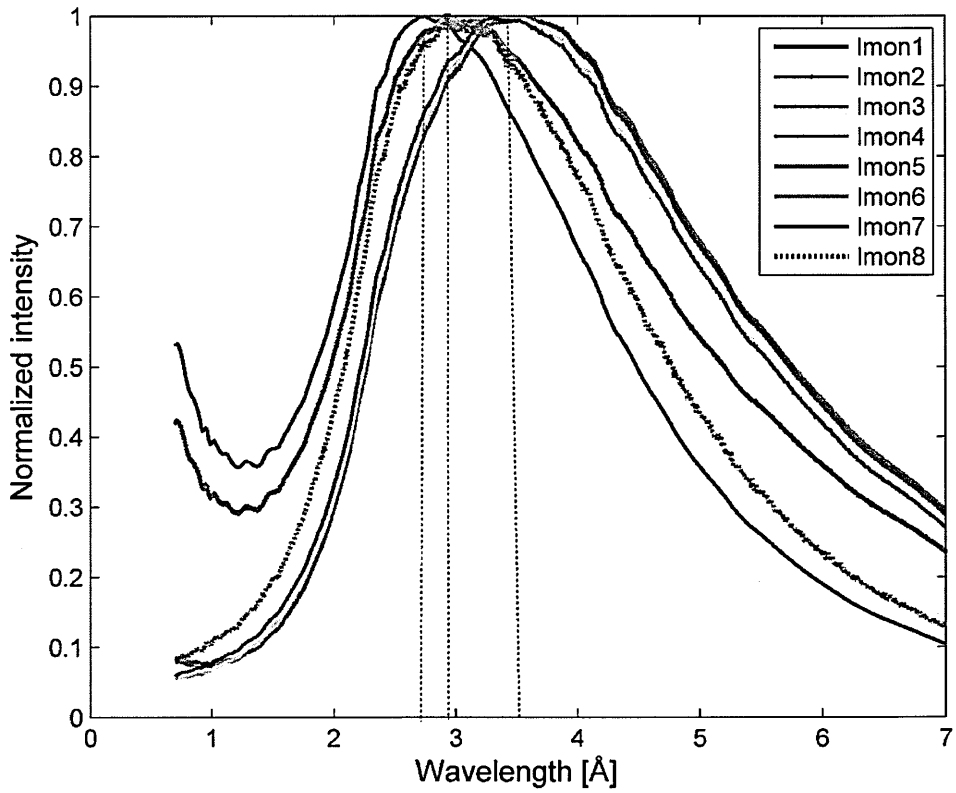

Figure 4.2.4: *The normalized neutron intensity distribution as function of wavelength for different positions of the lambda monitors in the instrument. The maximum intensity after moderator is obtained for wavelength 2.8 Å.*

The same model was applied, using same number of neutrons, for the wavelength band 2-14 Å at frequency 5 Hz (Figure 4.2.3). As for the previous case, the neutron intensity distributions, as a function of wavelength for different positions in the instrument were evaluated. The behaviour of the maximum neutron intensity (respectively, total neutron intensity) is the same with the previous from the single frame-bandwidth. Hence, the maximum neutron intensity (respectively, total neutron intensity) decreases and the maxima of the distributions shift with increasing beam flight path. The peak obtained at around 9 Å in the double-frame bandwidth distribution is an artefact of the ISIS moderator McStas module.

The results presented in Figure 4.2.2, Figure 4.2.3 and Figure 4.2.4 are important as they help us to understand the evolution of the spectra up to the point of measurement.

Another important aspect is to investigate the wavelength distribution as a function of position on the camera placed at the sample position. This study will have an impact on the characteristics of images obtained by IMAT. In particular, we note that whereas reactor based imaging instruments will have a uniform, or nearly uniform, wavelength distribution across the beam, we may expect that, due to the guide characteristics, the distribution of wavelengths at the IMAT sample position is likely to be non-uniform. This fact may have implications for experimental methods and/or data processing as applied on IMAT and so requires investigation.

In order to analyse this aspect we added six small lambda monitors of size 1×2 cm^2 positioned as function of position on the camera placed to the IMAT McStas model as indicated in Figure 4.2.5. The camera is represented in McStas IMAT instrument by the PSD monitor of size 20×20 cm^2.

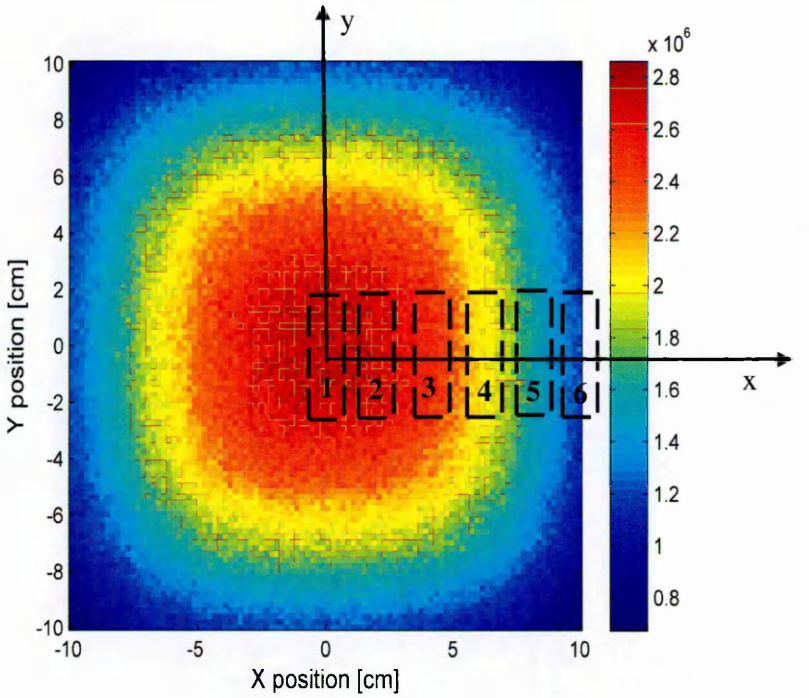

Figure 4.2.5: *Position of lambda monitors (shown against the intensity distribution for reference) as a function of position on the camera (relative to the camera centre) as follows: lmon1 at 0m, lmon2 at 0.02m, lmon3 at 0.04m, lmon4 at 0.06m, lmon5 at 0.08m and lmon6 at 0.10m.*

Lambda monitor 1 is placed in the centre of the PSD monitor followed by the other 5 monitors. The centre of last lambda monitor (6) is at 0.10 m on X-axis (i.e. on the edge of the PSD monitor). This setup was used for experiments with wavelength bands, 0.7-7 Å and 2-14 Å.

(a)

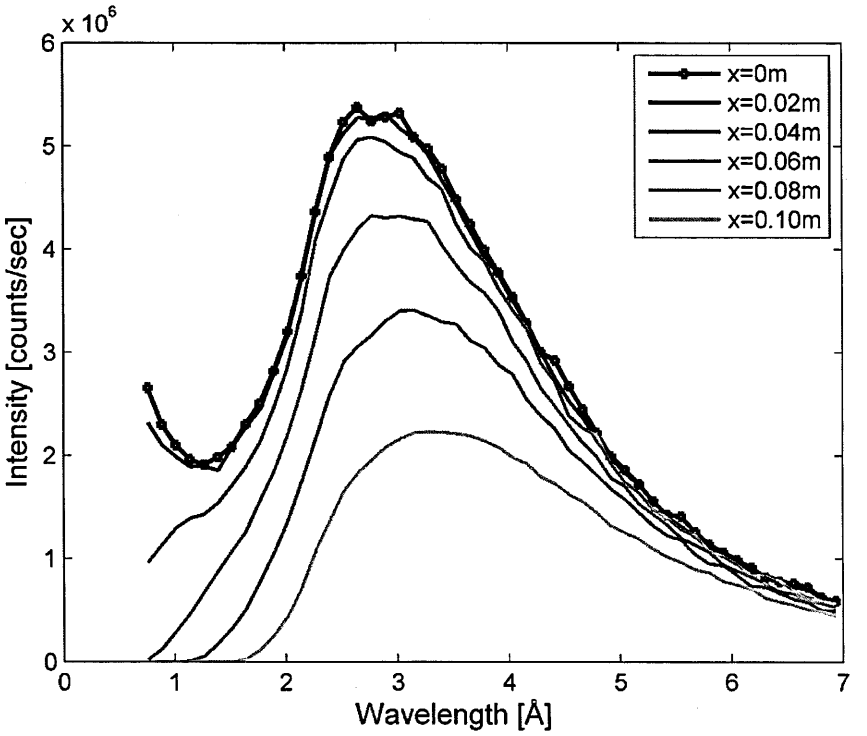

(b)

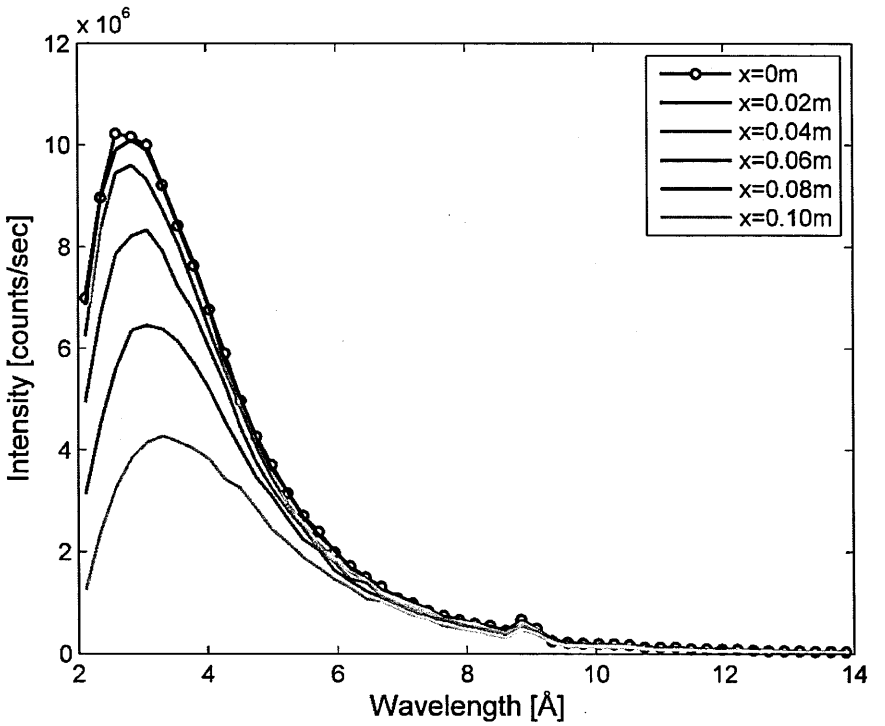

Figure 4.2.6: *The wavelength distribution as function of position on the PSD monitor placed at 10 m after the pinhole for wavelength band 0.7-7Å (a) and 2-14Å (b).*

As shown in the Figure 4.2.6 the neutron intensity decreases as we move away from the centre of the beam along the X-axis position. The decrease is observed from the centre of the monitor corresponding to the higher energy neutrons, i.e. shorter wavelengths, towards the edge of the PSD monitor, i.e. lmon6. The wavelength spectrum shape on the monitors placed in the centre (x=0) or in the immediate vicinity (x=0.02 m) is similar with the one obtained on the monitor placed after the moderator (lmon1 from Figure 4.2.2) because the centre of the PSD 'sees' both shorter and longer neutron wavelengths. Considering short wavelength neutrons which are passing straight through the guide there is a higher proportion centred in the middle of the PSD monitor. Moving along the X-axis of the monitor the short wavelength fraction drops off, and the long wavelength neutrons contribute even more to the spectrum. The maximum of the spectrum shifts to higher wavelengths as we move to the edge of the monitor.

4.2.2 Beam profiles: from pinhole to beam stop

Once neutrons are collimated by the pinhole, the beam is adjusted by the jaws and, after having passed through the sample and detector, is finally stopped by a "beam stop". The role of the beam stop is to block the "unattenuated" portion of the beam, including the high energy neutrons and gamma radiation which have not been removed by the T0 chopper. At the same time, the beamstop ensures that no unwanted neutrons and gamma radiation (generated in the beam tube) can reach the detectors.

In order to investigate the beam tube design, from the pinhole to the sample position, and the size of the beam stop, the beam profiles along the flight path, from the pinhole to the beamstop were analysed. For this study the IMAT instrument components in McStas were set up as in the Section 4.1.3, eliminating the jaws and placing PSD monitors on the jaws positions, i.e. at 1.5 m, 3 m, 4.5 m, 6 m and 7 m, plus the sample positions (one at 5 m after pinhole and the other at 10 m after pinhole), and at 12.5 m, and the exit of the

beamstop at 15 m from the pinhole. The PSD monitors used were larger with 80×80 cm^2 (and 100×100 pixels) to ensure the full beam was captured. 10^{10} neutrons were generated in both wavelength bands: 0.7-7 Å and 2-14 Å.

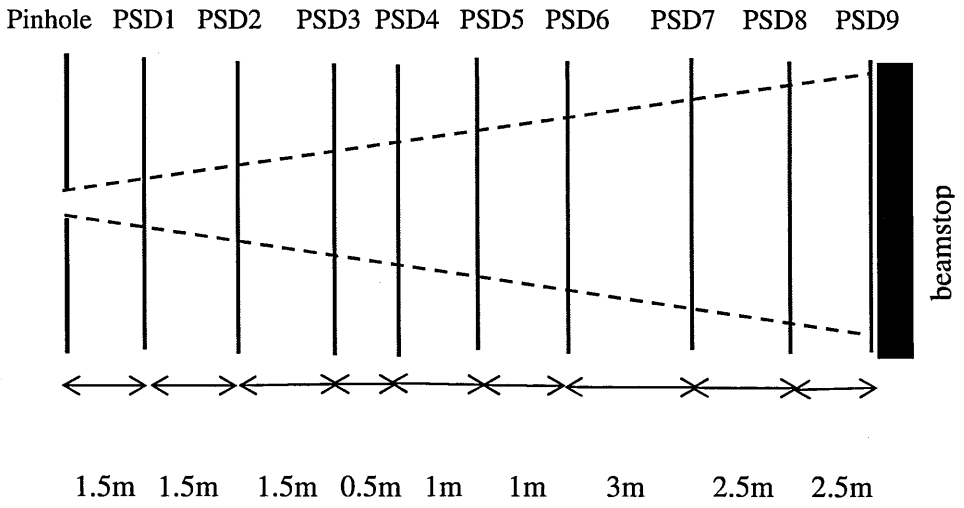

Figure 4.2.7: *Positions of the PSD monitors (with 80×80 cm^2 size) along the beam flight path from the pinhole to the beamstop.*

The simulations were performed using two pinhole sizes: 20 mm and 80 mm diameter. The total neutron flux is the same for all positions because the larger monitors used captured the entire neutron beam. However, the maximum neutron flux decreases because the neutrons are increasingly spreading out on each monitor as the flight path increases (Figure 4.2.8, Figure 4.2.9). Specifically, the position at 5 m from the pinhole has a high maximum neutron flux. This position, i.e. at 5 m, will be considered as an additional position for high intensity imaging experiments. The FWHM values are calculated according the later description from Figure 4.2.11.

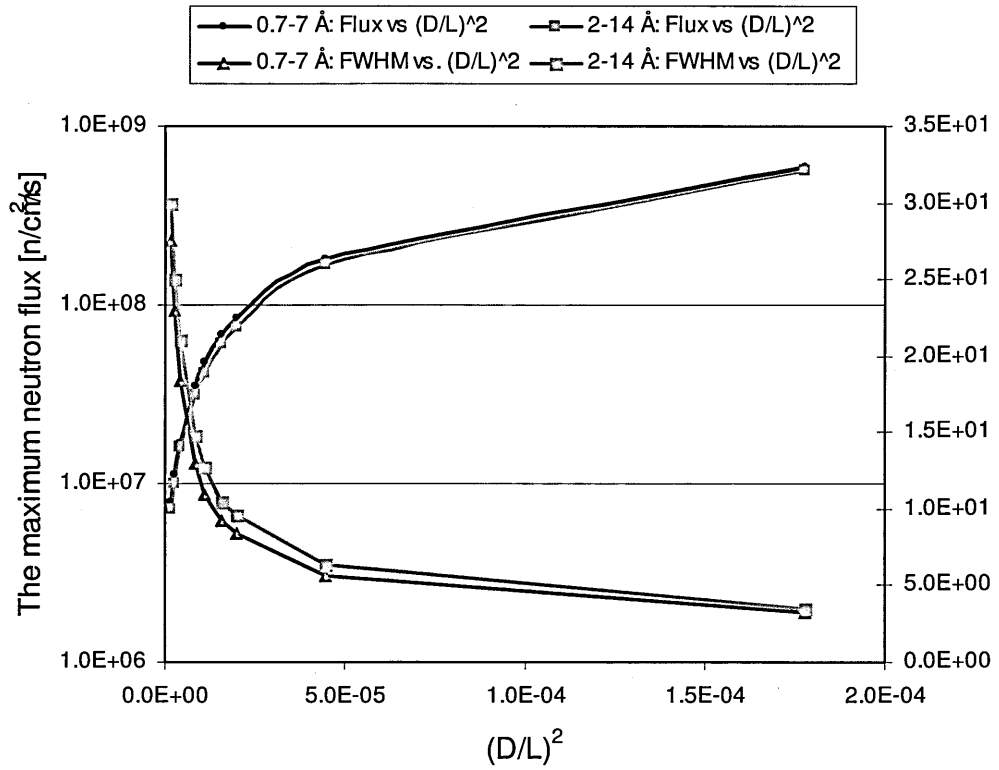

Figure 4.2.8: *The maximum neutron flux and FWHM as a function of* $(D/L)^2$ *calculated for the pinhole D= 0.02m. The flux is plotted in logarithmic scale.*

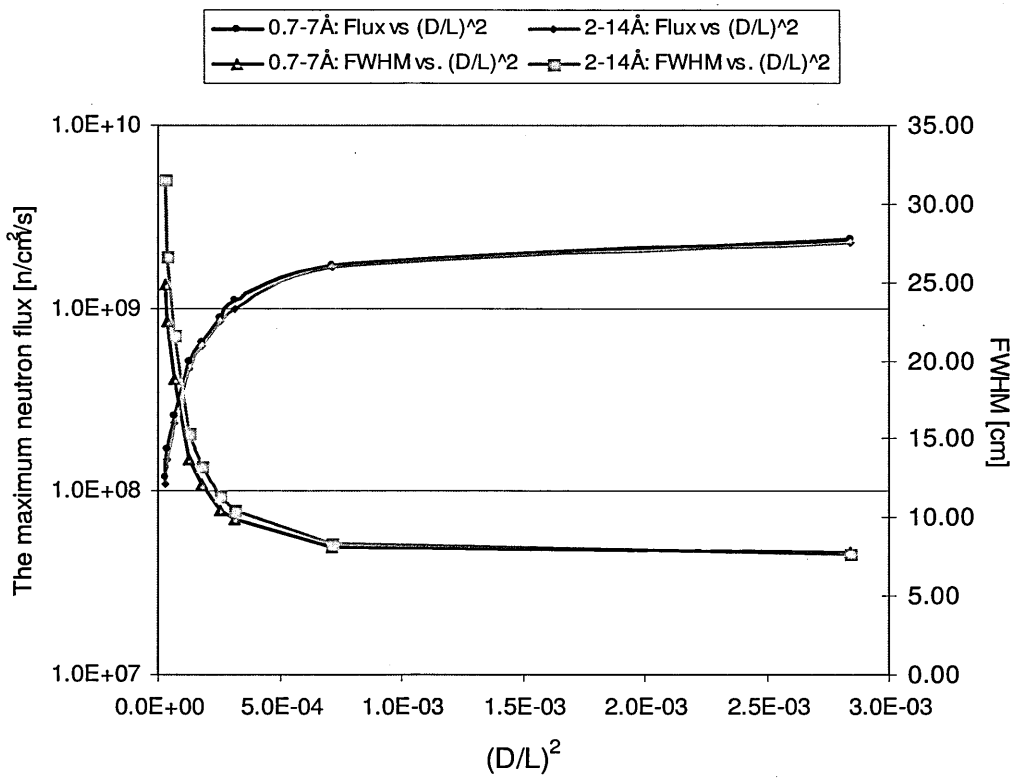

Figure 4.2.9: *The maximum neutron flux and FWHM as a function of* $(D/L)^2$ *calculated for the pinhole D= 0.08m. The flux is plotted in logarithmic scale.*

The maximum neutron flux plotted in Figure 4.2.8 and Figure 4.2.9 (for each position of the monitor) was calculated by dividing the maximum neutron intensity by the corresponding pixel size (80×80 μm^2).

The beam size at the detector position is defined by divergent beam and the distance L. As the pinhole aperture and distance between pinhole and sample define the spatial resolution of the instrument, so a small aperture diameter D combined with a long distance L enables a high spatial resolution. Hence, the ratio L/D should be as big as possible and the sample needs to be positioned as close as possible to the detector such that the image of the sample projected onto the detector could be considered to be created by a parallel-beam perpendicular onto the detector. For an imaging instrument with a neutron guide where no additional pinhole is used, the beam divergence at the end of the straight neutron guide and at the sample position is defined by the angle θ_c (Section 3.4.1) of total reflection of neutrons from the interior walls of the neutron guide. Moreover, the divergence is constant within the cross section of the guide. In that case the critical angle θ_c is proportional to the neutron wavelength and for the IMAT coated supermirror guide we have $\theta_c = 0.1^\circ \times \lambda \times m$ [61, 81]. Hence, if no pinhole is used the beam divergence depends on the wavelength and an effective L/D ratio determines the quality of the projection. The IMAT spectrum at the end of the neutron guide is already known (see section 4.2.1), so L/D ratio (or the effective divergence) could be estimated from the wavelength at flux maximum (in our case, 3 Å) in the centre of the detector through the formula, $L/D = 1/\tan(2\theta_c)$ yielding to a L/D=32 for 3 Å and m=3.

In fact the IMAT imaging instrument has a pinhole placed after the guide and the non-zero divergence is given by the source extended, i.e. non-zero pinhole, as it is detailed in Section 4.2.3 of this thesis.

On the other hand, the maximum neutron flux is proportional with $(D/L)^2$ ratio (Figure 4.2.8 and Figure 4.2.9). To obtain a high signal to noise ratio in the projection a

high neutron flux is required for each measurement. Therefore, the setup of the neutron radiography experiments is often a compromise between high spatial resolution and a high signal to noise ratio. From the figures we can conclude that the positioning of the monitor on a long flight path such as 15 m from the pinhole resulted in a reduction of the maximum neutron flux by almost 88% than that of the flight path of at 5 m and a reduction of the maximum neutron flux by almost 54% than of the flight path of at 10 m.

The beam profile data for all positions have been obtained selecting a horizontal central line through the PSD intensity distribution (Figure 4.2.10). Due to the symmetry of the guide and pinhole geometry, and in the absence of gravity, the beam profiles obtained selecting horizontal or vertical lines across the monitor are same.

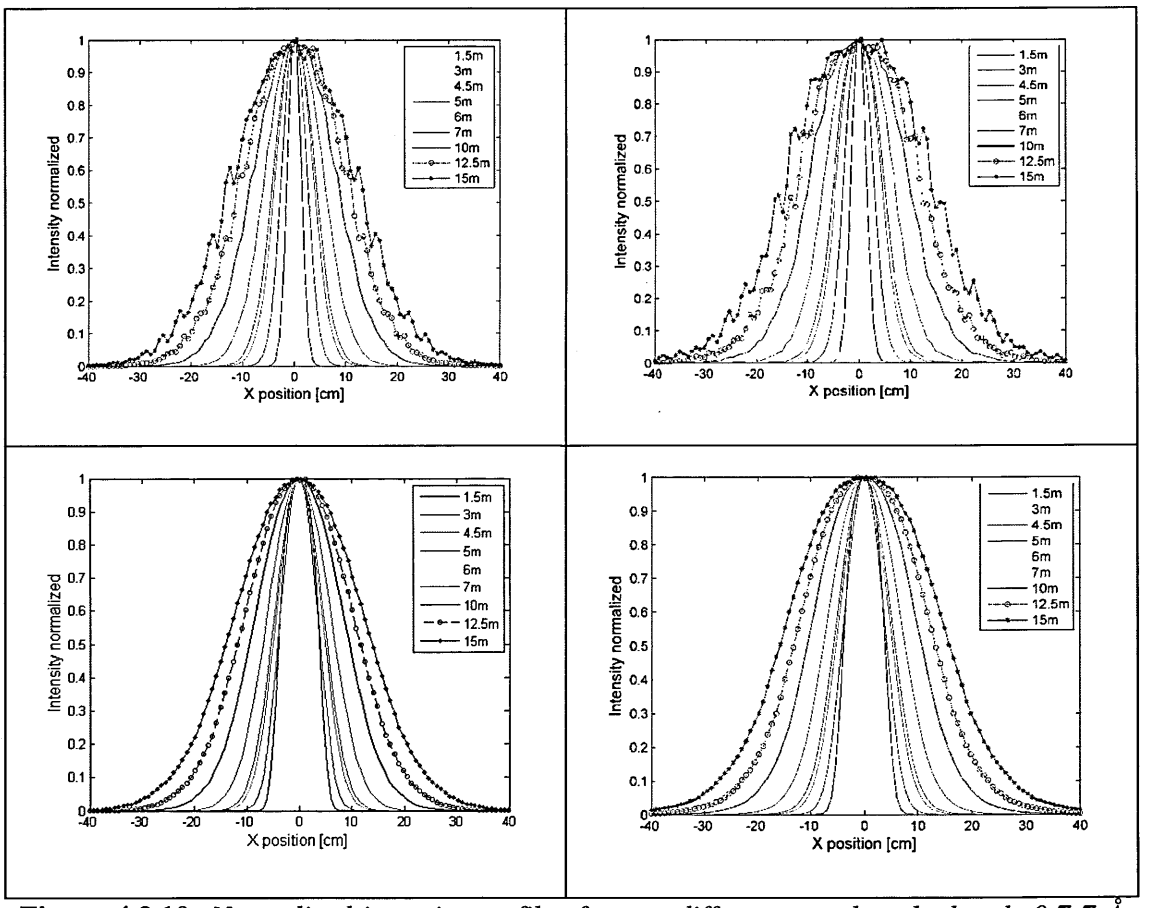

Figure 4.2.10: *Normalized intensity profiles for two different wavelengths bands 0.7-7 Å (left column) and 2-14 Å (right column) using a pinhole radius 0.01 m (first row) and pinhole radius 0.04 m (second row).*

The beam profiles represented in Figure 4.2.10 can be approximated by a Gaussian distribution (Figure 4.2.11). The neutron intensity distribution remains Gaussian at every point in the flight path from the pinhole to the beamstop due to the guide and the circular pinhole. An ideal profile shape of the neutron beam would be a flat plateau.

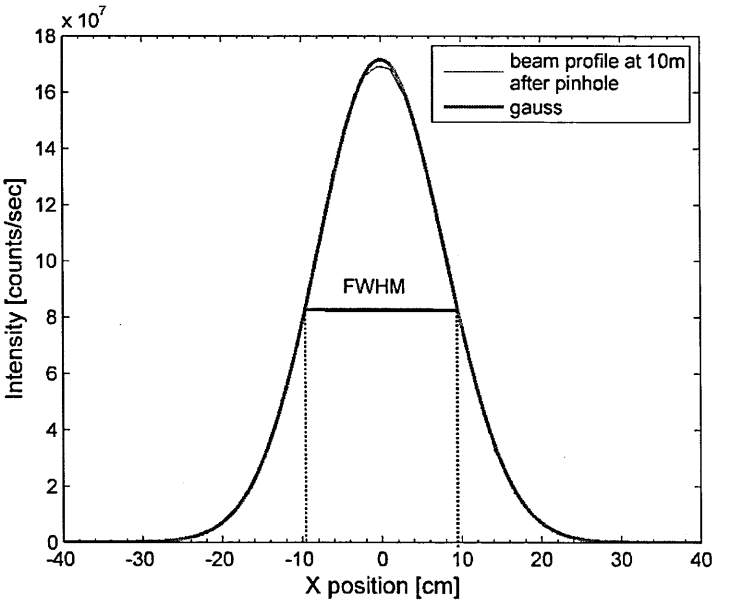

Figure 4.2.11: *The circular pinhole of diameter is 0.08 m produced a neutron beam with an approximated Gaussian profile. The FWHM is calculated for each beam profile.*

The width of the neutron beam is measured calculating the Full-Width at Half Maximum (FWHM) and represents a measure of the beam diameters at the detector position (Figure 4.2.8, Figure 4.2.9). The sample position 10 m has the advantage of a large viewable area with FWHM almost 20 cm confirming the camera field-of-view of 20×20 cm^2. On the other hand, the beam tube could be designed as a tapered tube with entrance size next to the pinhole smaller than the exit size. A large imaging size of 30×30 cm^2 will be allowed at the beamstop entrance.

4.2.3 Beam divergence at sample position

The image quality of the neutron radiography depends on, among other things, the beam divergence, i.e. a greater divergence implies a greater blurring, as already mentioned in paragraph 2.3.2. Divergence causes blurring because in a divergent neutron beam neutrons travelling in a range of different directions can all pass through the same point in a sample, causing this point to be projected as an area of finite size on the camera. The key quantity of divergence is the angular range of neutron paths that can pass through a particular point. The divergence of a beam at a point is defined as the maximum angle formed between neutrons trajectories passing through that point (Figure 4.2.12).

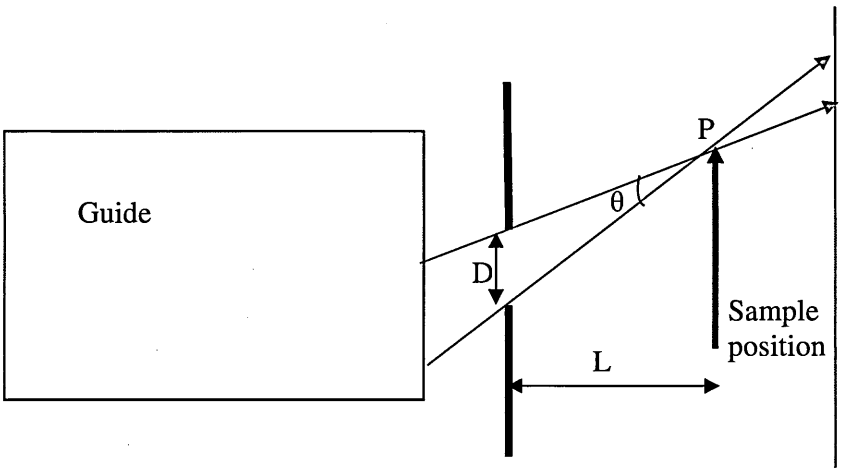

Figure 4.2.12: *In a divergent beam neutrons travelling in a range of directions can all pass through a single point 'P' in an object. The angular range is characterised by the angle θ, and is determined by two quantities, the diameter of the pinhole 'D' and the distance, L, between the pinhole and the point 'P'.*

In the case where we have an infinitely small pinhole, the neutrons travelling in one direction can pass through the point 'P' obtaining an infinitely sharp (though unfortunately infinitely faint) image. In that case the divergence is zero and hence there is no blurring of the image.

Considering the case where we have a beam with a range of neutron energies and an infinitely small pinhole we get a situation like that shown in Figure 4.2.13. Within the guide we have neutrons with lower energy (green) and neutrons with higher energy (red). The neutrons are travelling with trajectories that form an angle α with the guide horizontal axis, in the range $0 \leq \alpha \leq \theta_{crit}(\lambda)$, where $\theta_{crit}(\lambda)$ represents the critical angle which depends on the material of the neutron guide and the neutron wavelength. Using the previous definition of divergence we can say that *within the guide* the neutron beam shown in Figure 4.2.13 has a divergence and that the maximum angle formed between neutrons passing through a single point is $2\theta_{crit}(\lambda)$ where $\theta_{crit}(\lambda)$ is that associated with the lower energy neutron (green) neutrons (as this is the maximum $\theta_{crit}(\lambda)$). Once the beam has passed through the infinitely small pinhole however, although the beam is spreading out, the divergence is zero. The beam has zero divergence after the pinhole because only one neutron trajectory passes through every point. The beam however spreads at an angle determined by the trajectories within the guide, which is in turn defined by $\theta_{crit}(\lambda)$ for each wavelength. Hence we get the lambda dependant distribution on the PSD monitor.

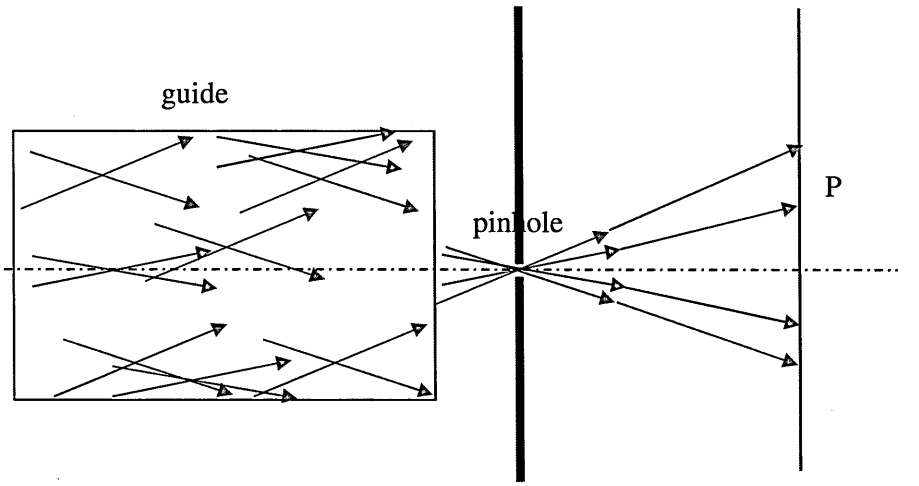

Figure 4.2.13: *Infinitely small pinhole situation. Range of neutron energies is represented: lower energy (green) and higher energy (red) and energy dependant divergence within guide. After pinhole the beam spreads, but has zero divergence.*

If the pinhole is open, as shown in Figure 4.2.14, the divergence beyond the pinhole is as well as within the guide.

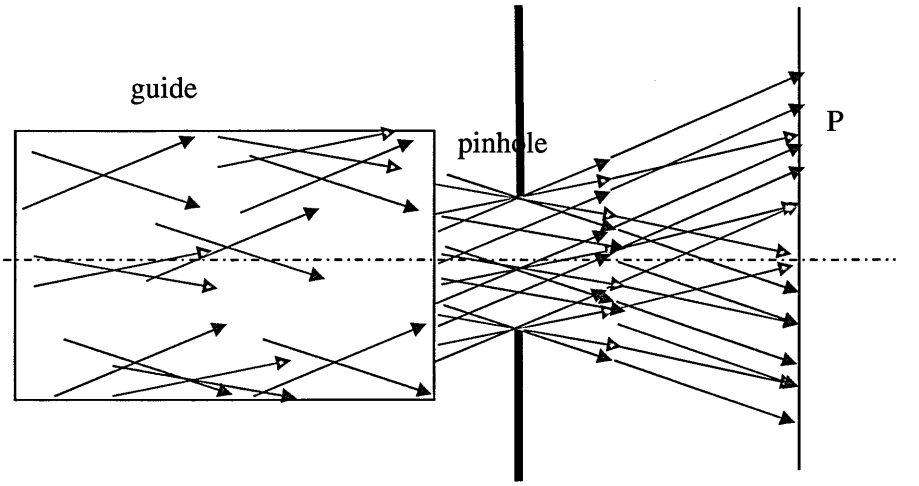

Figure 4.2.14: *Finite size pinhole situation. The beam beyond the pinhole is now divergent.*

All above discussions of the divergence are in accordance with the definition based on the L/D ratio. A small pinhole (infinite L/D) ratio is the ideal case.

The standard divergence/wavelength monitor from McStas calculates the divergence as the angle between neutron trajectory and the horizontal axis and hence is only appropriate for monitors placed on the beam axis and it was, in fact, designed for calculating divergence of 'parallel' beams for diffraction. In order to calculate the correct divergence for IMAT in imaging mode, the divergence/wavelength monitor from McStas required slight modification. Thus, we need to subtract the angle formed between the line from the centre of the monitor and the centre of the pinhole (dashed red line) and the neutron trajectory (full red line), i.e. the bisector angle $\beta -$ shown on the figure below.

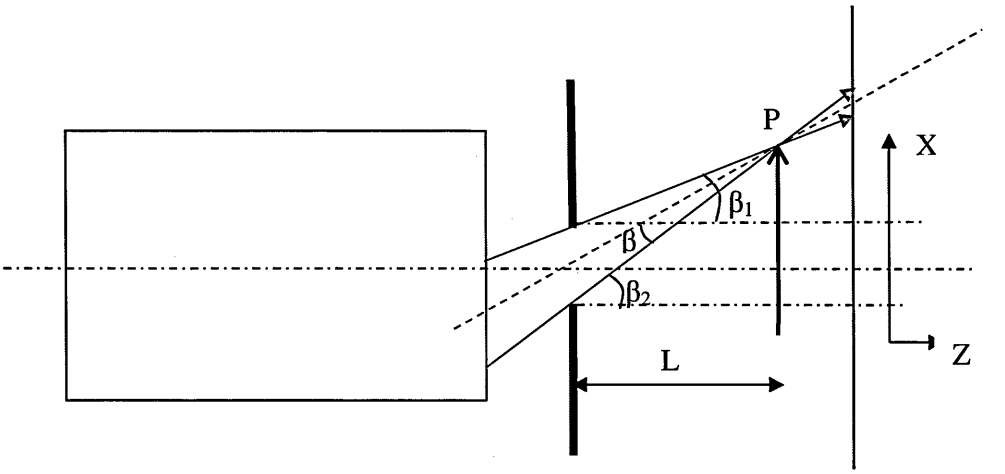

Figure 4.2.15: *McStas calculates the angle between the neutron trajectory and the axis of the guide (black dashed line on figures), i.e. β_1 and β_2. The correct divergence calculated for IMAT-imaging mode in McStas is represented by the angle β formed between the line from the centre of the monitor and the centre of the pinhole (dashed red line) and the neutron trajectory (full red line).*

It was of interest to calculate the divergence on the sample position as a function of position on the monitor in two cases: theoretical, calculated using the divergence formula (4.2.1) and measured, following McStas modelling.

The theoretical maximal divergence of a neutron going through the pinhole and arriving onto the different positions on the monitor placed at 10 m after the pinhole could be easily calculated by use of Figure 4.2.16, but independent of the wavelength.

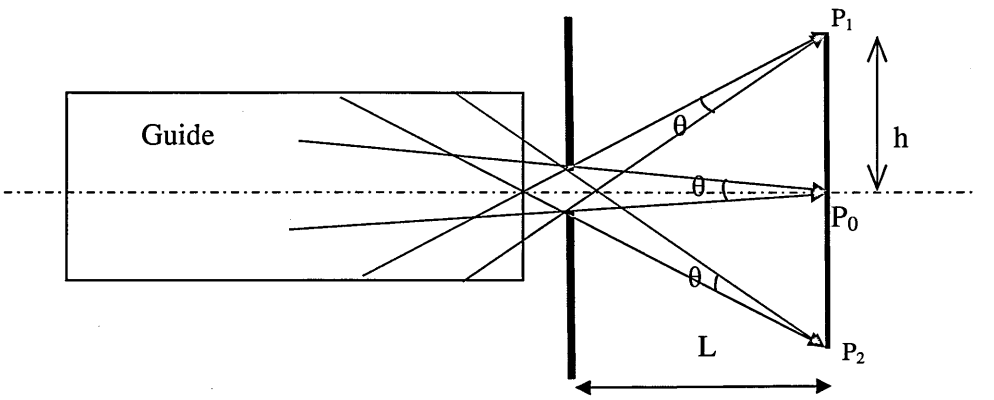

Figure 4.2.16: *Theoretical calculations of the maximal divergence as a function of position on the camera (placed on the sample position). P_1, P_0 and P_2 are different positions on the camera, which, in this instance is placed at the sample position.*

Considering a pinhole with radius R (say 0.02 m), the monitor placed beyond the pinhole at L=10 m and the position on the monitor, h, where the neutron is arriving (in our case, 0.0, 0.02, 0.04, 0.06, 0.08 and 0.10 m) we can calculate the divergence on these positions on the monitor based on the formula:

$$\theta = \text{atan}\frac{2RL}{h^2 + L^2 - R^2} \tag{4.2.1}$$

For each position the divergence angle varies very slightly and has the approximative value 0.23°. Equation (4.2.1) could be approximated through the general equation of the divergence, i.e. $\theta = \text{atan}\frac{D}{L}$ independent of the neutron position on the monitor. These theoretical results could be compared with the output from the modified divergence/wavelength monitor from McStas as described below.

The divergence/wavelength monitor code from McStas was modified to calculate the β angle (where $\theta = 2\beta$) following the description from Figure 4.2.15. Then, divergence/wavelength monitors were set-up at different points along X-axis. These monitors should be as small as possible (as the ideal was to measure divergence at a point) but they need to be big enough to obtain reasonable statistics in each one. Hence, they had

50 channels distributed over their sizes, 1×2 cm^2, and they had been positioned as smaller lambda monitors from Figure 4.2.5. The set-up IMAT imaging instrument in McStas was same as the one defined in paragraph 4.1.3. The pinhole radius was considered 0.02 m and 10^{10} neutrons were generated in the both wavelength bands.

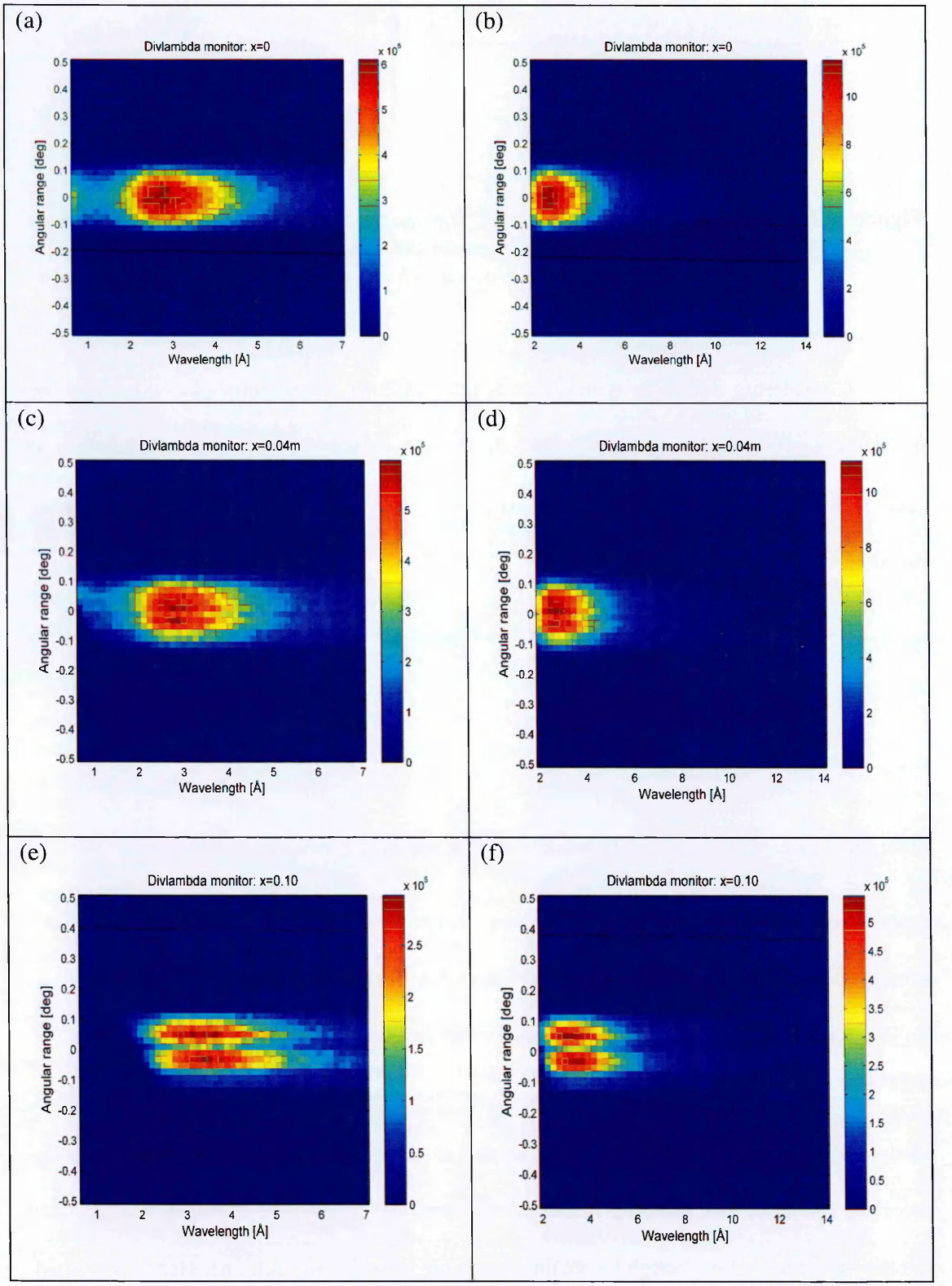

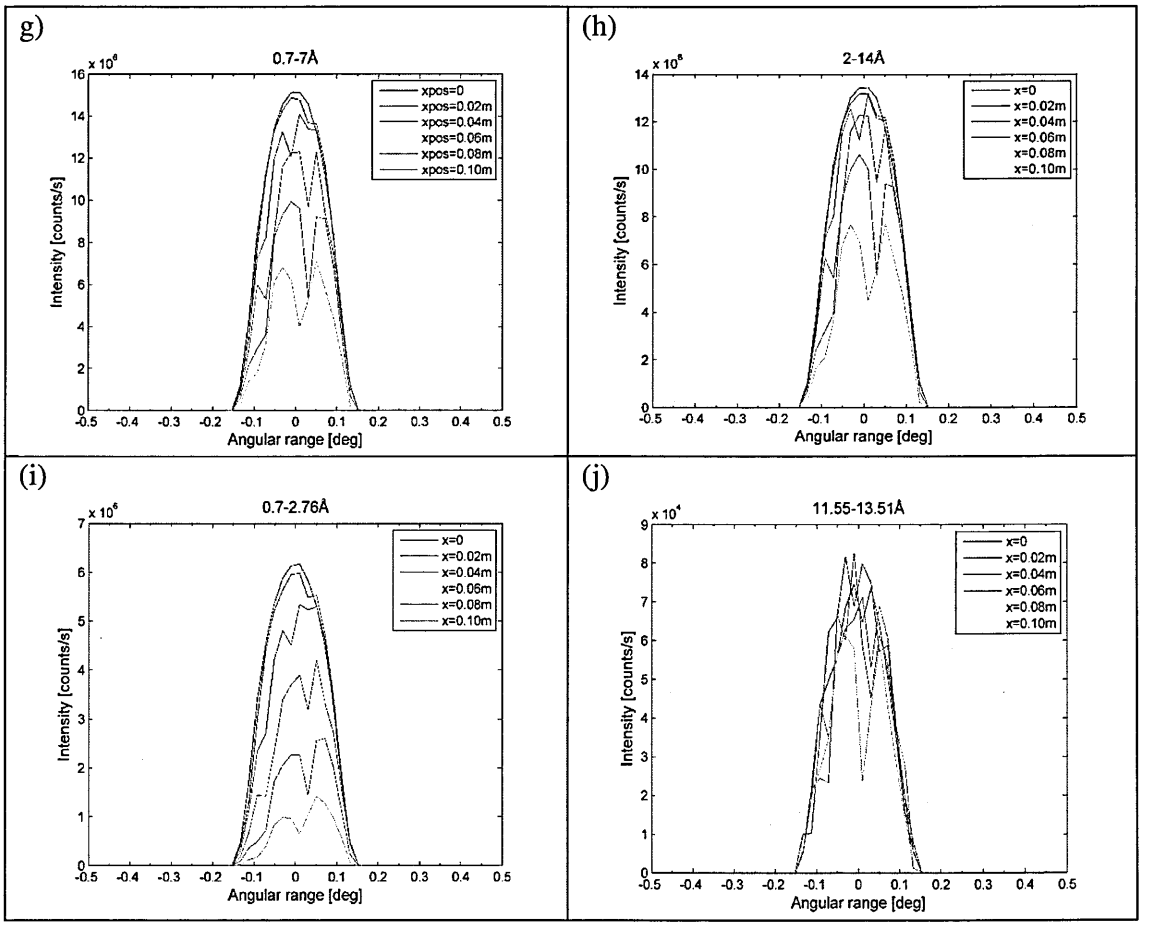

Figure 4.2.17: *Neutron intensity distribution as function of both divergence and wavelength for position x=0 (a, b), x=0.04 m (c, d) and x=0.10 m (e, f). In white beam experiments the maximum divergence will be 0.28° in both frame bandwidths (0.7-7 Å and 2-14 Å) (g, h). For a short wavelength band the beam divergence is same for all monitors positions while the neutron intensity drops off with almost 70% from the centre camera to its edge (i); Same angular distribution is obtained for a long wavelength band (j).*

Each divergence/wavelength monitor output is a distribution of neutron intensity as a function of both divergence and wavelength (Figure 4.2.17 a, b, c, d, e, f). Summing all columns from the monitor output (0.7-7 Å or 2-14 Å) as shown in Figure 4.2.17 g, h we can retrieve useful information about the divergence on different positions on camera, appropriate to white-beam experiments with IMAT. The angular range could be approximate from -0.14° to 0.14° for all positions of the divergence/wavelength monitor. Selecting one short wavelength band (Figure 4.2.17 i) and one long wavelength band (Figure 4.2.17 j) and repeating the previous procedure (with summing columns from the

monitor output for correspondent wavelength band) one should remark that the angular distribution is same, so the maximum beam divergence in energy selective measurements will be almost 0.28°. All intensity plots show noise mainly due to the low counting statistics plus larger dips which correspond to the previously observed artefacts caused by the instrument gaps. We need to mention that the maximal divergence values are read of the graphs by eye, so they are not very precise and for this reason they are compared with the calculated values.

4.2.4 Neutron intensity distribution and neutron flux at the sample position for different pinholes and wavelength bands 0.7-7Å and 2-14 Å

In general neutron imaging applications require a large beam (of the order of few cm^2) and benefit from the highest possible neutron flux. Hence, IMAT in the imaging mode will use a wide neutron beam emanating from a pinhole to study extended objects in a single acquisition or in a scanning mode with a detector screen of 20×20 cm^2.

In order to calculate the neutron flux at the sample position and study the white-beam intensity distributions on the imaging screen for different pinhole sizes with diameters of 0.005 m, 0.01 m, 0.02 m, 0.04 m and 0.08 m, a number of McStas simulations using "open beam" (no sample) and 10^{10} neutrons were performed based on the final IMAT design (with PSD monitor placed on the sample position) as described in section 4.1.3. For each pinhole the corresponding jaws opening was calculated. Figure 4.2.18 below shows that with the decreasing of pinhole size the intensity distributions on the imaging screen are more inhomogeneous, exhibiting geometric patterns. As it was demonstrated in paragraph 3.5.2, the main cause of the geometric artefacts is that there are regions of the detector which look at points on the guide or moderator system from which no neutrons emanate, such as chopper gaps or regions outside of the moderator.

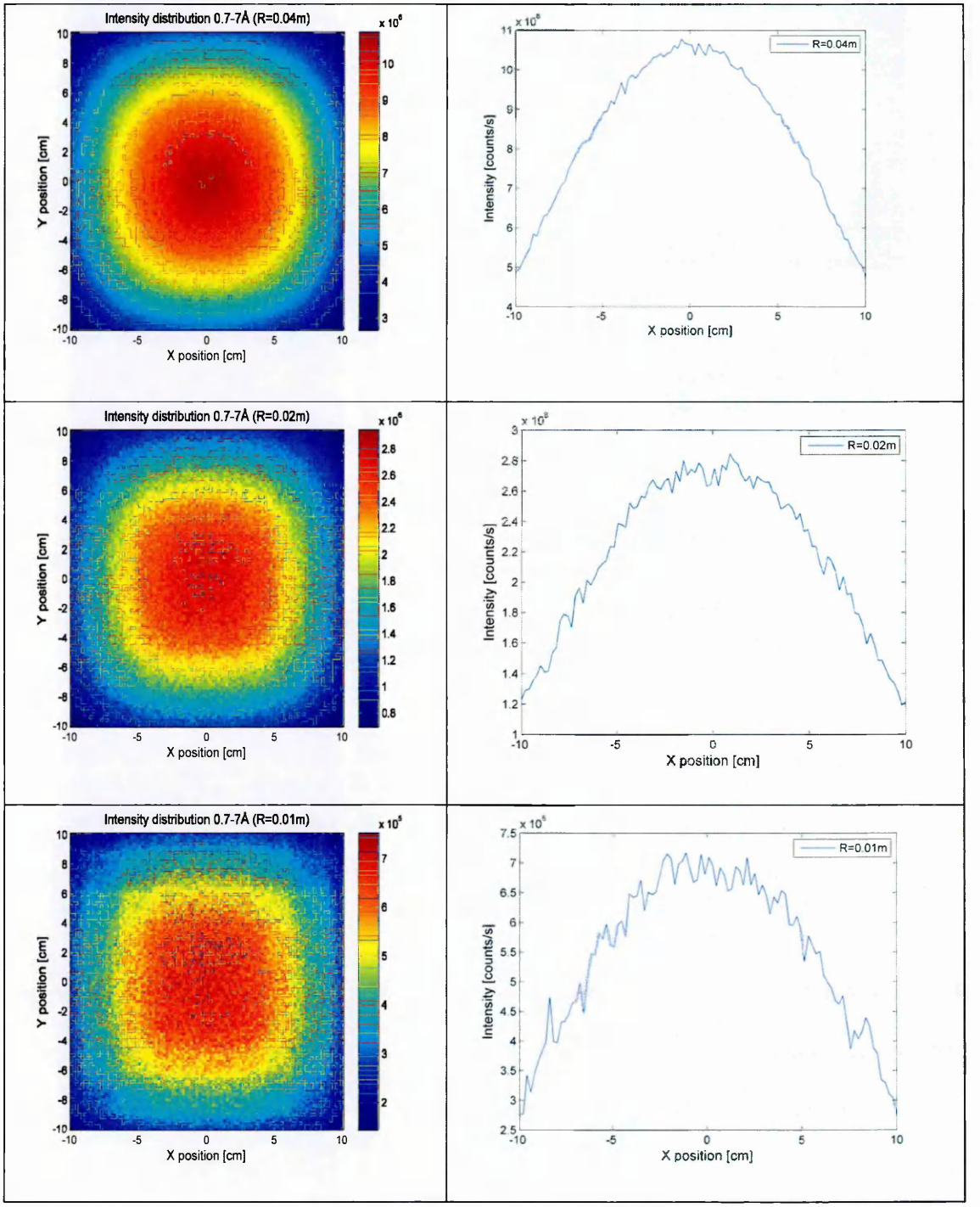
Intensity distribution 0.7-7Å (R=0.04m)
x 10^6
Y position [cm]
X position [cm]
x 10^6
R=0.04m
Intensity [counts/s]
X position [cm]
Intensity distribution 0.7-7Å (R=0.02m)
x 10^6
Y position [cm]
X position [cm]
x 10^5
R=0.02m
Intensity [counts/s]
X position [cm]
Intensity distribution 0.7-7Å (R=0.01m)
x 10^5
Y position [cm]
X position [cm]
x 10^5
R=0.01m
Intensity [counts/s]
X position [cm]

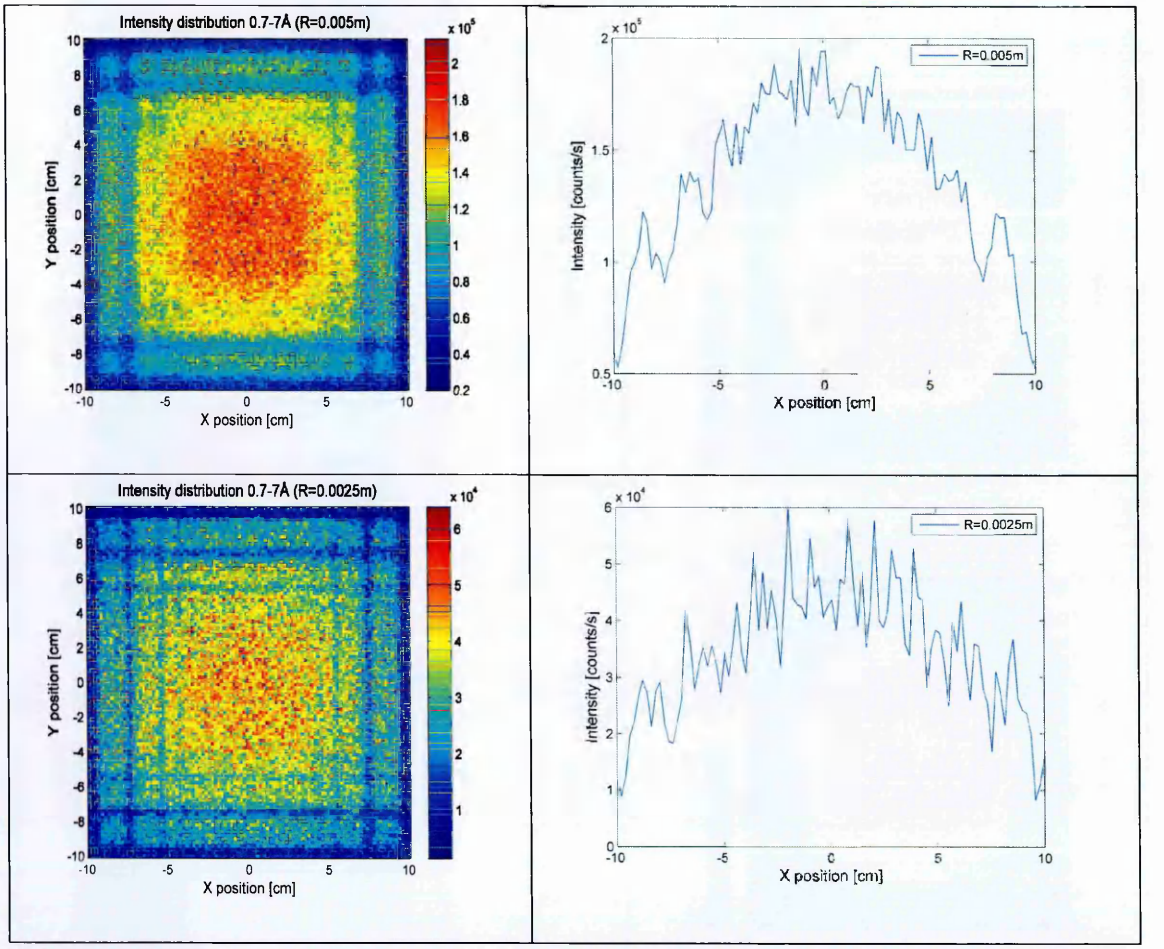

Figure 4.2.18: *Intensity distributions on the imaging detector for five different pinholes with diameter of 80, 40, 20, 10 and 5mm (left column). The coloured maps show the neutron intensity as a function of horizontal and vertical position on a 20×20cm^2 monitor screen. For each image, the horizontal intensity profile through the centre of the screen (y=0 mm) is displayed in the right column.*

For the lower L/D (larger pinhole) these stripes are present but are washed-out because by the increased pinhole size allows a range of neutron trajectories to reach each point on the detector (similar to the divergence argument), some of which will arrive from proper reflecting parts of the guide; this will tend to decrease the depth of the artefact, i.e. it will wash it out. Hence, the number of artefacts is higher for a small pinhole and with increasing the pinhole diameter the artefacts depths decrease (Figure 4.2.18). For a better visualization of the artifacts the profiles plots of the monitors were considered, by selecting one horizontal line through the centre of the monitor and plotting it as neutron intensity function depending on the monitor horizontal position parameter. The neutron intensity

distribution on the PSD monitor is symmetrical, so may equivalently plot horizontal or vertical sections through the monitor.

The widths of the stripes are of the order of several millimetres (e.g. 10 mm) and the intensity drop between the area without stripe and one stripe, i.e. the artefact depth, can be of the order of 20% for a pinhole size of 20 mm diameter.

From each PSD monitor output we can extract useful values such as total neutron intensity and maximum neutron intensity. Knowing that 100×100 pixels are distributed on the PSD monitor with size 20×20 cm^2, the total neutron flux (neutrons/cm^2/seconds) was determined by dividing the total neutron intensity to the monitor size area and moreover, the maximum neutron flux was acquired after dividing the maximum neutron intensity to the pixel size (where 1pixel has the dimension 0.2×0.2 cm^2).

Converting the neutron intensity for each pixel into the neutron flux and then plotting the average of the neutron flux from all rows as a function of the horizontal monitor position one could investigate where the neutron flux drops off below 50%.

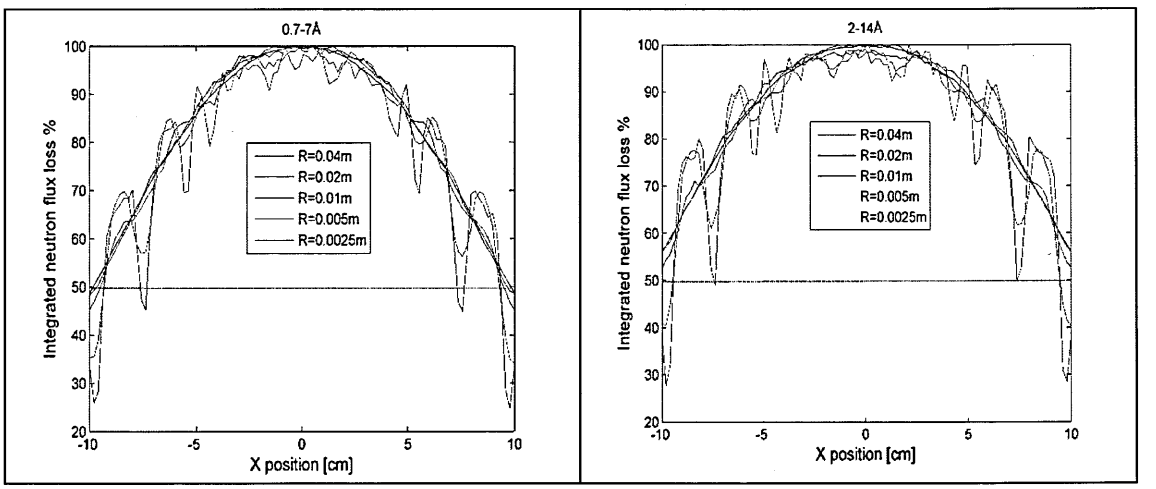

Figure 4.2.19: *Integrated neutron flux over the PSD monitor. The neutron flux drops off below 50% for all pinholes in the single-frame bandwidth (left image) and for pinhole radius 0.0025m and 0.005m in the double-frame bandwidth (right image).*

Figure 4.2.19 shows the integrated neutron flux loss along the monitor position. One should remark that while, in the single-frame bandwidth, there is a drop-off below 50% of the neutron flux for all pinholes, for double-frame bandwidth 2-14 Å there is a drop-off down 50% only for the smallest simulated pinhole (R=0.0025 m and R=0.005 m) corresponding to the monitor position at ±9.3 cm. In Table 4.2.2 the total neutron flux, the maximum neutron flux for each pinhole and the selected wavelength bands, also the calculated FWHM of the neutron intensity distribution profiles are displayed.

Table 4.2.2: *Results obtained for different pinholes and the used wavelength bands*

Wavelength band (Å)	Pinhole size-diameter (m)	L/D	FWHM (cm)	Total neutron flux ($n/cm^2/s$)	Maximum neutron flux ($n/cm^2/s$)	Divergence (°)
0.7-7	0.005	2000	18.6	6.92×10^5	1.52×10^6	0.0286
	0.01	1000	18.6	2.78×10^6	5.14×10^6	0.0573
	0.02	500	18.8	1.12×10^7	1.94×10^7	0.1146
	0.04	250	19.15	4.44×10^7	7.15×10^7	0.2292
	0.08	125	19.7	1.72×10^8	2.69×10^8	0.4584
2-14	0.005	2000	18.9	6.88×10^5	1.50×10^6	0.0286
	0.01	1000	18.9	2.77×10^6	4.63×10^6	0.0573
	0.02	500	>20	1.12×10^7	1.66×10^7	0.1146
	0.04	250	>20	4.44×10^7	6.43×10^7	0.2292
	0.08	125	>20	1.72×10^8	2.43×10^8	0.4584

Figure 4.2.20 and Figure 4.2.21 outline the maximum neutron flux, respectively variation of the integrated neutron flux, depending on the pinhole diameter.

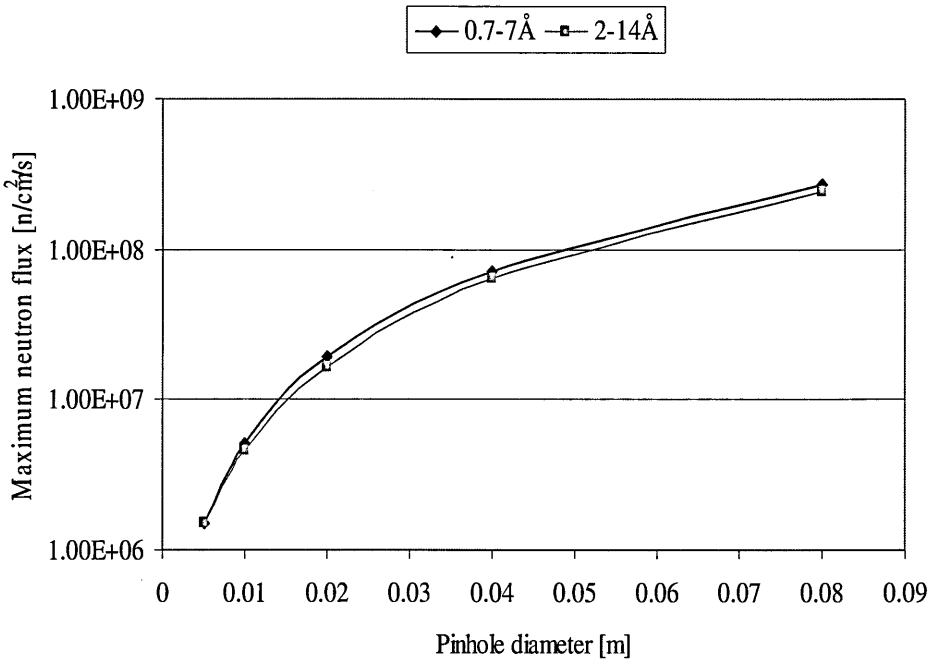

Figure 4.2.20: *Maximum neutron flux calculated on the PSD monitor placed on the sample position for different pinholes (0.005 m, 0.01 m, 0.02 m, 0.04 m and 0.08 m. The maximum flux is plotted in log scale.*

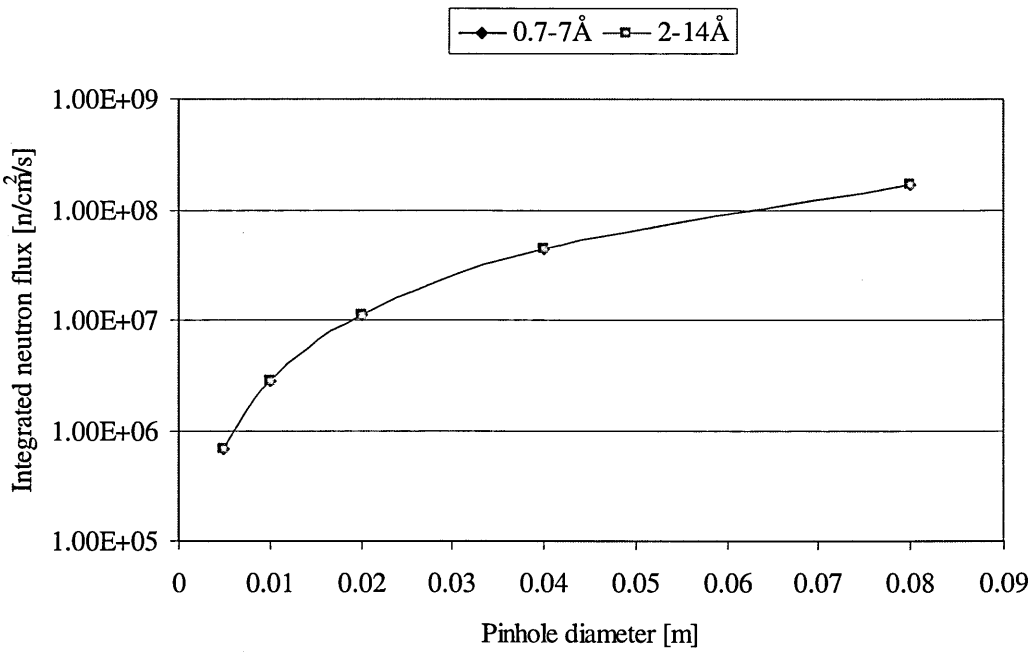

Figure 4.2.21: *Integrated neutron flux calculated on the PSD monitor placed on the sample position for different pinholes (0.005 m, 0.01 m, 0.02 m, 0.04 m and 0.08 m). The integrated flux is plotted using a log scale.*

The highest neutron flux is obtained for the largest pinhole with diameter of 0.08 m (i.e., L/D=125) which may be optimal for real-time experiments when fast processes are investigated. By decreasing the pinhole size down to 0.005 m the diameter (increasing respectively, L/D to 2000) the neutron flux decreases by almost 99%, being possible in future to develop high-resolution tomography applications on IMAT.

4.2.5 Neutron intensity profiles and neutron flux dependent on the wavelength bands

IMAT will go beyond the standard neutron radiography, taking advantage of the pulsed source for optimal energy discrimination. The energy-resolved imaging mode at IMAT will be based on the time-of-flight method and will measure 2D radiographies as function of wavelength providing new opportunities for resolving wavelengths. Among the opportunities offered by the energy-dependent imaging mode could be mentioned the ability to increase the contrast between two materials which can be achieved by the selection of suitable wavelengths or bands of wavelengths and by creating ratios of the radiographs, as detailed in paragraph 2.3.4.1. With a TOF capable imaging detector a multitude of radiographies at different wavelengths will be recorded simultaneously. The goals of this section are: to study the wavelength dependent neutron intensity profiles at the sample position , flux values and FWHM dependent on the wavelength bands, such as, 1-2 Å, 3-4 Å, 6-7 Å, and 13-14 Å. Two pinhole diameters (0.02 m and 0.08 m) were considered here. The instrument was set-up in McStas as previously. One PSD monitor with 100×100 pixels distributed over 20×20 cm^2 was placed on the sample position.

To investigate the neutron intensity distribution on the sample position and to compare the FWHMs for each wavelength band the intensity was integrated over the entire PSD monitor by summing all lines from the monitor output, dividing by the maximum

intensity on the line obtained and then multiplying by 100. This step was repeated for all wavelength bands selected and both pinhole sizes. The plots of the integrated intensity normalized as function of monitor size are shown in Figure 4.2.22 and discussed below.

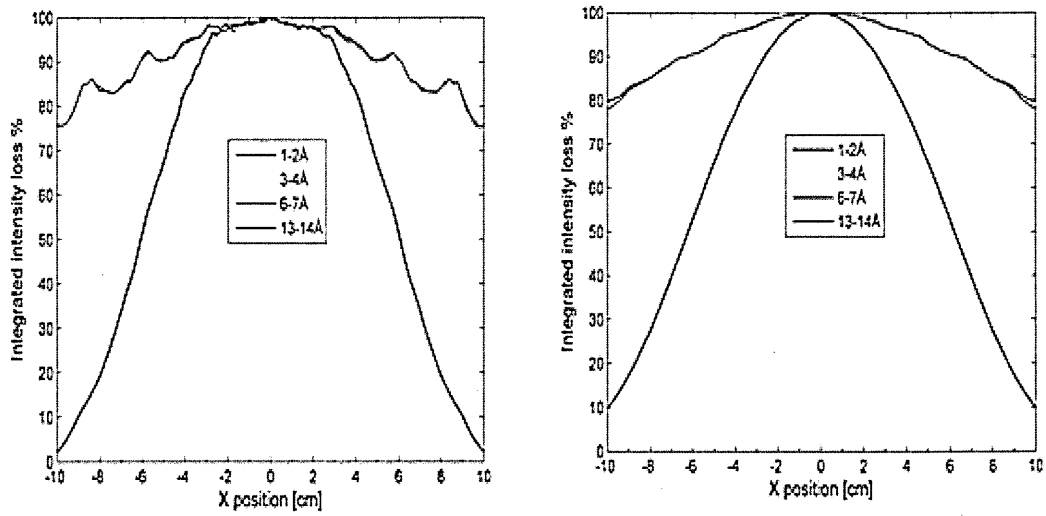

Figure 4.2.22: *Profile plots of the integrated neutron intensity distributions for different wavelength bands and pinholes of radius=0.01 m (left) and radius=0.04 m (right).*

If the pinhole size is fixed, the neutron flux is dependent on the wavelength band. This is shown in the results presented in Table 4.2.3 (the total neutron flux was calculated by dividing the total neutron intensity to the monitor size 20×20 cm^2 and the maximum neutron flux by dividing the maximum intensity to the correspondent pixel size 2×2 mm^2).

Table 4.2.3: *Total neutron flux and maximum neutron flux for different pinhole sizes and different wavelength bands.*

Pinhole radius (m)	Wavelength band (Å)	FWHM (cm)	Total neutron flux ($n/cm^2/s$)	Maximum neutron flux ($n/cm^2/s$)
0.01	1-2	11.8	0.81×10^6	2.4×10^6
	3-4	19.2	0.33×10^7	4.86×10^6
	6-7	> 20	0.64×10^6	0.82×10^6
	13-14	> 20	2.16×10^4	0.27×10^5
	0.7-7	18.8	1.12×10^7	1.94×10^7
	2-14	> 20	1.12×10^7	1.66×10^7

0.04	1-2	12.2	1.25×10^{7}	0.34×10^{8}
	3-4	> 20	0.51×10^{8}	0.72×10^{8}
	6-7	> 20	1.01×10^{7}	0.12×10^{8}
	13-14	> 20	0.34×10^{6}	0.41×10^{6}
	0.7-7	19.7	1.72×10^{8}	2.7×10^{8}
	2-14	> 20	1.72×10^{8}	2.43×10^{8}

While the neutron flux (total and maximum) is higher for short neutrons wavelength (e.g. 1-2 Å) than foe long wavelength neutrons (e.g. 13-14 Å), the low-energy neutrons have the advantage of a large viewable area (more than 20 cm) (Figure 4.2.22). Hence, for long wavelength neutrons (> 6 Å) a large FWHM is available at the cost of a lower neutron flux. In paragraph 4.2.1 we have remarked that the maximum neutron flux is obtained for wavelengths around 3 Å; this is accentuated through the results from Table 4.2.3 and Figure 4.2.22 for bandwidth 3-4 Å. An important feature for the collection of radiographies is represented by the presence of artefacts. In the Figure 4.2.22 fewer artefacts are revealed in the shorter wavelength distribution than in the long-wavelength band. Higher energetic neutrons are less reflected by the neutron guide and they are more concentrated, i.e. have a higher proportion in the monitor's centre compared to neutrons of the same energies at the edge of the 20×20 cm^2 monitor, while the long wavelength neutrons (which are more reflected by the neutron guide and have a higher divergence) are spread across the entire monitor, so the artefacts are more visible in the radiography.

4.3 IMAT imaging applications

The ability of the IMAT instrument to perform imaging experiments, such as neutron radiography, neutron tomography or energy-selective measurements, is investigated in this section based on McStas modelling. As it is known the attenuation is generally wavelength dependent. In this chapter we perform simulations using two different sample models, one in which the attenuation is modelled as wavelength independent and one in which

wavelength dependent attenuation is modelled. For these experiments, the IMAT instrument, as modelled in McStas, was defined as in Section 4.2.1 and Appendix 3, with changes regarding the size or positions of the monitors as follows: one PSD monitor with size of 20×20 cm^2 and 1024×1024 pixels (which substitutes the CCD camera component in McStas) and one wavelength-sensitive monitor, i.e. lambda-monitor (to interpret the energy-selective measurements) with size, 20×20 cm^2, and 1000 channels will be inserted in the instrument model after the sample as specified below. A large collimation ratio L/D is required to produce a sharper image. For this reason, a small pinhole with diameter of 5 mm was selected. As discussed in Section 4.2.4 in this situation a large number of artefacts are visible. These artefacts will be corrected and the image quality improved using *flatfield correction.* By recording the transmitted neutron beam through the sample and by recording the open beam intensity as well (without sample) and by dividing these two measured radiographies the transmission through the sample is calculated and the inhomogeneities of the beam and detector are eliminated; the transmission depends on the sample thickness and attenuation coefficient inside the sample, and it is equal 1 in the region without sample. This last statement is valid only for the wavelength independent attenuation model as we will see latter in this chapter.

4.3.1 Neutron radiography with IMAT imaging virtual instrument

A larger collimation ratio will produce a sharper image, but unfortunately at the cost of a lower neutron flux. Moreover, the computing limitations and the time consuming procedure (around 25 hours per simulation) restricts the number of neutrons and hence the quality of the image we could achieve in these simulations.

The sample geometry has been chosen to allow reasonable quality images to be obtained in a reasonable amount of time. Hence, an empty cylinder with height of 10 cm, outer radius of 4 cm and inner radius of 2 cm to fit with the monitor size was considered.

To minimise the magnification effect a longer distance L=10 m (defined in the Stage-1 of the IMAT instrument development) between the pinhole and sample was set-up. Moreover, a PSD monitor will be placed behind the pinhole (for simulations both with the sample and for open beam measurements), very close to the sample position (sample position to monitor distance is 10 cm) to reduce the sample blur, due to the divergence, as far as possible.

As shown in Figure 4.3.1, two radiographies were collected using the PSD monitor: one for the open beam (a) and the other with the sample in the beam (b). The artefacts are clearly visible in both situations.

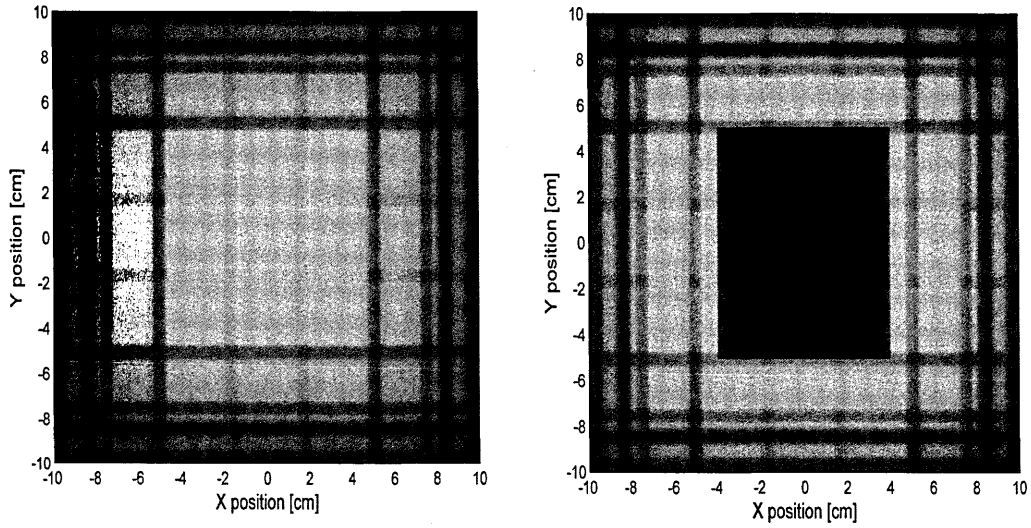

(a) (b)

Figure 4.3.1: *(a) Open beam radiography; (b) Sample radiography.*

As mentioned before each point from the sample is blurred up to geometrical resolution $d = \frac{l}{L/D}$ and in addition to the blurring effect the image size is magnified (enlarged) with the magnification factor $M = \frac{L+l}{L}$, where L is the pinhole-sample distance and l is the sample-detector distance (see section 2.3.2). According to the previous formulas the geometrical resolution for our images is 0.1 mm and the magnification factor is 1.01. A

comparison between the magnification factor calculated and the measured magnification will be given in the below section.

4.3.2 Neutron tomography with IMAT imaging virtual instrument

Based on the results obtained for the simulated neutron radiography with IMAT virtual instrument described above a neutron tomography data set was produced. Using the fact that the geometry of the sample is symmetric, 360 different two-dimensional projections of this specimen were taken (without sample rotation) and three open beam images for corrections using 10^{12} neutrons in the wavelength band 0.7-7 Å.

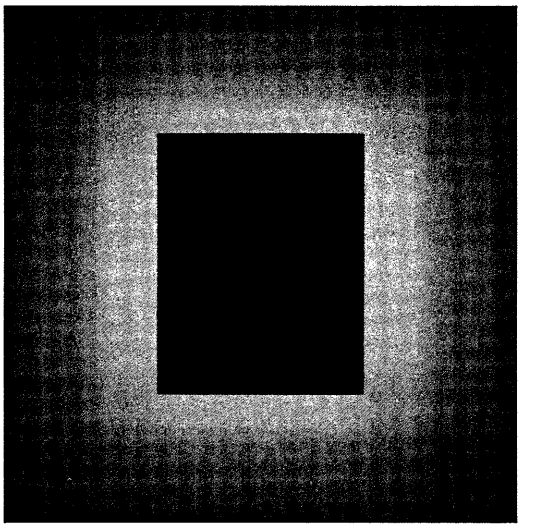

Figure 4.3.2: *Neutron radiography of a cylinder after correction. The dark area in the radiography is associated with high attenuation while light area is associated with high transmission.*

The direction of the neutron beam is perpendicular to the cylinder axis penetrating the whole depth of the sample. Figure 4.3.2 shows a radiography obtained after flat-field correction. Firstly, all projections from McStas are saved as tiff files and then imported into the Octopus software where the sample is reconstructed and thus slices are obtained. The procedure is entirely similar to that developed in the compilation of the data from a

real neutron tomography experiment conducted, for example, at the NEUTRA imaging instrument at PSI (see Chapter 1).

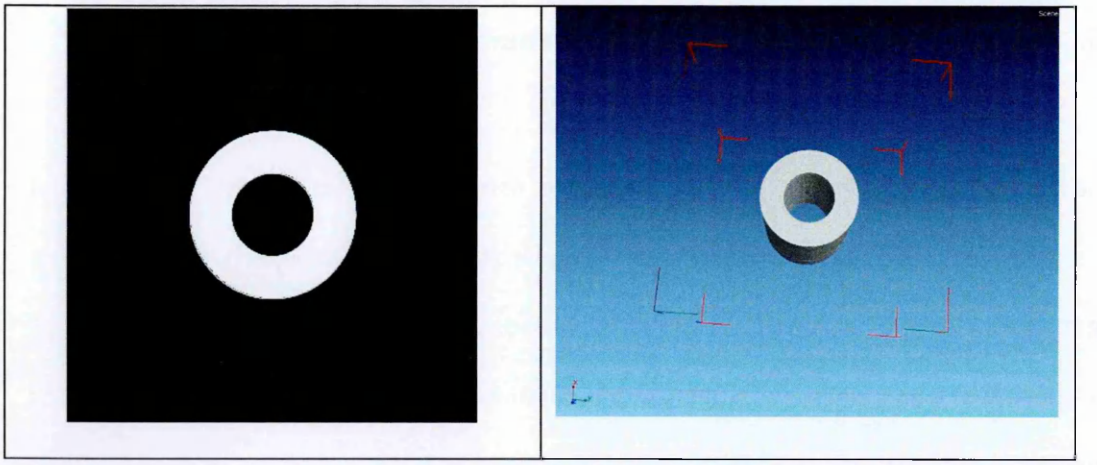

Figure 4.3.3: *Slice obtained after applying Octopus software (left image); 3D volume rendering of the cylinder from VgStudio (right image).*

The tomography was then subsequently segmented and meshed using the commercial Volume Graphics software package VGStudio Max 2.0. The volumetric cylinder is generated (Figure 4.3.3), according to the description in Sections 2.3.3.1 and 2.3.3.2.

Using the caliper tool from VgStudio the sample reconstructed was measured and the outer diameter was found approximatively, 8.09 cm and cylinder height 10.11 cm. These values are comparable with the values obtained based on the calculated magnification factor, i.e. the outer diameter 8.08 cm and cylinder height 10.1 cm.

4.3.3 Preliminary investigation into wavelength dependent attenuation effects

While in the previous paragraphs we were more interested in the sample reconstruction using a simple wavelength independent attenuation model, in this section we model wavelength dependent effects using the virtual IMAT imaging instrument. The transmission spectrum of a neutron beam, in the cold or thermal energy range (as the

IMAT instrument will run), through a polycrystalline specimen shows the Bragg edges related directly to the lattice spacing (see section 2.3.4.1). For this reason the sample in the instrument was changed, and a virtual specimen, iron (bcc) powder described in McStas as the BraggEdge_Powder component [164, 165] was selected. The module created in McStas [164] for this component was designed to simulate only transmission and no additional scattering events are modelled. It was preferred to use this component because it was already tested on ENGIN-X instrument at ISIS ([164], [166]). The iron (bcc) powder was selected because it has a high coherent cross section and its structure, body-centred cubic, produces several well separated Bragg edges and a low absorption coefficient. The sample geometry selected was a rectangular plate with same width and height 16 cm and 5 cm thickness. The dimensions of the sample and its positioning on the instrument were chosen in such way that the artefacts will pass through the sample's radiography (Figure 4.3.4 a).

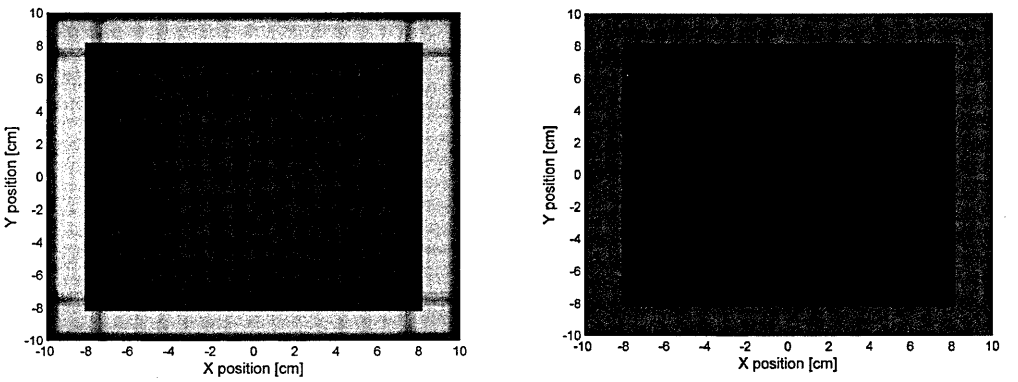

(a) (b)

Figure 4.3.4: *(a) Sample's radiography with visible artefacts passing through it. (b) Flat fielded image of the sample.*

The position of the sample and the instrument settings were as in the previous sections. It is not my intention here to discuss the Bragg edges of the iron powder sample in the time-of-flight transmission experiments. This is already extended in the literature [11, 164, 166].

The energy-resolved imaging mode on IMAT will be based on the time-of-flight and measured 2D radiographies as a function of wavelength. With the TOF capable imaging detector (one that will measure full part or a large part of the IMAT frame of 0.1 sec with sufficiently small histogramming bin-width or timing resolution) a multitude of radiographies at different wavelengths will be recorded simultaneously.

In the simulated IMAT instrument there are not yet developed the same capabilities of the TOF imaging detectors as that expected to be used on IMAT, a lambda-monitor was selected to stand for them. In this context the lambda monitor represents a time of flight detector with perfect time resolution.

Two simulations were done using the entire wavelength band 0.7-7 Å one with sample and the other without sample. Figure 4.3.5 shows the simulated data for iron (bcc) powder sample compared to open beam image over the lambda-monitor.

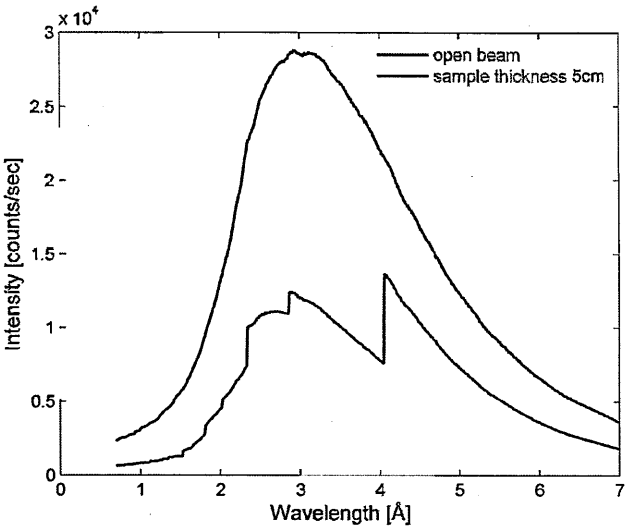

Figure 4.3.5: *The neutron transmission spectrum displaying characteristics Bragg edges from the (bcc) powder sample compared to open beam image at the IMAT virtual instrument over the single frame bandwidth 0.7-7Å.*

Using the transmission formula (2.3.2) the transmission is calculated and the Bragg edge spectrum is plotted as function of wavelength (Figure 4.3.6).

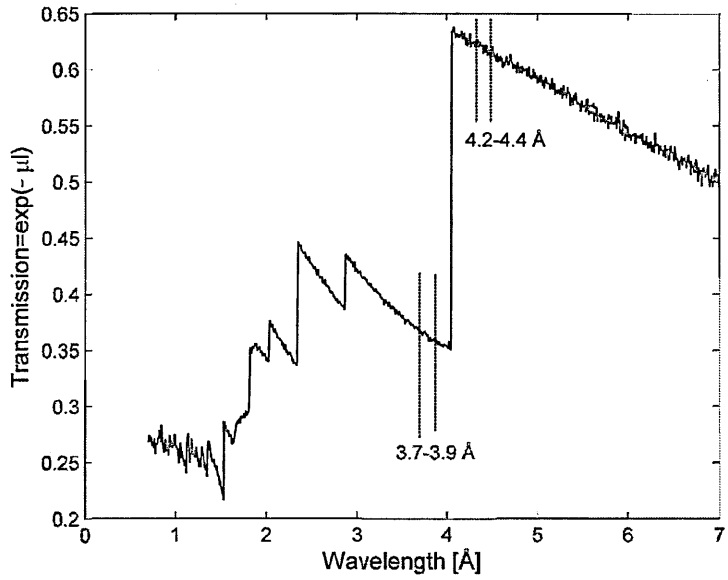

Figure 4.3.6: *The ideal neutron transmission spectrum obtained using a lambda monitor and displaying characteristic Bragg edges from the (bcc) powder sample of the IMAT virtual instrument over the single frame bandwidth 0.7-7Å. Also shown are two narrow energy selected around the Bragg edge 4 Å.*

Beam hardening

A step forward from the above result is the study of the variations of attenuation coefficients, as calculated from tomography data, due to the wavelength distributions. In the case of the monoenergetic beam, the Lambert-Beer law $I = I_0 e^{-\mu l}$ is defined as a linear relationship between the proportion of radiation absorbed and the path length through the material. In the case of a polychromatic beam this assertion is not valid because different wavelengths are absorbed differently. Generally, this effect is well known in the context of X-ray imaging and is called beam hardening and describes the fact that low energy X-rays, are more easily attenuated than higher energy X-rays [167]. This beam hardening effect is considered less important for neutrons, though it is still present. Here, it is not our intention to give a detailed description of this effect, only to make an introduction to a future investigation subject of IMAT instrument.

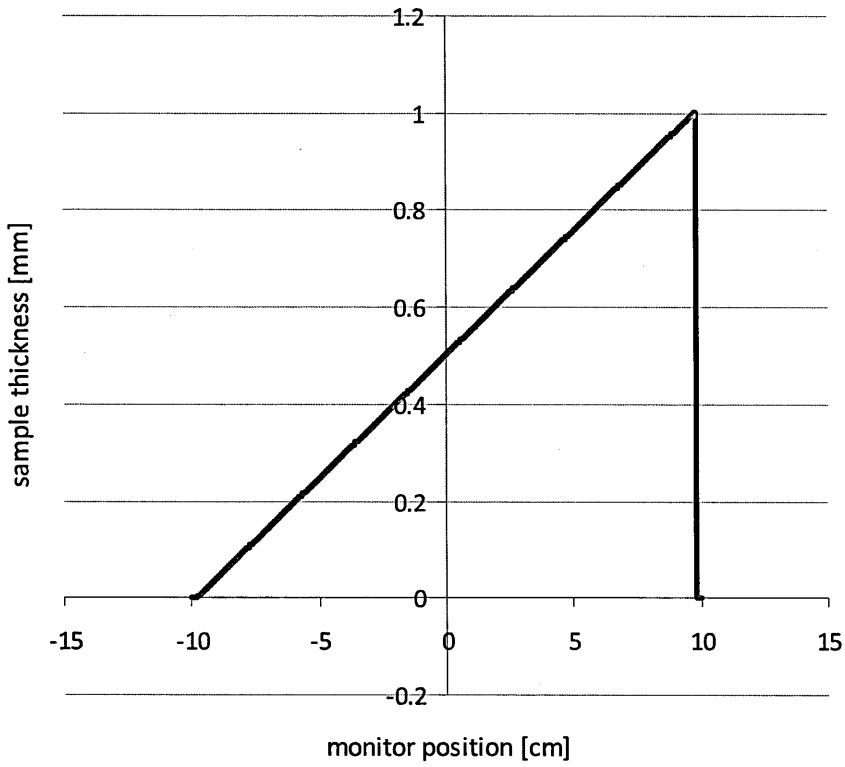

Figure 4.3.7: *The tapered sample used in the theoretical model.*

A basic theoretical model was created using the previous sample (bcc iron powder), but changing its geometry because in the previous simulated radiography the beam hardening effects were not visible because the sample was parallel sided. Hence, a tapered sample with thickness varying from 1 mm up to 1.004 m was considered (Figure 4.3.7).

Two different narrow wavelengths bands were selected: one at the left of the Bragg edge, 3.7-3.9 Å and the other at the right of the Bragg edge, i.e. 4.2-4.4 Å (see Figure 4.3.6) with their corresponding intensities in the open beam image I_{01}, and I_{02}. For each wavelength an attenuation coefficient was defined μ_1, and μ_2. Given the sample thickness and the open beam intensities, the intensities for images with sample I_1 and I_2 were calculated using the Lambert-Beer law. As previously discussed (section 4.3.1) the flat field images are calculated by dividing the sample's image to the open beam image. However, given the energy selective imaging capability of IMAT there are two approaches to flat-fielding that may be considered:

1. White-beam: naively the flat-field image dividing the total image with sample by that without sample, taking no account of wavelength bands. In the case of our wavelength model this gives $FF_{total}=\frac{I_1+I_2}{I_{01}+I_{02}}=e^{-\tilde{\mu}l}$ where $\tilde{\mu}$ is the effective attenuation coefficient.

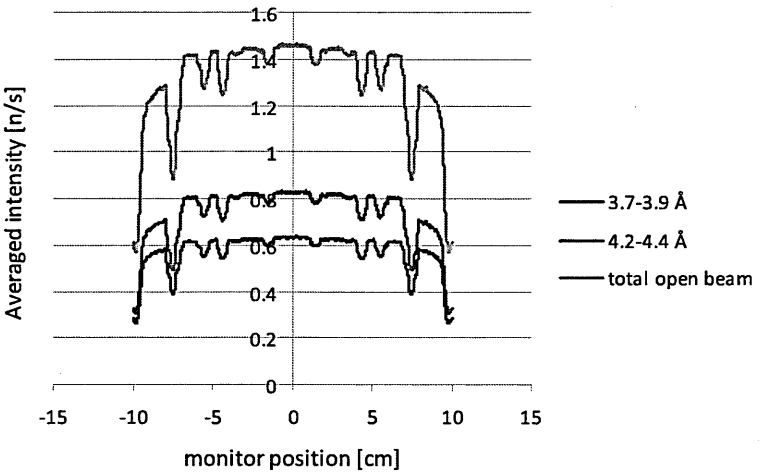

Figure 4.3.8: *Open beam profiles for both wavelength bands selected and total open beam.*

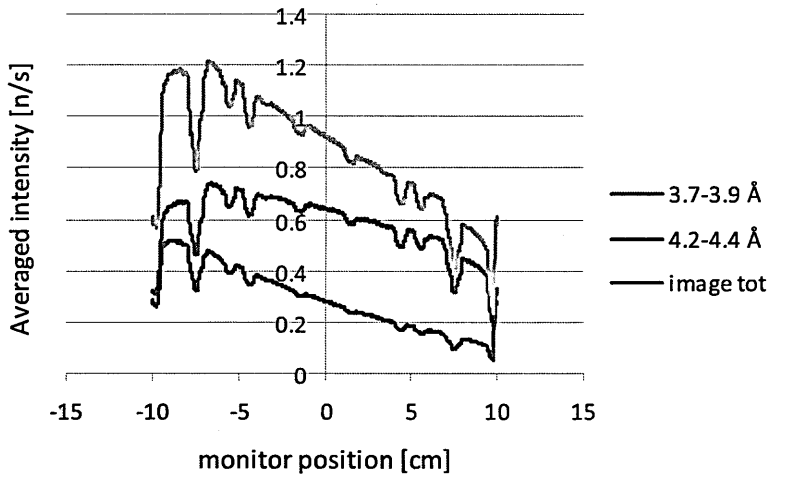

Figure 4.3.9: *Image calculated for both wavelength bands selected and total image taking into account the sample thickness and attenuation coefficients.*

2. Energy selective: An energy selective flat-fielding approach may be done for the individual wavelengths so that we may recover the individual wavelength dependent attenuation coefficients, i.e. $\mu_1=-\frac{1}{l}\ln\left(\frac{I_1}{I_{01}}\right);\mu_2=-\frac{1}{l}\ln\left(\frac{I_2}{I_{02}}\right)$.

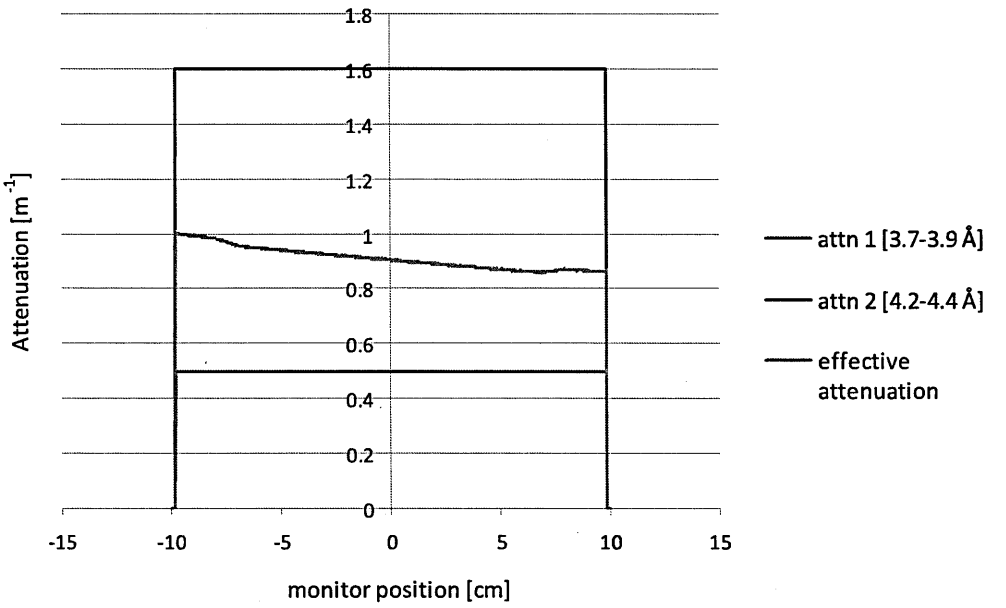

Figure 4.3.10: *The attenuation coefficients for both selected wavelength bands and the effective attenuation calculated are plotted as position on the monitor. The effective attenuation coefficient (green line) depends on the sample thickness.*

Calculating the effective attenuation coefficient from the white-beam approach, i.e. $\tilde{\mu}=-\frac{1}{l}ln(F_{total})$ and comparing it with the attenuation coefficients from the energy-selective flat-fielding one should say that the effect of the beam hardening is visible for white-beam case for IMAT instrument (Figure 4.3.10) in a non-parallel sample.

4.4 Conclusions

IMAT will be placed on port W5 on ISIS TS-2, which operates at 10 Hz. IMAT will view the broad pulse coupled moderator, at an angle of 1° (horizontal) from the nominal W5 axis. It will be built on a 56 m flight path from the moderator to the sample position. The total length of the straight, square supermirror neutron guide is about 44 m, with a cross section of the guide of 100×100 mm^2 in the 2 m shutter section and a cross section of

95×95 mm^2 for the main guide. Two positions for the sample will be available: the main position for a flight path of 56m from the moderator centre (i.e. 10 m after pinhole) enabling imaging and diffraction experiments and the 2^{nd} sample position 51 m (i.e. 5 m after pinhole) for high intensity imaging experiments. The neutron guide will have gaps for different instrument hardware components such as vacuum gate valves, choppers or neutron monitors which need to be minimised. In the imaging mode, a remote-controlled pinhole selector will offer a choice of five apertures (D=0.08 m, 0.04 m, 0.02 m, 0.01 m and 0.005 m) defining different L/D ratios (125, 250, 500, 1000 and 2000) where L=10 m is the distance from pinhole selector to the imaging camera and D is the pinhole diameter. The pinhole selector will have also a large open position allowing the beam to pass through for diffraction experiments.

The performance simulations of the present IMAT design were investigated including: wavelength distribution of the neutron flux along the beamline from the moderator to the sample position and the wavelength distribution as a function of position on the camera placed at the sample position. Once the neutrons are passing through the pinhole the beam is adjusted by the jaws and after passing through the sample and detector they are stopped by the beam stop. In order to investigate the beam tube design, from the pinhole to the sample position, and the size of the beam stop, the beam profiles along the flight path, from the pinhole to the beamstop were analysed. On the other hand the image quality of the neutron radiography depends on the beam divergence. A study of the divergence at the sample position in two cases: theoretical, calculated using the divergence formula and measured, following McStas modelling, is presented. Results as FWHM, total neutron flux, maximum neutron flux and beam divergence depending on the wavelength band and collimation ratio are obtained. Moreover, taking the advantage of the pulsed source, the energy-dependant imaging mode will be developed on IMAT. The wavelength dependent neutron intensity profiles at the sample position, flux values and FWHM

dependent on the wavelength bands, such as, 1-2 Å, 3-4 Å, 6-7 Å, and 13-14 Å are investigated.

In the last section of the chapter, the ability of IMAT to develop imaging applications is exploited, by using two kinds of sample: one sample applied in the neutron radiography and tomography experiments where wavelength is independent of the attenuation and the (bcc) powder sample used to model wavelength dependent effects in energy-selective imaging.

5 Combined imaging and diffraction techniques

While neutron tomography provides three-dimensional maps of attenuation coefficients, thereby giving the opportunity of visualising the inside of an object in a non-destructive manner, neutron diffraction methods provide information on the distance between crystallographic lattice planes at specific points which is used for neutron strain scanning.

The present chapter reports a method for exploiting this complementarity between neutron tomography and neutron diffraction and illustrates this method's application to various samples from different fields.

5.1 Introduction

The complementarity of the tomography and diffraction methods was exploited and elaborated in a new technique entitled "Tomography Driven Diffraction" (TDD) [14]. TDD is an extension of methods developed for engineering strain scanning experiments, in which both the instrument and sample is used to plan and control diffraction measurements [168, 169]. At the beginning the method was produced using virtual sample models obtained by laser scanning the sample, but this approach has been found to have the following disadvantages:

- the laser scans give only the object shape and cannot be used to reveal internal features;
- the laser scanning approach often does not work well for some cultural heritage objects because the surfaces cannot be colour-sprayed to enhance the laser contrasts.

The advantage of the extension reported in this chapter, in which a tomography dataset replaces the laser data, is that the available information will now include the internal as well as external geometry.

The TDD method is demonstrated in this chapter by the investigation of two different structurally and geometrically complex samples drawn from engineering and heritage sciences. The viability of the TDD approach was proved using combinations of individual tomography and diffraction instruments such as, in this case, NEUTRA (PSI) and ENGIN-X (ISIS). In the near future, the TDD could be applied on the combined imaging-diffraction instrument IMAT (ISIS).

5.2 Outline of the Tomography Driven Diffraction technique

In contrast to a tomography experiment, in which the characteristics of the whole sample are revealed, in terms of dimensions, shape, internal defects or density, a diffraction experiment for neutron strain scanning only measures over a small sampling volume of a few cubic millimetres (known as the *gauge volume*) (see section 2.4.2).

There are two difficulties associated with many diffraction experiments:

i) Identifying and marking the points of interest that we wish to measure;

ii) Controlling the diffraction instrument so that these points are brought to the instrument focus or gauge volume.

The answer to these difficulties can reside in the tomography diffraction complementarity of our method, as summarized by the following three steps:

- identify and mark for measurement the features of interest as revealed in the sample tomography;
- determine the position of these features in relation to the diffraction instrument focus;
- establish how to move the instrument to measure the features once we have information about the position of the sample.

5.3 TDD for engineering samples

The residual stresses have important consequences on the performance of engineering components and can be measured with different direct methods [123]. Some of the methods can be either destructive (e.g. hole drilling [170, 171], slitting [172] or contour method [173, 174]) or non-destructive such as X-ray (laboratory or synchrotron) or neutron diffraction. As a particular situation, in welding, residual stresses are formed in the structure as the result of differential contractions, which occur as the weld metal solidifies and cools to ambient temperature [175].

Using neutron diffraction residual stresses can be measured non-destructively within the interior of the samples in small test volumes (down to $1\times1\times1$ mm^3) and in thick specimens (up to few cm) [123].

5.3.1 Sample description

In order to demonstrate the potential contribution of TDD to the measurement of residual stress we have applied the method to the investigation of a component from a nuclear power station. In a complex pipe to pipe intersection, known as a bifurcation (Figure 5.3.1) in the boilers of the UK's Advanced Gas Cooled Reactors (AGRs) a number of creep cracks have been found [176]. These creep cracks shorten the life of these components and residual stress is a possible contributing cause.

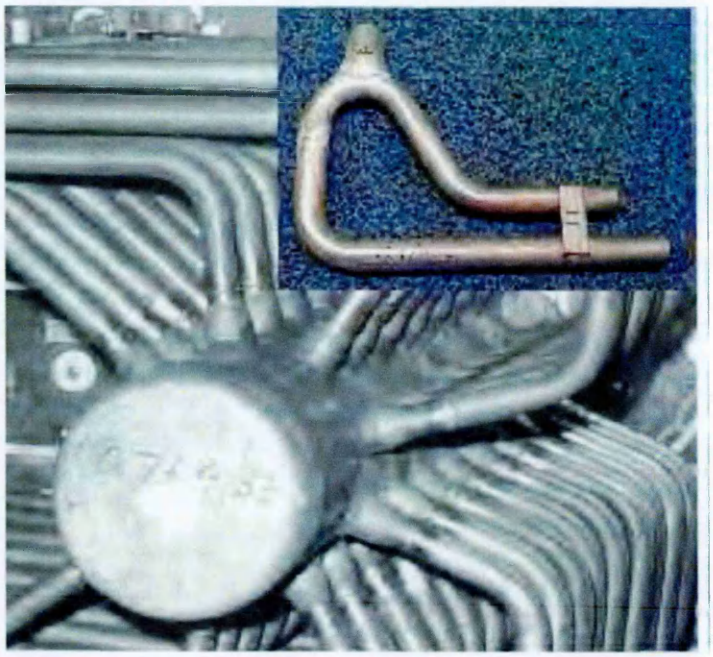

Figure 5.3.1: *Photograph of completed bifurcation [176].*

The purpose of the analysis was to accurately quantify the distribution and magnitude of residual stresses present in a mock-up bifurcation component after the fabrication cycle and so provide information on possible failure mechanisms allowing fabrication, durability and performance to be improved. The relevance of the selection of this sample for the demonstration of the TDD approach is that the geometry of the sample (Figure 5.3.2) is complex and the measurements points needed to be sited accurately in relation to both the external and internal geometry of fabrication welds. Without tomography data this would have been both difficult and time consuming.

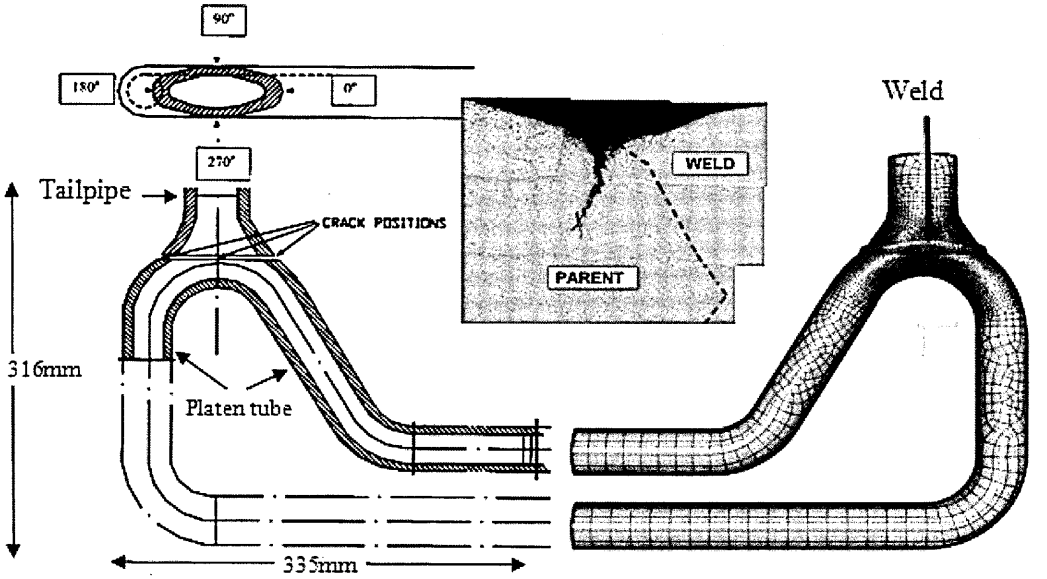

Figure 5.3.2: *The geometry of the bifurcation, finite element model and creep damage [176].*

The bifurcation material is AISI Type 316H stainless steel and the outline fabrication cycle is:

(a) cold bending of the platen-side tube; (b) cold swaging of the tailpipe transition stub; (c) cutting off the extrados of the bend and machining weld preps on the two parts; (d) welding (without prior heat treatment); (e) inspection by radiography prior to post weld treatment (PWHT); (f) joining to the rest of the secondary superheater stage platen; (g) a nominal solution heat treatment of the assembly as a whole; and (h) internal pressure proof test (27 MPa).

In this section the detailed results obtained from neutron diffraction experiment and finite element analysis will not be shown. Our mainly intention is to explain the TDD method for an engineering sample.

Preliminary step to the experiment

The first step of the process was to attach four (a minimum of three are required) identical steel spheres of 1 cm in diameter at different points on the surface of the sample (Figure 5.3.3). These are named "fiducial spheres" and the coordinates of the centres of

these spheres are used as reference points at a later stage when accurate correspondence between the virtual and real laboratories needs to be established.

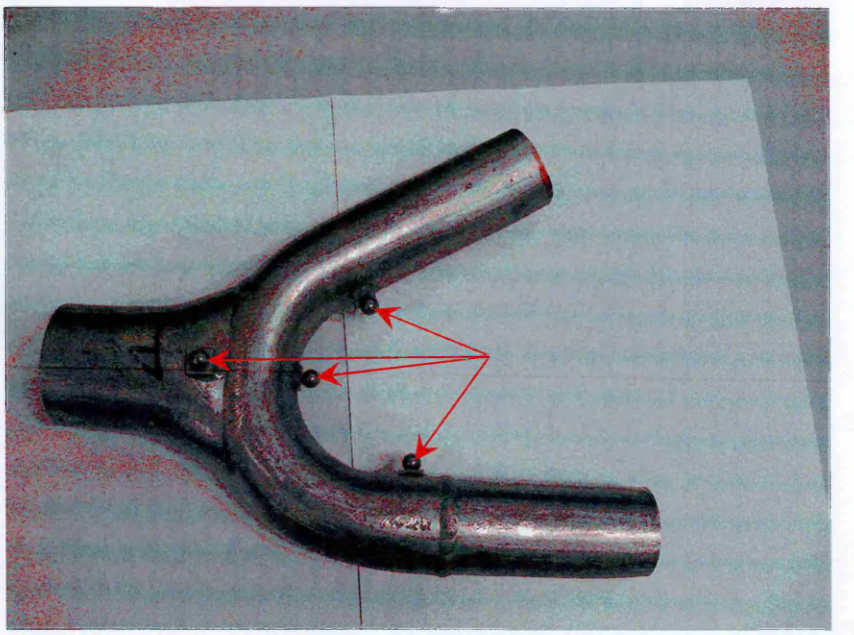

Figure 5.3.3: *The photograph of the sample with four steel spheres attached indicated by the red arrows.*

5.3.2 Neutron imaging experimental description

The neutron tomography experiment on the bifurcation sample was performed at the NEUTRA station [7] at the Swiss neutron source SINQ of the Paul Scherrer Institute. The samples were placed on top of a rotary table at position 3 of the beamline (at the end of the beamline, at 13.131 m distance from the target station and 10.547 m distance from the aperture where we gain the best spatial resolution and a large field of view). On this position the beam diameter is 40 cm with collimation ration L/D=550. The approximate neutron flux on this position is 3×10^{6} [$n\times cm^{-2}sec^{-1}mA^{-1}$] [7]. The distance between the rotational axis and the scintillator screen was 11.5 cm. During a 360° rotation of the sample, 625 neutron radiographic projections of the sample were taken (Figure 5.3.4). The

detector system was based on a CCD camera (Andor 1024 [177]) with 1024x1024 pixels. This camera was equipped with a 50 mm Pentax objective and viewed a mirror which reflected the light generated by the incident neutrons in the scintillator screen. The recording time per image was 20 seconds at a proton current of 1.31 mA. The field of view was approximately 200×200 mm^2.

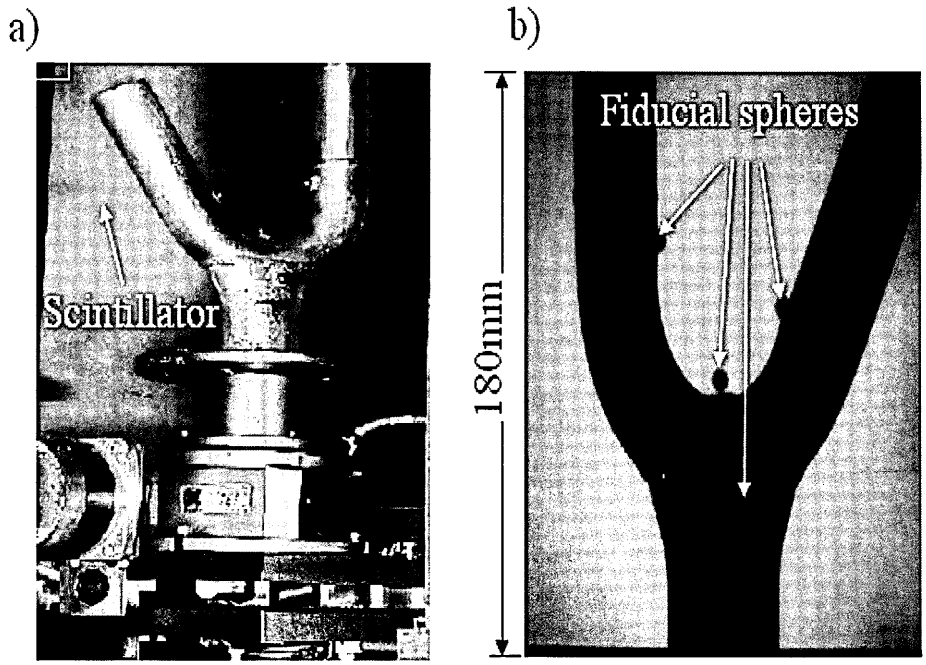

Figure 5.3.4: *Collecting tomography data. a) Mock up bifurcation mounted on the NEUTRA rotation stage in front of the scintillator screen; b) Example radiography.*

Virtual sample model

The reconstruction of the neutron data was achieved with tomography processing software developed at PSI used for reconstructing and viewing tomography data [178]. The corrections (flat-field and dark field) were applied to projections before calculating the object volume by the filtered back-projections algorithm (see section 2.3.3.1) included in the reconstructing software. The tomography was then subsequently segmented and meshed using the commercial Volume Graphics software package VGStudio Max 2.0 [70].

From the segmented volume obtained in VGStudio we extracted a polygonal surface model of STL format (Figure 5.3.5).

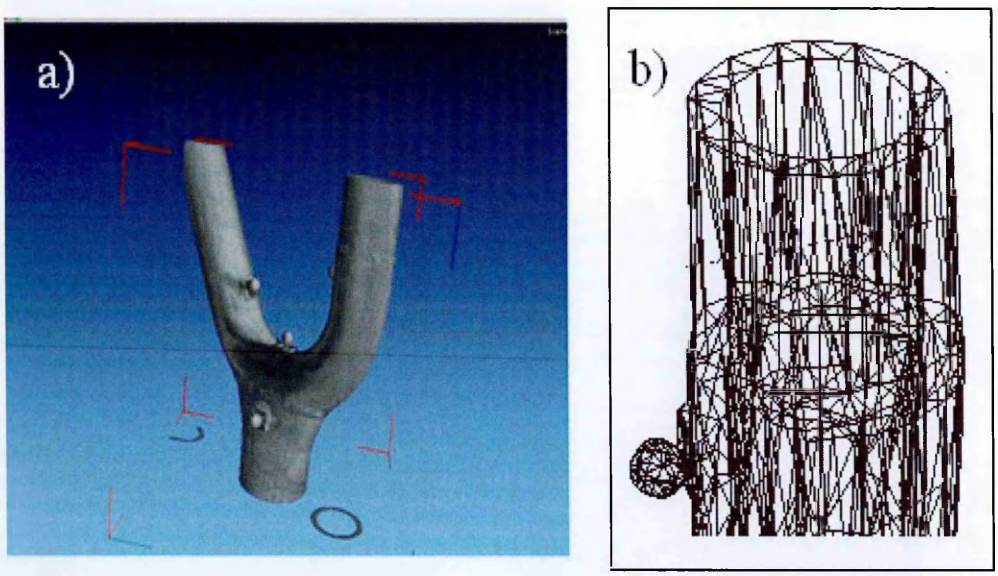

Figure 5.3.5: *Segmenting and meshing the tomography data. a) Segmented tomography. b) Surface of segmentation meshed and output as triangular Standard Lithographic STL file.*

The STL model was then imported into the virtual instrument software Strain Scanning Simulation Software (SScanSS) [168] which was developed as a collaboration between The Open University and ISIS for the purpose of supporting engineering strain scanning experiments. This software was designed to provide tools necessary for planning, optimizing and executing experiments. The approach allows the user to control the instrument by indicating the measurement points on the virtual sample, which until now has been obtained by scanning samples with precision laser scanners.

5.3.3 Neutron diffraction application of TDD

In the upcoming paragraphs we present the tomography driven diffraction instrumental concept applied to the bifurcation sample.

5.3.3.1 The measurement points

The measurement points were selected on the sample in the areas where cracking had been observed: two areas on the crotch (crotch1 – 5points and crotch2 – 5points) other two areas on the sample's flank (flank1 - 6points and flank2 - 6points) and the last region surrounding the sample, exactly on the ring weld, 16points (Figure 5.3.6). These points were defined graphically in SScanSS on sections generated by the intersection of a user defined plane with the 3D model.

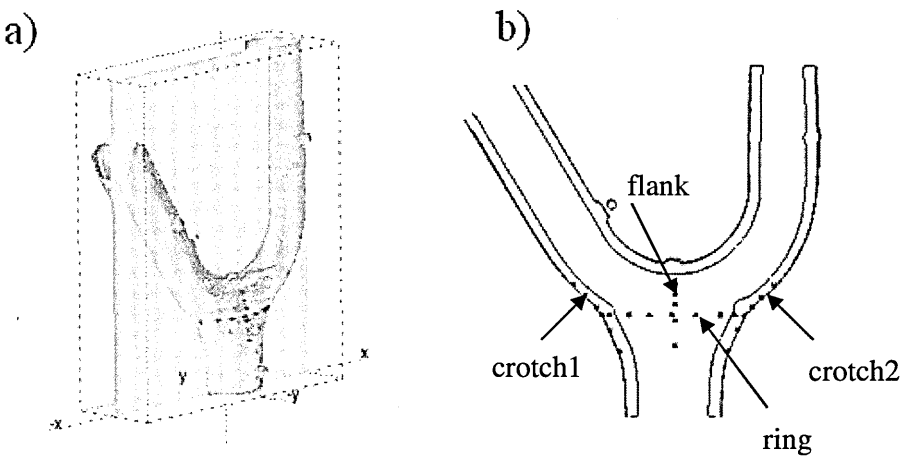

Figure 5.3.6: *Selecting measurement points. a) Generating section through virtual sample. b) Measurement points placed on section (red).*

5.3.3.2 The virtual instrument

SScanSS [179] allows the selection of a number of virtual diffraction instrument models corresponding to instruments in use at various facilities worldwide such as ENGIN-X (ISIS) [168], KOWARI (ANSTO) [180], NRSF2 (ORNL) [179] and VULCAN (SNS) [181]. This software helps scientists and users:

- To visualize the instrument features and to understand better the measurement process;
- To place and orientate a complex sample on the instrument;
- Automatically generate the machine control scripts required to make the measurements;
- To provide options for automatically optimizing other important experimental parameters such as the measurement counting time and collision prevention.

The experiments described in this chapter were performed using the ENGIN-X engineering strain scanner at ISIS in the UK, [6]. The ENGIN-X virtual instrument (Figure 5.3.7) is loaded into SScanSS including 3D models of the components of the real instrument.

ENGIN-X uses two diffraction banks set at 90° to the incident beam, which allow simultaneous measurement of two strain components. Due to the complex geometry of the sample we also employed a triple axis goniometer [182] to allow for flexible sample positioning. At the start of the experiment, we mounted the sample on the goniometer, so that all three strain components would be accessible and could be measured at every measurement point (this was verified by simulation prior to the start of the experiment).

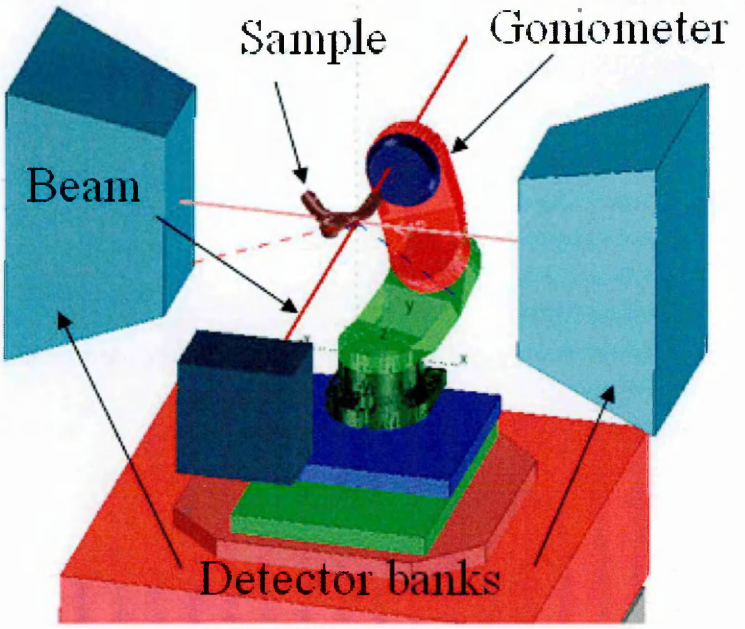

Figure 5.3.7: *The virtual ENGIN-X instrument. The virtual laboratory comprising the sample and instruments models. SScanSS calculates how to move the positioning system, comprising the triple axis goniometer and the* x, y, z, Ω *table, so that the required strain components are measured.*

5.3.3.3 Initializing the virtual laboratory

The most important requirement before starting the experiment is to have accurate correspondence between virtual and real laboratories in terms of the position of the sample on the instrument. Having this in mind, the procedures followed are:

i) to find the positions of the fiducial points in the virtual sample coordinate system;

ii) to measure the coordinates of the centres of the spheres on the real sample on the real instrument using a coordinate measurement machine (CMM) or touch probe [183];

iii) to find the transformation matrix that maps the positions of the virtual fiducial points to the real ones and apply this transformation to the whole of the virtual sample. This matrix is calculated automatically in SScanSS using a least-squares procedure [169].

The last step is to bring the measurement points within the sample to the instrument's focus. The instrument movements required to do this are calculated within the

SScanSS virtual laboratory and then exported as a simple text file which is read by OpenGenie [184], the ISIS control software [183].

5.3.4 Diffraction scans

The ENGIN-X instrument (Figure 5.3.8) has three pairs of incident slits. While the first two pairs are located along the incident beam path, within the neutron guide at the distances of 4 m and 1.5 m respectively from the sample position, the third slit-component (jaws3) has adjustable horizontal and vertical blades to control the height and width of the incident beam. These slits were each set to 2 mm, and as the gauge length defined by the collimator was also 2 mm the measurements were made with a $2\times2\times2$ mm^3 gauge volume. The wavelength range was between 0.56 and 3.1 Å corresponding to a $d-$spacing range of 0.4 to 2.2 Å. The stress-free lattice parameter d_0 was obtained from measurements made at the ends of the tubes away from any weld stress.

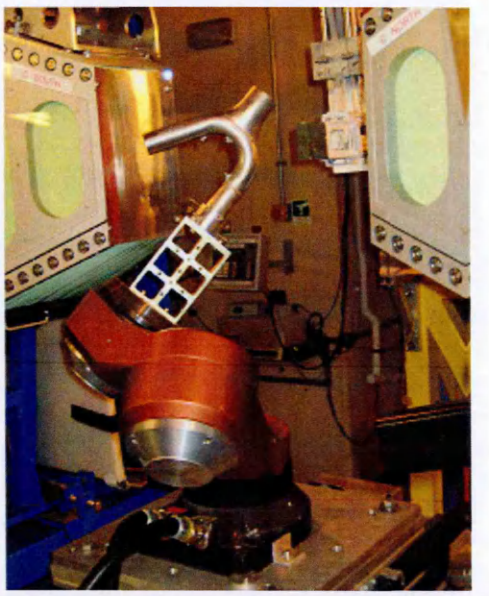

Figure 5.3.8: *Sample mounted on ENGIN-X for diffraction measurements.*

ENGIN-X is equipped with a software suite for full analysis of diffraction spectra. The diffraction patterns were fitted with a steel structure model using the GSAS analysis package for obtaining the lattice parameter [120]. Figure 5.3.9 illustrates a typical diffraction pattern recorded during this experiment, where the neutron intensity is plotted versus the lattice spacing d.

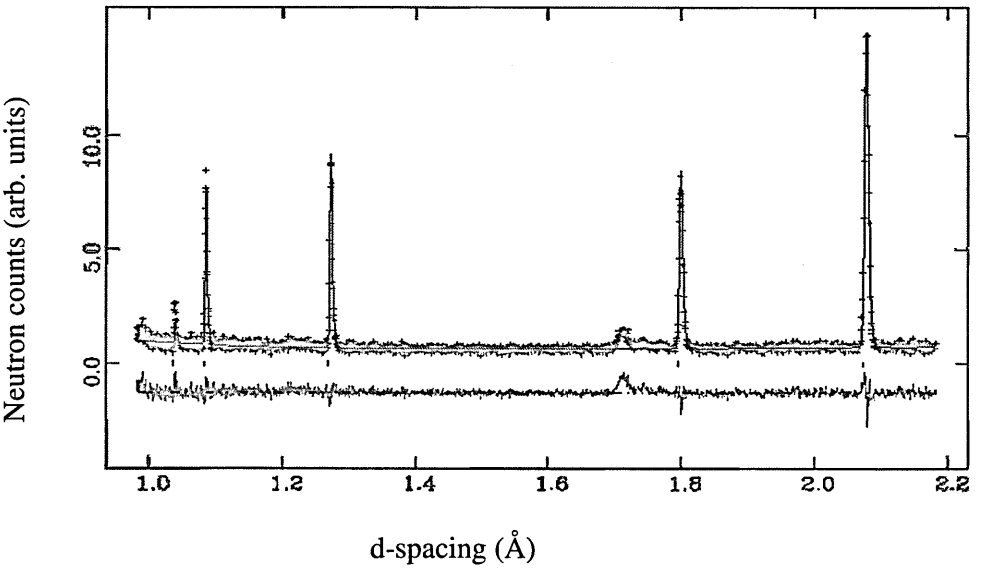

Figure 5.3.9: *Diffraction spectrum obtained at ENGIN-X for one measurement point selected on the weld ring. The TOF data was analysed using Rietveld method.*

From the lattice parameter for each measurement point (d_x) and the measured stress-free reference lattice parameter for each detector bank (d_0), the elastic strain ε_{xx} along a direction 'x' (for example) was calculated using formula (2.4.9).

The strains $\varepsilon_{xx}, \varepsilon_{yy}, \varepsilon_{zz}$ measured in the three orthogonal directions (transverse, longitudinal, through thickness) were combined with the appropriate elastic constants and used to calculate the stress, $\sigma_{xx}, \sigma_{yy}, \sigma_{zz}$ in each direction using Hooke's law given by the relation (2.4.10), where the macroscopic values of material properties used were Young's modulus E=168.2 GPa and Poisson's ratio, ν=0.294, respectively. The stress values obtained from these measurements provided information on the stress within this

sample as well as assisting in the verification of finite element method predictions which are frequently used to predict residual stresses in complex components.

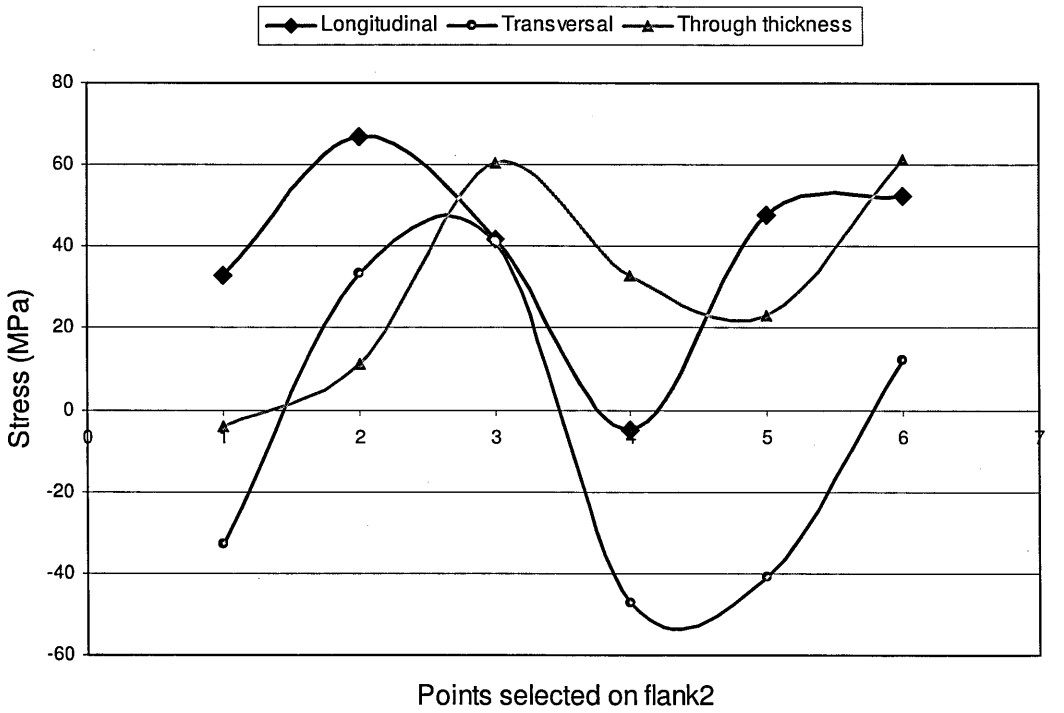

Figure 5.3.10: *Stress calculated for the points selected on the flank 2 of the bifurcation sample.*

Figure 5.3.10 is an example of the plot of the stress values calculated from the neutron diffraction measurements for the points selected on one flank of the sample (see Figure 5.3.6) showing that in the mock-up bifurcation component, after the fabrication cycle, the residual stresses have been reduced.

For engineering the ability to guide residual strain diffraction measurements accurately in relation to internal features is a valuable new possibility and our technique was already successfully applied for other engineering samples, such as stresses adjacent to cavities within turbine blades measurements [185].

5.4 TDD applied in archaeometry

Another challenge for the tomography driven diffraction method is study of archaeological and art-historical objects where the positions and coordinates of the internal features that may be of interest is often not known a-priori. The inside of the objects could be made visible using neutron tomography. Details about sample composition, production techniques of the objects interesting for archaeologists are not evaluated through neutron tomography alone. Using TDD, internal structures made visible by applying neutron imaging techniques can be readily identified and marked for further characterisation by neutron diffraction.

The first experiment was for testing the TDD method to see if this is suitable for studying compositional variations in an object. Based on this test, we did a second experiment on an art-historical sample obtaining useful and interesting results on its structure and compositions and not on residual stresses as in the engineering sample.

5.4.1 Description of samples

For the trial experiment we used a replica bronze statue (Figure 5.4.1 a) with 25 cm height which represents the large and complex objects often encountered in art history and archaeology [186]. It was one of the several replica statues produced at the Rijksmuseum Amsterdam in order to reconstruct Renaissance bronze casting technologies. For the replica statues, the lost wax casting Renaissance bronze technique [187] was applied, where the generic term bronze was used for copper alloys of which the exact composition is not always known. The lost wax casting process is described as follows [35]: a clay core that functions as the body of the sculpture is covered with a wax layer that forms the geometry and final appearance of the future sculpture. Through the wax, iron 'core pins'

are inserted into the clay body and left protruding. Around this wax layer, and attached to the pins, a clay layer is mounted that functions as a supporting outer mould. The wax is, by means of a connected wax funnel system, still in contact with open air. The complete construction is heated in a kiln and the wax melts out from between the two clay parts which remain connected and held in position by the iron core-pins. After the wax has completely disappeared molten metal can be cast through the same opening from which the wax melted out. After solidification of the metal the outer mould can be taken away. In most cases the iron core pins remain in the bronze after it has been cast and finished, however they can be concealed using finishing techniques.

(a) (b)

Figure 5.4.1: *(a) Replica statue; (b) Striding Nobleman (Renaissance Bronze), c.1610, Rijksmuseum Amsterdam, Inv. BK-16083, Height 35cm [188].*

The second object selected was the Striding Nobleman (Figure 5.4.1b), a Renaissance copper alloy statue. Initially, it was thought that the Nobleman statue is a work by the sculptor Hendrick de Keyser[4], but after an examination using X-ray

[4] Hendrick de Keyser (1565-1621) was a Dutch sculptor and architect.

radiography [189] a bar was observed inserted inside the back of the statue that de Keyser never used in his bronzes.

5.4.2 Measurements on replica statue

In this section we would like to emphasize the results obtained for a trial experiment using the replica bronze statue.

5.4.2.1 Preliminary steps

The fiducial points were provided by attaching a number of steel spheres (with 1 cm diameter) on the surface of the replica statue. The tomographic images of the sample were obtained at the NEUTRA instrument from PSI using same instrument settings. The virtual sample model was extracted as a meshed surface of segmentation (Figure 5.4.2 a) and then imported into the ENGIN-X virtual instrument (Figure 5.4.2 c, d) elaborated in the SScanSS software.

5.4.2.2 Selecting the measurement points

From the tomography data many internal structures and features were revealed, such as internal cavities or the pins used in the casting process. Three different measurement points were placed (Figure 5.4.2 b) at selected small but compositionally distinctive features:

1. one point at the intersection of a steel pin with the wall of the casting;
2. a second point within the wall for comparison with the point 1;
3. the last point in the area where we suspect a casting cavity in the wall.

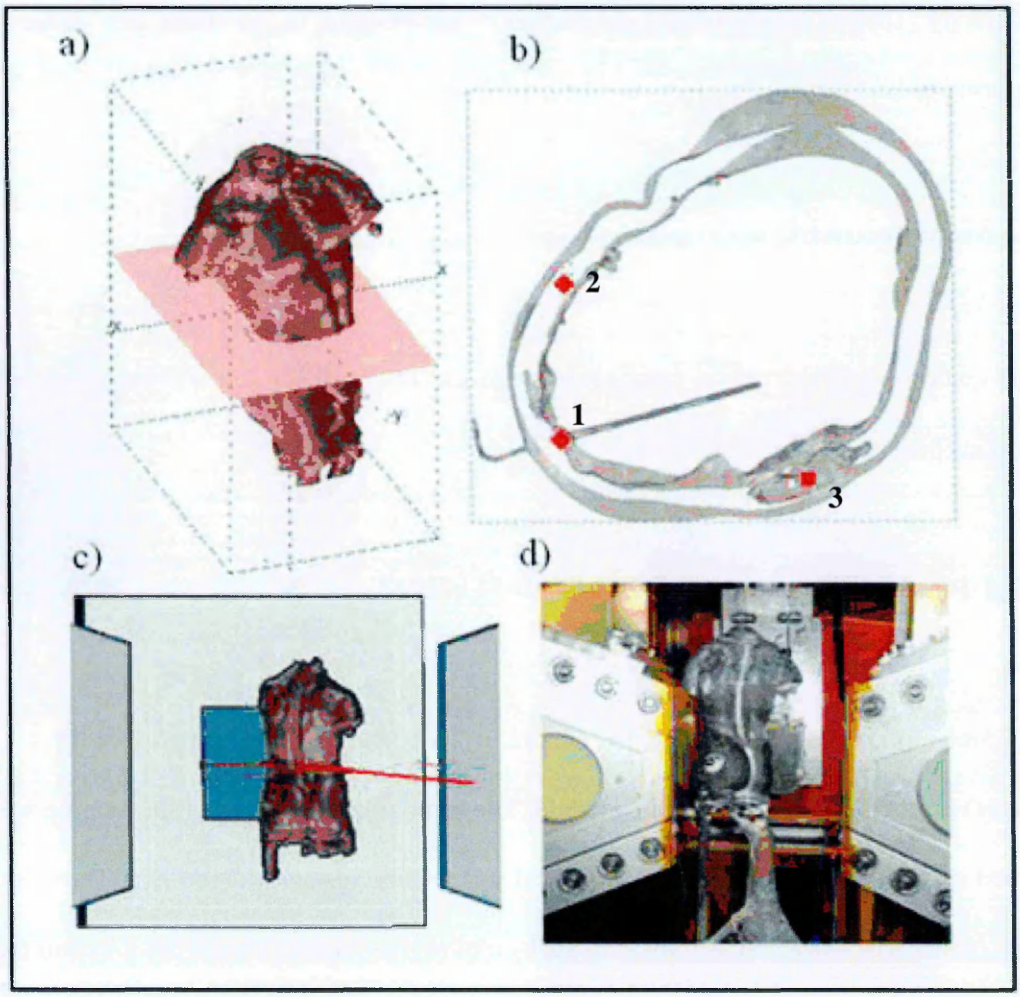

Figure 5.4.2: *Steps in TDD method on replica statue. (a) 3D model of the statue with selected plane; (b) selected measurements points and the corresponding simulated gauge volumes; (c) virtual sample and instrument; (d) real sample and instrument.*

5.4.2.3 Collecting the diffraction data

The settings of the real and virtual ENGIN-X instruments were similar to the settings used in the engineering bifurcation experiment. The only difference is that the sample was mounted directly on the rotation table and the goniometer system was not used. The slits and collimator were each set to 2 mm, defining a gauge volume of $2\times2\times2$ mm^3. The data for the points selected show low counting statistics mainly because the path lengths of the

neutrons through the material are longer. For data gathering we applied the same software, OpenGenie connected to the ENGIN-X instrument.

5.4.2.4 Results

After plotting the diffraction data there were observed peaks of bronze from the measurement points inside the wall of the sample. For the point chosen at the intersection of the pin with the statue's wall the diffraction pattern shows both the presence of the bronze peaks from the casting and fcc-iron from the pin. From the archaeological point of view the presence of (fcc) iron rather than (bcc) ferritic iron would indicate that the object measured was a copy not an original artefact. (Figure 5.4.3)

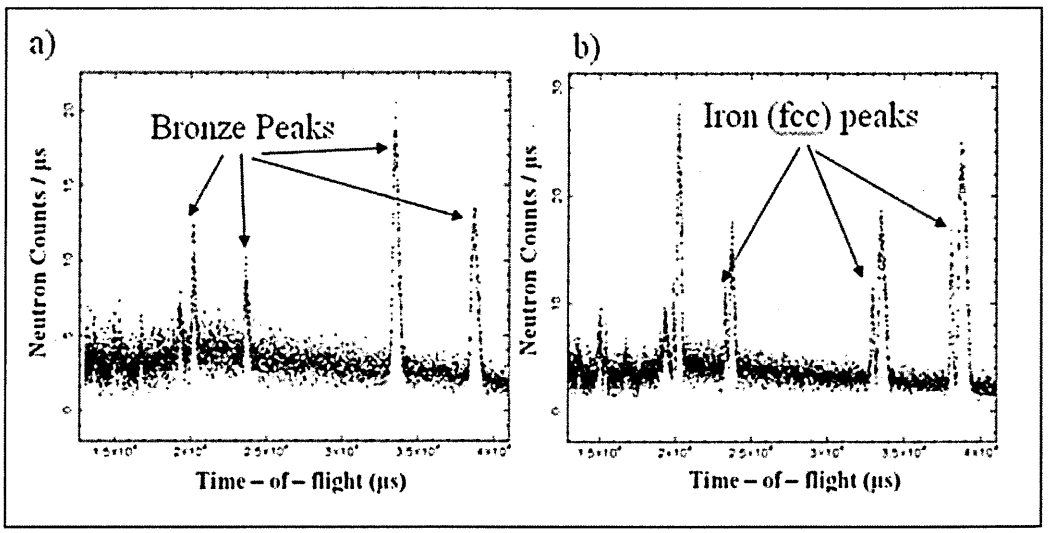

Figure 5.4.3: *Diffraction patterns for points selected in the replica statue. (a) Diffraction pattern collected inside the wall, showing the peaks of bronze; (b) Diffraction pattern from volume point where pin passes through casting, showing bronze and fcc-iron peaks.*

Low measured counts from points placed in the centre of apparent cavities within the wall of the statue indicated that they were indeed cavities rather than artefacts of the segmentation, providing that we could accurately locate such features for measurements.

The results from these measurements demonstrate the viability and practicability of the TDD approach in the investigation of complex archaeological samples in a non-destructive manner.

5.4.3 Investigation of Striding Nobleman statue

Following the success of the previous study a beamtime application was made to study the structure and composition of the Renaissance statue called the Striding Nobleman. It must be emphasized that before this research it was difficult to determine the composition of an alloy inside of a sculpture at a pre-determined point. It was observed that a Renaissance bronze statuette (the Striding Nobleman) from the Rijksmuseum's exhibition is magnetic[5] and it was suspected that the material compositions differ between the cast walls of the statue and the various internal constructional elements revealed by the tomography data. In the particular study of production techniques of this statuette two main aspects were of interest: the structure of the sculpture and the alloys that were used.

Because this object is precious and unique, the approach of attaching steel balls as "fiducial points" cannot be applied, so it was necessary to find an alternative strategy of employing prominent features of the statues itself.

5.4.3.1 Neutron imaging – experimental description

The neutron tomography experiment was performed earlier at the neutron imaging facility, NEUTRA, at PSI and it was not part of my study. For this reason, here, we present only few preliminary aspects to the application of TDD. Because the field of view was 27.2 cm

[5] This was discovered earlier using neodymium-based magnets to check for magnetic materials on bronze statues in the Rijksmuseum, to locate hidden parts of iron core pins which were used in the construction process of these statuettes.

the entire object was measured in two individual datasets by shifting the sculpture in height. Both datasets were stacked for reconstructing the entire sample using the VgStudio software. After reconstruction it was revealed that the statue is hollow, indirectly cast with separately cast arms and lower legs attached to the body by brazing and reinforced with bronze or brass rods in the shoulders and knees (Figure 5.4.4). Details about the imaging experiment are presented in [35].

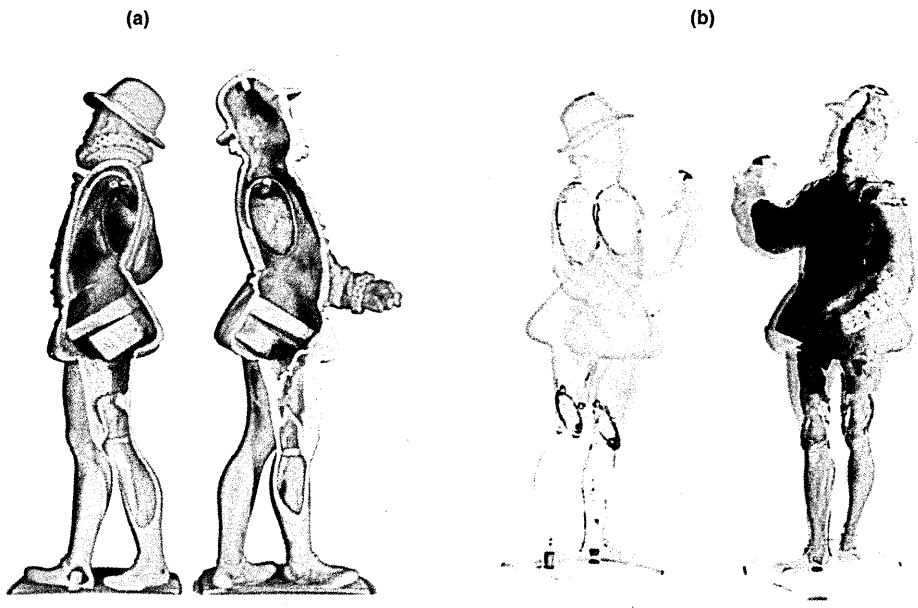

Figure 5.4.4: *Neutron tomography data of the Striding Nobleman. (a) Alloy/metal distribution; (b) Distribution of solder joints and hollow parts.*

After tomographic reconstruction the wall thicknesses can be estimated at any point (with an accuracy of 0.25 mm), two heavy wedge-shaped copper alloy plugs in the interior of the lower body and an arched insertion soldered in the statue's back (Figure 5.4.4 a). From the attenuation distribution of the neutrons the metal welds are visible in Figure 5.4.4 b (red colours). On the other hand from the attenuation map of the different copper alloys and the iron it was not possible to determine the metal compositions used in the statue. No indications of iron core pins were visible in the neutron tomography data. For this reason, it was necessary to extend our investigations to neutron diffraction measurements with Rietveld refinements.

5.4.3.2 Application of TDD method

A polygon surface model was extracted from VgStudio and imported into the SScanSS software. The required internal structures were identified on SScanSS generated sections through the model and measurements points were identified and marked. (Figure 5.4.5)

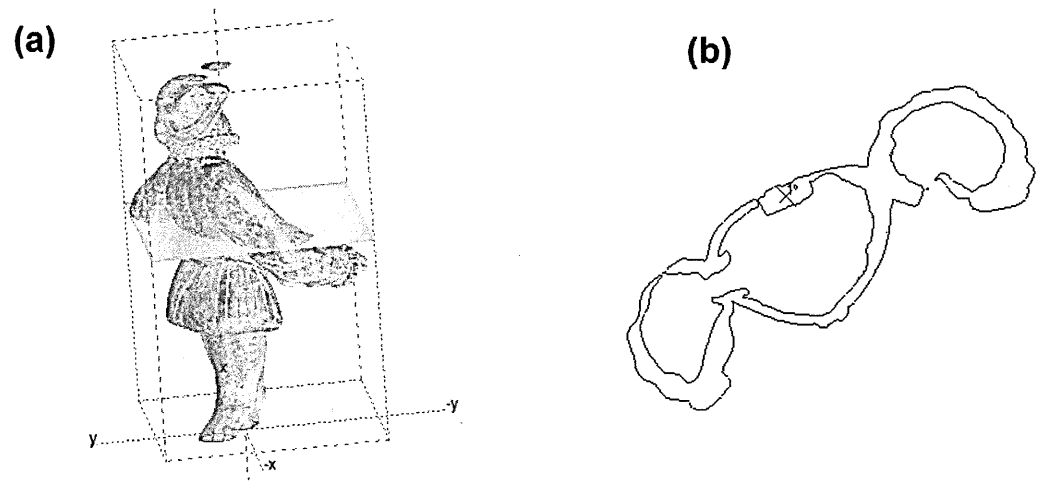

Figure 5.4.5: *Tomography data in SScanSS laboratory. (a) Cutting plane in the sample; (b) Placing the measurement points in the sample.*

The next step was to combine the virtual sample described as an STL model with the virtual ENGIN-X instrument model prior to generating the instrument control scripts.

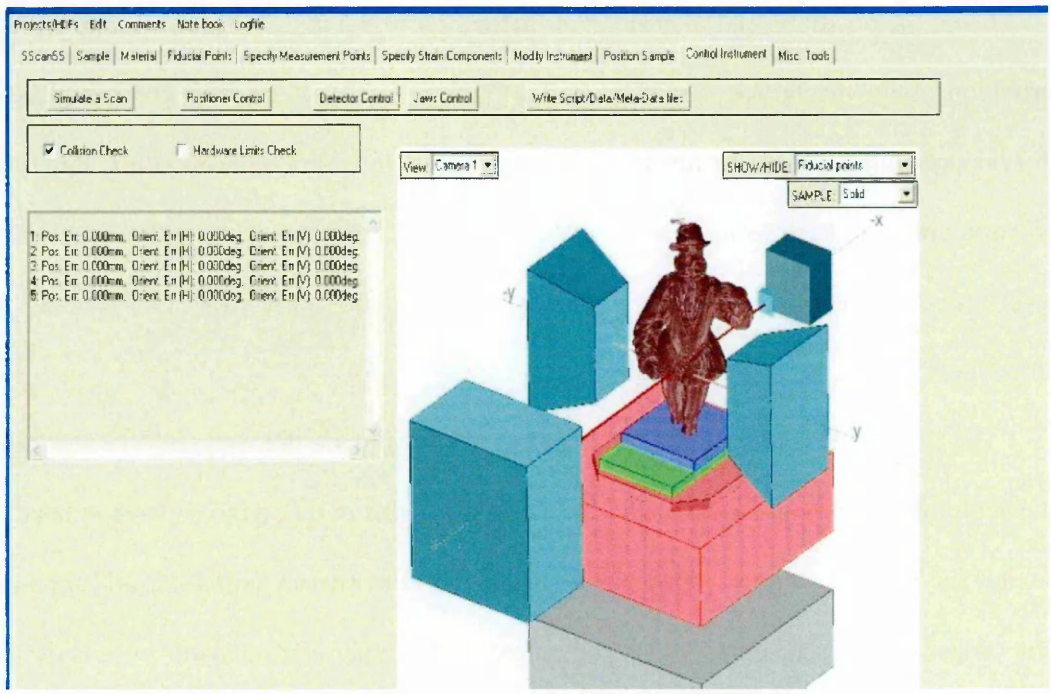

Figure 5.4.6: *Virtual sample positioned in the virtual ENGIN-X instrument*

To determine the initial position of the statue and to correctly align it within the virtual SScanSS laboratory we used as fiducial markers the fingers of the hands and the tip of the nose of the Striding Nobleman. The position of these features was measured using a touch-probe. As in the previous experiments, the SScanSS software was used to automatically generate the required instrument control scripts (Figure 5.4.6).

5.4.3.3 Neutron diffraction results

The size of the gauge volume used through the measurements was adjusted by the jaws and the pair of radial collimators in front of the neutron scintillation detectors at 4×5×2 mm^3 with a beam cross-section of 4×5 mm^2 (width × height) and a diffracting length of 2 mm along the beam direction as determined by the collimators. Applying the TOF method a full diffraction spectrum is obtained from a single measurement. The scattered neutrons are recorded in the two 90° detector banks, on either side of the sample position and at a distance of 1.5 m from the sample.

From the positions and intensities of diffraction peaks in the spectra we can extract information about the lattice parameter and weight fractions of crystallographic phases, such as copper alloys, lead, ferrite and corrosion phases. In addition, information about the microstructure and the material treatment can be deduced from the shape and intensities of the diffraction peaks, for example, whether or not the alloy was left as-cast or homogenized.

The diffraction pattern were collected from 34 points on the wall and internal parts of the sculpture: 20 points on the wall scan along front, one point on the support at back, 3 points on the internal wedge-shaped plugs, 4 points on the internal collar bar and 6 points on the proper right leg (Figure 5.4.7). The collection time per analysis point was about 30 minutes.

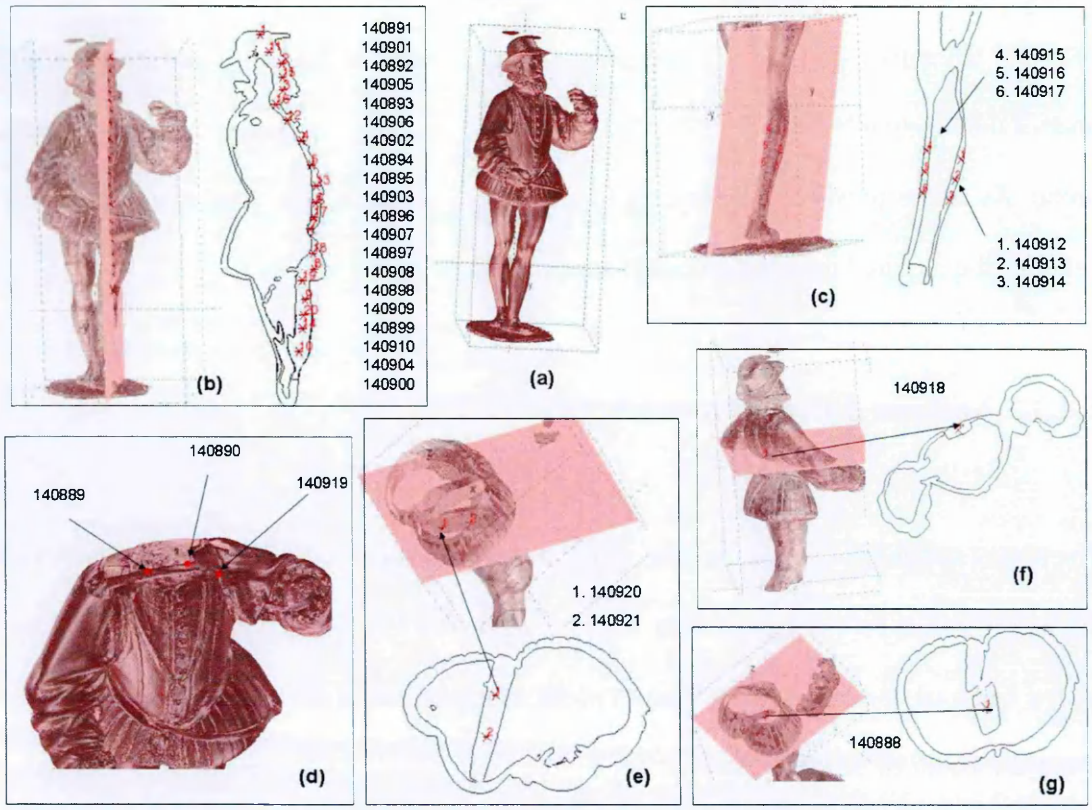

Figure 5.4.7: *Neutron analysis points selected on the tomography data in SScanSS software with the specific run numbers associated*

All the experimental data were analysed by the Rietveld method with the General Structure Analysis System (GSAS) and they are presented in the Table 5.4.1. The following crystal structures were included in the Rietveld model to fit the data, where u is the Debye-Waller factor [127]:

(1) α-phase (space group $Fm\bar{3}m$) with a lattice parameter in a range from a=3.6145 to a=3.67 Å; u=0.01 Å^2;

(2) Pb-phase (space group $Fm\bar{3}m$), u=0.034 Å^2; Pb does not dissolve into the copper lattice, and can therefore be observed as a separate phase with a characteristic Bragg peak at 2.86 Å;

(3) ferritic Fe phase (space group $Im\bar{3}m$), u=0.0041 Å^2;

(4) cuprite Cu_2O (space group $Pn\bar{3}m$), u=0.019 Å^2;

(5) Fe-Ni-Cu Cu-type phase (space group $Fm\bar{3}m$) with a lattice parameter of 3.588 Å and a composition of 1/3Fe, 1/3Ni, 1/3Cu, respectively, and u=0.01 Å^2.

The Debye-Waller parameters used are empirical values determined from pure materials.

Table 5.4.1: *Neutron diffraction results for Striding Nobleman statue.*

Analysis points	Rietveld refinement results						Calculated	
	Lattice parameter (Å)	Copper Alloy (wt %)	Pb (wt %)	Alpha Fe (wt %)	Cu_2O (wt %)	Fe-Ni-Cu (wt %)	Cu (wt %)	Zn (wt %)
Wall scan along front (Fig.5.4.7b)								
140891	3.6506	96.8	2.5	0.7	(<0.3)	-	83.4	16.6
140892	3.6514	96.4	3.1	0.5	(<0.1)	-	83.1	16.9
140893	3.6500	96.2	2.8	0.2	(<0.2)	0.8	83.7	16.3
140894	3.6496	99.0	(<3.5)	1.0	(<0.1)	-	83.0	17.0

140895	3.6501	98.9	(<2.3)	1.1	(<0.6)	-	82.8	17.2
140896	3.6506	95.6	3.3	1.1	(<0.3)	-	82.9	17.1
140897	3.6494	98.4	(<5.3)	1.6	(<0.9)	-	83.2	16.8
140898	3.6507	100	(<2.0)	(<0.2)	(<0.1)	-	83.4	16.6
140899	3.6511	96.2	3.5	0.3	(<0.2)	-	83.2	16.8
140900	3.6517	95.4	3.5	1.1	(<0.2)	-	82.9	17.1
140901	3.6508	96.2	3.3	0.5	(<0.2)	-	83.3	16.7
140902	3.6509	95.0	3.9	1.1	(<0.4)	-	83.0	17.0
140903	3.6510	95.8	3.1	1.1	(<0.1)	-	83.0	17.0
140904	3.6512	96.0	3.2	0.8	(<0.1)	-	83.2	16.8
140905	3.6502	95.5	3.6	0.1	(<0.2)	0.8	83.6	16.4
140906	3.6504	96.6	2.5	0.9	(<0.5)	-	83.2	16.8
140907	3.6507	95.2	3.7	1.1	(<0.1)	-	83.1	16.9
140908	3.6501	95.2	3.7	0.4	(<0.1)	0.7	83.6	16.4
140909	3.6511	95.9	3.0	0.5	(<0.1)	0.6	83.2	16.8
140910	3.6513	95.9	3.7	0.4	(<0.1)	-	83.1	16.9
Support at back (Fig. 5.4.7f)								
140918	3.6654	100	(<3.3)	(<0.1)	(<1.0)	-	77.0	23.0
Internal wedge-shaped plugs (Fig.5.4.7e, Fig.5.4.7g)								
140888	3.6524	94.5	5.5	(<0.1)	(<0.5)	-	82.7	17.3
140920	3.6499	100	(<5.3)	(<0.5)	(<1.1)	-	83.7	16.3
140921	3.6494	97.2	2.8	(<0.1)	(<0.1)	-	84.0	16.0
Internal collar bar (Fig.5.4.7d)								
140889	3.6160	97.0	(<1.4)	(<0.2)	3.0	-	98.6	1.4
140890	3.6159	97.0	(<0.3)	(<0.3)	3.0	-	98.6	1.4
140911	3.6162	97.9	(<1.4)	(<0.1)	2.1	-	98.5	1.5
140919	3.6513	95.4	3.6	1.0	(<0.3)	-	83.2	16.8
Proper right Leg (Fig.5.4.7c)								
140912	3.6626	100	(<4.2)	(<0.1)	(<0.3)	-	77.6	22.4

140913	3.6623	100	(<6.4)	(<0.1)	(<0.8)	-		77.6	21.7
140914	3.6606	100	(<6.4)	(<0.6)	(<1.1)	-		77.9	22.1
140915	3.6534	97.4	2.6	(<0.1)	(<0.1)	-		82.4	17.6
140916	3.6537	97.9	2.1	(<0.1)	(<0.1)	-		82.3	17.7
140917	3.6528	97.5	2.5	(<0.2)	(<0.3)	-		82.5	17.5

The lattice constant of the copper alloy depends on the presence of alloying elements such as Sn, Zn, Sb and As. From the lattice parameters of the α-phase, the contents of the alloying elements can be obtained according to Vegard's rule, for example using a calibration curve for binary Cu-Sn alloys. Partitioning of the copper alloy into Cu and Zn in Table 5.4.1 was achieved in a similar way using an experimental calibration curve for Cu-Zn system [190].

The variation in alloy composition is determined from the lattice parameter of the copper-type phase. A phase fraction entry in brackets (see Table 5.4.1), e.g. (<2) indicates an upper limit of a phase not actually observed in the data, based on the counting statistics. For the Striding Nobleman statue only three different copper alloy compositions were observed.

The main alloy of the sculpture, i.e. inside the wall, shows a copper alloy which is characterized by an average lattice parameter of 3.6506 Å (e.g. point 140891) and which varies only slightly for the wall scan. Further crystallographic phases are observed inside the wall of the statue: a Pb-phase with an average content of 3.5wt%, and a ferritic Fe-phase with an average content of 0.8wt%. Considering that the X-ray fluorescence measurements predominantly identify Zn as the alloying elements [35], the Zn-contents in the copper alloy phase can be estimated to be 16.8wt% (Table 5.4.1). This calculation, however, ignores the effects of other alloying elements on the copper-alloy lattice. It should be noticed that at some isolated points on the front side of the statue, small amounts (0.8wt%) of a secondary fcc phase with a lattice parameter of 3.588 Å is found. The lattice

constant of this phase is characteristically lower than the lattice constant of pure copper. The elemental composition is interpreted based on the lattice parameter observed and match with the Fe-Ni-Cu database entry.

The point from the internal support bar in the back of the sculpture (140918) has a slightly larger lattice parameter, and corresponding Zn content (23%).

The lattice parameter of the alloy on one side of the proper right leg is slightly increased (points 140912, 140913, 140914) pointing to a different alloy composition. The data for these points (Figure 5.4.7 c) show considerably lower counting statistics mainly because the path lengths of the neutrons through the material are longer. We have also considered a partially filled gauge volume for explaining the reduced counts for these points but came to the conclusion that this cannot account for the observed increase of the lattice parameter.

The alloy compositions of internal wedge-shaped plugs in the lower part of the sculpture (points 140888, 140920, 140921) are comparable to the composition of the wall.

In contrast, the internal collar bar at the height of the shoulders (Figure 5.4.7 d) exhibits a completely different alloy composition, as indicated by a lattice parameter of 3.616 Å (point 140889) which is close to the lattice parameter of pure copper. The calculated Zn content of 1.5% is hardly significant. Additionally the collar bar exhibits a small amount of Cu_2O (which could be caused by reheating the sculpture and where no flux could protect the Cu from oxidizing).

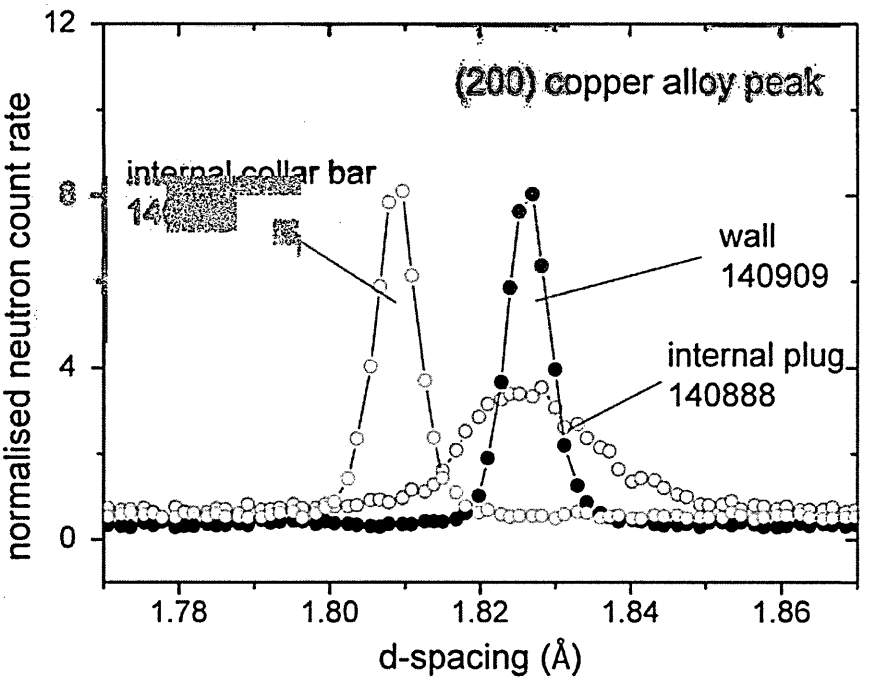

Figure 5.4.8: *Comparison of neutron diffraction peak profiles, (200) Bragg peak, for different analysis points.*

Additional information can be obtained from the analysis of the shape of the Bragg peaks. Figure 5.4.8 compares the (200) Bragg peak for the wall, internal collar bar, and the internal support plugs. From these plots we can remark that the peak positions are indicative of the lattice parameter, i.e. Zn content, which is the same for wall and plug but different for wall and collar bar. Another assumption is that the profiles of the wall peaks are narrow, almost matching the instrument resolution, indicating a homogenized copper alloy (which could indicate heat treatment). The very large widths of the peak profiles of the internal plugs, even though with the same composition as the wall, are rather indicative of as-cast alloys, exhibiting segregated, dendritic microstructures.

The results from this experiment show that combining neutron tomography and neutron diffraction techniques we can obtain new insights into the composition and hence production techniques of Renaissance copper alloys statues. Also, the ferrite inclusions obtained throughout the object is the answer to the question about magnetic attraction of the statuette to a permanent magnet.

5.5 Conclusions

The experiments applied on the engineering sample (bifurcation) and cultural heritage samples (replica statue and Nobleman statue) carried out at the NEUTRA and ENGIN-X instruments illustrated several advantages of the application of the tomography driven diffraction method.

In the archaeological research field, TDD offers the ability to conveniently and rapidly characterise features that are visible within a tomography as variations in attenuation coefficients, but whose exact compositional and microstructural nature is not known.

Taking into account the previous experience in the engineering field where the method is applied regularly using laser generated virtual models we can say that positioning accuracy of at least 0.1 mm can be easily achieved. This level of positioning accuracy is comparable to using the traditional method of finding the surface of the sample by means of repeated wall scans. For experiments, such as surface investigations, where the highest degree of positioning accuracy is essential it is the possibility of augmenting the fiducial point based positioning approach with wall scan data.

The alignment of the sample using the SScanSS software realized an important gain of time available for measurement, which is very beneficial during the short period of time generally allocated for neutron experiments.

Using two separate imaging and diffraction instruments at the different locations requires extra travelling expenses and the movement of the samples between the instruments. This is not optional, especially when we have an artefact or a valuable object such as the Striding Nobleman statue. Because the TDD method is ideally suitable on the coupled imaging-diffraction instruments, one future development is to apply this technique on combined imaging and diffraction instruments such as the JEEP synchrotron X-ray

station at DIAMOND in the UK or the future IMAT neutron instrument at ISIS. On such instruments it will be possible to perform the tomography, mark the measurement points and proceed to the diffraction measurements as one continuous process without the need for any sample movement or repositioning.

6 Conclusions and future work

6.1. Summary and main conclusions

The purpose of this research was to make specific contributions to the design and optimization of the IMAT instrument in imaging mode and to develop a combined imaging and diffraction technique, Tomography Driven Diffraction, which would utilise the unique features of this instrument.

6.1.1. IMAT – instrument optimization

The IMAT instrument is currently being built on a cold moderator on the ISIS second target station (TS-2) offering a combination of imaging and spatially resolved diffraction applications such as neutron radiography, neutron tomography, energy-selective imaging, neutron strain scanning, crystallographic structure and phase analysis, and texture analysis. The two main areas of investigation regarding the design and optimization of the imaging mode of the IMAT instrument have been:

- **Modelling, investigation and optimisation of individual instrument components.**
- **Evaluation of complete IMAT design.**

The design of the IMAT instrument was challenging due to the combination of both measurement modes, imaging and diffraction, which imposes constraints on the individual parts of the instrument, but particularly on the neutron guide which was required for obtaining a good time resolution for diffraction and energy-selective imaging. All the

calculations for IMAT imaging part were done using Monte Carlo simulations performed by the McStas software package.

The use of a neutron guide was unusual for an imaging instrument and this component was optimised, by varying its geometrical dimensions and reflectivities, in order to maximise the neutron flux on the sample position for imaging and diffraction experiments and obtain symmetric open beam images. Also, the spatial and spectral homogeneity of the neutron beam profile was considered. The large cross section of the straight neutron guide (95×95 mm^2) provides a flux for imaging on the sample position of 10^7 [$n/cm^2/s$] at higher energies at reasonable costs and a symmetric open beam field for neutron imaging. The combination of pulsed source operation with a neutron guide allows for energy-selective imaging with high wavelength resolution. On the other hand, the simulated data shows that, particularly with decreasing pinhole size, the intensity distribution on the imaging screen, at the sample position is inhomogeneous, exhibiting geometric patterns (i.e. artefacts or stripes). The primary cause of the geometric artefacts was found to be that there are regions of the detector at the sample position, which look at points on the guide/moderator system from which no neutrons emanate, such as chopper gaps or regions outside of the moderator. These image artefacts can be reduced at source by consideration of the guide geometry, and further corrected by pixel-by-pixel normalisation at the data processing stage. For the lower L/D values these artefacts are present but they are washed out due to the higher divergence and corresponding lower resolution.

Depending on the requirements of particular imaging experiments (for example do they require higher neutron flux or higher spatial resolution) the L/D collimation ratio can be varied for different pinhole sizes and for a fixed distance L (L=10 m) between pinhole and imaging detector. Increasing the pinhole size (so, decreasing L/D) the neutron flux is increased, but also the blurring due to the larger beam divergence.

The maximum neutron beam diameter for imaging on IMAT, corresponding to the maximum field-of-view (FOV), was chosen to be 200 mm at the sample position whereas the minimum beam size for diffraction will be 1 mm. The maximum FOV for imaging is given by the pinhole-camera distance but also limited by the operational space available at the sample position for sample movements and the diffraction detector installations. The choice of a maximum FOV is also constrained by the requirement to build a compact, transportable camera box.

Preliminary studies into the IMAT's expected performance were made using simulated tomography experiments. Such experiments were carried out using different McStas sample models. The first such model modelled attenuation as wavelength independent and was used to investigate the reconstruction of a cylindrical sample. The second enabled wavelength dependent attenuation and was used to investigate more subtle wavelength dependent effects such as beam hardening.

6.1.2. Tomography driven diffraction on the IMAT instrument

A main driver for this thesis was to develop a method for making use of the natural complementarity between the neutron tomography and neutron diffraction. The result was the Tomography Driven Diffraction (TDD) method [14] in which geometry information extracted from tomographies is used to guide diffraction measurements. The advantage of the TDD method is that the tomography data replace the previously used laser scan data and so provide information about internal as well external geometry of the sample, in the sense of dimensions, shape, internal defects or density. Using such data, in conjunction with the virtual laboratory provided by the strain scanning simulation software SScanSS [168] enables the placing and control of diffraction measurements, which, in contrast to a tomography experiment only measure over a volume of a few cubic millimetres known as the gauge volume. The method was tested using experiments applied on samples drawn

from engineering and cultural heritage research. These experiments were carried out using the NEUTRA and ENGIN-X instruments and supported the viability of the tomography driven diffraction method. For engineering the ability to guide residual strain diffraction measurements accurately in relation to internal features was demonstrated to be a valuable new possibility to the measurement of stress within an engineering sample. In the archaeological research field, TDD offers the ability to conveniently and rapidly characterise features that are visible within a tomography, as variations in attenuation coefficients, but whose exact compositional and microstructural nature is not known.

The concept, TDD, will be a useful tool to the IMAT instrument which combines imaging and diffraction on one beamline. Hence, TDD will utilize IMAT tomography data for diffraction scans on IMAT. Moreover, the method can be applied to ENGIN-X with imaging data from IMAT.

6.2. Future work

Whilst we have provided useful results for the design and optimization of the IMAT imaging part, we have also discovered other areas where improvements can be made through future work:

- Continue with further simulations of white beam and energy selective radiography and tomography experiments in order to more fully explore issues of image quality and processing.

- Because we used a lambda monitor rather than a TOF monitor, the need to perform simulations using a proper TOF monitor in McStas will be addressed in the future.

- Throughout most of this work, the gravitation effect was neglected; however, a preliminary study was carried out into the effect of the gravity on the radiography blurring. This preliminary research on the gravity effect on the image could be developed by simulating these effects depending on the pinhole size enabling the expected resolution to be calculated depending on the collimation ratio, the distance between sample and monitor and the gravitational effect. Moreover, useful information on the radiographies could be obtained by comparing the blurring effect due to gravity with the blurring effect depending on the divergence or due to the finite resolution of the cameras. Given the energy selective capability of IMAT the possibility might exist to reduce the effect of gravitational blurring, which is essentially an energy dependent phenomenon.

- In the monoenergetic beam the Lambert-Beer law $I = I_0 e^{-\mu l}$ is defined as a linear relationship between the proportion of radiation absorbed and the path length through the material. In the case of a polychromatic beam this statement is not valid because different wavelengths are absorbed differently. Generally the attenuation coefficients are integrated over all energies in the neutron spectrum and the flatfield correction applied. IMAT will take the advantage of the pulsed source which will offer the possibility of applying wavelength dependant flat-fielding which may be advantageous. This issue needs to be addressed in future work.

- Due to limited beam time, more work on determining the accuracy, under different experimental circumstances, of sample positioning using the TDD method is required. Issues to be investigated in the future would include:
    - effect of distortions and artefacts in tomography data;
    - best type of fiducial points to use;

- effects of magnification in tomography data;
- to investigate advantages of combining tomography and laser data in order to improve positioning accuracy.

- Using two separate imaging and diffraction instruments at the different locations requires extra travelling expenses and the movement of the samples between the instruments. Because the TDD method is also suitable on the coupled imaging-diffraction instruments, one future development is to apply this technique on IMAT instrument. On such instrument it will be possible to perform the tomography, mark the measurement points and proceed to the diffraction measurements as one continuous process.

Appendix 1

Calculation of the projection of the image onto the moderator, reflection angle and number of neutron reflectivities in the guide

```
#include<iostream>
#include<cmath>
#include<stdio.h>
#include<conio.h>
#define pi 3.14159265

int main()
{
FILE* fout = fopen("out100.csv", "w");

float image,pinhdet=10,xguide=42.8,guidepinh=1.5,modguide=1.7,
yguide=0.055,theta,xa,x0,x1,yn1,yn2,xn,y0,c,EF;
int n;
image=0;
while (image<0.10){
    image=image+0.001;
    std::cout <<"Image value"<<image<<std::endl;
    std::cout << "pinhdet"<<pinhdet<< std::endl;
    std::cout << "xguide"<<xguide<< std::endl;
    std::cout << "guidepinh"<<guidepinh<< std::endl;
    std::cout << "modguide"<<modguide<< std::endl;
    std::cout << "yguide"<<yguide<< std::endl;
    xa=modguide+xguide+guidepinh+pinhdet;
    x0=modguide+xguide+guidepinh;
    x1=x0+(x0-xa)*yguide/image;
    c=image/pinhdet;
    theta=atan(c)*180/pi;
    yn1 = -yguide;
    yn2 = yguide;
if ((modguide<x1)&&(x1<(modguide+xguide)))
{
   std::cout << "reflections:YES" <<std::endl;
   int k = 1;//number of reflections
    n=1;
    int nmax=0;
    float yprint=0;
    float EFmax=0;
    while (n<12)
    {
          xn=(2*n-1)*(x1)-2*(n-1)*x0;
          std::cout<<"xn"<<xn<<std::endl;
          if ((modguide<xn)&&(xn<(modguide+xguide)))
          {
              if (n%2==1)
              {   EF=yn1+xn*image/(xa-x0);
                  nmax=n;
                  EFmax=EF;
                  yprint = yn1;
```

```
                }
                else
                {
                    EF=yn2-xn*image/(xa-x0);
                    EFmax=EF;
                    nmax=n;
                    yprint = yn2;
                 }
                std::cout<<"has reflections:"<<nmax<<std::endl;
            }
            else
            {
            break;
            }
            k++;
            n++;
    };
    /*if ((-0.055<EFmax)&&(EFmax<0.055)) {*/
    std::cout <<"("<<xn<<","<<yn1<<","<<EFmax<<"
"<<nmax<<")"<<std::endl;
    fprintf(fout, "%f,%f,%f,%f,%d\n",theta,image, EFmax,yprint,
nmax);

}

  else {        EF=-image*(modguide+xguide+guidepinh)/pinhdet;
                /* if ((-0.055<EF)&&(EF<0.055))
               {*/ std::cout <<"("<<EF<<")"<<std::endl;
                fprintf(fout, "%f,%f,%f",theta,image,EF);
                fprintf(fout, ",%d\n",0);
                std::cout<<"reflections:"<<0<<std::endl;}
std::cout << "The arc tangent of " << c << " : "
<<theta<<std::endl;
  }
getch();
fclose(fout);
return 0;
}
```

Appendix 2

IMAT imaging instrument modelled in McStas (initial stage)

```
DEFINE INSTRUMENT IMAGING(l_min=0.1,l_max=10)

DECLARE
%{
   double e_min, e_max;

%}
INITIALIZE
%{
      e_min=81.799/l_max/l_max;
      e_max=81.799/l_min/l_min;


%}
TRACE

COMPONENT moderator = ISIS_moderator(
    Face = "w5", E0 = e_min, E1 = e_max, dist = 1.699,
    xw = 0.11, yh = 0.11, modXsize = 0.11, modYsize = 0.11,
    CAngle = 0, SAC=1)
  AT (0,0,0) ABSOLUTE

COMPONENT myguide = Guide(
    w1 = 0.095, h1 = 0.095, w2 = 0.095, h2 = 0.095, l = 42.8, m = 3)
  AT (0, 0, 1.7) RELATIVE moderator

COMPONENT PSDdet1 = PSD_monitor(
    nx = 100, ny = 100, filename = "PSD1.dat",
  xmin =-0.1, xmax =0.1, ymin = -0.1, ymax =0.1)
  AT (0.0, 0.0, 42.8001) RELATIVE myguide

COMPONENT lmon1 = L_monitor(
    nchan = 1000, filename = "lmon1.dat",  xmin = -.10,
    xmax =.10, ymin = -.10,
    ymax = .10, Lmin = l_min,
    Lmax = l_max)
  AT (0.0, 0.0, 42.8002) RELATIVE myguide

COMPONENT pinhole1 = Circular_slit(radius=0.01)
  AT (0.0, 0.0, 46) RELATIVE moderator

COMPONENT PSDdet2= PSD_monitor(
    nx = 100, ny = 100, filename = "PSD2.dat",
  xmin =-0.1, xmax =0.1, ymin = -0.1, ymax =0.1)
  AT (0.0, 0.0, 10) RELATIVE pinhole1

COMPONENT lmon2 = L_monitor(
    nchan = 1000, filename = "lmon2.dat",  xmin = -.10,
    xmax =.10, ymin = -.10,
    ymax = .10, Lmin = l_min,
    Lmax = l_max)
  AT (0.0, 0.0, 0.001) RELATIVE PSDdet2

END
```

Appendix 3

IMAT imaging instrument modelled in McStas (last stage)

```
DEFINE INSTRUMENT IMAGING (l_min=2, l_max=14)

DECLARE
%{
   double e_min, e_max;

%}
INITIALIZE
%{
      e_min=81.799/l_max/l_max;
      e_max=81.799/l_min/l_min;
%}
TRACE

COMPONENT moderator = ISIS_moderator(
    Face = "w5", E0 = e_min, E1 = e_max, dist = 1.699,
    xw = 0.11, yh = 0.11, modXsize = 0.11, modYsize = 0.11,
    CAngle = 0, SAC=1)
  AT (0,0,0) ABSOLUTE

COMPONENT PSDdet1 = PSD_monitor(
    nx = 100, ny = 100, filename = "PSD1.dat",
  xmin =-0.1, xmax =0.1, ymin = -0.1, ymax =0.1)
  AT (0.0, 0.0, 1.699) RELATIVE moderator

COMPONENT lmon1 = L_monitor(
    nchan = 1000, filename = "lmon1.dat", xmin = -.10,
    xmax =.10, ymin = -.10,
    ymax = .10, Lmin = l_min,
    Lmax = l_max)
  AT (0.0, 0.0, 1.699) RELATIVE moderator

COMPONENT myguide1= Guide(
    w1 = 0.1, h1 = 0.1, w2 = 0.1, h2 = 0.1, l = 2, m = 3)
  AT (0, 0, 1.7) RELATIVE moderator

COMPONENT PSDdet2 = PSD_monitor(
    nx = 100, ny = 100, filename = "PSD2.dat",
  xmin =-0.1, xmax =0.1, ymin = -0.1, ymax =0.1)
  AT (0.0, 0.0, 3.749) RELATIVE moderator

COMPONENT lmon2 = L_monitor(
    nchan = 1000, filename = "lmon2.dat", xmin = -.10,
    xmax =.10, ymin = -.10,
    ymax = .10, Lmin = l_min,
    Lmax = l_max)
  AT (0.0, 0.0, 3.749) RELATIVE moderator

COMPONENT myguide2= Guide(
    w1 = 0.095, h1 = 0.095, w2 = 0.095, h2 = 0.095, l = 8.05, m = 3)
  AT (0, 0, 3.75) RELATIVE moderator

COMPONENT PSDdet3 = PSD_monitor(
    nx = 100, ny = 100, filename = "PSD3.dat",
```

```
  xmin =-0.1, xmax =0.1, ymin = -0.1, ymax =0.1)
  AT (0.0, 0.0, 11.899) RELATIVE moderator

COMPONENT lmon3 = L_monitor(
    nchan = 1000, filename = "lmon3.dat",  xmin = -.10,
    xmax =.10, ymin = -.10,
    ymax = .10, Lmin = l_min,
    Lmax = l_max)
  AT (0.0, 0.0, 11.899) RELATIVE moderator

COMPONENT myguide3= Guide(
    w1 = 0.095, h1 = 0.095, w2 = 0.095, h2 = 0.095, l = 0.275, m = 3)
  AT (0, 0, 11.9) RELATIVE moderator

COMPONENT PSDdet4 = PSD_monitor(
    nx = 100, ny = 100, filename = "PSD4.dat",
  xmin =-0.1, xmax =0.1, ymin = -0.1, ymax =0.1)
  AT (0.0, 0.0, 12.224) RELATIVE moderator

COMPONENT lmon4 = L_monitor(
    nchan = 1000, filename = "lmon4.dat",  xmin = -.10,
    xmax =.10, ymin = -.10,
    ymax = .10, Lmin = l_min,
    Lmax = l_max)
  AT (0.0, 0.0, 12.224) RELATIVE moderator

COMPONENT myguide4= Guide(
    w1 = 0.095, h1 = 0.095, w2 = 0.095, h2 = 0.095, l = 0.5, m = 3)
  AT (0, 0, 12.225) RELATIVE moderator

COMPONENT PSDdet5 = PSD_monitor(
    nx = 100, ny = 100, filename = "PSD5.dat",
  xmin =-0.1, xmax =0.1, ymin = -0.1, ymax =0.1)
  AT (0.0, 0.0, 13.074) RELATIVE moderator

COMPONENT lmon5 = L_monitor(
    nchan = 1000, filename = "lmon5.dat",  xmin = -.10,
    xmax =.10, ymin = -.10,
    ymax = .10, Lmin = l_min,
    Lmax = l_max)
  AT (0.0, 0.0, 13.074) RELATIVE moderator

COMPONENT myguide5= Guide(
    w1 = 0.095, h1 = 0.095, w2 = 0.095, h2 = 0.095, l = 7.3, m = 3)
  AT (0, 0, 13.075) RELATIVE moderator

COMPONENT PSDdet6 = PSD_monitor(
    nx = 100, ny = 100, filename = "PSD6.dat",
  xmin =-0.1, xmax =0.1, ymin = -0.1, ymax =0.1)
  AT (0.0, 0.0, 20.424) RELATIVE moderator

COMPONENT lmon6 = L_monitor(
    nchan = 1000, filename = "lmon6.dat",  xmin = -.10,
    xmax =.10, ymin = -.10,
    ymax = .10, Lmin = l_min,
    Lmax = l_max)
  AT (0.0, 0.0, 20.424) RELATIVE moderator

COMPONENT myguide6= Guide(
    w1 = 0.095, h1 = 0.095, w2 = 0.095, h2 = 0.095, l = 25.275, m = 3)
  AT (0, 0, 20.425) RELATIVE moderator

COMPONENT PSDdet7 = PSD_monitor(
    nx = 100, ny = 100, filename = "PSD7.dat",
```

```
  xmin =-0.1, xmax =0.1, ymin = -0.1, ymax =0.1)
  AT (0.0, 0.0, 45.701) RELATIVE moderator

COMPONENT lmon7 = L_monitor(
    nchan = 1000, filename = "lmon7.dat",  xmin = -.10,
    xmax =.10, ymin = -.10,
    ymax = .10, Lmin = l_min,
    Lmax = l_max)
  AT (0.0, 0.0, 45.701) RELATIVE moderator

COMPONENT pinhole= Circular_slit(radius=0.0025)
  AT (0.0, 0.0, 46) RELATIVE moderator

COMPONENT slit1 = Slit(
    xmin = -0.017125, xmax = 0.017125, ymin = -0.017125, ymax = 0.017125)
  AT (0.0, 0.0, 1.5) RELATIVE pinhole

COMPONENT slit2 = Slit(
    xmin = -0.03175, xmax = 0.03175, ymin = -0.03175, ymax = 0.03175)
  AT (0.0, 0.0, 3) RELATIVE pinhole

COMPONENT slit3 = Slit(
    xmin = -0.046375, xmax = 0.046375, ymin = -0.046375, ymax = 0.046375)
  AT (0.0, 0.0, 4.5) RELATIVE pinhole

COMPONENT slit4 = Slit(
    xmin = -0.061, xmax = 0.061, ymin = -0.061, ymax = 0.061)
  AT (0.0, 0.0, 6) RELATIVE pinhole

COMPONENT slit5= Slit(
    xmin = -0.07075, xmax = 0.07075, ymin = -0.07075, ymax = 0.07075)
  AT (0.0, 0.0, 7) RELATIVE pinhole

COMPONENT PSDdet8 = PSD_monitor(
    nx = 100, ny = 100, filename = "PSD8.dat",
  xmin =-0.1, xmax =0.1, ymin = -0.1, ymax =0.1)
  AT (0.0, 0.0, 10) RELATIVE pinhole

COMPONENT lmon8 = L_monitor(
    nchan = 1000, filename = "lmon8.dat",  xmin = -.10,
    xmax =.10, ymin = -.10,
    ymax = .10, Lmin = l_min,
    Lmax = l_max)
  AT (0.0, 0.0, 10) RELATIVE pinhole

END
```

Bibliography

1. Kockelmann, W., Kirfel, A., *Neutron diffraction imaging of cultural heritage objects.* Archeometriai Muhely, 2006. **2.**
2. Glascock, M., Neff, H., *Neutron activation analysis and provenance research in archaeology* Meas. Sci. Technol., 2003. **14**(9).
3. Révay, Z., Belgya, T., *Principles of the Pgaa Method*, in *Handbook of Prompt Gamma Activation Analysis with Neutron Beams*, L. Molnár, Editor. 2004, Kluwer Academic Publishers: London. p. 1-30.
4. Anderson, I., McGreevy, R., Bilheux, H., *Neutron Imaging and Applications - A reference for the Imaging Community.* Neutron Scattering Applications and Techniques. 2009: Springer US. 400.
5. Willis, B.T.M., Carlile, C.J., *Experimental Neutron Scattering.* 2009, Oxford: Oxford University Press.
6. Santisteban, J.R., Daymond, M.R., James, J.A., Edwards, L., *ENGIN-X: a third-generation neutron strain scanner.* J. Appl. Cryst., 2006. **39**: p. 812-825.
7. Lehmann, E.H., Vontobel, P., Wiezel, L. , *Properties of the radiography facility NEUTRA at SINQ and its potential for use as European reference facility.* Nondestructive Testing and Evaluation 2001. **16**(2-6): p. 191-202.
8. Kockelmann, W., Zhang, S.Y., Kelleher, J.F., Nightingale, J.B., Burca, G., James, J.A., *IMAT - a new imaging and diffraction instrument at ISIS.* Physics Procedia, 2012. **to appear.**
9. Bilheux, H., Penumadu, D., Watkin, K., Ankner, J. *Neutron Sciences Division Prospect for Imaging Capabilities* in *SNS-HFIR User Group Meeting* 2007. Oak Ridge National Laboratory, USA.
10. Kiyanagi, Y., et al., *Design study of the imaging beam line at J-PARC MLF, ERNIS.* Nuclear Instruments and Methods in Physics Research Section A: Accelerators, Spectrometers, Detectors and Associated Equipment, 2011. **651**(1): p. 16-20.
11. Santisteban, J.R., et al., *Engineering applications of Bragg-edge neutron transmission.* Applied Physics A: Materials Science & Processing, 2002. **74**: p. s1433-s1436.
12. Kockelmann, W., Frei, G., Lehmann, E.H., Vontobel, P., Santisteban, J.R., *Energy-selective neutron transmission imaging at a pulsed source.* Nuclear Instruments and Methods in Physics Research A, 2007. **578**: p. 421-434.
13. Lefmann, K., Willendrup, P. K., Udby, L., Lebech, B., Mortensen, K., Birk, J. O., KlenØ, K., Knudsen, E., Christiansen, P., Saroun, J., Kulda, J., Filges, U., Konnecke, M., Tregenna-Piggott, P., Peters, J., Lieutenant, K., Zsigmond, G., Bentley, P., Farhi, E., *Virtual experiments: the ultimate aim of neutron ray-tracing simulations.* Journal of Neutron Research, 2008. **16**(3): p. 97-111.
14. Burca, G., James, J. A., Kockelmann, W., Fitzpatrick, M. E., Zhang, S. Y., Hovind, J., van Langh, R., *A new bridge technique for neutron tomography and diffraction measurements.* Nuclear Instruments and Methods in Physics Research Section A, 2011. **651**(1): p. 229-235.
15. Sinha, S.K. *Science with light and neutron sources.* in *Proceeding of the 2011 Particle Accelerator Conference.* 2596-2598 (2011). New York, USA.
16. Rodríguez-Carvajal, J., *Recent Advances in Magnetic Structure Determination by Neutron Powder Diffraction.* Physica B, 1993. **192**: p. 55-69.
17. Riste, T., *Neutron-Scattering Studies of Critical Magnetic Phenomena.* Journal of Applied Physics, 1968. **39**(2): p. 528-532.

18. *The Paul Scherrer Institute.* [cited 2009 02-04]; Available from: http://www.psi.ch/.
19. Arzumanov, S., Bondarenko, L., Chernavsky, S., Fomin, A., Morozov, V, Panin, Y., Drexel, W., Schreckenbach, K., Geltenbort, P., Pendlebury, M., *Neutron life time value measured by storing ultracold neutrons with detection of inelastically scattered neutrons.* Phys.Lett., 2000. **B483**: p. 15-22.
20. Dierick, M., *Tomographic Imaging Techniques using Cold and Thermal Neutron Beams*, in *Faculty of Sciences, Department of Subatomic and Radiation Physics.* 2005, Gent: GENT. p. 183.
21. Koerner, S., E. Lehmann, and P. Vontobel, *Design and optimization of a CCD-neutron radiography detector.* Nuclear Instruments and Methods in Physics Research Section A, 2000. **454**(1): p. 158-164.
22. *Swiss Light Source.* [cited 2009 03-02]; Available from: http://www.psi.ch/sls/.
23. *SINQ, PSI.* [cited 2009 03-04]; Available from: http://sinq.web.psi.ch/.
24. *The Harwell Science and Innovation Campus.* [cited 2008 31-02]; Available from: http://www.harwelloxford.com/.
25. *Diamond Light Source.* [cited 2008 12-04]; Available from: http://www.diamond.ac.uk/.
26. *ISIS.* [cited 2008 12-02]; Available from: http://www.isis.stfc.ac.uk/.
27. *EPN-Campus.* [cited 2008 20-04]; Available from: http://www.epn-campus.eu/.
28. *ESRF.* [cited 2008 20-04]; Available from: http://www.esrf.eu/.
29. *ILL.* [cited 2008 04-20]; Available from: http://www.ill.eu/.
30. Parker, S.F., Carlile, C. J., Pike, T., Tomkinson, J., Newport, R. J., Andreani, C., Ricci, F. P., Sacchetti, F., Zoppi, M., *TOSCA: a world class inelastic neutron spectrometer.* Physica B: Condensed Matter, 1997. **241-243**(0): p. 154-156.
31. Hutchings, M.T., Krawitz, A., ed. *Measurement of residual and applied stress using neutron diffraction.* NATO ASI. Vol. 216. 1992. 588.
32. Pettersson, O.A., et al., *A facility for biomedical experiments with thermal neutrons.* Phys. Med. Biol., 1993. **38**: p. 1081-1088.
33. Zucali, M., et al., *Quantitative texture analysis of glaucophanite deformed under eclogite facies conditions (Sesia-Lanzo Zone, Western Alps): comparison between X-ray and neutron diffraction analysis.* Geological Society, London, Special Publications, 2002. **200**(1): p. 239-253.
34. Schwarz, D., Vontobel, P., Lehmann, E.H., Meyer, C.A., Bongartz, G., *Neutron tomography of internal structures of vertebrate remains: a comparison with X-ray computed tomography.* Palaeontologia Electronica. **8**(2): p. 11.
35. van Langh, R., James, J., Burca, G., Kockelmann, W., Zhang, S.Y., Lehmann, E., Estermann, M., Pappot, A., *New insights into alloy compositions: studying Renaissance bronze statuettes by combined neutron imaging and neutron diffraction techniques.* Journal of Analytical Atomic Spectrometry, 2011. **26**(5): p. 949-958.
36. Kockelmann, W., Kirfel, A., Siano, S., Frost, C.D., *Illuminating the past: the neutron as a tool in archaeology* Physics Education, 2004. **39**(155).
37. Filges, D., Goldenbaum, F., *Handbook of Spallation Research - Theory, Experiments and Applications.* 2009: WILEY-VCH Verlag GmbH&Co.
38. Kim, S.H. *The Status of the SNS Linac.* in *13th international Conference on Accelerator & Beam Utilization.* 2009. Korea.
39. Bauer, G.S., Dai, Y., Wagner, W., *SINQ layout, operation, applications and R&D to high power.* J. Phys. IV France 2002. **12**(8): p. 3-26.
40. Adams, D. *Proton beam line for the ISIS Second Target Station.* in *9th European Particle Accelerator Conference* 2004. Lucerne, Switzerland.

41. Kobayakawa, H., Boine-Frankenheim, O., *Synchrotrons and Storage Rings*, in *Digital Encyclopedia of Applied Physics*. 2003, Wiley-VCH Verlag GmbH & Co. KGaA.
42. Stacey, W.M., *Nuclear Reactor Physics*. 2nd ed. 2007: Wiley, John & Sons Inc.
43. Clause, K.N. *Triple axis spectrometers*. in *Trends and techniques in neutron beam research for medium and low flux research reactors*. 1997. Mumbai: International Atomic Energy Agency, Vienna.
44. Andersen, K., *Reactor&Spallation Neutron Sources*, in *Oxford School of Neutron Scattering*. 2011: Oxford.
45. Drexel, W.J., *Instrument Control and Data Acquisition System of the ILL High Flux Reactor Neutron Beam Instruments.* Nuclear Science, IEEE Transactions on, 1982. **29**(1): p. 123-126.
46. Carlile, C.J., *ILL in the changing international context.* Physica B: Condensed Matter, 2006. **385-386**(Part 2): p. 961-965.
47. Neuhaus, J., Petry, W., *Forschungsneutronenquelle Heinz Maier-Leibnitz (FRM II).* Neutron News, 2007. **18**: p. 13-15.
48. Hahn-Meitner-Institut, *Neutron-Scattering Instrumentation at the Research Reactor BER II*, M. Tovar, Robertson, T., Michaelsen, R., Editor. 2001, Hahn-Meitner-Institut: Berlin.
49. Sakurai, F., Horiguchi, Y., Kobayashi, S., Takayanagi, M., *Present status and future prospect of JRR-3 and JRR-4.* Physica B., 2002. **311**(1): p. 7-13.
50. Kennedy, S., *Construction of the neutron beam facility at Australia's OPAL research reactor.* Physica B., 2006. **285**: p. 949-954.
51. Lee, C.-H., Kang, Y-H, Kuk, I-H. *Proceedings of the 15th Meeting of the International Collaboration on Advanced Neutron Sources*. 2000. Tsukuba, Japan.
52. Chen, D.F., et al., *Development of neutron scattering on 60 MW research reactor in CIAE.* Physica B: Condensed Matter, 2006. **385-386**(Part 2): p. 966-967.
53. Taylor, A., *A journey through ISIS*. 2009, Science and Technology Facilities Council.
54. Jones, K.W., Schoenberg, K.F. *Operational status and future plans for the Los Alamos neutron science centre (LANSCE).* in *LINAC08*. 2008. Victoria, BC, Canada.
55. Mason, T.E., et.al., *The Spallation Neutron Source in Oak Ridge: A powerful tool for materials research.* Physica B., 2006. **385-386**: p. 955-960.
56. Nagamiya, S., *Overview of the J-PARC Project* J. Neutron Res., 2005. **13**(1): p. 7-10.
57. Schober, H., et al., *Tailored instrumentation for long-pulse neutron spallation sources.* Nuclear Instruments and Methods in Physics Research Section A: Accelerators, Spectrometers, Detectors and Associated Equipment, 2008. **589**(1): p. 34-46.
58. KENS. *Time-of-flight method.* 2004 [cited 2009 04-12]; Available from: http://neutron-www.kek.jp/kens2/kens_e/intro/intro03.html.
59. Thomason, J., *Introduction to the ISIS Accelerator and Targets*. 2011.
60. ISIS. *Technical description of the Second Target Station.* 2000 [cited 2012 RAL-TR-2000-032]; http://www.isis.stfc.ac.uk/about-isis/target-station-2/science/science-case-for-a-second-target-station-at-isis8174.html].
61. Schillinger, B., Lehmann, E., Vontobel, P., *3D neutron computed tomography: requirements and applications.* Physica B: Condensed Matter, 2000. **276-278**: p. 59-62.
62. Kak, A.C., Slaney , M., *Principles of Computerized Tomographic Imaging (Classics in Applied Mathematics)*. 1988, IEEE Press: University of Michigan.
63. Domanus, J.C., *Collimators for thermal neutron radiography. An overview.*, J.F.W. Markgraf, Editor. 1987, D. Reidel Publishing Co.

64. Domanus, J.C., ed. *Practical neutron radiography.* 1992, Kluwer Academic Publishers Dordrecht: Holland/Boston:USA/London:England.
65. Sartain, C.C., *PINEX: The pinhole neutron experiment.* 1958, Lawrence Livermore National Lab., CA (United States).
66. *Radon , J., Uber die Bestimmung von Funktionen durch ihre Integralwerte langs bestimmter Mannigfaltigkeiten.* Math_Nat.Kl, Ber.Verb.Sachs.Akad.Wiss.Leipzig, 1917. **69**: p. 262-277.
67. Ali, A.M., et al., *Image reconstruction techniques using projection data from transmission method.* Annals of Nuclear Energy, 2004. **31**(12): p. 1415-1428.
68. Dierick, M., B. Masschaele, and L. Van Hoorebeke, *Octopus, a fast and user-friendly tomographic reconstruction package developed in LabView (R).* Measurement Science & Technology, 2004. **15**(7): p. 1366-1370.
69. *LabView.* 1986 [cited 2009 02-06]; Available from: http://www.ni.com/labview/.
70. *Volume Graphics GmbH, VGStudioMax 2.0.* [cited 2009 02-04]; Available from: http://www.volumegraphics.com/products/vgstudiomax/index.html.
71. Materna, T., et al., *The cold neutron tomography set-up at SINQ.* Nuclear Instruments and Methods in Physics Research Section A: Accelerators, Spectrometers, Detectors and Associated Equipment, 2004. **525**(1-2): p. 69-73.
72. Banhart, J., *Advanced tomographic methods in research and engineering.* 2008: Oxford University Press.
73. Kardjilov, N., B. Schillinger, and E. Steichele, *Energy-selective neutron radiography and tomography at FRM.* Applied Radiation and Isotopes, 2004. **61**(4): p. 455-460.
74. Lehmann, E.H., et al., *Neutron imaging - Detector options in progress.* Journal of Instrumentation, 2011. **6**(01): p. C01050.
75. Lehmann, E., *Energy-selective neutron imaging. Radiography and tomography.* 2010, PSI.
76. Kardjilov, N., et al., *New features in cold neutron radiography and tomography Part II: applied energy-selective neutron radiography and tomography.* Nuclear Instruments and Methods in Physics Research Section A: Accelerators, Spectrometers, Detectors and Associated Equipment, 2003. **501**(2-3): p. 536-546.
77. Treimer, W., Strobl, M., Kardjilov, N., Hilger, A., Manke, I., *Wavelength tunable device for neutron radiography and tomography.* Applied Physics Letters 2006. **89**: p. 203504/1-3.
78. Baruchel, J., Cloetens, P., Härtwig, J., Ludwig, W., Mancini, L., Pernot, P., Schlenker, M., *Phase imaging using highly coherent X-rays: radiography, tomography, diffraction topography.* Journal of Synchrotron Radiation, 2000. **7**(3): p. 196-201.
79. Lehmann, E., et al., *Neutron imaging at the spallation source SINQ.* 2006, Paul Scherrer Institut: Villigen.
80. Allman, B.E., et al., *Imaging: Phase radiography with neutrons.* Nature, 2000. **408**(6809): p. 158-159.
81. Kardjilov, N., *Further developments and applications of radiography and tomography with thermal and cold neutrons* in *Fakultät für Physik.* 2003, Technischen Universität München: München. p. 133.
82. McMahon, P.J., Allman, B.E., Jacobson,D.L., Arif,M., Werner,S.A., Nugent, K.A. , *Quantitative Phase Radiography with Polychromatic Neutrons.* Phys. Rev. Lett., 2003. **91**(14).
83. Strobl, M., Treimer, W., Hilger, A., *First realisation of a three-dimensional refraction contrast computerised neutron tomography.* Nucl. Instr. & Methods B, 2004. **222**(653).

84. Lehmann, E., et al., *Non-destructive testing with neutron phase contrast imaging.* Nuclear Instruments and Methods in Physics Research Section A: Accelerators, Spectrometers, Detectors and Associated Equipment, 2005. **542**(1-3): p. 95-99.
85. Schillinger, B., et al., *Detection systems for short-time stroboscopic neutron imaging and measurements on a rotating engine.* Nuclear Instruments and Methods in Physics Research Section A: Accelerators, Spectrometers, Detectors and Associated Equipment, 2005. **542**(1-3): p. 142-147.
86. Hillenbach, A., et al., *High flux neutron imaging for high-speed radiography, dynamic tomography and strongly absorbing materials.* Nuclear Instruments and Methods in Physics Research Section A: Accelerators, Spectrometers, Detectors and Associated Equipment, 2005. **542**(1-3): p. 116-122.
87. Cippo, E.P., et al., *Imaging of cultural heritage objects using neutron resonances.* J. Anal. At. Spectrom, 2011. **26**.
88. Postma, H. and P. Schillebeeckx, *Neutron Resonance Capture and Transmission Analysis*, in *Encyclopedia of Analytical Chemistry*. 2006, John Wiley & Sons, Ltd.
89. *ANCIENT CHARM.* [cited 2011 08-04]; Available from: http://ancient-charm.neutron-eu.net/ach.
90. Kardjilov, N., et al., *Three-dimensional imaging of magnetic fields with polarized neutrons.* Nat Phys, 2008. **4**(5): p. 399-403.
91. Hilger, A., Kardjilov, N., Strobl, M., Treimer,W., Banhart, J., *The new cold neutron radiography and tomography instrument CONRAD at HMI Berlin.* Physica B, 2006. **385-386**: p. 1213-1215.
92. Coldea, R., Tennant, D. A., Habicht, K., Smeibidl, P., Wolters, C., Tylczynski, Z., *Direct Measurement of the Spin Hamiltonian and Observation of Condensation of Magnons in the 2D Frustrated Quantum Magnet Cs_{2}CuCl_{4}.* Physical Review Letters, 2002. **88**(13): p. 137203.
93. Lake, B., et al., *Spins in the Vortices of a High-Temperature Superconductor.* Science, 2001. **291**(5509): p. 1759-1762.
94. Brandstätter, G., et al., *Neutron diffraction by the flux line lattice in YBa2Cu3O7-[delta] single.* Physica C: Superconductivity, 1997. **282-287**(Part 4): p. 2089-2090.
95. Lehmann, E.H., et al., *Neutron imaging--detector options and practical results.* Nuclear Instruments and Methods in Physics Research Section A: Accelerators, Spectrometers, Detectors and Associated Equipment, 2004. **531**(1-2): p. 228-237.
96. Schillinger, B. and E. Lehmann, *Detectors for Neutron Imaging.* Neutron News, 2006. **17**(1): p. 19-21.
97. Lehmann, E. and P. Vontobel, *The use of amorphous Silicon flat panels as detector in neutron imaging.* Applied Radiation and Isotopes, 2004. **61**(4): p. 567-571.
98. Sauli, F., *GEM: A new concept for electron amplification in gas detectors.* Nuclear Instruments and Methods in Physics Research Section A: Accelerators, Spectrometers, Detectors and Associated Equipment, 1997. **386**(2-3): p. 531-534.
99. Sauli, F., *Imaging with the gas electron multiplier.* Nuclear Instruments and Methods in Physics Research Section A: Accelerators, Spectrometers, Detectors and Associated Equipment, 2007. **580**(2): p. 971-973.
100. Cortesi, M., Zboray, R., Adams, R., Dangendorf, V., Prasser, H.M., *Concept of a novel fast neutron imaging detector based on THGEM for fan-beam tomography applications.* Journal of Instrumentation, 2012. **7**.
101. Tremsin, A.S., McPhate, J.B., Vallerga, J.V., Siegmund, O.H.W., Hull, J.S., Feller, W.B., Crow, L., Cooper, R.G., *High resolution neutron imaging at high counting rates with noiseless readout*, in *Proc. IEEE Nuclear Science Symp.* 2007: Honolulu. p. 270-275.
102. Domanus, J.C., *Neutron radiography, Techniques and Applications.* 1987, Risø National Laboratory. p. 33.

103. Strobl, M., Manke, I., Kardjilov, N., Hilger, A., Dawson, M., Banhart, J., *Advances in neutron radiography and tomography.* J. Phys.D: Appl.Phys., 2009. **42**.
104. Oswald, S.E., et al., *Quantitative Imaging of Infiltration, Root Growth, and Root Water Uptake via Neutron Radiography.* Vadose Zone Journal, 2008. **7**(3): p. 1035-1047.
105. Sakaguchi, H., et al., *Visualization of hydrogen in hydrogen storage alloys using neutron radiography.* International Journal of Hydrogen Energy, 2000. **25**(12): p. 1205-1208.
106. Sakaguchi, H., et al., *Analysis of hydrogen distribution in hydrogen storage alloy using neutron radiography.* Journal of Alloys and Compounds, 2003. **354**(1-2): p. 208-215.
107. Kardjilov, N., et al., *Industrial applications at the new cold neutron radiography and tomography facility of the HMI.* Nuclear Instruments and Methods in Physics Research Section A: Accelerators, Spectrometers, Detectors and Associated Equipment, 2005. **542**(1-3): p. 16-21.
108. Goers, D., et al., *In situ neutron radiography of lithium-ion batteries: the gas evolution on graphite electrodes during the charging.* Journal of Power Sources, 2004. **130**(1-2): p. 221-226.
109. Kardjilov, N., et al., *Applied neutron tomography in modern archaeology.* Nuovo cimento della Societa Italiana di Fisica C-Geophysics and space physics 2007. **30**(1).
110. Festa, G.e.a., *Neutron techniques in cultural heritage.* Archeometriai Műhely, 2006. **2**: p. 32-36.
111. Festa, G., et al., *Composition and corrosion phases of Etruscan Bronzes from Villanovan Age.* MEASUREMENT SCIENCE & TECHNOLOGY 2008. **19**(3).
112. Bragg, W.L. *The Diffraction of Short Electromagnetic Waves by a Crystal.* 1913: Proceedings of the Cambridge Philosophical Society.
113. Brokmeier, H.G., *Texture analysis by neutron diffraction.* Material Science Forum, 1994(157-162): p. 59-70.
114. Paradowska, A.M., Tremsin, A., Kelleher, J., Zhang, S.Y., Paddea, S., Burca, G. James, J.A., et al., *Modern and Historical Engineering Components Investigated by Neutron Diffraction on ENGIN-X.* Journal of Solid Mechanics and Materials Engineering, 2012. **6**(6): p. 408-418.
115. Hansen, T., Henry, P., Fischer, H., Torregrossa J., Convert, P., *The D20 instrument at the ILL: a versatile high-intensity two-axis neutron diffractometer* Meas. Sci. Technol., 2008. **19**(3).
116. Bennington, S., *Neutron Scattering - an introduction.* 2011, ISIS.
117. Pynn, R., *Neutron scattering - A Primer.* 1990, Los Alamos Science.
118. Windsor, C.G., *Pulsed Neutron Scattering.* 1981, London: Taylor and Francis.
119. Rietveld, H.M., *A profile refinement method for nuclear and magnetic structures.* Journal of Applied Crystalography, 1969. **2**: p. 65-71.
120. Pawley, G.S., *Unit-cell refinement from powder diffraction scans.* J. Appl. Crystallogr., 1981. **14**: p. 357-361.
121. Young, R.A., ed. *The Rietveld method.* 1993, Oxford University Press.
122. Allen, A., et al., *Measurement of internal stress within bulk materials using neutron diffraction.* NDT International, 1981. **14**(5): p. 249-254.
123. Withers, P.J., Bhadeshia , H.D.K.H, *Residual Stress Part 1 - Measurement Techniques.* Materials Science and Technology, 2001. **17**: p. 355-365.
124. Withers, P.J. and P.J. Webster, *Neutron and Synchrotron X-ray Strain Scanning.* 2001, Blackwell Publishing Ltd. p. 19-33.
125. Withers, P.J., Bhadeshia, H.K.D.H., *Residual Stress Part 2 - Nature and Origins.* Materials Science and Technology, 2001. **17**: p. 366-375.

126. Hill, R.J., Howard, C.J., *Quantitative phase analysis from neutron powder diffraction data using the Rietveld method.* Journal of Applied Crystalography, 1987. **20**: p. 467-474.
127. Larson, A.C., Von Dreele, R.B., *General Structure Analysis System (GSAS).* 2004, Los Alamos National Laboratory Report LAUR 86-748
128. Toby, B.H., *EXPGUI, a graphical user interface for GSAS.* J.Appl.Cryst., 2001. **34**: p. 210-213.
129. Matthies, S., Pehl, J., Wenk, H.R., Lutterotti, L., Vogel, S.C., *Quantitative texture analysis with the HIPPO TOF diffractometer.* J.Appl.Cryst., 2005. **38**(3): p. 462-465.
130. Copley, J.R.D., *The Joy of Acceptance Diagrams.* Journal of Neutron Research, 1993. **1**(2): p. 21-36.
131. Metropolis, N., Ulam, S., *The Monte Carlo method.* J.Amer.Statist.Assoc., 1949. **44**.
132. Forster, R., Godfrey, T., Alcouffe, R., Dautray, R., Forster, A., Ledanois, G., Mercier, B., *MCNP - a general Monte Carlo code for neutron and photon transport. in: Monte-Carlo Methods and Applications in Neutronics, Photonics and Statistical Physics.* 1985, Springer Berlin / Heidelberg. p. 33-55.
133. Seeger, P.A., Daemen, L.. *The neutron instrument simulation package, NISP*, in *SPIE - Advances in Computational Methods for X-Ray and Neutron Optics*, M. Sanchez del Rio, Editor. 2004. p. 109-123.
134. Lefmann, K., Nielsen, K., *McStas a general software package for neutron ray-tracing simulations*, in *Neutron news*. 1999. p. 20.
135. Zsigmond, G., Lieutenant, K., Mezei, F., *Monte Carlo simulations of neutron scattering instruments by VITESS: virtual instrumentation tool for ESS.* Neutron News, 2002. **13**(4): p. 11-14.
136. Lee, W.T., et al. *IDEAS - a Monte Carlo simulation package for neutron-scattering instrumentation.* 2002: Springer.
137. Willendrup, P., Farhi, E., Lefmann, K. *McStas 1.7 - a new version of the flexible Monte Carlo neutron scattering package* in *Proceedings of the Third European Conference on Neutron Scattering* 2004.
138. *McStas.* [cited 2008 10-04]; Available from: http://neutron.risoe.dk/.
139. Seeger, P.A., Daemen, L.L., Farhi, E., Lee, W.T., Passell, L., Šaroun, J., Wang, X.L., Zsigmond, G., *Monte Carlo Code Comparisons for a Model Instrument.* Neutron News, 2002. **13**(4): p. 24.
140. ANSI-C, *http://publicaa.ansi.org/sites/apdl/Documents/Standards%20Action/2005%20PDFs/SAV3648.pdf.*
141. Dev-CPP. *http://www.bloodshed.net/dev/packages/index.html.* [cited 2009 02-08].
142. PERL. *http://www.perl.org/.* [cited 2009 02-08].
143. MATLAB. *http://www.mathworks.com/products/matlab/.* [cited 2009 02-08].
144. Scilab. *http://www.scilab.org/.* [cited 2009 02-08].
145. PgPlot. *http://www.astro.caltech.edu/~tjp/pgplot/.* [cited 2009 02-10].
146. Shankland, K., Griffin, T., *Grid powers up at ISIS.* Scientific computing world, 2005(Oct/Nov).
147. Kockelmann, W., Oliver, E.C., Radaelli, P.G., *IMAT- An imaging and materials science & engineering facility for TS-II.* 2007, ISIS Second Target Station Project.
148. Tremsin, A.S., McPhate, J. B., Steuwer, A., Kockelmann, W., M Paradowska, A., Kelleher, J. F., Vallerga, J. V., Siegmund, O. H. W., Feller, W. B., *High-Resolution Strain Mapping Through Time-of-Flight Neutron Transmission Diffraction with a Microchannel Plate Neutron Counting Detector.* Strain, 2012. **48**(4): p. 296-305.
149. Arai, M., *J-Parc and the prospective neutron sciences.* Pramana - Journal of physics, 2008. **71**(4): p. 629-638.

150. Maier-Leibnitz, H. and T. Springer, *The use of neutron optical devices on beam-hole experiments on beam-hole experiments.* Journal of Nuclear Energy. Parts A/B. Reactor Science and Technology, 1963. **17**(4-5): p. 217-225.
151. Liouville, J., *Note sur la theorie de variation de constantes arbitraires.* J.Math. Pures Appl., 1838. **3**(9).
152. *http://www.swissneutronics.ch/products/concept-supermirror.html.*
153. *http://www.mirrotron.kfkipark.hu/history.html.* 2011.
154. Schoenborn, B.P., Caspar, D.L.D., Kammerer, O.F., *A novel neutron monochromator.* J. Appl. Cryst., 1974. **7**: p. 508-510.
155. Saxena, A.M., Schoenborn,B.P., *Multilayer neutron monochromators.* Acta Cryst. A, 1977. **33**: p. 805-813.
156. Mezei, F., *Novel polarized neutron devices: supermirror and spin component amplifier.* Communications on Physics, 1976. **1**: p. 81-85.
157. Oliver, E.C., *Effect of curved guide on IMAT.* 2008.
158. Manochine, S., *New software tools for simulations of new instruments for the future neutron sources*, in *Technische Universität Berlin.* 2005: Berlin. p. 144.
159. Kockelmann, W., Zhang, S.Y., Chapon, L.C., Burca, G., James, J.A., *IMAT: performance evaluation report.* 2010, ISIS.
160. Zhang, S.Y., *Private communication.* 2010: ISIS, UK.
161. Gorini, G., *PANAREA: Progretto per l'Applicazione Dei Neutroni alla Ricerca in Elletronica e Archaeometria.*, in *Project funded by CNR within the CNR-STFC agreement concerning scientific research at the ISIS neutron spallation source (2008-2014).*
162. Tremsin, A., McPhate, J.B., Kockelmann, W.A., Vallerga, J.A., Siegmund, O.H.W., Feller, W.B., *Energy-resolving neutron transmission radiography at the ISIS Pulsed Spallation Source with a high-resolution neutron counting detector.* IEEE TRANSACTIONS ON NUCLEAR SCIENCE, 2009. **56**(2931).
163. Kockelmann, W., Chapon, L. C., *IMAT choppers.* 2010.
164. Boin, M., *Developments towards the tomographic imaging of local crystallographic structures*, in *DDEM.* 2010, The Open University: Milton Keynes. p. 219.
165. Boin, M., Hilger, A., Kardjilov, N., Zhang, S.Y., Oliver, E.C., James, J.A., Randau, C., Wimpory, R.C. , *Validation of Bragg edge experiments by Monte Carlo simulations for quantitative texture analysis.* J. Appl. Cryst. , 2011. **44**(5): p. 1040-1046
166. Santisteban, J.R., Edwards, L., Steuwer, A., Withers, P.J., *Time-of-flight neutron transmission diffraction.* Journal of Applied Crystalography, 2001. **34**: p. 289-297.
167. Brooks, R.A., Chiro, G., *Beam Hardening in X-ray reconstructive tomography.* J. Phys. Med. Biol., 1976. **21**: p. 390-398.
168. James, J.A., Santisteban, J.R., Edwards, L., Daymond, M.R., *A virtual Laboratory for Neutron and Synchrotron Strain Scanning.* Physica B., Condensed Matter, 2004. **350**: p. 743-746.
169. James, J.A., Edwards, L., *Application of robot kinematics methods to the simulation and control of neutron beam line positioning systems.* Nuclear Instruments and Methods in Physics Research A, 2007. **571**: p. 709-718.
170. Kelsey, R.A., *Measuring Non-Uniform Residual Stresses by the Hole-Drilling Method*, in *SESA.* 1956. p. 181-194.
171. Jang, J.-i., et al., *Assessing welding residual stress in A335 P12 steel welds before and after stress-relaxation annealing through instrumented indentation technique.* Scripta Materialia, 2003. **48**(6): p. 743-748.
172. Cheng, W., Finnie, Iain, *Residual Stress Measurement and the Slitting Method.* Mechanical Engineering Series Vol. XIV. 2007: Springer.

173. Johnson, G., *Residual stress measurements using the contour method.* 2008, University of Manchester.
174. Prime, M.B., *Cross-sectional mapping of residual stresses by measuring the surface contour after a cut.* Journal of Engineering Materials and Technology, 2001. **123**(2): p. 162-168.
175. Paradowska, A., et al., *A neutron diffraction study of residual stress due to welding.* Journal of Materials Processing Technology, 2005. **164-165**(0): p. 1099-1105.
176. Hartnell, P., *Manufacture of Reproduction Superheater Bifurcations and Tube Butt welds for Creep-Fatigue Testing by British Energy.* 2008.
177. *http://www.andor.com/scientific_cameras/.* 2011.
178. Rivers, M. *http://cars9.uchicago.edu/software/idl/tomography.* 2010.
179. James, J.A., Oliver, E.C., Paradowska, A., Hubbard, C.R., Schmidlin, J., Edwards, L., *Robotics methods for beam line instrument simulation and control*, in *NOBUGS2008.* 2008.
180. Brule, A. and O. Kirstein, *Residual stress diffractometer KOWARI at the Australian research reactor OPAL: Status of the project.* Physica B: Condensed Matter, 2006. **385-386, Part 2**(0): p. 1040-1042.
181. Wang, X.L., et al., *VULCAN--The engineering diffractometer at the SNS.* Physica B: Condensed Matter, 2006. **385-386**(Part 1): p. 673-675.
182. Kockelmann, W., Chapon, L. C., Radaelli, P. G., *Neutron texture analysis on GEM at ISIS.* Physica B: Condensed Matter, 2006. **385-386, Part 1**(0): p. 639-643.
183. Oliver, E.C., Santisteban, J., James, J.A., Daymond, M., Dann, J., *ENGIN-X user manual.* 2004, ISIS, Rutherford Laboratory.
184. Campbell, S.I., *Open Genie-Analysis and Control.* 2002.
185. Pierret, S., et al., *Combining neutron diffraction and imaging for residual strain measurements in a single crystal turbine blade.* NDT & E International, 2012. **45**(1): p. 39-45.
186. Van Langh, R., Lehmann, E., Hartmann, S., Kaestner, A., Scholten, F., *The study of bronze statuettes with the help of neutron-imaging techniques.* Analytical And Bioanalytical Chemistry, 2009. **395**(7): p. 1949-1959.
187. Bewer, F.G., *A Study of the Technology of Renaissance Bronze Statuettes*, in *Dept. of Archaeological Conservation and Materials Science.* 1996, University College of London: London. p. 601.
188. Scholten, F., Verber, M., *From Vulcan's forge: Bronzes from the Rijksmuseum Amsterdam 1450-1800*, R. Amsterdam, Editor. 2005.
189. Rijksmuseum. *http://www.rijksmuseum.nl/tentoonstellingen/werkplaats-van-vulcanus.*
190. Siano, S., Bartoli, L., Zoppi, M., Kockelmann, W., Daymond, M., Dann, J.A., Garagnani, M.G., Miccio, M. *Microstructural bronze characterisation by time of flight neutron diffraction.* in *Archaeometallurgy in Europe.* 2003.